Towards High Precision Measurements of Higgs Boson Properties in the Di-Tau Decay with the ATLAS Detector

Dissertation
zur
Erlangung des Doktorgrades (Dr. rer. nat.)
der
Mathematisch-Naturwissenschaftlichen Fakultät
der
Rheinischen Friedrich-Wilhelms-Universität Bonn

vorgelegt von
Lena Maria Herrmann
aus
Saarlouis

Bonn, September 2024

Angefertigt mit Genehmigung der Mathematisch-Naturwissenschaftlichen Fakultät der Rheinischen Friedrich-Wilhelms-Universität Bonn

Gutachter/Betreuer:	Prof. Dr. Klaus Desch
Gutachter:	Prof. Dr. Jochen Dingfelder
Tag der Promotion:	02.12.2024
Erscheinungsjahr:	2025

Acknowledgements

To all the great people who paved my way, offered help and support and shared formative memories. You made my journey all the more colorful! Thank You!

Abstract

The Standard Model of particle physics (SM) describes the known fundamental particles and their interactions. The model is found to be incomplete with a need for extensions in order to cover all current experimental observations. The Higgs boson is associated to the Higgs field, which is responsible for the acquisition of the elementary particle masses. With its central role in the SM, the Higgs and precision measurements of its properties provide anchor points for possible model extensions.

The Higgs decay into two τ leptons is well-suited to explore the boson's properties. The distinct decay signature and high branching ratio of the decay channel offer strong sensitivity in the measured observables and provide prominent access to the Yukawa coupling of leptons to the Higgs boson. The differential exploration of the available phase-space promises hints for unknown physics phenomena. The selection of phase-space regions is based on the Simplified Template Cross-Section (STXS) approach, which is optimized to reduce theoretical uncertainties while maximizing sensitivity for physics beyond the SM.

The $H \rightarrow \tau\tau$ measurement employs a binned-profile likelihood fit and is based on the ATLAS Run 2 dataset recorded at the Large Hadron Collider (LHC). The most precise cross-section measurement in the Vector-Boson-Fusion (VBF) production mode to date yields a value of $0.93^{+0.17}_{-0.15}$ relative to the SM prediction. A selection of 18 phase-space regions are measured in the STXS analysis approach. Eight VBF-related regions comprise the first measurements of the high $p_T^H > 200\,\text{GeV}$ and high $m_{jj} > 1.5\,\text{TeV}$ phase-space region $\left(1.29^{+0.39}_{-0.34}\right)$, as well as the most precise exploration of the low $p_T^H < 200\,\text{GeV}$ region in combination with a high $m_{jj} > 1.5\,\text{TeV}$ selection $\left(0.12^{+0.34}_{-0.33}\right)$.

Precision in SM measurements necessitates the validation and optimization of advanced analysis strategies within a collaborative effort. Towards an improved reconstruction of the second largest background in the analysis, the misidentified τ leptons (fakes), a decay-mode dependent fake estimation is investigated. Apart from a more detailed description of the background, the new approach enables the definition of phase-space regions with increased signal over background ratio. To improve sensitivity by reduced uncertainties, a combination of fake-templates across phase-space regions is implemented. The combination of templates reduces statistical uncertainties on the shape and adds to the stability of the fit setup.

In the upcoming high-luminosity era of the LHC, reliable and computationally efficient reconstruction is a core-requirement. The optimization of a Recurrent Neural Network for electron particle identification bridges the current reconstruction algorithms to the future of object reconstruction in high-energy physics.

Contributions From The Author

Particle physics experiments reach levels of complexity that necessitate a global, collaborative approach to produce scientific output. The work of this thesis is conducted under the umbrella of the ATLAS collaboration, which comprises a total of ~ 6000 members and ~ 3000 scientific authors [1]. The following list of project involvements central to this thesis highlight the personal contribution of the author.

Particle Identification in the Transition Radiation Tracker

In the scope of the ATLAS qualification task, which grants ATLAS authorship, a Recurrent Neural Network for electron identification in the Transition Radiation Tracker is optimized. The research is summarized in an internal note [2].

- The model is improved in terms of its complexity (architecture, selection of inputs or activation functions) resulting in a reduction of required computing resources.
- Batch-training of sequenced data with variable length is improved by the application of masking layers.
- A model is trained and evaluated on the Run 3 gas geometry and prepared for the application in upstream software frameworks.
- The interchangeability of muons and pions as background samples is investigated.

The Run 2 $H \rightarrow \tau\tau$ Cross-Section Measurement

The Legacy Run 2 $H \rightarrow \tau\tau$ Cross-Section Measurement is based on a binned profile likelihood fit following the Simplified Template Cross-Section approach. The results are published in [3]. In the scope of the analysis, following projects are pursued:

- The non-τ (fake) background is studied by exploring strategies to enhance the sensitivity of the measurement. The efforts comprise:
  - a decay-mode dependent fake estimation as well as a re-definition of signal regions to reduce the background contamination.
  - the preparation of a decay-mode dependent efficiency correction factor measurement to account for the imperfect reconstruction.

  - a combination of fake templates across phase-space regions to reduce the statistical uncertainties on the fake template shape and to increase the fit setup stability.

- Various scrutinizing tests are conducted to validate the fit setup. Examples are
  - the investigation of nuisance parameter pulls and constraints followed by studies with adapted fit-setup configurations.
  - the assessment of impact from different symmetrization strategies on nuisance parameters.
  - the investigation of the role of systematic uncertainty groups.
  - the investigation of setup changes and their impact on the PoIs.
  - the validation of combined fake templates in the fit setup.

- Direct contributions to the production of the final physics results are
  - an improvement of the analysis setup by implementing and validating the combined fake templates.
  - the preparation and execution of the fit setup to yield the final results.
  - the execution of a share of computationally expensive ranking plot.
  - the representation of the analysis group in conferences as well as collaboration-internal approval talks.

Contents

1 Introduction **1**

2 The Standard Model **5**
2.1 Theoretical Foundation 6
2.1.1 Lagrange Formalism 6
2.1.2 Electromagnetic Interaction 8
2.1.3 Quantum Chromodynamics 9
2.1.4 Weak Interaction 10
2.1.5 Electroweak Unification 10
2.2 Higgs Mechanism 12
2.2.1 Electroweak- Symmetry Breaking 12
2.2.2 Yukawa Interaction 14
2.3 Particle Profiles 14
2.3.1 τ Lepton 14
2.3.2 Higgs boson 17
2.4 Beyond the Standard Model 17

3 Methodology of Data Collection & Simulation **21**
3.1 Large Hadron Collider 21
3.1.1 Operation 21
3.1.2 Luminosity 22
3.1.3 The High-Luminosity LHC 23
3.2 The ATLAS Detector 24
3.2.1 Coordinate System 25
3.2.2 The Sub-systems 26
3.2.3 Data Acquisition & Processing 28
3.3 Simulation 30
3.3.1 Methodology 30
3.3.2 Specification of Generated Events 31

4 Event Reconstruction **33**
4.1 Electrons 33
4.2 Muons 35
4.3 Jets 36
4.4 Missing Transverse Energy 37

4.5 Hadronic τ-Leptons . . . 38
4.6 Di-Tau Mass Reconstruction . . . 41
4.6.1 Collinear Approximation . . . 41
4.6.2 Missing Mass Calculator . . . 42
4.6.3 Neural Network . . . 43

5 Particle Identification with the Transition Radiation Tracker 45
5.1 Outline . . . 45
5.2 Recurrent Neural Networks . . . 46
5.3 The Setup . . . 47
5.4 Training Prerequisites . . . 50
5.4.1 Event Selection . . . 50
5.4.2 Figure of Merit . . . 51
5.5 Reduction of Complexity . . . 52
5.5.1 Input's Relevance . . . 53
5.5.2 Number of Nodes . . . 53
5.5.3 Activation Function . . . 54
5.6 Background Validation . . . 56
5.6.1 Validation Strategy & Results . . . 56
5.7 Run 3 performance on MC . . . 57
5.8 Outlook . . . 59

6 H$\rightarrow \tau\tau$ Simplified Template Cross-Section Analysis 61
6.1 Binned Profile Likelihood Fit . . . 61
6.1.1 Nuisance Parameters . . . 63
6.1.2 Minimization & Parameter Uncertainties . . . 65
6.2 STXS-Framework . . . 66
6.2.1 Target Phase-Space . . . 67
6.3 Event Selection . . . 68
6.4 Event Categorization . . . 70
6.5 Background Estimation . . . 72
6.5.1 $Z \rightarrow \tau\tau$ Estimation via Parametrized Object Level Embedding . . . 73
6.5.2 Estimation of misidentified τ processes . . . 74
6.5.3 Top Background . . . 74
6.5.4 Others . . . 75
6.6 Systematic Uncertainties . . . 75
6.7 Analysis Design . . . 75
6.7.1 Event Sub-Categorization . . . 75
6.7.2 Alternative Settings . . . 77
6.8 Improvements of the Legacy Setup . . . 79

7 Studies of the non-τ Background 81
7.1 Fake Estimation Methods . . . 81
7.1.1 Matrix Method . . . 81
7.1.2 Fake Factor Method . . . 82

7.2 Fake Background Estimation in the $\tau_{\text{had}}\tau_{\text{had}}$ Channel . . . 85
7.2.1 Application . . . 86
7.2.2 Systematic Uncertainties . . . 88
7.3 Decay-Mode Dependent Fake Estimation . . . 89
7.3.1 Motivation . . . 89
7.3.2 Fake Factor Calculation . . . 89
7.3.3 Validation . . . 91
7.3.4 Signal Region Split . . . 93
7.3.5 Decay-Mode Efficiency Correction Factors . . . 94
7.3.6 Systematic Uncertainties . . . 96
7.3.7 Outlook . . . 98
7.4 Fake Template Combination . . . 99
7.4.1 Combination Strategy . . . 99
7.4.2 Systematic Uncertainties . . . 103

8 Fit Results **107**
8.1 Asimov Studies . . . 107
8.1.1 Setting 18 Parameters of Interest . . . 108
8.1.2 Combined Fake Templates . . . 111
8.2 Partially Unblinded Fits . . . 114
8.2.1 Random Scaling . . . 114
8.3 Unblinded STXS Results . . . 120
8.3.1 Post-Fit Studies of the Background . . . 120
8.3.2 Inclusive & Production Mode Dependent Measurement . . . 123
8.3.3 18 PoI Result . . . 124
8.4 Analysis Landscape & Perspectives . . . 130
8.4.1 CMS Run 2 Results . . . 130
8.4.2 Lessons learned & Consequences for Future Measurements . . . 130

9 Conclusion **133**

A Auxiliary Material for Chapter 5 **135**

B Auxiliary Material for Chapter 6 **141**

C Auxiliary Material for Chapter 7 **143**

D Auxiliary Material for Chapter 8 **155**

Bibliography **177**

List of Figures **191**

List of Tables **195**

CHAPTER 1

Introduction

This thesis addresses the *Higgs boson cross-section measurement in the vector-boson fusion production mode with a focus on the falsely identified tau background in the di-tau channel with the ATLAS detector*. That says it all, right? A singular title only condenses the main acts out of three years of research, the facets and fascination of particle physics are hardly conveyed. Across generations, physicists dedicate their time and energy to explore the properties of elementary particles in hopes to complete the underlying theory of nature.

In 2012, the world turned the spotlight on CERN (**C**onseil **E**uropéen pour la **R**echerche **N**ucléair) in Geneva, Switzerland, where the experiments along the world's largest particle accelerator, the Large Hadron Collider (LHC), presented their latest measurement results. In a live-streamed seminar, a particle discovery was announced and attributed to the last missing piece of the Standard Model of particle physics (SM), the Higgs boson. The all-embracing nature of the Standard Model spans from the early universe, right after the big bang to the present day and describes the building blocks of matter and their interactions.

The discovery initiated a series of measurements, revealing the particle's properties including mass, spin and decay-width as well as the exploration of its couplings to decay-products. Higgs measurements at CERN are lead by the two multi-purpose detectors ATLAS and CMS. Over the course of the second data taking period, both experiments have confirmed the Higgs boson within the predictions of the SM. The Higgs boson is a central component of the theory, as its associated field, the Higgs field, is responsible for the acquisition of the elementary particle masses. As of today, the Higgs properties agree with the SM prediction to a level of ~10% [4].

From experimental observations in astro- and high-energy physics, the theory is found to be incomplete. Phenomena, such as matter/ anti-matter asymmetry or dark matter are not yet covered by a theoretical description. Consequently, SM extensions are required, which might become accessible by precision measurements of the Higgs boson's properties.

The next-generation high-luminosity LHC is set to provide another magnitude of collisions to the experiments. The resulting amount of measurement data drastically reduces the statistical uncertainty on the pivotal physics observables. A new pinnacle of precision and improved sensitivity to beyond the Standard Model (BSM) physics will be accessible in upcoming data taking periods. The Higgs couplings are expected to be measured with a precision of 1-5% [4].

The future perspective of high-energy physics strives to push the precision frontier further with next-generation accelerator facilities, so-called Higgs factories. The aspired precision of Higgs

coupling-measurements extends to the sub-percent regime [5].

The Higgs boson can be produced and decays through different channels. So far, all accessible combinations of Higgs production channels and decay-modes were measured. Each individual measurement faces individual challenges that result in different levels of sensitivity for the targeted observable. Responsible factors are for example, the production cross-section, the decay branching fraction, the reconstructed mass resolution, the selection efficiency or the level of background contribution in the final state.

The Higgs boson decay into two τ leptons lies at the heart of this thesis. The di-tau channel ($H \rightarrow \tau\tau$) is of particular interest due to its strong coupling to the Higgs field in conjunction with the high mass of the τ lepton. The so-called Yukawa-coupling is central to the SM and describes the individual coupling of a lepton-class particle to the Higgs field. Large background contributions complicate the measurement in the di-tau channel. The most dominant background are $Z \rightarrow \tau\tau$ events, which not only exhibit a detector signature similar to the signal process, but also a similar invariant mass. Missing neutrinos from the τ lepton decay complicate the di-tau mass reconstruction and decrease the separation power of signal and background. Misidentified τ leptons or "fakes" constitute the second dominant background.

The first evidence of the Higgs boson decaying into a pair of τ leptons was found in Run 1 data, recorded between 2009 and 2013 [6, 7]. The observation was established from a combination of ATLAS and CMS results [8]. According to the latest ATLAS results [9], good sensitivity of the di-tau channel is observed in the vector boson fusion (VBF) production mode. Here, background can be largely reduced due to the selection of two jets from hard scattering.

With a production cross-section of $\sim 4\,\text{pb}$ [10], an integrated luminosity of $140\,\text{fb}^{-1}$ [11] and a branching fraction of $\sim 6\%$ [12] about 33600 VBF $H \rightarrow \tau\tau$ events are expected in the Run 2 dataset. This amount of data allows the differential exploration of phase-space regions, which are sensitive to BSM physics. Possible new interactions of particles that modify the Higgs production mechanism are likely to occur for boosted Higgs bosons [13]. The di-tau channel provides good sensitivity in this high p_T^H regime.

The current $H \rightarrow \tau\tau$ cross-section measurement takes on the search for new physics by exploring the available phase-space in detail. Possible deviations of the measurement from the Standard Model prediction are potential hints for BSM physics. The phase-space region selection is based on the Simplified Template Cross-Section (STXS) approach, which is optimized to reduce theoretical uncertainties, while maximizing sensitivity for BSM physics. The collaborative work is summarized in a dedicated publication [3]. In order to advance in the precision domain, not only more data but also novel approaches in data analysis need to be developed. The latter is crucial to exploit the full physics potential of the current dataset, which can indicate directions for future measurements. A gain in sensitivity can either be achieved by an improved signal to background ratio or reduced uncertainties. Both aspects are addressed in fake-related studies.

The theoretical introduction in Chapter 2 provides a self-contained overview of the topic, by setting the Higgs and the τ lepton in context with the SM-theory. The methodology of data collection at the LHC and the principles of simulation are discussed in Chapter 3. Both are key aspects of ATLAS data analysis, where the theoretical prediction represented by simulated Monte Carlo samples is compared to the measurement data. For both, simulation as well as measurement, consistent data reconstruction yields physically meaningful quantities. The applied procedure results in objects associated to particles, like electrons, or event properties, like missing energy, and is discussed in Chapter 4. An important reconstructed property is the particle identification score. It represents the

probability of correct particle type assignment and enables to balance signal purity against background rejection. For electron identification, a Recurrent Neural Network was developed in former studies, which uses measurements of the ATLAS Transition Radiation Tracker as input. This network is optimized in terms of CPU-consumption and trained for the current Run 3 detector conditions as discussed in Chapter 5. The remaining chapters are dedicated to the $H \rightarrow \tau\tau$ analysis and study improvements of the analysis setup. In Chapter 6, the general analysis outline is presented. Apart from the STXS framework, the selected binning, background estimation strategies and novelties in property reconstruction are highlighted. Striving for increased measurement precision, different approaches to improve the fake background reconstruction are discussed in Chapter 7. A τ lepton decay-mode dependent reconstruction enables a phase-space split into regions with improved signal over background ratio. A reduction of shape uncertainties is achieved by a combination of fake templates across suited phase-space regions. The latter is addressed in Chapter 8, which is dedicated to the measurement results of the Run 2 $H \rightarrow \tau\tau$ analysis. The focus of discussion is placed on fake-related novelties as well as central aspects necessary for the validation of the setup. A final summary is given in Chapter 9.

CHAPTER 2

The Standard Model

Our understanding of the universe is primarily based on a comprehensive theory, known as the Standard Model of particle physics. It describes the fundamental particles as well as their interactions. Developed throughout the 20th century, the Standard Model is constructed upon 26 independent variables[1] [14]. These variables comprise the twelve fermion masses, the three coupling strengths of the gauge interactions, two parameters of the Higgs potential, eight flavor mixing angles and the strong CP-phase. These parameters are not predicted by the theory itself and require experimental determination. Over the past 40 years, the Standard Model theory withstood tremendous validation campaigns. The first experimental confirmation was the observations of weak currents [15] in 1973. A decade later, in 1983, the mediator particles of the weak force, the $W^{\pm}$ and Z bosons, were observed by CERN's UA1 and UA2 collaborations [16–18]. Subsequent precision measurements, especially those focusing on the Z boson's properties, were conducted at accelerators, such as the Large Electron-Positron Collider (LEP). Within a few decades, all Standard Model fermions were discovered. The J/Ψ particle, indicating the presence of the c-quark, was observed in 1974 [19, 20], followed by the discovery of the bottom quark at Fermilab in 1977 [21]. The top quark was one of the later findings, discovered in 1995 [22]. However, a significant piece was still missing — the Higgs boson. Its existence is crucial to validate the mechanism responsible for the mass acquisition of elementary particles.

The discovery of the Higgs boson in 2012 [23, 24] marked a significant milestone in particle physics. The Standard Model was further scrutinized and emerged to be a robust and successful description of various phenomena in nature. However, not all observations are adequately understood and not described by the theory, which is why today's research focuses on exploring physics beyond the Standard Model. Precision measurements of key parameters within the theory have become a focal point of scientific research, offering potential insights into physics beyond the Standard Model. This thesis is part of the ongoing effort to uncover hints that may lead to a broader understanding of our universe.

The following chapter provides a brief overview of the Standard Model, with an emphasis on topics relevant to the direct understanding of this thesis. For readers interested in further details, various books and papers, such as [14], are recommended.

[1] The number of 26 parameters assumes neutrinos to be Dirac fermions and also takes the strong CP phase into account, which is close to zero.

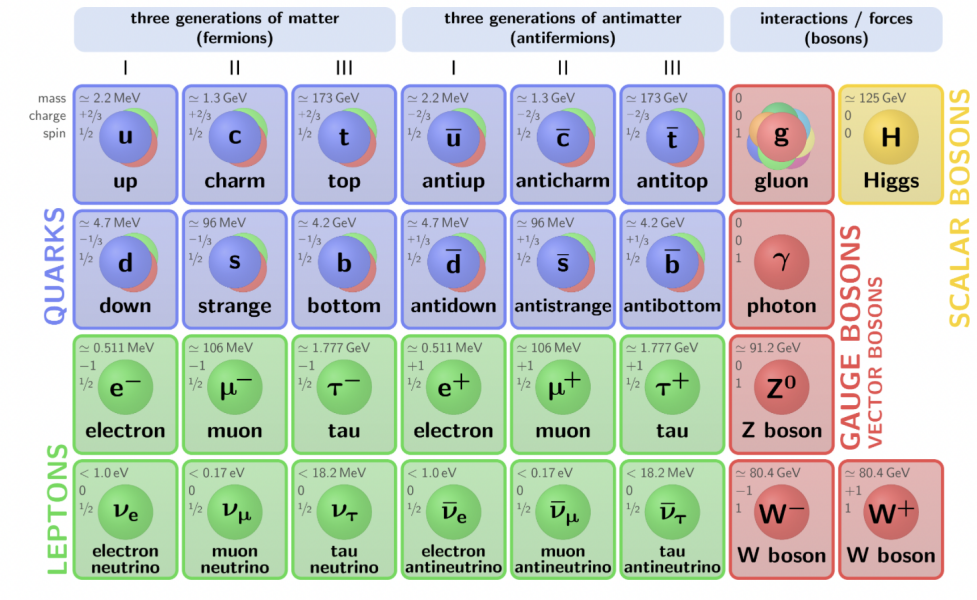


Figure 2.1: The Standard Model particles and their corresponding anti-particles. Quarks are depicted in blue, leptons in green, the gauge bosons in red and the Higgs boson in yellow. Particles that carry color-charge are marked by colored fields. Credit [25].

2.1 Theoretical Foundation

The Standard Model is built on the principles of Quantum Field Theory (QFT), which interprets particles as excitations of quantum fields, with each type of particle corresponding to a different field. At its core, the Standard Model categorizes elementary particles into three families: quarks, leptons, and gauge bosons (see Figure 2.1). Quarks and leptons, the building blocks of matter, are spin-1/2 particles known as fermions. Each fermion has an anti-particle partner with identical properties but opposite charge. Gauge bosons, which are spin-1 particles, mediate the fundamental forces, each differing in range and strength. The Standard Model describes three fundamental forces: electromagnetism, the weak force, and the strong force. Quarks, which carry a color charge, interact via the strong force. Electrically charged particles participate in electromagnetic interactions, and both quarks and leptons engage in weak interactions.

The Standard Model is a gauge theory based on the concept of symmetries, utilizing the gauge groups $SU(3)_C \times SU(2)_L \times U(1)_Y$. A gauge group defines the symmetry transformations under which the Standard Model Lagrangian remains invariant, which ensures the consistency of the theory and the validity of its physical laws. The $SU(3)_C$ group corresponds to the strong force. The weak and the electromagnetic force are described by the unified $SU(2)_L \times U(1)_Y$ group, which is spontaneously broken by the Higgs mechanism, described in Section 2.2.

2.1.1 Lagrange Formalism

To describe the dynamics of the quantum fields, Lagrangian densities are used to derive the field equations. The Standard Model Lagrangian consists of different components, capturing the dynamics

and interactions of different particle fields. Apart from the kinetic dynamics of gauge and spin-1/2 particles, mass acquisition of particles as well as the Higgs properties are covered. Furthermore, interaction terms between fermion and gauge fields are included [26]. The Standard Model Lagrangian is a combination of the aforementioned contributions, such that

$$\mathcal{L}_{\mathrm{SM}} = \mathcal{L}_{\mathrm{kin}}^{\mathrm{Lepton}} + \mathcal{L}_{\mathrm{IA}} + \mathcal{L}_{\mathrm{kin}}^{\mathrm{gauge}} + \mathcal{L}_{\mathrm{kin}}^{\mathrm{Higgs}} + \mathcal{L}_{\mathrm{V(\Phi)}}^{\mathrm{Higgs}} + \mathcal{L}_{\mathrm{Yukawa}}. \tag{2.1}$$

These individual contributions follow themselves Lagrange-specific rules, which are driven by the involved particle fields.

- **Scalar Fields:** The Lagrangian describing the dynamics of the Higgs field, which is a scalar field Φ, follows the form [14]

$$\mathcal{L}_{\mathrm{scalar}} = \frac{1}{2}\partial_\mu \Phi \partial^\mu \Phi - V(\Phi), \tag{2.2}$$

  with the space-time derivative ∂_μ. The term $\frac{1}{2}(\partial_\mu \Phi)(\partial^\mu \Phi)$ describes the kinetic energy of the scalar field. The term $V(\Phi)$ represents the potential energy. For a scalar field, the potential typically takes the form [14]

$$V(\Phi) = \frac{1}{2}m^2\Phi^2 + \frac{\lambda}{4}\Phi^4. \tag{2.3}$$

  The first term corresponds to the rest mass of the field, with the mass m of its field quanta. The second term describes the field's self-interaction with the corresponding coupling constant λ. To derive the equations of motions, the Euler-Lagrange equation[2], which, when applied on a scalar field, results in the Klein-Gordon wave equations [14].

- **Dirac Fields:** The dynamics of free Dirac Fermion fields follows [26]

$$\mathcal{L}_{\mathrm{Dirac}} = \bar{\Psi}(i\gamma^\mu \partial_\mu - m)\Psi, \tag{2.4}$$

  with the fermion field Ψ, the fermion mass m and the gamma matrices γ^μ. The fermion field Ψ, is a four-component spinor, consisting of the two spin-configurations of the particle and the corresponding anti-particle, respectively. Following the Euler-Lagrange equations, the equation of motions for spinor fields can be derived resulting in the Dirac equation [14].

- **Gauge Fields:** The dynamics of gauge fields is described by [26]

$$\mathcal{L}_{\mathrm{kin,gauge}} = -\frac{1}{4}F_{\mu\nu}F^{\mu\nu} \tag{2.5}$$

  with the field strength tensor $F^{\mu\nu}$, which takes derivatives of the gauge fields into account.

In general, kinetic energy terms include partial derivatives, mass terms are expressed by squared fields and interactions between particle and gauge fields contain the field representatives, multiplied by a constant factor representing the coupling strength.

[2] $\frac{d}{dt}\left(\frac{\partial \mathcal{L}}{\partial \dot{q}}\right) - \frac{\partial \mathcal{L}}{\partial q} = 0$ with the generalized coordinates q and their time derivative $\dot{q}$[14]

2.1.2 Electromagnetic Interaction

The electromagnetic force acts on particles that carry an electric charge. Its strength decreases with the inverse square of the distance between the charges. The underlying quantum field theory is Quantum Electrodynamics (QED). The massless photon γ is the force carrier. In the Standard Model, the electromagnetic force is embedded as a $U(1)_{\text{em}}$ gauge symmetry, which emerges from the spontaneous symmetry breaking of the $SU(2)_L \times U(1)_Y$ symmetry group. The $U(1)_{\text{em}}$ symmetry describes local phase-transformation of the kind [26]

$$\Psi(x) \rightarrow \Psi'(x) = e^{i\alpha(x)}\Psi(x), \tag{2.6}$$

where $\Psi(x)$ is the wave function of the charged particle.

The electromagnetic interaction emerges from the Dirac Lagrangian in Equation 2.4, which describes fermions such as electrons. Gauge invariance is preserved if the Lagrangian remains unchanged under the symmetry transformation. To satisfy this requirement, the electromagnetic field A_μ is introduced. The coupling strength of charged particles to the field is in the low energy regime described by the electromagnetic coupling strength [14]

$$\alpha_{\text{em}} = \frac{e^2}{4\pi\epsilon_0\hbar c} = \frac{1}{137}, \tag{2.7}$$

with the elementary charge e, the permittivity of free space ϵ_0, the Plack constant $\hbar = h/2\pi$ and the speed of light c.

The electromagnetic field transforms under the local gauge transformation as follows[26]

$$A_\mu \rightarrow A_\mu - \frac{1}{e}\partial_\mu\alpha(x) \tag{2.8}$$

To maintain the invariance of the Lagrangian under the local gauge transformation, the partial derivative ∂_μ is replaced by the gauge covariant derivative D_μ, which incorporates the electromagnetic field A_μ. The gauge covariant derivative is defined as [26]

$$\partial_\mu \rightarrow D_\mu = \partial_\mu + ieA_\mu \tag{2.9}$$

Apart from describing the behavior of a Dirac particle in an electromagnetic field, it is also necessary to describe the field dynamics themselves. The Lagrangian of the free electromagnetic field is based on the gauge Lagrangian in Equation 2.5 with [26]

$$F_{\mu\nu} = \partial_\mu A_\nu - \partial_\nu A_\mu, \tag{2.10}$$

where $F_{\mu\nu}$ is the electromagnetic field strength tensor. Consequently, the Lagrangian describing the electromagnetic interaction is given by [26]

$$\mathcal{L}_{\text{em}} = \underbrace{\bar{\Psi}(i\gamma^\mu\partial_\mu - m)\Psi}_{\text{free fermion field}} \underbrace{- e\bar{\Psi}\gamma^\mu\Psi A^\mu}_{\text{IA}} \underbrace{- \frac{1}{4}F_{\mu\nu}F^{\mu\nu}}_{\text{gauge}}. \tag{2.11}$$

This Lagrangian can be divided into three parts: the free fermion field term, which includes the

kinetic and mass terms, the interaction term (IA) between the fermion and the gauge field and the term describing the dynamics of the gauge field itself.

According to Noether's theorem [27], every continuous symmetry gives rise to a conserved quantity. This theorem also applies to $U(1)_{\text{em}}$ symmetry, which leads to the conservation of electric charge.

2.1.3 Quantum Chromodynamics

Quantum Chromodynamics (QCD) is the quantum field theory that describes the strong interaction. The strong force couples to color charge, which exists in three flavors: red, green and blue. Quarks carry color charge, so their fields exist as triplets in color space. The underlying symmetry group is $SU(3)_c$, a special unitary group of degree three, which describes the transformation between the three color charges. It is a non-Abelian transformation, meaning that the group operations are non-commutative. The force carriers are gluons, which themselves carry color charge. Eight different gluons exist, which are associated to eight generators of the group G^a_μ, where $a \in [1, 8]$. To maintain gauge invariance, the covariant derivative is introduced as follows [14]:

$$D_\mu = \partial_\mu - i g_s \frac{\lambda^a}{2} G^a_\mu \tag{2.12}$$

The covariant derivative includes the strong coupling constant g_s, and the eight Gell-Mann matrices λ^a, which serve as the generators [3] of the $SU(3)_c$ gauge group. The dynamics of the gauge fields G^a_μ are based on the gauge Lagrangian in Equation 2.5 with the field strength tensor G^a_μ given by[14]:

$$G^a_\mu = \partial_\mu G^a_\nu - \partial_\nu G^a_\mu - g_s f^{abc} G^b_\mu G^c_\nu. \tag{2.13}$$

The structure constants f^{abc} describe the commutation relations of the Gell-Mann matrices. The term $g_s f^{abc} G^b_\mu G^c_\nu$ accounts for the self-interaction of gluons.

By combining the quark and gluon components, the QCD Lagrangian is defined as follows [26]

$$\mathcal{L}_{\text{QCD}} = -\frac{1}{4} G^a_{\mu\nu} G^{\mu\nu}_a + \sum_f \bar{\Psi}_f (i\gamma^\mu D_\mu - m_f)\Psi_f. \tag{2.14}$$

It takes the sum over all quark flavors into account.

The strong force is limited to a range approximately the size of a nucleus (fm). It is characterized by its running coupling strength α_S. At very short distances the strong coupling constant α_S approaches zero, resulting in colored objects being nearly free, a phenomenon known as *asymptotic freedom*. However, at larger distances, the potential of the strong force increases, causing quarks to combine into color-neutral objects. This regime with the coupling strength in the order of one is described by the term *confinement*. The cause of this phenomenon lies in the self-interaction of the force carrying gluons. If two quarks separate, virtual gluons are exchanged, which undergo attractive interactions among themselves due to their color-charge. In an intuitive model, the color fields are squeezed into a tube with a constant energy density. The stored energy increases proportional to the distance of the quarks, which is why quarks are only observed in confined states.

[3] The $SU(3)_c$ flavor transformations can be expressed in terms of the Gell-Mann matrices according to $\hat{U} = \exp\left(i\alpha\frac{\lambda}{2}\right)$ [14].

2.1.4 Weak Interaction

The weak force is integrated into the Standard Model through electroweak unification, as discussed in Section 2.1.5. A distinctive feature of the weak interaction is its ability to change the flavor of quarks. Its range is in the order of *am*, a direct consequence of its massive mediator particles, the $W^{\pm}$ and Z boson. One peculiarity of the interaction is the violation of parity, which was experimentally demonstrated by the Wu experiment investigating β-decays [28]. Parity conservation means that physical laws remain unchanged under spatial inversion, $(x, y, z) \rightarrow (-x, -y, -z)$. Parity violation implies that the weak force distinguishes between left-handed chiral particles and right-handed chiral anti-particles. For massless particles, this corresponds to distinguishing between left-handed and right-handed helicity states, where the spin direction is opposite or in line with the direction of motion, respectively. The theoretical description is the vector minus axial vector V-A theory, which states that the weak force only couples to left-handed chiral particles or right-handed chiral anti-particles. The chiral projection operators, which decompose any Dirac spinor into a left-handed and a right-handed component read [14]

$$P_R = \frac{1}{2}(1+\gamma^5), \quad P_L = \frac{1}{2}(1-\gamma^5), \quad \text{with} \quad \gamma^5 = \begin{pmatrix} 0 & \mathcal{I} \\ \mathcal{I} & 0 \end{pmatrix} \tag{2.15}$$

Left-handed chiral particles are grouped into isospin doublets, where the components can transform into each other under the weak interaction. In contrast, right-handed particles, such as u_R, are isospin singlet states and do not transform under $SU(2)_L$. For example [26]:

$$\begin{pmatrix} u \\ d \end{pmatrix}_L, \begin{pmatrix} \nu \\ e \end{pmatrix}_L, \qquad u_R, d_R, e_R. \tag{2.16}$$

Quarks, such as *u,d,c,s,t,b*, are mass eigenstates with well-defined masses across all interactions. However, down-type quarks *d,s,b* are no weak eigenstates *d',s',b'*, they undergo mixing. The relation between weak eigenstates and mass eigenstates is described by the Cabibbo-Kobayashi-Maskawa (CKM) matrix [29, 30].

$$\begin{pmatrix} d' \\ s' \\ b' \end{pmatrix} = \begin{pmatrix} V_{\mathrm{ud}} & V_{\mathrm{us}} & V_{\mathrm{ub}} \\ V_{\mathrm{cd}} & V_{\mathrm{cs}} & V_{\mathrm{cb}} \\ V_{\mathrm{td}} & V_{\mathrm{ts}} & V_{\mathrm{tb}} \end{pmatrix} \begin{pmatrix} d \\ s \\ b \end{pmatrix} \tag{2.17}$$

The individual components V_{ij} of the CKM matrix are complex numbers, which can be parametrized by three mixing angles and one complex phase. This complex phase is responsible for charge-parity (CP)[4] violation, which is essential, although not yet sufficient, to explain phenomena such as matter/anti-matter asymmetry (see Section 2.4).

2.1.5 Electroweak Unification

The electromagnetic and weak force are unified in one coherent theory, the electroweak unification, which is based on the $SU(2)_L \times U(1)_Y$ symmetry group. The unification was developed by Weinberg, Salam and Glashow and awarded by the Nobel prize in 1979 [31].

[4] The charge operator *C* replaces a particle by its anti-particle

$SU(2)_L$ The gauge group $SU(2)_L$, is a special unitary group of degree two. It describes the symmetry of the weak isospin, which can be interpreted as a "weak charge," analogous to the electric charge in electromagnetic interactions. The subscript L indicates that the symmetry group applies to left-handed particles only. The associated gauge bosons W^1, W^2 and W^3 are initially massless.

$U(1)_Y$ The gauge group $U(1)_Y$, is a unitary group of degree one with the corresponding gauge boson B. The gauge symmetry is associated to the weak hypercharge Y, which is related to the electric charge Q and the weak isospin I_3 via the Gell-Mann-Nishijima relation [26]:

$$Q = I_3 + \frac{Y}{2} \tag{2.18}$$

The $U(1)_Y$ is associated with the electromagnetic interaction before symmetry breaking.

According to the gauge boson Lagrangian in Equation 2.5, the contribution of the electroweak interaction is given by [26]:

$$\mathcal{L}_{\text{gauge}} = -\frac{1}{4} W^a_{\mu\nu} W_a^{\mu\nu} - \frac{1}{4} B_{\mu\nu} B^{\mu\nu}, \text{ with } a = 1, 2, 3 \tag{2.19}$$

To maintain invariance for a Dirac field transforming under $SU(2)_L \times U(1)_Y$, the covariant derivative is introduced [26]

$$D_\mu = \partial_\mu + i\frac{g}{2}\tau^a W^a_\mu + ig'\frac{Y}{2} B_\mu, \tag{2.20}$$

where g and g' are the coupling constants corresponding to the $SU(2)_L$ and $U(1)_Y$ gauge fields, respectively. The Pauli matrices are represented by τ^a, and Y denotes the hypercharge of the field. Since right-handed states are $SU(2)_L$ singlets, the corresponding covariant derivative simplifies by excluding the term involving the W^a_μ gauge fields.

The physical bosons $W^\pm, Z^0, \gamma$ result from a gauge boson mixing, caused by the electroweak symmetry breaking described in Section 2.2.1. By breaking the $SU(2)_L \times U(1)_Y$ symmetry group, the electromagnetic symmetry group $U(1)_{\text{em}}$ emerges and the physical bosons acquire their masses [26]. The physical bosons result from the gauge boson mixing as follows:

$$W^\pm = \frac{1}{\sqrt{2}}(W^1 \mp iW^2) \tag{2.21}$$

$$Z^0 = \cos\theta_W W^3 - \sin\theta_W B \tag{2.22}$$

$$\gamma = \sin\theta_W W^3 + \cos\theta_W B \tag{2.23}$$

The mixing is described by the Weinberg angle θ_W, which also relates the electromagnetic charge e with the coupling constants g or g', respectively [26].

$$e = g\sin\theta_W = g'\cos\theta_W \tag{2.24}$$

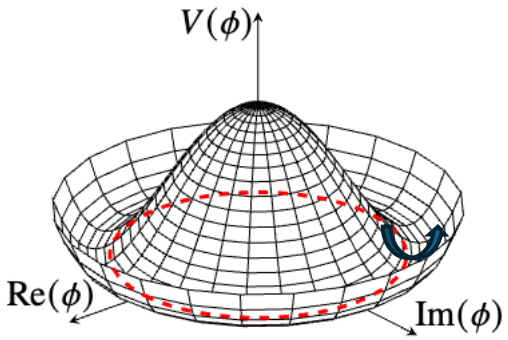


Figure 2.2: Illustration of the Mexican hat potential with $\mu < 0$, which is essential for the mass acquisition via spontaneous symmetry breaking. Minima of the potential are described by the red circle. The four degrees of freedom of the Higgs field transform under the spontaneous symmetry breaking into three Goldstone bosons and the physical Higgs boson, which arises from the radial excitation, illustrated by the blue arrow. Credit [25].

2.2 Higgs Mechanism

All elementary massive particles, independent of classification into fermions or gauge bosons, acquire their mass through their interaction with the Higgs field.

The formal approach to introduce the Higgs mechanism for mass acquisition differs for fermions and bosons as outlined in Section 2.2.1 and 2.2.2, respectively. While the weak gauge boson masses arise from the kinetic term of the Higgs Lagrangian, the fermion masses result from the Yukawa interactions with the Higgs field.

2.2.1 Electroweak- Symmetry Breaking

The electroweak symmetry breaking of the $SU(2)_L \times U(1)_Y$ group provides mass to the weak gauge bosons. In the mechanism, the Higgs field is introduced as weak isospin doublet of two complex scalar fields, one neutral Φ^0 and one charged Φ^+ [14]

$$\Phi = \begin{pmatrix} \Phi^+ \\ \Phi^0 \end{pmatrix} = \frac{1}{\sqrt{2}} \begin{pmatrix} \Phi_1 + i\Phi_2 \\ \Phi_3 + i\Phi_4 \end{pmatrix}. \tag{2.25}$$

The covariant derivative acting on the Higgs field is constructed to maintain invariance under $SU(2)_L \times U(1)_Y$ local gauge transformation and is described in Equation 2.20.

The corresponding Lagrangian follows [14]

$$\mathcal{L}(\Phi) = (D_\mu \Phi)^\dagger (D_\mu \Phi) - V(\Phi), \tag{2.26}$$

where V(Φ) represents the potential of the Higgs field. It is given by [14]

$$V(\Phi) = \mu^2 \Phi^\dagger \Phi + \lambda (\Phi^\dagger \Phi)^2, \tag{2.27}$$

where λ is a dimensionless positive number to ensure a finite minimum. The potential necessitates a negative μ^2 to form the characteristic "Mexican hat" shape, like depicted in Figure 2.2.

The minimum states of the potential are the degenerate solutions fulfilling [14]

$$\Phi^{\dagger}\Phi = \frac{1}{2}(\Phi_1^2 + \Phi_2^2 + \Phi_1^3 + \Phi_2^4) = \frac{-\mu^2}{2\lambda} := \frac{v^2}{2} \tag{2.28}$$

The minimum of the potential has infinite possible solutions along a ring at the bottom of the "Mexican hat" potential (Figure 2.2). The overall potential is symmetric, so that none of the minimum states is favored over the other. Once a specific physical minimum on this circle is chosen, referred to as the non-zero vacuum expectation value v, the global U(1) symmetry is spontaneously broken [5]. To obtain the massless, electrically neutral photon, the minimum must have non-zero contributions only in the neutral component of the doublet. Therefore, the vacuum expectation value of the field is chosen to be [14]

$$\langle\Phi\rangle = \frac{1}{\sqrt{2}}\begin{pmatrix}0\\ v\end{pmatrix} \tag{2.29}$$

Expanding the field in the ground state leads to [14]

$$\Phi = \frac{1}{\sqrt{2}}\begin{pmatrix}\Phi_1(x) + i\Phi_2(x)\\ v + \eta(x) + i\chi(x)\end{pmatrix}. \tag{2.30}$$

The four degrees of freedom of the Higgs field transform under the spontaneous symmetry breaking into three Goldstone bosons and the physical Higgs boson. The physical Higgs boson arises from the excitation along the quadratically changing direction of the potential, while the excitations in the plane of the minimum are the three massless *Goldstone bosons*, described by the non-physical fields Φ_1, Φ_2, χ_4. The concept is illustrated in Figure 2.2.

In the unitary gauge, the Goldstone boson fields are set to zero, such that the Higgs doublet is described by [14]

$$\Phi = \frac{1}{\sqrt{2}}\begin{pmatrix}0\\ v + h(x)\end{pmatrix}. \tag{2.31}$$

Here, the physical Higgs field is described by h(x). Incorporating the Higgs field in the unitary gauge, described in Equation 2.31, into the Standard Model Lagrangian, reveals the real boson definitions of Equation 2.21, 2.22, 2.23 and the corresponding mass terms [14]

- $m_W = \frac{gv}{2}$, the W-boson mass.
- $m_Z = \frac{v}{2}\sqrt{g^2 + g'^2}$, the Z-boson mass.
- $m_\gamma = 0$, the massless photon.
- $m_H = \sqrt{2\lambda}v$, the Higgs boson mass.

[5] Another vivid example of spontaneous symmetry breaking can be found in magnetism. In a conceptual experiment, the parallel spin alignments ($\uparrow\uparrow, \downarrow\downarrow$) of adjacent spins are favored over anti-parallel ($\uparrow\downarrow$) ones. There is no preference in all $\uparrow$ or all $\downarrow$ states, indicating symmetry. As soon as one spin chooses one of the two possible orientations with equal probability, all other spins will align accordingly and the symmetry will be *spontaneously* broken. In contrast, the symmetry can be *explicitly* broken when an external magnetic field favors for example $\uparrow$ over $\downarrow$ [26].

2.2.2 Yukawa Interaction

The mass acquisition of fermions relies on the Yukawa interaction, which describes the fermion interaction with the Higgs field. According to Equation 2.4, the mass in the Dirac Lagrangian has the form [14]

$$m\overline{\psi}\psi = m(\overline{\psi}_L\psi_R + \overline{\psi}_R\psi_L), \tag{2.32}$$

which highlights the contributions of the left-handed isospin doublets, and the right-handed isospin singlets.

The Yukawa interaction term in the Lagrangian is [14]

$$\mathcal{L}_Y = -g_f(\overline{\psi}_L\Phi\psi_R + (\overline{\psi}_L\Phi\psi_R)^\dagger), \tag{2.33}$$

with the Higgs scalar field Φ and the Yukawa coupling constant g_f, describing the coupling of the fermion f to the Higgs field. The expression $\overline{\psi}_L\Phi\psi_R$ is invariant under the $SU(2)_L \times U(1)_Y$ symmetry group. Incorporating the Higgs field after spontaneous symmetry breaking in the unitary gauge into the Yukawa lagrangian results in [14]

$$\mathcal{L}_Y = -\frac{g_f}{\sqrt{2}}v(\overline{\psi}_L\Phi\psi_R + \overline{\psi}_R\Phi\psi_L) - \frac{g_f}{\sqrt{2}}h(\overline{\psi}_L\Phi\psi_R + \overline{\psi}_R\Phi^\dagger\psi_L) \tag{2.34}$$

The first part of the equation describes the coupling of the fermion to the Higgs field, mirroring the form of the mass term of Equation 2.4, leads to the relation [14]

$$g_f = \sqrt{2}\frac{m_f}{v} \tag{2.35}$$

Consequently, the coupling strength of the fermions to the Higgs field g_f is proportional to their mass. The second term of Equation 2.34 describes the coupling of the fermion to the Higgs boson. The previous approach only yields mass terms for down-type fermions due to the form of the Higgs doublet after symmetry breaking. To obtain a mass description for up-type quarks, the charge conjugate of the Higgs field $\Phi^C = -i\sigma_2\Phi^*$ [14] needs to be considered in Equation 2.34. The mass acquisition of neutrinos remains unclear. There are two primary hypotheses: one involves mass acquisition via a Dirac mass term, similar to the approach discussed in this section, while the other involves Majorana masses, which interpret particles as their own anti-particles. A more detailed discussion is given in Section 2.4.

2.3 Particle Profiles

This Section provides the particle profiles of the main actors of the thesis. In order to understand reconstruction and analysis choices, characteristic properties of τ-leptons and Higgs bosons are examined.

2.3.1 τ Lepton

The τ lepton, with a mass of 1776.86 ± 0.12 MeV [12], is the heaviest known lepton, approximately 3500 times heavier than the electron. It was discovered in the 1970's in e^+e^- collisions at SLAC and was named after the Greek letter τ, meaning 'the third', referring to it being the third charged

lepton [32]. Due to its strong coupling to the Higgs field, it has a large mass, making it particularly well-suited to investigate the Yukawa interaction, introduced in Section 2.2.2. The τ lepton has a lifetime of [33]

$$\tau_\tau = \frac{1}{\Gamma(\tau)} \approx \left\{ \Gamma(\mu) \left(\frac{m_\tau}{m_\mu} \right)^5 \left[2 + N_C (|V_{\text{ud}}|^2 + |V_{\text{us}}|^2) \right] \right\}^{-1} = 3.3 \times 10^{-13}\,\text{s}, \tag{2.36}$$

which is determined as the inverse decay width $\Gamma(\tau)$. An approximation of the lifetime can also be determined by taking the well-studied muon into account. The decay-width scales with the fifth power of the mass. The expression in the square brackets considers the different τ decay channels. The factor two describes the possible leptonic decays into muons and electrons. The remaining expression describes the hadronic decays, where the factor $N_C = 3$ includes the three possible colors. From the finite life-time arises a decay length L, representing the mean distance the τ-lepton travels in the detector before decaying. According to special relativity,

$$L = \gamma\beta c\tau_\tau \approx 50\,\mu\text{m}\frac{p}{\text{GeV}} \quad \text{with} \quad \beta = \frac{p}{E} \quad \text{and} \quad \gamma = \frac{E}{m}. \tag{2.37}$$

The τ lepton is heavy enough to either decay into hadrons [6], mostly πs due to the low mass of their constituent quarks, or into light leptons and the corresponding neutrino, like illustrated in the Feynman diagram of Figure 2.3. The neutrino is a weakly interacting particle and consequently not measured in the detector. The directly measurable decay-products of the τ lepton are denoted as the visible products $\tau_{\text{had-vis}}$. Leptonic decays occur in roughly 1/3 of the cases as listed in Table 2.4(a). Hadronic decays are more likely (65%) since the three quark colors provide additional phase space. Hadronic τ lepton decays are further differentiated depending on the number of charged tracks, as well as the number of neutral particles involved in the decay. Five different decay-modes are reconstructed within ATLAS, differentiating events with either one or three charged tracks from $\pi^\pm$ or $K^\pm$, and a variable number of neutral pions. The selected notation is summarized in Table 2.4(a) and counts the number of charged tracks (prong, p), as well as the number of neutral pions (neutral, n). The relative branching ratios per τ decay-mode are also visualized in the pie-chart of Figure 2.4(b). The hadronic τ decay does not only occur via the hadronization of the produced quarks. In some cases, intermediate resonances are formed, which subsequently decay into the observed mesons. Depending on the decay-mode, different resonances contribute. In the case of a resonant decay, the invariant mass of the visible τ decay products $\tau_{\text{had-vis}}$, corresponds to the rest mass of the resonance, such as

- *1p1n:* $m(\tau_{\text{had-vis}}) = m_\rho = 775\,\text{MeV}$ [12]
- *3p0n:* $m(\tau_{\text{had-vis}}) = m_{a_1} = 1\,250\,\text{MeV}$ [34].

Di-tau events are classified according to the decay-channel. Double-leptonic decays are referred to as $\tau_{\text{lep}}\tau_{\text{lep}}$, semi-leptonic decays as $\tau_{\text{lep}}\tau_{\text{had}}$ and double hadronic decays as $\tau_{\text{had}}\tau_{\text{had}}$. Reconstruction methods within the detector are explained in Section 4.5.

[6] Hadrons are composite particles which comprise at least two confined quarks [14].

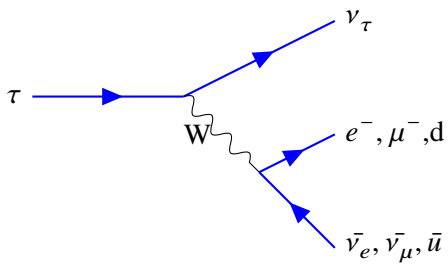
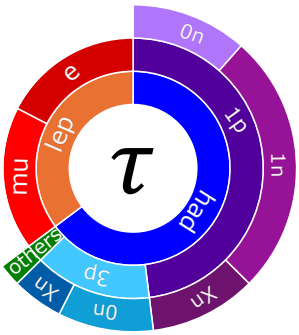


Figure 2.3: Feynman diagram of possible τ lepton decays. In a leptonic decay, light leptons are produced together with their corresponding neutrinos. In a hadronic decay, quarks are produced, which form a QCD jet. Independent of the τ decay mode, missing energy is caused by a τ neutrino.

Decay mode		Notation	BR [%]
hadronic			**64.79**
	1 prong		**48.01**
	$\tau^\pm \rightarrow \nu_\tau h^\pm$	*1p0n*	11.51
	$\tau^\pm \rightarrow \nu_\tau h^\pm \pi^0$	*1p1n*	25.93
	$\tau^\pm \rightarrow \nu_\tau h^\pm > 1\pi^0$	*1pXn*	10.57
	3 prong		**14.55**
	$\tau^\pm \rightarrow \nu_\tau h^\pm h^\pm h^\mp$	*3p0n*	9.46
	$\tau^\pm \rightarrow \nu_\tau h^\pm h^\pm h^\mp > 0\pi^0$	*3pXn*	5.09
	others		**2.23**
leptonic			**35.21**
	$e^- \bar{\nu}_e \nu_\tau / e^+ \nu_e \nu_\tau$		17.82
	$\mu^- \bar{\nu}_\mu \nu_\tau / \mu^+ \nu_\mu \nu_\tau$		17.39

(a) Quantification



(b) Visualization

Figure 2.4: τ decay branching ratios (BR). Data taken from [12]. Notation: h and p represent charged particles $\pi^\pm$or $K^\pm$, whereby the vast majority are pions. n represents solely neutral π^0. The contribution of the remaining hadronic decays like decays in five charged particles or decays including neutral K^0 are summarized in *others*. The numbers listed in Table a) are visualized in the pie-chart of b).

2.3.2 Higgs boson

The Higgs boson is the only spin 0 boson and is neither a matter constituent (fermion) nor a force exchanging particle. It is the boson associated with the Higgs field, which is responsible for the mass acquisition of elementary particles and thus, central to the whole theory. It has a mass of 125 GeV [35]. The value is a free parameter of the theory and of peculiar interest for theorists because of its large impact on BSM physics. The measured mass of 125 GeV is a bit too large for the long time popular SUSY [7] model [36], which would provide potential dark matter candidates and a solution to the hierarchy problem, which are further discussed in Section 2.4. Since all massive particles couple to the Higgs boson, various Higgs production modes and decay channels can be differentiated.

Production Modes The main leading order Feynman diagrams of the known Higgs-production modes are depicted in Figure 2.5. These include the gluon-gluon fusion production, where the Higgs boson is produced via an intermediate quark loop (Figure 2.5(a)), the production via the fusion of vector-bosons (Figure 2.5(b)), the radiation of the Higgs boson off a vector boson (Figure 2.5(c)) and the production in association with two top quarks or a gauge boson (Figure 2.5(d) and 2.5(e)). The expected cross-sections per production mode are determined using perturbation theory. The leading order calculation represents the tree-level, which is the fundamental Feynman diagram, such as those depicted in Figure 2.5. Higher order calculations add additional Feynman diagrams into the calculation, which include additional vertices of particle loops. The more loops included in the calculation, the higher the order, the more precise the calculation.

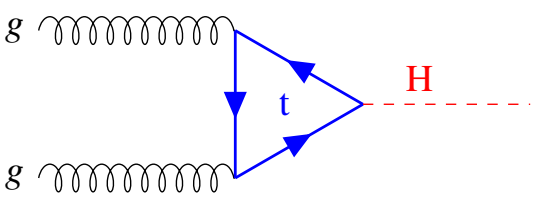
The theoretical Higgs boson production cross-sections are summarized in Table 2.6(a) for a center-of-mass energy of $\sqrt{s} = 13.6\,\text{TeV}$ and in Figure 2.6(b) as a function of $\sqrt{s}$ in proton-proton collisions. Depending on the production mode, up to next-to-next-to-next-to leading order (N3LO) is achieved like discussed in [35]. At the LHC, the dominant production cross-section is gluon-gluon fusion, followed by vector-boson fusion.

Decay Channels: The theoretical branching ratios of the most frequent Higgs decays are listed in Table 2.7(a) for a Higgs mass of $m_H = 125\,\text{GeV}$ and as a function of m_H in Figure 2.7(b). The main actor of this thesis is the $H \to \tau\tau$ channel which is, with a branching fraction of 6%, promising to probe the Yukawa coupling. The accuracy of 1.6% relies on electroweak NLO corrections [35].

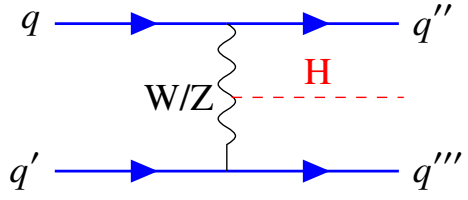
2.4 Beyond the Standard Model

The Standard Model theory has been validated by experiments up to a high extent. Despite its remarkable success, the theory is still incomplete. New phenomena have been observed experimentally that are not yet accounted for by the model. Furthermore, limitations in the theory suggest the existence of a theoretical envelop that encompasses additional extensions as well as a unified description of the forces. Pressing beyond the Standard Model searches are listed below.

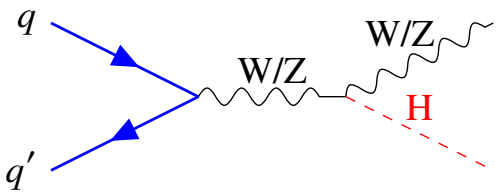
[7] Supersymmetry (SUSY) is an extension of the Standard Model, where each particle has a so called super-partner, which shares the same properties except the spin. Even though simple SUSY models became unlikely, more advanced models cannot be rejected but do need validation by experiments.



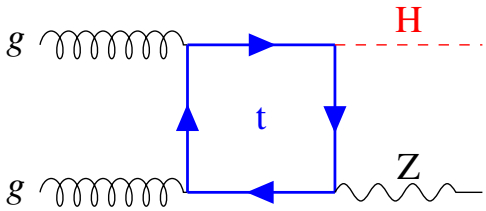
(a) gluon-gluon fusion (ggH)



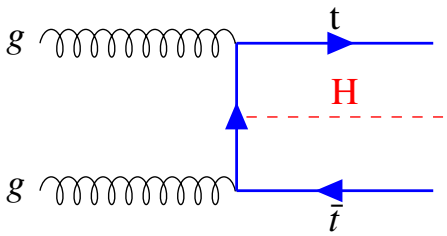
(b) vector-boson fusion (VBF)



(c) production in association with a vector boson (VH) from quark-quark interaction



(d) production in association with a vector boson from gluon-gluon interaction

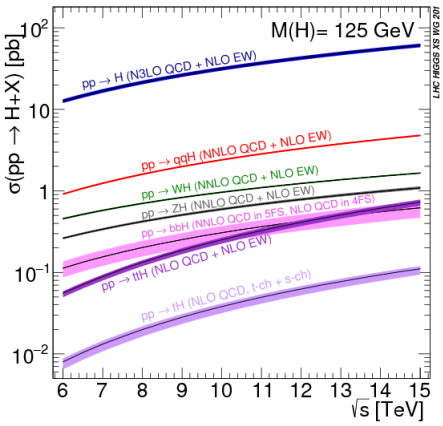


(e) associated production with a top quark pair ($t\bar{t}H$)

Figure 2.5: Leading order Feynman diagrams of the main Higgs production modes.

Production-Mode	σ_H [pb]
total	$59.2^{+5\%}_{-7\%}$
ggF	$52.2^{+5.6\%}_{-7.4\%}$
VBF	$4.1^{+2.1\%}_{-1.5\%}$
WH	$1.46^{+1.8\%}_{-1.9\%}$
ZH	$0.95^{+4.0\%}_{-3.6\%}$
$t\bar{t}H$	$0.57^{+6.9\%}_{-9.9\%}$

(a) σ_H at $\sqrt{s}$ = 13.6 TeV

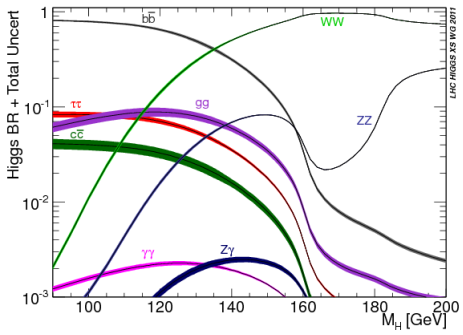


(b) σ_H as a funtion of $\sqrt{s}$

Figure 2.6: Cross-sections of SM Higgs boson production modes at $\sqrt{s}$ = 13.6 TeV and as a function of the center of mass energy in pp collisions [35].

Decay channel	Branching ratio	Rel. uncertainty
$H \to \gamma\gamma$	2.27×10^{-3}	2.1%
$H \to ZZ$	2.62×10^{-2}	±1.5%
$H \to W^+W^-$	2.14×10^{-1}	±1.5%
$H \to \tau^+\tau^-$	6.27×10^{-2}	±1.6%
$H \to b\bar{b}$	5.82×10^{-1}	$^{+1.2\%}_{-1.3\%}$
$H \to c\bar{c}$	2.89×10^{-2}	$^{+5.5\%}_{-2.0\%}$
$H \to Z\gamma$	1.53×10^{-3}	±5.8%
$H \to \mu^+\mu^-$	2.18×10^{-4}	±1.7%

(a) Higgs branching ratios at $m_H = 125\,\text{GeV}$



(b) Higgs branching ratios as a function of m_H

Figure 2.7: Branching ratios of the SM Higgs boson at $m_H = 125\,\text{GeV}$ a) and as a function of m_H b) [35]. The di-tau final state is with a branching ratio of 6% promising to probe the Yukawa-coupling.

Matter-Antimatter Asymmetry According to the Big Bang theory, matter and antimatter should have been produced in equal amounts. The current universe consists however mainly of matter - an imbalance that is not fully covered by the Standard Model theory. The CP violation of the weak interaction incorporates different physics laws for matter and anti-matter. The observed amount of CP violation is however not yet sufficient to explain the observed discrepancy. Beyond the Standard Model extensions, such as baryogenesis, try to explain matter/anti-matter asymmetries while building on three Sakharov conditions that need to be fulfilled [37]:

- **Baryon Number Violation:** Baryon number violating processes need to be included into the theory.
- **C and CP Violation:** Charge and charge-parity need to be violated to produce a preference for matter.
- **Departure from Thermal Equilibrium:** In thermal equilibrium, matter and anti-matter balance out. Therefore, a phase-transition, such as the electroweak transition from a symmetric Higgs potential at high temperatures to the broken symmetry at low temperatures, is crucial.

Neutrino Masses Neutrinos are considered to be massless by the Standard Model. Experimental observations have shown neutrino flavor oscillations, which require a non-zero mass of at least two neutrinos. Two different approaches to include neutrino masses in the Standard Model are explored in current research [14].

- **Dirac Particle:** If a neutrino is a Dirac particle, which acquires its mass via a Yukawa coupling, the corresponding coupling constant is unnaturally small. This fact gives the hint to another mechanism.
- **Majorana Particle:** A majorana particle is its own anti-particle, which can apply for neutral particles, such as neutrinos. In such a case, the Lagrangian can be extended without breaking gauge invariance since right-handed neutrinos transform like left-handed anti-neutrinos as singlets. An experimental validation for neutrinos being Majorana particles is a neutrinoless double β-decay.

Dark Matter Rotational curves of galaxies indicate the existence of unknown matter that is not yet described by the Standard Model. It accounts for roughly 23% of the mass in the universe [14]. The hypothetical matter candidate is attributed as 'dark' since it does not interact electromagnetically and consequently does not absorb or emit light. Hypothetical candidates are Axions or weakly interacting particles [14].

Hierarchy problem The Hierarchy problem questions the large scales between the electroweak and the Planck scale or in other words the fact that the gravitational force, which is associated with the Planck scale, is approximately a factor of 10^{30} weaker than the weak force[14]. The electroweak scale is defined through the spontaneous symmetry breaking of the Higgs' field potential, which also impacts the mass of the Higgs boson. The extension of the Standard Model theory to high energies, as it would be needed for the grand unified theories, also means additional quantum corrections that add to the Higgs mass. These contributions need to cancel up to a high precision in order to avoid a diverging Higgs mass approaching the Planck scale. To achieve this cancellation, an enormous fine-tuning of the theory is needed, which seems unnatural given the fact that both scales differ by several orders of magnitude.

Grand Unified Theories: The coupling constants of the Standard Model forces run with energy. At high energy scales, they even tend to converge. Thus, starting from the mid 20th century, theorists looked for one unified theory that describes them all. According to this point of view, the Standard Model forces, that we know today, are low-energy manifestations of an even bigger picture. The description of the electromagnetic and weak force in an combined, electroweak theory was established in the 1960s by Glashow, Salam and Weinberg [14]. The search for a even more inclusive, grand unified theory is still a hot topic of research.

CHAPTER 3

Methodology of Data Collection & Simulation

High-energy physics experiments rely not only on sophisticated theories but also on complex infrastructures, including advanced accelerators and experimental setups, as well as extensive computing resources. A fundamental understanding of the physics, the detector response and readout similarly informs the detector instrumentation as well as simulations that provide an account of the theory expectations of the underlying processes. The CERN accelerator complex, associated figures of merit as well as the conceptual design of the ATLAS experiment is presented by the following chapter. Furthermore, the concepts of Monte Carlo simulation is discussed.

3.1 Large Hadron Collider

The international organization CERN (**C**onseil **e**uropéen pour la **r**echerche **n**ucléaire) is directly associated to the LHC (**L**arge **H**adron **C**ollider). With a circumference of 27 km, the LHC is the currently largest particle accelerator of the CERN accelerator complex. It delivers beams of protons or heavy ions to multiple experiments along the research facility in Geneva, Switzerland. The accelerated particles reach velocities close to the speed of light, which is achieved by a chain of pre-accelerators (see Figure 3.1). Since 2020 the acceleration of protons starts in *Linac4* (Linear Accelerator 4), where negative hydrogen ions are pushed to energies of 160 MeV [38]. After stripping two electrons of the H^- ions, pure protons are injected into the *Proton Synchrotron Booster* (PSB), which accelerates the particles to 2 GeV [39]. Next in line, the *Proton Synchrotron* (PS) provides protons of energies of up to 25 GeV [40], followed by the *Super Proton Synchrotron* (SPS) that reaches energies up to 450 GeV [41]. Protons are injected into the LHC, where two counter-rotating beams reach energies of up to 7 TeV [42] each. The beams are steered into collision at four intersection points (IS), the sites of the four main experiments: ATLAS, CMS, LHCb and ALICE.

3.1.1 Operation

The proton-beams are a non-continuous stream of particles and consist of proton bunches with a spacing of 25 ns [42]. The particles are circulated by 1232 dipole and 392 quadrupole magnets that take care of beam bending and focusing, respectively. The acceleration is facilitated by the electric field of 16 radio-frequency cavities [42]. The center-of-mass energy $\sqrt{s}$, the energy available in the

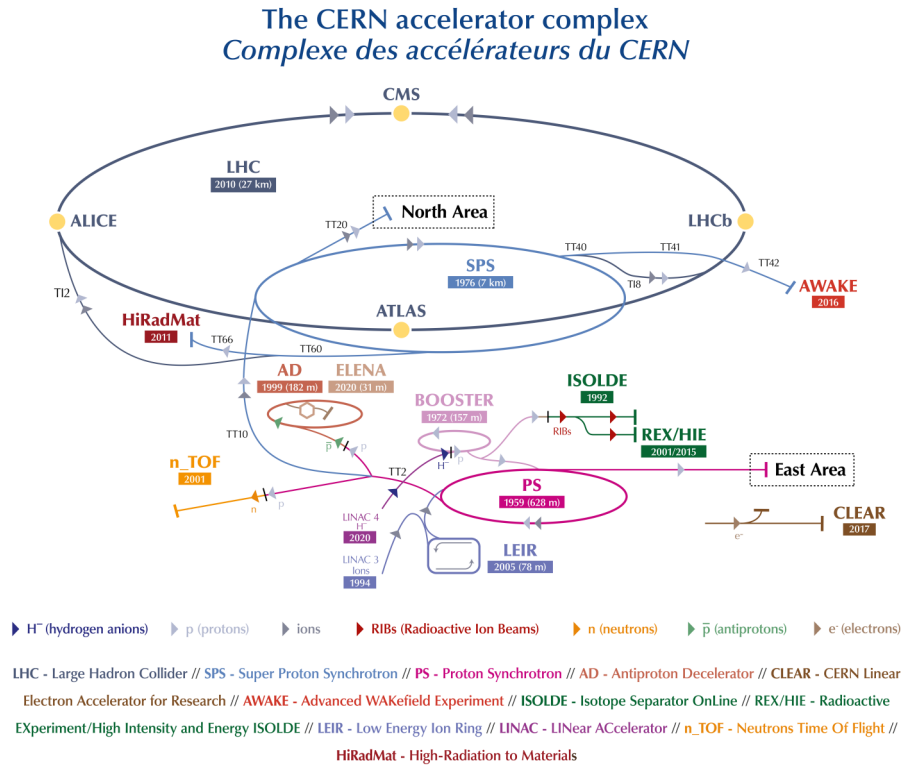


Figure 3.1: The CERN accelerator complex comprises *Linac 4*, the *Proton Synchrotron Booster*, the *Proton Synchrotron*, the *Super Proton Synchrotron* and the *LHC* [43]. The different accelerator structures are color-coded, as indicated by the legend.

collision, is

$$s = (\mathbf{p}_1 + \mathbf{p}_2)^2 = \left(\begin{pmatrix} E \\ \vec{p} \end{pmatrix} + \begin{pmatrix} E \\ -\vec{p} \end{pmatrix}\right)^2 = 4E^2. \tag{3.1}$$

The four-momenta $\mathbf{p}_1$ and $\mathbf{p}_2$ combine energy and momentum information. Due to the opposing rotation of beams, the three-momenta $\vec{p}$ cancel and the center-of-mass energy yields $\sqrt{s} = 14\,\text{TeV}$.

3.1.2 Luminosity

Besides the center-of-mass energy, the luminosity $\mathcal{L}$ is an important characteristic of a particle accelerator. As a measure for the achieved collision rate, the luminosity can be scaled with the production cross-section σ of a certain particle, which measures the interaction probability of the target process [1], in order to calculate the expected production rate

$$\frac{dN}{dt} = \mathcal{L}\sigma. \tag{3.2}$$

[1] The cross-section is measured in barn, which represents an area: $1\text{barn} = 10^{-28}\,\text{m}^2$ [14]. The larger the 'effective area', the larger the probability of this specific interaction to occur.

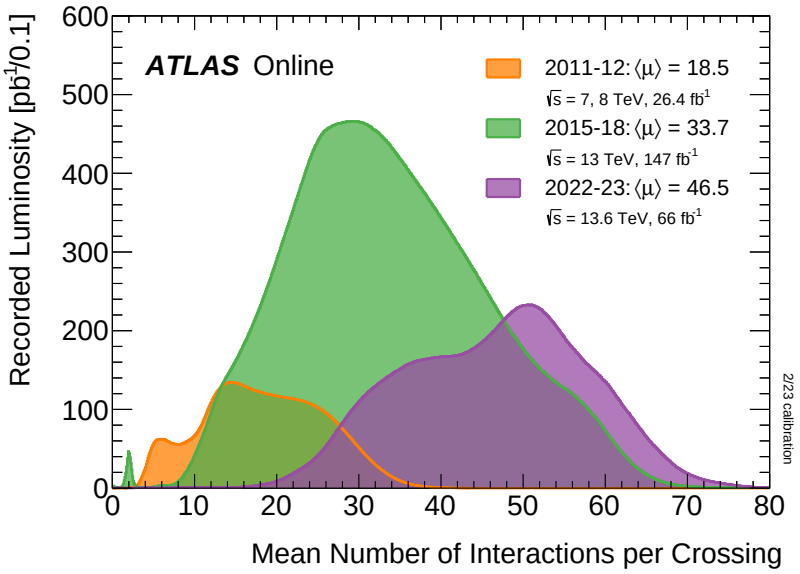


Figure 3.2: Average number of interactions per bunch-crossing between the years 2011 and 2023 [44]. The Run 1 profile at $\sqrt{s} = 7, 8$ TeV is shown in orange, the Run 2 profile at $\sqrt{s} = 13$ TeV in green and the current Run 3 profile at $\sqrt{s} = 13.6$ TeV in violet.

The luminosity depends on the collision frequency f, the number of particles per beam bunch n_i and the root-mean-square beam size in horizontal σ_x and vertical σ_y direction [14]

$$\mathcal{L} = f \frac{n_1 n_2}{4\pi \sigma_x \sigma_y}, \quad [\mathcal{L}] = \mathrm{s}^{-1}\,\mathrm{m}^{-2}. \tag{3.3}$$

Typically, the time integrated luminosity $\mathcal{L}_{\mathrm{int}}$ is specified for a given run period. In case of Run 2 (2015-2018) 140.1 fb^{-1} or 140.1 $\times$ 10^{39} m^{-2} [11] have been recorded.

The gain in measurement statistics from high collision rates in high-luminosity operation push the precision frontier. At the same time, unprecedented event rates push the experiments to their limits. Detector technologies, trigger and data acquisition systems as well as the reconstruction and analysis techniques are under permanent development to make use of the physics potential. An illustration of the increasing collision rate over past years is shown in Figure 3.2. In the current Run 3, an average of $\sim$ 45 interactions occur per bunch-crossing, compared to $\sim$ 20 interactions in Run 1.

3.1.3 The High-Luminosity LHC

A prerequisite for reduced statistical uncertainties are larger data sets. For that purpose, accelerator upgrades are foreseen with the objective to increase the integrated luminosity by one order of magnitude [45]. In the projected timeline, the High-Luminosity LHC (HL-LHC) will operate in the years 2029-2038 [46]. Promising physics perspectives were explored as exemplified in Figure 3.3 showing the uncertainty on the Higgs cross-section measurements per-production-mode normalized to the SM predictions for combined ATLAS and CMS performance in the HL-LHC project. In this scenario not statistical but theory uncertainties dominate the measurement. With the accelerator

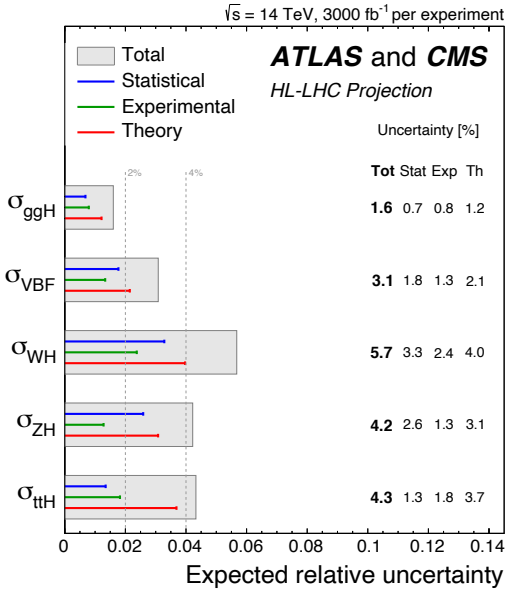


Figure 3.3: Expected uncertainty on Higgs cross-section measurements per-production-mode normalized to the SM predictions for combined ATLAS and CMS performance in the HL-LHC project [47]. The grey box indicates the total uncertainty. The blue, green and red lines indicate the statistical, experimental and theoretical contributions, respectively.

upgrade, the experiments need to undergo major upgrades to cope with the high pile-up environment, which will reach an average of up to 200 interactions per bunch-crossing [45]. The main challenges revolve around the following aspects:

- The increased detector occupancy needs to be compensated for with higher granularity. Therefore, many detector systems develop alternative or complementary systems, such as the new inner tracking detector (ITk) or a new high granularity timing detector (HGTD) for ATLAS.
- The higher trigger rates require a more sophisticated trigger scheme and readout architecture.
- A more complex event reconstruction is connected to intensive software development.
- Higher radiation doses call for specialized detector research and development (R&D) programs.

3.2 The ATLAS Detector

The ATLAS detector is one of the two largest experiments at the LHC, measures 44 m in length, 25 m in diameter and weights in at around 7 000 000 kg [48]. The barrel like structure almost completely covers the solid angle. The multipurpose detector is intentionally designed to verify the existence of a Higgs-like particle. It measures all detectable types of decay products and allows for a comprehensive exploration of the boson. The various sub-detectors are specialized in the detection of individual particle types or kinematic properties and are arranged in an onion-like barrel structure around the interaction-point, as depicted in Figure 3.4. The first time operation of the ATLAS detector is linked to

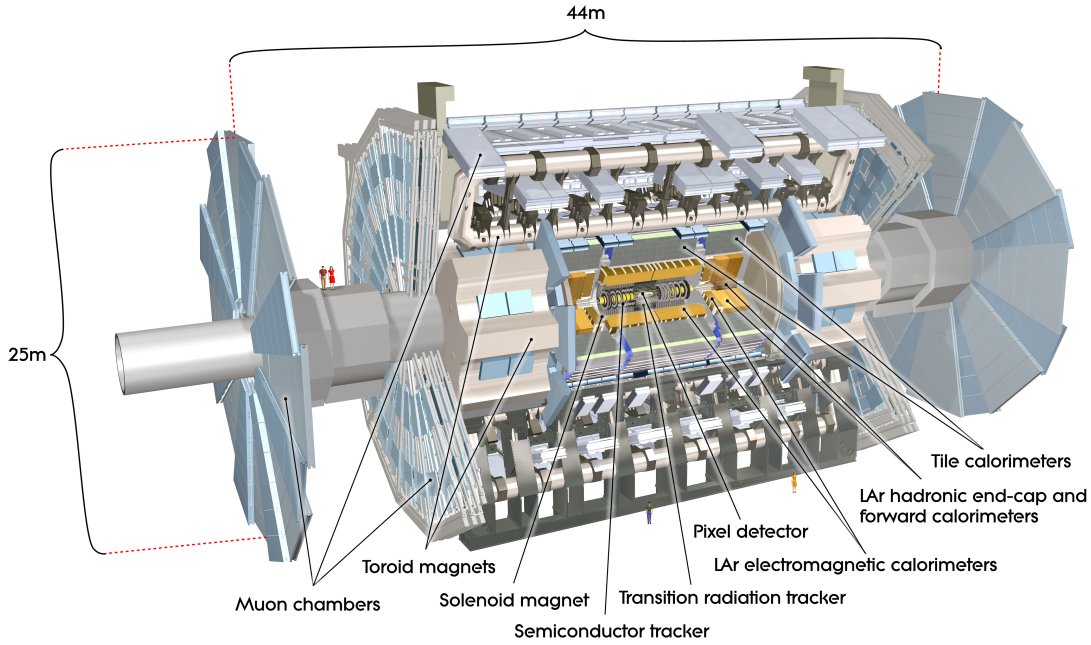


Figure 3.4: Schematic view of the ATLAS detector in Run 2 [50]. Following an onion-like structure, the Inner Detector is surrounded by electromagnetic and hadronic calorimeters and the magnet system. The outermost shell consists of muon detectors.

the LHC, which delivered first particle collisions in 2009 [49]. Since then, various upgrade campaigns match increasing technical requirements imposed by increasing luminosity.

3.2.1 Coordinate System

The ATLAS coordinate system, illustrated in Figure 3.5, has its origin in the center of the detector, which coincides with the nominal interaction point. Following a right handed coordinate system, the z-axis is oriented along the beam pipe, the x-axis point towards the centre of the LHC ring and the y-axis is oriented upwards. The transverse plane is described by the azimuthal angle ϕ around the z-axis and the radius r. The spherical coordinate system is complemented by the polar angle θ [3]. The following two measures are frequently used to describe spatial distributions.

- **The pseudorapidity η** measures the inclination of a particle relative to the beam axis. It is defined based on the polar angle θ

$$\eta = -\ln \tan\left(\frac{\theta}{2}\right). \tag{3.4}$$

  Values range from $-\infty$ for opposite beam direction to ∞ in orientation of the beam. The difference in pseudorapidity between two objects $\Delta\eta$ is Lorentz-invariant under longitudinal boosts.

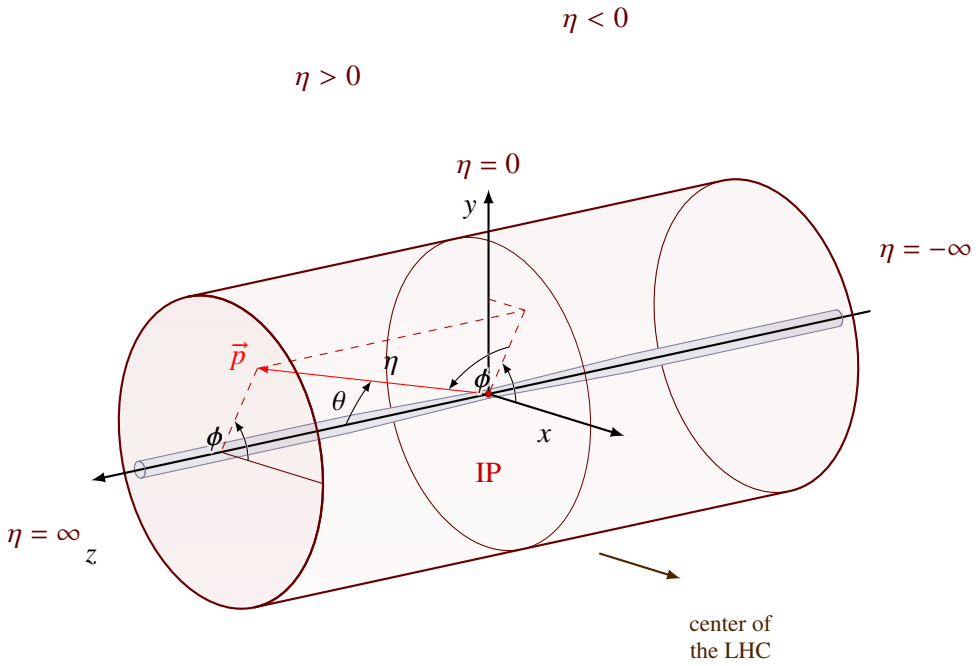


Figure 3.5: ATLAS coordinate system [25]. The x-axis points towards the center of the LHC, the y-axis upwards and the z-axis in direction of the beam.

- The **angular distance measure ΔR** between two objects is defined as

$$\Delta R = \sqrt{(\Delta\eta)^2 + (\Delta\phi)^2} \tag{3.5}$$

3.2.2 The Sub-systems

The Inner Detector is the inner-most part of the ATLAS detector. Due to its direct proximity to the interaction point, it is exposed to the highest flux of particles. Therefore, high granularity is a central characteristic that allows to differentiate incoming particles. The Inner Detector is responsible for tracking as well as vertex reconstruction, which corresponds to the location of a particle decay resulting in new secondary-particle tracks. The Inner Detector itself consists of three different sub-detectors - the Pixel Detector, the Semiconductor Tracker and the Transition Radiation Tracker (TRT).

- **Silicon Pixel Detector:** consists of four layers with a total of 92 million pixels and achieves a spatial resolution of 10 µm [51]. The innermost of the four layers, the IBL layer [52] was installed in an upgrade campaign in preparation of Run 2.
- **Semiconductor Tracker:** is based on silicon micro-strip sensors that provide a spatial resolution of 25 µm [51] and complement the Pixel Detector in terms of track reconstruction.
- **TRT:** The third and outermost part of the Inner Detector is used for tracking and particle identification (PID), which is further discussed in Chapter 5. The TRT consists of 298 304 gas

filled straws that form a barrel ($|\eta| < 0.625$) and two end-cap regions ($1 < |\eta| < 2$). In the barrel region, the 142 cm long straws are oriented parallel to the beam pipe and are arranged in three layers with 32 modules each. The end-caps feature 14 units of radially arranged drift tubes per side. Each straw has a diameter of 4 mm and is coated with a conductive material at negative electrical potential. At the center of the gas-filled tube, a 31 µm thick tungsten wire serves as the anode. Polypropylene foils and fibers are employed as radiator material between the straws [53].

Calorimetry : Calorimeters are designed to measure the particle energy by producing a measurable signal proportional to the amount of absorbed energy. In ATLAS, sampling calorimeters are deployed, which interleave high-density materials for absorption with active layers for energy measurement. Two types of calorimeters are differentiated, depending on the targeted interaction process.

- **The Electromagnetic Liquid Argon Calorimeter** is designed to measure the energy of electromagnetically interacting particles, predominantly electrons and photons. They interact with the high-density metal layers and convert into an electromagnetic shower, a cascade of bremsstrahlung and pair-production. In between an accordion-like structure, the active liquid argon is ionized and produces a measurable signal.
- **The Hadronic Tile Calorimeter** measures the energy of hadrons, which are not stopped by the Electromagnetic Calorimeter. Similar to the preceding sub-detector, high-density steel layers initialize a particle shower. Energy is measured in layers of plastic scintillators that emit photons upon particle interaction, which are converted in an electrical signal proportional to the deposited energy.

Apart from energy measurement, calorimeters also provide critical information for particle identification, as well as for the reconstruction of jets and missing transverse energy.

The Muon System is the outermost part of the ATLAS detector and consequently identifies the minimum ionizing particles, which are not stopped by the previous detector material. It uses various detector technologies, such as *Resistive Plate Chambers (RPC)*, *Thin Gap Chambers (TGC)*, *Monitored Drift Tubes* and *Micromegas*. Together, they form a precise and responsive setup, which achieves spatial and timing resolution in the order of $\sim 100\,\mu m$ and $\sim 2.5\,\mu s$, respectively[54]. The spatial resolution allows for reliable momentum measurements. The time resolution qualifies it to provide information to the trigger system. In the Phase-I upgrade, which started after Run 2, new small wheels (NSW) were installed, that provide improved tracking and trigger capabilities in high-rate environments [55].

The Magnet System is based on superconducting magnets, which enable the momentum and charge reconstruction in ATLAS. Due to the Lorentz force

$$\vec{F}_L = q(\vec{v} \times \vec{B}) \tag{3.6}$$

with the charge q, the velocity $\vec{v}$ and the magnetic field $\vec{B}$, particles experience a force perpendicular to their direction of motion, which curves their otherwise straight trajectory. Magnitude and direction of the curvature depends on the respective momentum and charge of the particle.

- The **Central Solenoid Magnet** provides a magnetic field of 2 T. It is only 4.5 cm thick to maintain a low material budget in the centre of the detector, where it surrounds the Inner Detector [56].
- The **Toroid Magnets** consist of 8 coils with a magnetic field of 3.5 T [56]. Two toroid magnets are placed in the end-caps, one in the barrel region.

3.2.3 Data Acquisition & Processing

With a LHC collision rate of 40 MHz and an event size of about 2 MB, roughly 80 TB become available each second of ATLAS operation [57]. The ATLAS data is read out from ~ 100 million electronic channels [58] across all sub-systems. For data acquisition, a sophisticated architecture is required for collection, filtering, processing and storage.

The Trigger System Only a ten thousandth of the provided data stream (~6 GB s^{-1} [57]) can be processed. Therefore, the data volume needs to be reduced to a selection of specific events of interest. Figure 3.6 shows the production cross-section of processes measured in different LHC programs. The production of known Standard Model processes covers several orders of magnitude in rate, which poses the central challenge in the design of multi-purpose trigger rules. Current physics programs probe the known Standard Model but, at the same time, do not want to sacrifice their sensitivity for physics beyond. Event selection is optimized to detect signatures of interest, which are often highly energetic or show rare topologies. The ATLAS event selection is performed in two trigger stages.

The Level-1 Trigger (L1) reduces the initial rate of 40 MHz to 100 kHz within 2.5 µs of processing latency, followed by a second High Level Trigger (HL), which cuts down the event rate to roughly 1 kHz in an additional 500 ms [57].

The L1 Trigger is primarily hardware-based and relies on muon and calorimeter information. The Muon Trigger System contributes RPCs, TGCs and the NSW signals, that all exhibit excellent time resolution. In a large share of detector signatures, muons indicate the presence of topologies from hard scattering events. The Level-1 Calorimeter Trigger evaluates energy depositions or special features, such as large radius jets. In addition, a topological Level-1 Trigger selects events based on spatial relations between particles.

The second stage, the HL Trigger is software-based and investigates topologies based on more-detailed information from the sub-systems. It applies offline-like algorithms for object reconstruction and physics selection.

Since the events of interest strongly depend on the current physics goals, different trigger chains target individual physics cases or monitoring purposes. Trigger chains are picked up in a run specific Trigger Menu, which defines write rates per individual chain. Depending on the Menu, the selection efficiency of rare processes is increased or the selection is optimized for calibration purposes. Generally, the Trigger Menu needs to scale with the available luminosity. Pre-defined Menus for pp or heavy-ion as well as cosmic runs are regularly checked for efficiency and reliability. In physics analyses, the selected triggers represent a list of cuts that is applied to the data set and consequently impact the sensitivity.

Data Processing Once an event passes the two trigger stages, it needs to be processed and recorded. Raw data consists of byte streams that hold detector information, the trigger as well as running

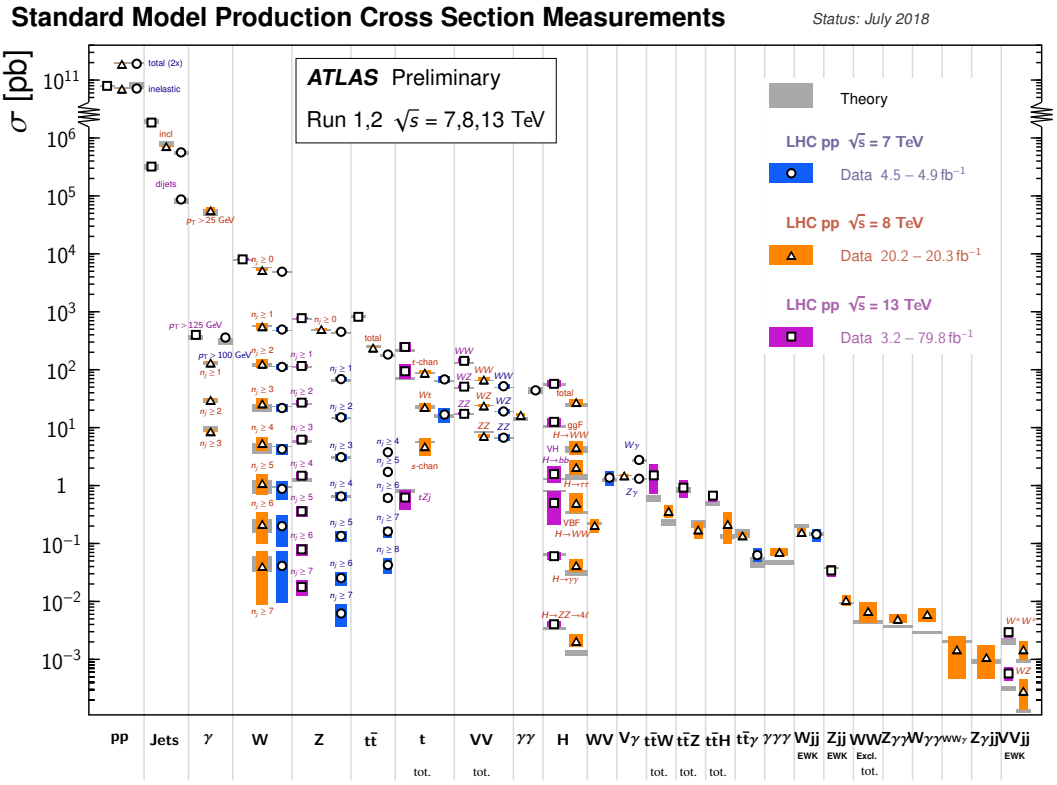


Figure 3.6: Cross-sections of Standard Model processes for different center-of-mass scenarios [59].

conditions. Files are stored and processed at the CERN Tier-0 computing site, where raw data is transformed into a suitable format for physics analysis, called *Analysis Object Data (AOD)*. The AOD format only contains reconstructed and reduced information of the highest relevance. Skimming, thinning and slimming techniques [60] remove pre-defined events, objects or variables from the final data format. These *NTuples* allow for readily available access to the information most-important for a given analysis. The associated software framework is called *Athena* [2]. In case reconstruction algorithms are updated, raw data files are reprocessed since they are stored to tape.

For physics analysis, simulated events need to be produced and filtered in an analogously way. The generation of physics processes is initiated in free space. The interaction between collision products and detector structures are considered in subsequent steps. The simulation of particle interactions with matter is computationally expensive, especially when fully simulating particle showers in the calorimeter stages. A fast simulation approach uses a parametrization instead. Subsequently, digitization is applied, which converts the simulated event into the raw data format. In order to mimic recorded data, pile-up is additionally simulated and overlaid.

The GRID, an international organization of computing sites is operated in order to deal with the required computing power. It contains Tier-1 sites for intensive tasks like Monte-Carlo event generation as well as smaller Tier-2 sites for computationally less expensive jobs.

[2] https://gitlab.cern.ch/atlas/athena

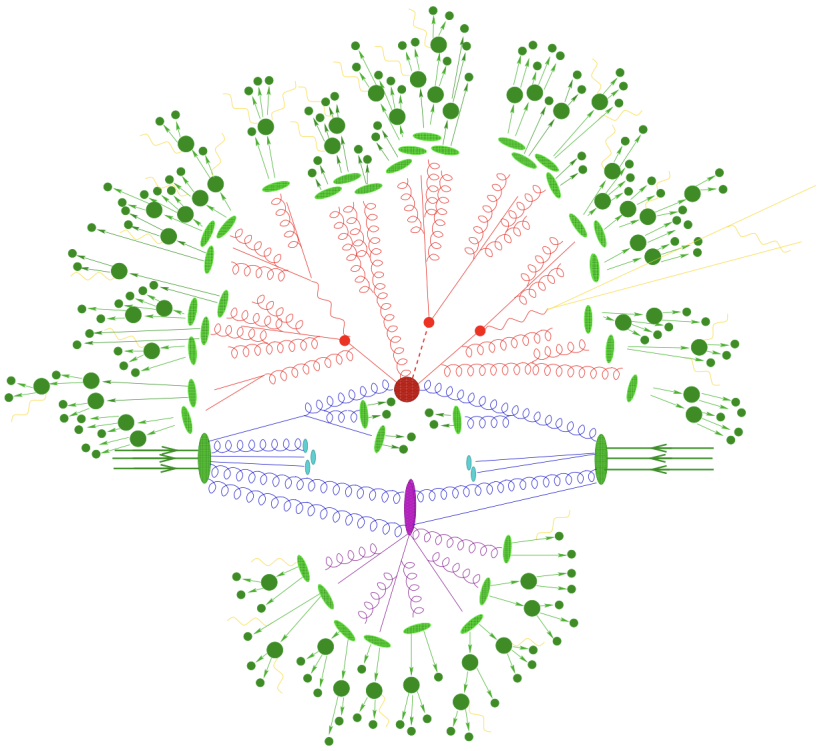


Figure 3.7: Illustration of a simulation of hadron-hadron collision. Different steps in the simulation chain are indicated by different colors and structures. The central red dot represents the hard collision point, which is surrounded by a tree-like parton-shower structure. The underlying event is represented in purple, hadronization and hadron decay are colored in green [61].

3.3 Simulation

Kinematic relations, correlations and physical assumptions require verification by comparing the theory expectation to the measured data. Artificial, SM-like events are simulated using Monte-Carlo (MC) techniques. These stochastic methods for numerical integration are applied to solve mathematical problems where analytic solutions are too complex. MC methods obtain a numerical result through random sampling and are especially suited to solve multidimensional problems, such as the simulation of proton-proton collisions, where each particle requires three dimensions in phase space.

3.3.1 Methodology

The simulation of proton-proton collisions is a highly complex task that considers initial hard scattering followed by the parton showering and hadronization as well as the impact of the underlying event. The latter describes all the activity not related to the primary hard scattering process. An overview of the processes considered in the event generation is sketched in Figure 3.7.

QCD Factorization separates the short-distance regime, where the strong coupling constant α_S is small and perturbative calculations hold truth, from the long distance regime, which is non-perturbative. The production cross-section of a process X factorizes in a perturbative hard scattering contribution and the non-perturbative contribution. The theorem contains the products of parton distribution functions $f_{a/b}$. They describe the probability of a specific parton, quark or gluon, carrying a given momentum fraction x of the proton. The production cross-section [61]

$$\sigma_{h_1 h_2 \to X} = \sum_{a,b \in \{q,g\}} \int dx_a \int dx_b f_a^{h_1}(x_a, \mu_F^2) f_b^{h_2}(x_b, \mu_F^2) \int d\Phi_{ab\to X} \frac{d\hat{\sigma}_{ab}(\Phi_{ab\to X}, \mu_F^2)}{d\Phi_{ab\to X}}. \tag{3.7}$$

further depends on the factorization scale μ_F, separating the perturbative from the non-perturbative regime.

Parton-level The hard scattering process is determined as a fixed-order perturbation theory. In the calculation of the cross-section, a central role is taken by the matrix element $\mathcal{M}$, which describes the probability amplitude of a scattering process. The valid phase-space is sampled by generating momenta following the matrix element calculations.

Parton Showering Partons produced in the hard scattering process emit further partons, resulting in a parton shower. The process continues until the energy of individual partons is reduced enough for hadronization to take over ($\sim$ 1 GeV [61]).

Hadronization At the hadronization stage, partons transform into color-neutral hadrons. This process is described by the phenomenological Lund String [62] and Cluster Model [63]. The Lund String Model interprets the color field as strings, connecting quarks and anti-quarks. As the string stretches to larger distances, it breaks into new quark/anti-quark pairs. The existing partons combine into hadrons. In the Cluster Model, color-neutral clusters are formed and decay into color-neutral hadrons. Both models rely on parameters that are tuned to experimental data.

Underlying event Apart from the primary hard scattering process, multiple parton interactions as well as initial and final state radiation occur, both adding to the event complexity. Event generators include models that are tuned with experimental data.

Detector Simulation For a realistic prediction in close resemblance of experimental data, the passage of particles through matter and expected detector responses are simulated with the GEANT4 [64] toolkit. It allows a flexible inclusion of detector geometries and material properties.

3.3.2 Specification of Generated Events

Event generators simulate the entire chain of processes that act during proton-proton collisions. Common generators, which are also used for event generation within this thesis are SHERPA v2.2.1 [65], POWHEG [66–69] and PYTHIA [70]. They are based on different models and are deployed depending on the specific step in the simulation chain. While POWHEG and SHERPA are best-suited for matrix element

calculation, PYTHIA is used for parton showering. τ decays and spin correlations are simulated with PYTHIA or SHERPA .

The event generation of the processes central to this thesis are specified in Table 3.1, comprising ggF, VBF, VH and $t\bar{t}H$ Higgs production as well as V + jets, $t\bar{t}$, single top and di-boson background processes. Apart from the generator, the PDF sets, the parameter tuning as well as the order of cross-section calculation used for sample normalization, is documented. For a more detailed view, refer to [3, 71].

Process	Generator		PDF set		Tune	Normalisation
	ME	PS	ME	PS		
Higgs boson						
ggF	POWHEG BOX v2	PYTHIA8	PDF4LHC15NNLO	CTEQ6L1	AZNLO	N^3LO QCD + NLO EW
VBF	POWHEG BOXV2	PYTHIA8	PDF4LHC15NNLO	CTEQ6L1	AZNLO	NNLO QCD + NLO EW
VH	POWHEGBOXV2	PYTHIA8	PDF4LHC15NNLO	CTEQ6L1	AZNLO	NNLO QCD + NLO EW
$t\bar{t}H$	POWHEG BOXV2	PYTHIA8	NNPDF3.0NNLO	NNPDF2.3LO	A14	NLO QCD + NLO EW
Background						
V + jets (QCD/EW)	SHERPA 2.2.1		NNPDF3.0NNLO		SHERPA	NNLO for QCD, LO for EW
$t\bar{t}$	POWHEGBOXV2	PYTHIA8	NNPDF3.0NNLO	NNPDF2.3LO	A14	NNLO + NNLL
Single top	POWHEG BOX v2	PYTHIA8	NNPDF3.0NNLO	NNPDF2.3LO	A14	NLO
Diboson	SHERPA2.2.1/2.2.2		NNPDF3.0NNLO		SHERPA	NLO

Table 3.1: Specification of event generation for important signal and background samples. The columns *ME* and *PS* provide information about the matrix element generator and parton shower. Detailed information on the selected PDF sets are presented in [72, 73], for the parameter tuning in [74, 75]. Further references, including normalization, are listed in [3]. Table adapted from [3].

CHAPTER 4

Event Reconstruction

To accurately describe the topology of $H \rightarrow \tau\tau$ events, it is essential to reconstruct all particle types, including electrons, muons, taus or composite objects like jets. Particle reconstruction leverages particle-type specific signatures across various sub-detectors. Identification scores and isolation properties are important variables in the reconstruction process. The identification score indicates the probability of correct particle type assignment, and isolation properties help to suppress background noise by evaluating unrelated signals (activity) around the object.

The reconstruction of measurement data collected between 2015 and 2018 is assigned to LHC Run 2, which amounts to a total integrated luminosity of $139\,\text{fb}^{-1}$ [77][1]. Standard Model processes are modeled using Monte Carlo (MC) simulation, as detailed in Section 3.3. Both, MC as well as measurement data samples are reconstructed according to the same criteria.

4.1 Electrons

Electrons are lightweight particles and frequently appear as decay-products of heavier particles, such as Z-bosons or in leptonic τ decays. The typical signature of an electron traversing the detector (see Figure 4.1) comprises a track in the Inner Detector, followed by an electromagnetic shower in the electromagnetic calorimeter. This shower encapsules a cascade of bremsstrahlung, where an electron radiates a photon, and pair production, where a photon converts into an e^+e^- pair [79]. The convolution of processes involving electrons and photons complicates the distinction between the individual detector signatures. The reconstruction is especially challenged when a photon converts into an electron-positron pair in the Inner Detector, leaving tracks that are unexpected due to the photon's electrical neutrality. To reduce the ambiguity, boosted-decision-trees (BDTs) are applied at analysis level. The electron reconstruction is documented in [80]. The object calibration, including associated uncertainties, is discussed in [81].

Reconstruction The reconstruction relies on energy clustering in the electromagnetic calorimeter. In addition, a successfully reconstructed track in the Inner Detector is required. Track finding is

[1] The luminosity measurement of the Run 2 data has been updated compared to the 2022 analysis, reducing the uncertainty from 1.7%[78] to 0.83% with an integrated value of $140.1\,\text{fb}^{-1}$ [77]. Following studies rely on the luminosity measurement of [77] and are marked accordingly. The final publication is based on the latest results.

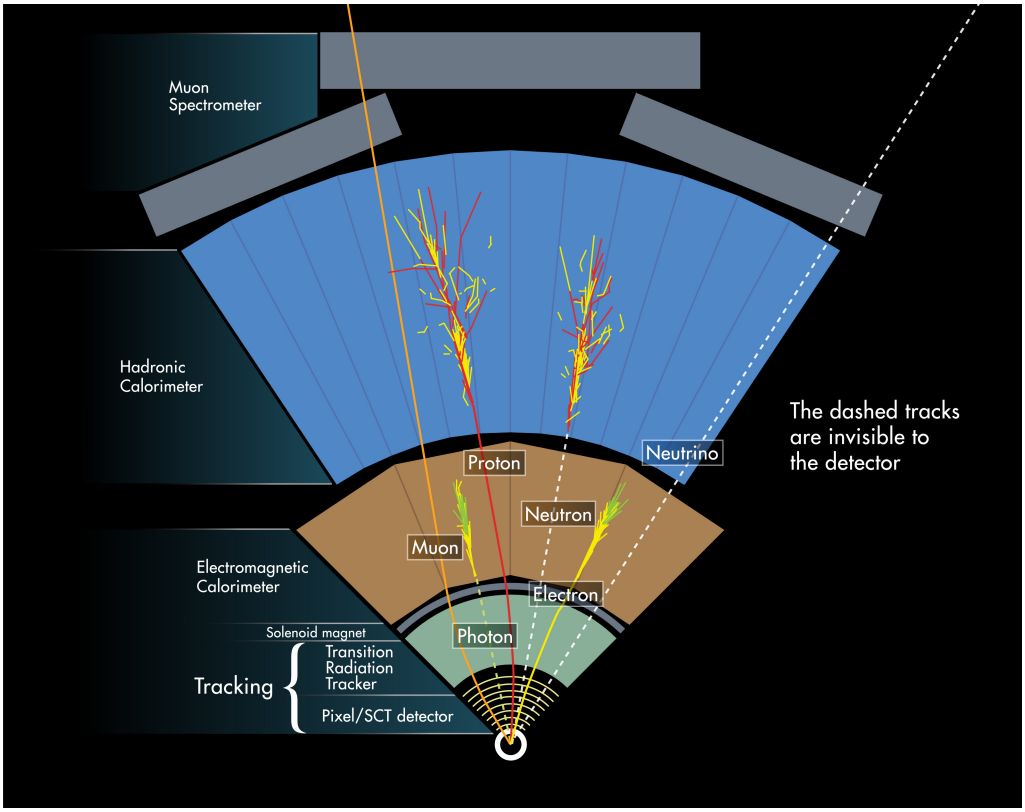


Figure 4.1: Particle signatures in the ATLAS detector [76]. Charged particles leave a track in the Inner Detector. Electrons and photons deposit their energy in the electromagnetic calorimeter while hadrons are stopped in the hadronic calorimeter. Muons are not stopped by the detector material and consequently deposit energy up to the outermost detector layer. Neutrinos do not deposit energy so that their presence is only indirectly reconstructible by calculating the missing transverse energy.

initially performed based on a pion hypothesis. A Gaussian sum filter [82] accounts for the non-linear energy loss of electrons caused by multiple scattering and bremsstrahlung and is applied in a second iteration. Subsequently, tracks are matched to electromagnetic clusters by applying cuts on η and Φ.

Identification: In Run 2, electron identification is based on a likelihood method [80]. Probability density functions of calorimeter and tracking variables are determined for signal $\mathcal{P}_S$ and background events $\mathcal{P}_B$, respectively. The likelihood of a particle candidate originating from signal or background processes is determined according to

$$\mathcal{L}_{S(B)} = \prod_{i=1}^{n} \mathcal{P}_{S(B),i}(x_i) \tag{4.1}$$

The likelihood ratio of the individual likelihoods is used as discriminant.

$$d_L = \frac{L_S}{L_S + L_B}$$

Values close to one are signal-like, while values close to zero are background-like. An alternative method for electron identification is based on a Recurrent Neural Network, discussed in Chapter 5.

Based on the likelihood-observable, four working points are defined: 'Very Loose','Loose', 'Medium' and 'Tight', which provide increasingly improved background rejection at the cost of signal efficiency. The working-points 'Loose', 'Medium' and 'Tight' provide signal efficiencies of 93%, 88% and 80%, respectively [80]. An illustrative explanation of the introduction of working points is given in Section 5.4.2.

Isolation: The isolation observable measures the activity in direct vicinity of the candidate object. The algorithm distinguishes between calorimeter and track-based isolation criteria, which either measure the deposited transverse energies or transverse momenta of tracks within a cone of radius $\Delta R = 0.2$ [83] around the given object. The isolation criteria is used to differentiate prompt particles resulting from the hard-scattering vertex or heavy-resonance decays from background caused by secondary decays. While prompt particles are expected to be isolated, non-prompt particles are often accompanied by close-by interactions. In analogy to the identification working points, isolation working points are defined, which provide a trade-off between signal efficiency and background rejection. The working points 'FCLoose' $\left(\frac{E_T^{\text{cone}}}{p_T} < 0.20, \quad \frac{p_T^{\text{cone}}}{p_T} < 0.15\right)$ and 'FCTight' $\left(\frac{E_T^{\text{cone}}}{p_T} < 0.06, \quad \frac{p_T^{\text{cone}}}{p_T} < 0.06\right)$ are defined by fixed requirements (prefix 'FC') on the isolation criteria [83]. The working point 'Gradient' is designed to provide fixed efficiencies of 90% at a transverse momentum of 25 GeV or 99% at 60 GeV [83].

4.2 Muons

A muon can be interpreted as the heavier version of an electron. Due to their large mass, muons interact less with the detector material, mainly via ionization. Muons are not stopped by the detector and deposit energy along their path through the inner detection layers out to the outermost sub-detectors, the Muon Spectrometers (see Figure 4.1). Their distinct signature allows for an identification efficiency of $\sim 99\%$ [84], making muons a valuable reference in data-based algorithms. The detailed reconstruction is documented in [84].

Reconstruction: Muon reconstruction heavily relies on signals from the Muon Spectrometers and the Inner Detector, supplemented by calorimeter information. As minimum ionizing particles, muons exhibit nearly constant energy loss along their trajectory[2]. Various reconstruction algorithms are used, that differ in the matching of different sub-detector information [84].

- **Combined Muons (CB)** are based on a combined fit of the hits from Muon Spectrometer tracks and matched Inner Detector tracks.
- **Muon Spectrometer Extrapolated Muon (ME)** are Muon Spectrometer tracks, which are extrapolated to the primary vertex after no matched Inner Detector track was found.

[2] The energy loss of charged particles passing through matter is described by the Bethe-Bloch formula, which includes a dependency on the velocity of the particle [12].

- **Inside-Out Combined Muons (IO)** are based on Inner Detector hits, which are extrapolated to at least three loosely-aligned Muon Spectrometer hits. All hits are used in a consecutive combined fit.
- **Segment-Tagged Muons (SE)** are based on Inner Detector tracks that are extrapolated to the Muon Spectrometer. The tracks additionally fulfill tight angular matching requirements with respect to a Muon Spectrometer segment.
- **Calorimeter-Tagged Muons (CT)** extrapolate Inner Detector tracks to the calorimeter, searching for energy depositions of a minimum-ionizing particle.

Identification: The working point definition is based on the different muon types. While muon candidates with 'Tight' and 'Medium' identification score solely rely on CB and IO muons, 'Loose' objects additionally take CT and ST muons into account. The efficiency of identifying muons across the full p_T-spectrum reaches efficiencies above 98%, 97% and 90%, respectively [84].

Isolation: In addition to track- and calorimeter-based isolation variables, the particle-flow-based isolation variable is defined as combination of the two individual isolation variables. The 'Loose' and 'Tight' working points require $\left(\frac{E_T^{\text{cone20}}}{p_T} < 0.30, \quad \frac{p_T^{\text{cone30}}}{p_T} < 0.15\right)$ and $\left(\frac{E_T^{\text{cone20}}}{p_T} < 0.15, \quad \frac{p_T^{\text{cone30}}}{p_T} < 0.04\right)$. The distance measure cone20 corresponds to $\Delta R = 0.2$ and cone30 describes $\Delta R = min(10\,\text{GeV}/p_T, 0.3)$ for $p_T^{\mu} < 50\,\text{GeV}$ [84]. Robustness against pile-up can be achieved by track-only working points due to the rejection of pile-up vertices. A 'TightTrackOnly' working point requires $\frac{p_T^{\text{cone30}}}{p_T} < 0.06$ [84].

4.3 Jets

Jets are collimated showers of particles and result from QCD *confinement*. High energy partons, quarks or gluons, produced in a hard scattering process, emit other gluons, split into more gluons and quark/anti-quark pairs. A parton shower emerges. As the energy of individual particles decreases, the process enters the hadronization stage, where quarks combine into color-neutral hadrons. This process creates a multitude of particles that propagate in a common direction through the detector and form a cone-like structure.

QCD jets typically deposit energy throughout the detector. They originate in the tracker and pass through the electromagnetic calorimeter up to the hadronic calorimeter, where most of the energy is deposited and the jet is stopped. The challenges in jet reconstruction are the correct assignment of particles to jets and the suppression of pile-up. The jet reconstruction workflow is documented in [85].

Reconstruction To reconstruct jets, tracker and calorimeter information is combined in the *Particle Flow Algorithm*. This approach profits from a superior momentum resolution for low energies in the tracker, where the resolution scales linearly, and the superior resolution of the calorimeter at high energies, where the resolution scales with $1/\sqrt{E}$ [85]. Reconstruction of calorimeter information originates from three-dimensional clusters of topologically connected cells (*topo-clusters*) that exceed a certain energy-to-noise ratio [86]. Tracker and calorimeter information are combined by a cell-based energy subtraction. This method adjusts the calorimeter measurement by the charged contribution measured by the tracking system. Track-cluster matching is also an important part

of vertex identification, which reduces contributions from pile-up. The reconstructed particles are called particle-flow objects. They are assigned to jets by a jet clustering algorithm. Objects are iteratively assigned based on their proximity and transverse momentum. The clustering priority follows ascending p_T, which goes along with the association of small distance measures for high momenta. The reconstructed energy is calibrated to mitigate fluctuations in the hadronization process and a shared energy deposition across several clusters. Reconstructed jet energy is calibrated against MC generated jets. The ratio of reconstructed and true momentum reveals important properties that inform calibration. The jet energy scale (JES) describes the mean of the distribution. The jet energy resolution (JER) is a measure of uncertainty and represents the width of the distribution. The calibration process corrects for both properties. They are measured with a precision of up to 5% for high p_T events and $\sim$ 1% for lower energies, respectively [87].

Flavor-Tagging QCD jets are distinguished according to their origin. Sophisticated flavor tagging algorithms separate b-,c- and light flavor jets from u,d,s-quarks or gluons. Deep-learning algorithms exploit the complex detector signatures to perform the classification. Latest developments study jet properties in Graph Neural Networks [88].

4.4 Missing Transverse Energy

The LHC proton beams are aligned along the $z-$axis and consequently, do not carry transverse momentum. Due to energy conservation, the sum of final state momenta equals zero. Deviations from zero imply that particles have left the detector undetected. This case is expected for weakly interacting SM neutrinos. Another contribution to missing transverse energy is the limited acceptance range of the detector. The total missing transverse momentum is determined as the negative vector sum of transverse momenta ($p_T = (p_x, p_y)$) of reconstructed objects [89].

$$p_T^{\text{miss}} = -\sum_{\substack{\text{selected}\\ \text{electrons}}} p_T^e - \sum_{\substack{\text{accepted}\\ \text{photons}}} p_T^\gamma - \sum_{\substack{\text{accepted}\\ \tau-\text{leptons}}} p_T^{\tau_{\text{had}}} - \sum_{\substack{\text{selected}\\ \text{muons}}} p_T^\mu - \sum_{\substack{\text{accepted}\\ \text{jets}}} p_T^{\text{jet}} - \sum_{\substack{\text{unused}\\ \text{tracks}}} p_T^{\text{track}} \tag{4.2}$$

The missing transverse energy E_T^{miss} is defined as the magnitude of the transverse momentum vector.

$$E_T^{\text{miss}} = |p_T^{\text{miss}}| = \sqrt{(p_x^{\text{miss}})^2 + (p_y^{\text{miss}})^2} \tag{4.3}$$

An overlap removal procedure is applied to prevent double counting of energy depositions used across different reconstructed objects.

Due to the presence of multiple neutrinos in final states involving τ leptons, missing transverse energy is a crucial analysis observable. Besides uncertainty propagation from the different objects involved, contributions from detector inefficiencies further add to the uncertainty of the observable. The resolution depends on various aspect, such as the energy of the event, pile-up or the number of jets, typically ranging from 5 GeV-20 GeV [89].

4.5 Hadronic τ-Leptons

τ-leptons exhibit a diverse decay spectrum that asks for various reconstruction algorithms. The topology of a leptonic τ-decay exhibits missing energy, which is caused by neutrinos as well as a reconstructed light lepton (electron or muon). Their reconstruction is described in Section 4.1 and 4.2. The signature of hadronically decaying τ-leptons is more complex and features dedicated algorithms for reconstruction.

Reconstruction The event topology of a hadronic τ decay features a neutrino, and one or three charged tracks as well as a variable number of accompanying neutral pions. The object reconstruction is detailed in [90]. The τ lepton reconstruction is initiated by jet signatures, which are reconstructed by the anti-k_T-algorithm with $R = 0.4$. In order to be an eligible $\tau_{\text{had-vis}}$ candidate, the seeding jet is required to fulfill $p_T > 5\,\text{GeV}$ and $|\eta| < 2.5$ [90].

Due to the non-vanishing lifetime of the τ lepton, the production vertex differs from the primary vertex. A dedicated vertex association algorithm considers tracks within $R < 0.2$ of the seed jet and identifies the production vertex. The latter is determined as the vertex with the highest p_T fraction [90]

$$f_{p_T} = \frac{\sum p_T(\text{track associated to vertex})}{\sum p_T(\text{all tracks})} \tag{4.4}$$

The properties of τ associated tracks are re-calculated with respect to the production vertex. Tracks associated to the τ object need to meet a set of criteria that entail the detection in the core region of $\Delta R < 0.25$, a match with hit requirements in different parts of the Inner Detector or a minimum transverse momentum of 1 GeV. In order to establish the correct τ lepton charge, the associated tracks need to be classified. Multivariate techniques are employed for track classification, distinguishing genuine τ related tracks from nearby activity in the detector. Either one or three tracks are selected maintaining a net charge of ± 1.

A critical property of the τ lepton is its energy, as it significantly impacts the $m_{\tau\tau}$ distribution. The τ energy scale is measured using a data tag-and-probe[3] approach and achieves a precision of 2-3% [91].

τ_{had} Identification Hadronically decaying τ leptons leave a cone-shaped signature in the detector, such as depicted in Figure 4.2(b). QCD jets, shown in 4.2(a), exhibit a similar, typically less collimated signature. To guarantee a reliable τ_{had}-identification, a Recurrent Neural Network (RNN) [92] differentiates the heavy leptons from jets.

The RNN utilizes both track and calorimeter information as inputs. In addition to collimation, information on the secondary vertex is another important observable used for training. The RNN yields a probability score per particle object and signals the correct identification of a τ_{had} candidate. The probability score is used to determine the efficiency of selecting τ_{had} objects and the corresponding background selection efficiency.

[3] The tag and probe technique assesses the performance of reconstruction or identification algorithms. Typically, a well understood process as $Z \to ll$ represents the basis. One of the leptons, the tag, is selected with stringent selection cuts to ensure genuineness, the other lepton, the probe, on the other hand is selected with only loose requirements. By determining the invariant mass of the di-lepton system and limiting it to a window around the Z-peak, the genuineness of the selected pair can also be confirmed. This technique allows to study events of the probe sample that would not pass the stringent selection.



(a) QCD jet (b) τ_{had}

Figure 4.2: QCD jet a) and τ_{had} b) signature. Both objects leave a cone-like structure in the detector, which is typically more collimated for τ_{had} candidates. Figure taken from [25].

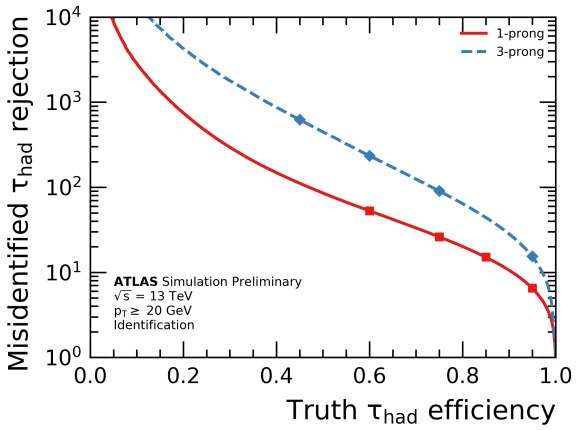


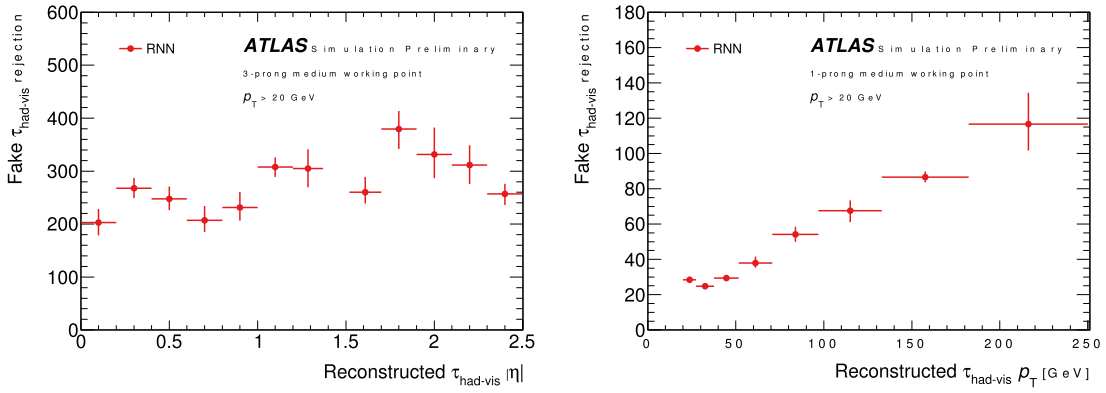
Figure 4.3: Background rejection of 1- and 3-prong τ_{had} candidates in dependence of the truth τ_{had} efficiency for the RNN based identification algorithm in red and blue, respectively. The working points very loose, loose, medium and tight are visualized by the coloured markers [93].

The background rejection power corresponds to the inverse background selection efficiency and is depicted in Figure 4.3 for 1-prong and 3-prong decays, respectively.

Four *working points* are defined to set the required signal purity of an analysis: very loose, loose, medium and tight. For 1-prong events, the working points correspond to signal efficiencies of 95%, 85%, 75% and 60% , respectively. For 3-prong events, the efficiencies are set to 95%, 75%, 60% and 45% [94].

The background rejection is not constant across the phase-space and scales with p_T and η of the reconstructed $\tau_{\text{had,vis}}$ candidate, as illustrated in Figure 4.4. The degree of variation also differs between 1-prong and 3-prong events.

Decay-Mode Reconstruction Many physics analyses do not only depend on the number of charged tracks but also on the detailed τ substructure and necessitate the reconstruction of decay-modes. The reconstruction of the hadronic τ decay distinguishes between five dominant decay-modes, which cover more than 90% of all hadronic decays, as summarized in Table 2.4(a). These modes are categorized based on the number of charged tracks (1- or 3-prong) and neutral pions (n).



(a) η-dependence for 3-prong events.

(b) p_T-dependence for 1 prong events.

Figure 4.4: Fake (non-τ) rejection for medium τ-ID in bins of the transverse momentum and the pseudorapidity. Both dependencies also vary with the number of charged tracks involved in the τ decay. Figure adapted from [92]

- 1p0n: $\pi^{\pm}$
- 1p1n: $\pi^{\pm}\pi^{0}$
- 1pXn: $\pi^{\pm}X\pi^{0}$
- 3p0n: $\pi^{\pm}\pi^{\pm}\pi^{\mp}$
- 3pXn: $\pi^{\pm}\pi^{\pm}\pi^{\mp}X\pi^{0}$

In place of charged pions, charged kaons can also be involved, which account for $\sim$ 3% of the hadronic decays [95].

The τ substructure is obtained with the *Tau Particle Flow* method [95]. Charged tracks are reconstructed with tracker information. The reconstruction of neutral pions is based on the energy deposits in the calorimeters [4]. The energy of π^{0} candidates is corrected from charged object contamination by calculating the energy difference between tracker and hadronic calorimeter.

The decay-modes are classified with a BDT [95], which uses the τ substructure as input. This approach outperforms a simplistic counting methodology of reconstructed tracks and π^{0}s. The BDT exploits additional information like the kinematics of the τ decay products or the ID of the π^{0}. Three different BDT trainings are used to classify decay-modes including neutral π^{0}s. Events with either one or three charged tracks and an abundance of π^{0} candidates are directly classified as 1p0n or 3p0n, respectively.

The efficiency of the BDT decay-mode classification for $\gamma^{*} \rightarrow \tau\tau$ events is illustrated in Figure 4.5. The method achieves reliable reconstruction efficiencies $\gtrsim$ 80% for the 1p0n, 1p1n and 3p0n decay-mode, which are the dominant modes that cover ~18%, ~40% and ~15% [12] of all hadronic decays. The efficiency decreases to $\sim$ 50% for decay-modes that involve more than one π^{0}. The total fraction of correct classification, the diagonal efficiency, is 72.9%.

Reprocessed Run 2 and upcoming Run 3 data will utilize a DeepSet neural network for decay-mode classification, which profits from an improved diagonal efficiency of 81.7% [90].

[4] Neutral Kaons are not reconstructed [95].

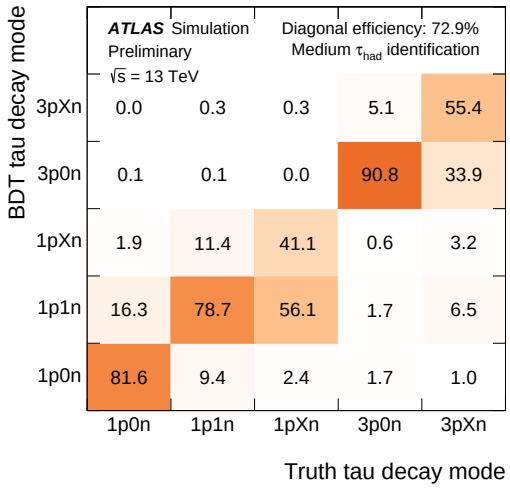


Figure 4.5: Reconstruction efficiency matrix for the five τ_{had} decay-modes with a BDT-based classifier in $\gamma^* \rightarrow \tau\tau$ events [90].

4.6 Di-Tau Mass Reconstruction

The reconstruction of the invariant di-tau mass is crucial to distinguish signal $H \rightarrow \tau\tau$ processes from the dominant $Z \rightarrow \tau\tau$ background.

Both bosons are close in mass with $m_H = 125\,\text{GeV}$ and $m_Z = 91\,\text{GeV}$ [12], which makes the di-tau mass resolution a prerequisite for efficient separation of the two processes. The presence of at least one neutrino per τ decay complicates the reconstruction and degrades the resolution. The conventional, analytical 4-momentum calculation

$$m_{\tau\tau}^2 = \left(\mathbf{p}_{vis}^{\tau_1} + \mathbf{p}_{\nu}^{\tau_1} + \mathbf{p}_{vis}^{\tau_2} + \mathbf{p}_{\nu}^{\tau_2}\right)^2 \tag{4.5}$$

is not applicable in this case since the neutrino momenta cannot be measured directly. Consequently, alternative techniques are employed.

4.6.1 Collinear Approximation

Collinear approximation [96] takes the missing transverse energy E_{mis}^T into account and compensates for the unmeasured neutrino four-momenta. The method is based on the following two simplified assumptions [97]

- the missing transverse energy is solely caused by neutrinos. Consequently, other sources, such as detector or reconstruction imperfections, are neglected.
- neutrinos are perfectly collinear with the visible decay products of the τ-lepton ($\Phi_\nu = \Phi_{\text{vis}}$, $\Theta_\nu = \Theta_{\text{vis}}$).

The x and y-component of the missing transverse energy are described by [97]

$$E_{T,x}^{\text{mis}} = p_{\text{mis},1} \sin\theta_{\text{vis},1} \cos\phi_{\text{vis},1} + p_{\text{mis},2} \sin\theta_{\text{vis},2} \cos\phi_{\text{vis},2}, \tag{4.6}$$

$$E_{T,y}^{\text{mis}} = p_{\text{mis},1} \sin\theta_{\text{vis},1} \sin\phi_{\text{vis},1} + p_{\text{mis},2} \sin\theta_{\text{vis},2} \sin\phi_{\text{vis},2}, \tag{4.7}$$

where $p_{\text{mis},1/2}$ represents the missing momentum of the neutrino system[5]. Considering the momentum fractions carried by the visible τ decay products

$$x_{1,2} = \frac{p_{\text{vis},1,2}}{p_{\text{vis},1,2} + p_{\text{mis},1,2}}, \tag{4.8}$$

the di-tau mass estimation is determined by

$$m_{\tau\tau} = \frac{m_{\text{vis}}}{\sqrt{x_1 x_2}} \tag{4.9}$$

The accuracy of approximation improves with the boost of the τ system as the decay-products are created with increased collimation. The method fails in scenarios where the two τs are produced back-to-back, due to the degeneration of the system of equations.

4.6.2 Missing Mass Calculator

The Missing Mass Calculator (MMC) is a likelihood-based algorithm designed to estimate the invariant di-tau mass. The algorithm minimizes a likelihood function through phase-space scans within a kinematically allowed region [97]. Similar to the collinear mass approximation, the MMC assumes neutrinos to act as the sole source of missing energy. Unlike previous assumptions, non-vanishing angles (θ_{3D}) between the neutrino system and the remaining visible decay products of the τ lepton are considered.

This leads to six unknown variables, the x, y and z-components of the τ neutrinos. Leptonic τ decays are described by eight unknown variables, which in addition comprise the invariant masses of the neutrino system $M\left(\sum_i \nu_i^{\tau_{\text{lep}}}\right)$. Despite these relations, the system remains underconstrained. Along with the missing transverse energy relations

$$E_{T,x}^{\text{mis}} = p_{\text{mis},1} \sin\theta_{\text{mis},1} \cos\phi_{\text{mis},1} + p_{\text{mis},2} \sin\theta_{\text{mis},2} \cos\phi_{\text{mis},2}, \tag{4.10}$$

$$E_{T,y}^{\text{mis}} = p_{\text{mis},1} \sin\theta_{\text{mis},1} \sin\phi_{\text{mis},1} + p_{\text{mis},2} \sin\theta_{\text{mis},2} \sin\phi_{\text{mis},2}, \tag{4.11}$$

and the invariant mass constraint of the two τ leptons,

$$m_{\tau,1}^2 = M\left(\sum_i \nu_i^{\tau_{1,\text{lep}}}\right)^2 + m_{\text{vis},1}^2 + 2\sqrt{\vec{p}_{\text{vis},1}^2 + m_{\text{vis},1}^2} \cdot \sqrt{\vec{p}_{\nu,1}^2 + M\left(\sum_i \nu_i^{\tau_{1,\text{lep}}}\right)^2} - 2|\vec{p}_{\text{vis},1}||\vec{p}_{\nu,1}| \cos\theta_{3D,1} \tag{4.12}$$

[5] In case of a leptonic τ decay, two neutrinos will be present.

$$m^2_{\tau,2} = M\left(\sum_i \nu_i^{\tau_{2,\text{lep}}}\right)^2 + m^2_{\text{vis},2} + 2\sqrt{\vec{p}^{\,2}_{\text{vis},2} + m^2_{\text{vis},2}} \cdot \sqrt{\vec{p}^{\,2}_{\nu,2} + M\left(\sum_i \nu_i^{\tau_{2,\text{lep}}}\right)^2} - 2|\vec{p}_{\text{vis},2}||\vec{p}_{\nu,2}|\cos\theta_{3D,2} \tag{4.13}$$

only four equations can be formulated. As there are more unknowns than equations, an exact solution is out of reach. The MMC algorithm solves the issue by scanning the valid parameter space. Since not every possible solution is equally likely, their probability is taken into account by evaluating a combined likelihood function. It considers event topologies, such as the angular distance between visible decay products of the τ lepton and the neutrino system as well as resolution effects of E^T_{mis}, information from the $p_{\tau_i^\nu}/p_{\tau_i^{\text{vis}}}$ ratio or the invariant mass of the involved neutrino system [98]. The sampling is performed by a Markov Chain using the Metropolis-Hastings algorithm [99]. It generates a sequence of samples from the probability distributions. The algorithm iteratively proposes new states and accepts or rejects them based on a specific acceptance criterion. The final mass estimate can be chosen from different evaluation techniques such as the solution with the highest probability or the most frequently reconstructed mass within all valid solutions.

In this thesis, the invariant mass of the di-tau system is estimated with the Missing Mass Calculator, which provides the superior resolution with respect to other available reconstruction algorithms. In some rare cases, the likelihood-based algorithm fails to reconstruct a mass. In order to recover these events, the collinear mass approximation is used instead. The mixed approach is denoted as *Mixed MMC/collinear Mass Estimator*.

4.6.3 Neural Network

Although not yet implemented in ATLAS software, neural networks present a promising alternative to the computationally-expensive likelihood-based MMC. It was demonstrated in previous work ([100, 101]) that a neural network offers comparable performance in terms of physics accuracy. Consequently, neural networks can replace the well-tested MMC in future studies.

CHAPTER 5

Particle Identification with the Transition Radiation Tracker

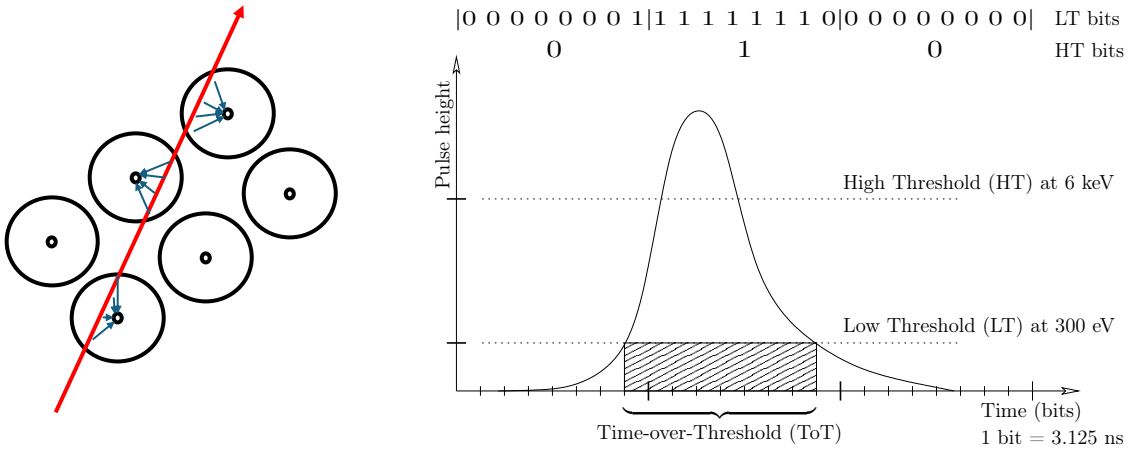
The content of the following chapter has also been largely documented in the ATLAS internal note referenced in [2], which follows similar structure und partially similar wording.

In the highly complex environment of proton-proton collisions, the combination of information from each sub-detector is crucial for a successful analysis of the recorded data. In the $H \rightarrow \tau\tau$ analysis, the Transition Radiation Tracker provides tracking information and also contributes to particle identification (PID). Especially for track momenta below 50 GeV [102], the sub-detector allows to reliably distinguish minimum ionizing particles like pions from ultra-relativistic electrons. Electrons cause signatures similar to 1-prong $\tau_{\text{had,vis}}$ objects and are consequently a dominant background in selections targeting τ leptons. In order to suppress electrons misidentified as τs, an electron veto is applied in the $H \rightarrow \tau\tau$ analysis. The veto is determined from calorimeter and tracking information, as well as the electron probability determined from TRT signals [90]. A Recurrent Neural Network was developed for electron identification [103] with the goal to outperform and replace the presently used likelihood-based electron identification score, introduced in Section 4.1. The initial RNN setup is further optimized and adapted to match the Run 3 requirements. The studies comprise a network training on the Run 3 detector conditions, a reduction of the required CPU expense while maintaining the network's performance as well as a validation of the interchangeability of muons and pions in their role as background process in the network's training.

5.1 Outline

The Transition Radiation Tracker is a gas-based straw tube detector that serves not only as a tracking device but also contributes to particle identification.

When a charged particle traverses a straw, it ionizes the gas within. The released electrons are accelerated by the electrical field within the tubes towards the centered wire, which represents the anode (Figure 5.1(a)). An avalanche of electrons is developed, which is detected in form of an electric pulse that is amplified, shaped, and read out using a 27-bit pattern. Two thresholds are defined - a low threshold checked in 24 bits every 3.125 ns, and a high threshold represented by the remaining 3 bits,



(a) Sketch of ionisation along the track.

(b) Electrical signal pulse in the TRT [104].

Figure 5.1: Sketch of signal creation along the track, depicted in a). The track (red arrow) traverses multiple straw tubes (black circles). The released electrons in the gas are accelerated towards the anode (blue arrows). The resulting electrical pulse is shown in b). Two different thresholds are defined, which are represented by 24 low and 3 high-threshold bits.

checked over a time of 25 ns each. A bit value of 0 indicates that the threshold was missed, while a value of 1 indicates that it was reached (Figure 5.1(b)).

High-threshold hits are typically initiated by X-ray photons, which deposit between 4 and 20 keV [105]. Minimum-ionizing particles reach about 2 keV [79] and consequently only meet the low-threshold requirements. X-ray photons result from transition radiation, an electromagnetic phenomenon that occurs when a highly relativistic particle transitions between two materials with different refractive indices. The polypropylene fibers and foam material embedding the straws, create multiple transition boundaries, which increases the rate of X-ray emission. The emission probability is proportional to the γ-factor of the crossing particle, which allows a differentiation between minimum ionizing particles like pions or muons (low γ-factor) and highly relativistic particles like electrons (high γ-factor).

The gas composition within the straws impacts the efficiency of high-threshold hit detection. During Run 1, the preferred gas mixture consisted of 70% Xenon (Xe), 27% Carbon Dioxide (CO_2), and 3% Oxygen (O_2) in all straws. Despite its superior X-ray absorption properties, Xenon has been progressively replaced by Argon (Ar), which is cheaper and more environmentally friendly while maintaining the tracking capabilities [53].

Figure 5.2 illustrates the changes in gas geometry between Run 2 and 3. Compared to previous compositions, the barrel is exclusively filled with Argon in Run 3.

5.2 Recurrent Neural Networks

Recurrent Neural Networks are specifically designed to process sequenced data. Through an internal loop-structure, they can maintain memory of previous elements in the sequence. The RNN training relies on minimizing a loss function, which compares the predicted network outputs to the true values.

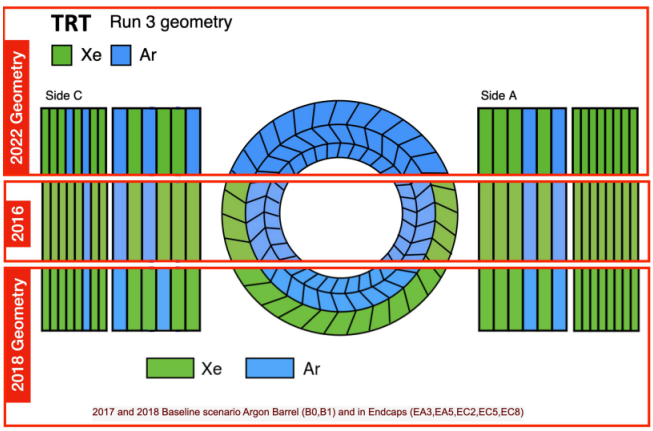


Figure 5.2: Changes in the TRT gas geometry over time. Adapted from [106].

During training, internal weights of the network are iteratively updated using gradient descent [1]. A back-propagation algorithm calculates the gradients of the loss function with respect to the network's weights, starting from the last layer and propagating back to the first.

Vanishing or exploding gradients present a challenge for RNNs and are caused by the multiplicative effects in each step of the sequence. They can lead to a loss of long-term memory. To address this, advanced network structures, such as Long Short-Term Memory (LSTM) networks [107] have been developed to better handle long-term dependencies.

The general network architecture follows a chain of repeating modules, as illustrated in Figure 5.3. Each chain link of the network is provided with an input sequence element x_t and produces a corresponding output h_t. The core component is the cell state, which transports information across several modules and promotes long-term memory. The information flow in the individual modules is controlled by three gates.

- **Forget Gate:** The forget gate decides which information to discard through the application of a sigmoid function. It outputs values between zero and one, where zero means to completely forget and one equates to completely keep the given information.
- **Input Gate:** The input gate decides which new information to store. A sigmoid layer rates the inputs relevance, while a tanh operation maps potential new input states onto a range from minus one to one.
- **Selection Gate:** The selection gate filters the final output of the module by applying tanh and sigmoid operations.

5.3 The Setup

The RNN architecture, illustrated in Figure 5.4, is optimized to meet external requirements that are dictated by the unique data structure used for training. LSTM layers are a key feature of the presented

[1] Gradient descent is an optimization algorithm. In the context of network training, it finds the loss function's minimum by iteratively updating the models parameter following the negative gradient of the loss function.

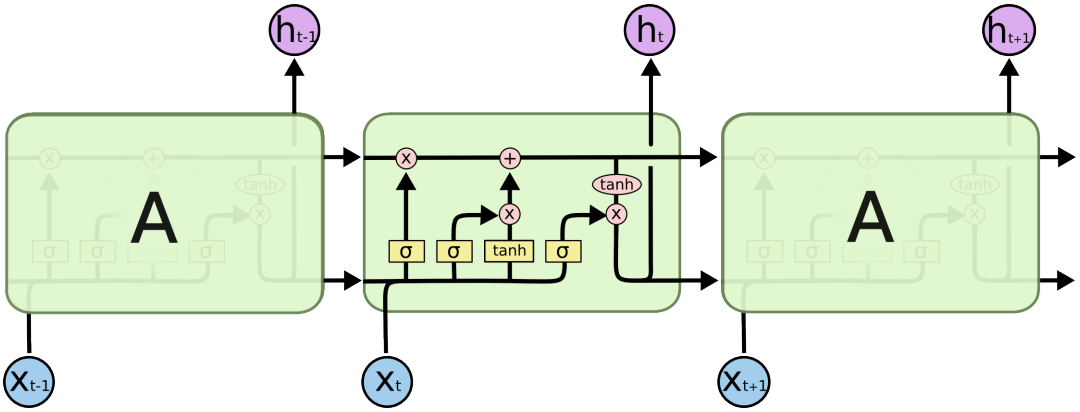


Figure 5.3: Schematic of a LSTM network [108]. Repeating network units are depicted in green. The network inputs per sequence element x_t are depicted in blue, the corresponding outputs h_t in violet.

setup and are well-suited to process particle tracks that consist of a sequence of consecutive hits. Hit information is either binary, such as the high-threshold information, or a continuous variable, such as the track length per straw. The LSTM layer can treat the hits of a single track as a cohesive unit.

The variable length of the processed sequence data reflects the different number of hits in different tracks and poses a challenge for batch training, where multiple tracks are processed simultaneously. A possible solution [2] is zero-padding in combination with masking. To ensure uniform hit lengths per batch, the longest sequence length in each batch is used as an upper limit, and all shorter sequences are padded with zeros to match this length. The added elements are marked with a flag by the masking layer. The hit-wise flags indicate whether the value is physically meaningful or not. This distinction is crucial to distinguish physical binary information from padded zeros.

In the initial RNN setup, the sequence length issue was addressed by truncating all sequences to 40 hits and applying zero padding to shorter sequences. This approach discards meaningful information, which is fully conserved in the current implementation.

For training, track-level information is used in addition to hits. An additional dense layer structure is used to process the concatenation of hit and track information, followed by a final single output representing the probability of electron-type candidates. The hyperparameter settings of the network are summarized in Table 5.1.

- Each layer structure is defined through an individual number of nodes and their activation functions, which rate the input's relevance.
- The learning rate is a property of the selected optimization algorithms and controls the step-wise update of the internal network weights.
- The batch size indicates how many events are processed at once during training.

[2] This approach was developed and tested in collaboration with Aleksandr Petukhov. Detailed information can be found in [109].

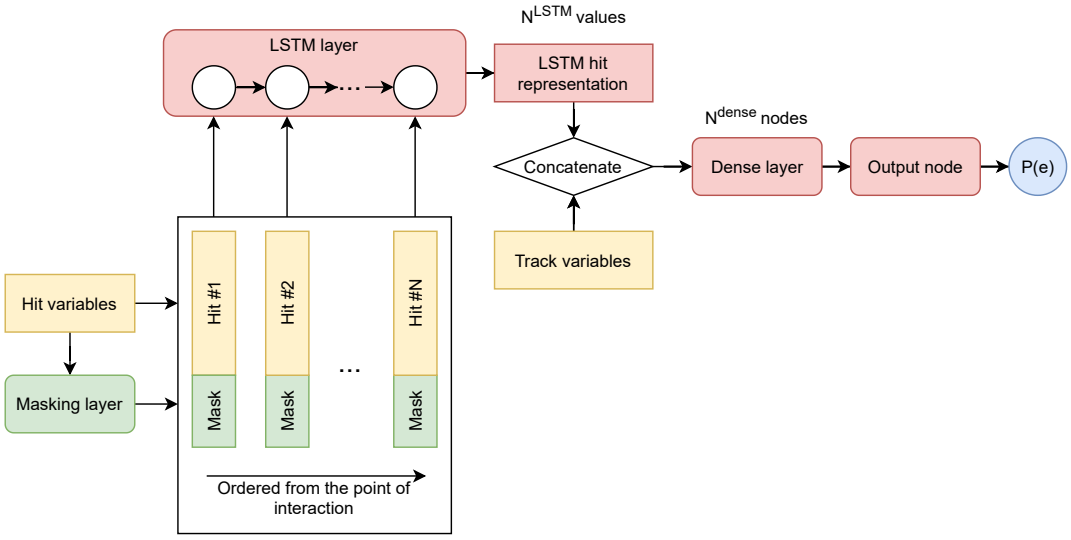


Figure 5.4: RNN architecture. Inputs are marked in yellow, network layers in red and the output node in blue. The masking layer in green enables batch training. Taken from [109].

Hyperparameter		Value
LSTM layer	nodes	64
	activation	tanh
	recurrent activation	sigmoid
Dense layer	nodes	128
	activation	ReLU=max(0,x)
Output layer	nodes	1
	activation	sigmoid
learning rate		0.0001
batchsize		256

Table 5.1: Default hyperparameter setting of the Run 2 setup. The activation and recurrent activation of the LSTM layer apply to the cell state and the gates, respectively.

5.4 Training Prerequisites

A prerequisite of an unbiased RNN training is a suited selection of training samples including an adequate event selection and pre-processing.

Sample Types

In the RNN training, electrons from $Z \rightarrow e^+e^-$ events are considered as signal. Two different background samples are investigated - muons from $Z \rightarrow \mu^+\mu^-$ decays and pions from a di-jet sample. The background-dependent outcomes are discussed in Section 5.6.

The presented studies solely rely on simulation. Details on the applied Monte Carlo generators are documented in Appendix A. [3]

The RNN training is based on NTuples, which are produced with custom TRT software, such as the TRTFramework[4], using AnalysisBase release 22.2.67.

5.4.1 Event Selection

The event selection for RNN training samples is summarized in Table 5.2. The upper half describes the requirements of the Inner Detector Track Selection `LoosePrimary` cut [110] while the lower half improves analysis-related demands by guaranteeing reasonable track properties.

category	selection
N(TRT hits)	≥ 9
N(Si hits)	≥ 7
N(shared modules)	≤ 1
N(Si holes)	≤ 2
N(pixel holes)	≤ 1
p	>2 GeV
p_T	[2,200] GeV
$\lvert\eta\rvert$	≤ 2
dE/dx	> 0

Table 5.2: Track selection: The upper limits are part of the InDetTrackSelection `LoosePrimary` selection [110]. The lower cuts are additionally applied to guarantee a good event selection. The TRT hit type definitions are listed in [111].

In di-jet samples, pion-candidates need to be truth-matched and additionally need to pass the requirements to become an electron candidate.

[3] The simulated Run 3 baseline gas geometry used in the following studies differs from the final gas configuration depicted in Figure 5.2. In the simulation EC2 and EC5 are filled with Argon. The final Run 3 geometry uses Argon in EC0, EC3, EC5, EC8, and EC10. This discrepancy is not expected to cause significant changes in the observed performance since the total fraction of Xe filling is only slightly reduced.

[4] https://gitlab.cern.ch/atlas-trt-software/TRTFramework

Input Variables

Track level as well as hit level variables cover crucial information for training describing the event kinematics as well as transition radiation related observables, such as high-threshold information. The selected variables for training are listed below.

Track Variables:

- $\boldsymbol{p}$: momentum
- $\boldsymbol{p_T}$: transverse momentum
- **fHTMB** : fraction of high threshold hits
- **PHF** : precision hit fraction
- **nXehits** : number of Xe hits
- **fAr** : fraction of Ar hits
- **trkOcc** : occupancy ($\propto$ particle density)
- **dEdx** : energy loss per path length dx [5]

Hit Variables:

- **hit_HitR** : R coordinate
- **hit_HitZ** : Z coordinate
- **hit_L** : track length in straw
- **hit_HTMB** : high threshold hit (1) or not (0)
- **hit_gasType** : hit gas type (Ar (1), Xe (0))
- **hit_tot** : time over threshold
- **hit_rTrkWire** : distance between track and wire
- **hit_isPrec** : precision hit (1) or not (0)

Re-weighting: The kinematic phase-space of signal and background samples need to match in RNN training, so that the network learns to perform particle identification based on particle properties and their correlations and is not biased by the distribution's shapes. In the initial setup, events were cut, so that the distributions of signal and background match in p_T and η. In the new setup, re-weighting is used instead, which allows to match and normalize the distributions without discarding events. Details on the re-weighting procedure are elaborated on in reference [109]. The track- and hit-level variables after the re-weighting are depicted in Figure A.1 and A.2.

Scaling & Offset: The feature ranges vary significantly between the different input variables. A standard scaler is applied, which shifts each observable mean to zero and scales it to unit variance.

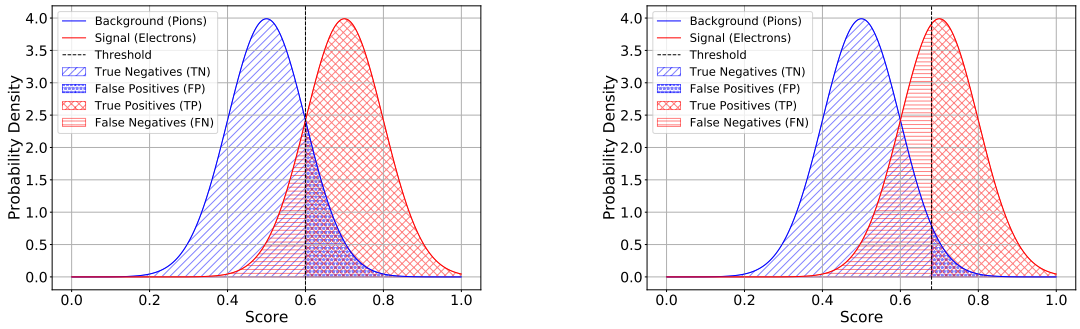
$$x_{\text{scaled}} = \frac{x - \mu_x}{\sigma_x}. \tag{5.1}$$

This pre-processing prevents large jumps in the internal RNN weights and consequently provides a more stable training environment. Binary variables remain unchanged.

5.4.2 Figure of Merit

To evaluate the RNN performance, a Receiver Operating Characteristic (ROC) curve is selected as figure of merit. The area over the curve (AOC) is used to measure the performance of a binary classifier. In the case of electron PID with the RNN, the output score of the RNN is used to differentiate

[5] The dE/dx variable is calculated as the sum of time over threshold measurements, which are normalized by their corresponding track lengths per straw. The variable is set to zero if for example certain hit quality requirements are not fulfilled. For more details see [112].



(a) High signal efficiency and low background rejection.

(b) High background rejection and low signal efficiency.

Figure 5.5: Idealized score distributions of background and signal samples. The blue distribution represents the RNN scores for background, the signal follows in red. The black threshold line defines the binary classifier. Events with scores smaller than the threshold are labelled as background, others are signal events. Depending on the threshold, the efficiencies to select signal events and to reject background events changes, which is illustrated by the two scenarios in 5.5(a) and 5.5(b).

signal and background events. Figure 5.5 exemplifies idealized Gaussian distributions of signal and background scores.

The score measures the probability of the evaluated object being signal. The signal distribution (electrons) peaks at higher scores than the background distribution (pions). To define a binary classifier, a set threshold represents the minimum score required for an event to be classified as signal. Due to the overlap between the two distributions, a small share of background events are labeled as signal (False Positives), while a fraction of signal events are labeled as background (False Negatives). The efficiency to select signal events and the efficiency to select background events are defined as

$$\epsilon_{\text{sig}} = \frac{\text{True Positive}}{\text{True Positive} + \text{False Negative}}, \quad \epsilon_{\text{bg}} = \frac{\text{False Positive}}{\text{False Positive} + \text{True Negative}}. \tag{5.2}$$

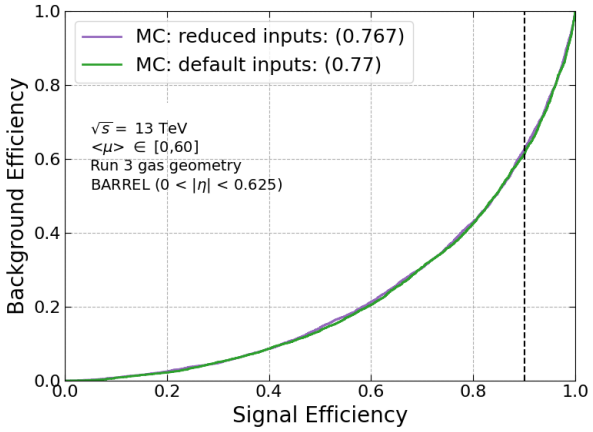
Depending on the threshold, background rejection can be improved at the cost of signal efficiency, as illustrated in the transition from Figure 5.5(a) to 5.5(b). This interplay is also reflected in ROC curves which map a background efficiency to a signal efficiency. As example consider Figure 5.6(b). The classifier's performance is measured by the area over this curve. An AOC value of one marks optimal separation between signal and background.

5.5 Reduction of Complexity

In the initial RNN development, performance was optimized without focus on the CPU usage [103]. Since the required consumption is a deciding factor for the integration of the RNN tool into the ATLAS event reconstruction algorithms, the setup's settings are reviewed in order to find a reasonable balance between performance and CPU usage in the RNN evaluation.

random variable	AOC **AOC_incl = 0.866**
~~fHTMB~~	0.86
hit_HTMB	0.51
~~PHF~~	0.866
hit_isPrec	0.772
~~fAr~~	0.865
~~fnXehits~~	0.862
hit_gasType	0.836

(a) Redundant Variables



(b) ROC curve

Figure 5.6: Investigation of the relevance of the inputs. Table a) shows the pairs of redundant inputs. Crossed out inputs do not add to the performance of the RNN and are consequently discarded. The AOC is determined without restrictions on η. Figure b) compares the ROC curves of the default input setting to the reduced one. The barrel region is selected as example to illustrate conserved performance.

5.5.1 Input's Relevance

Reviewing the default inputs, listed in Section 5.4.1, reveals that some information is represented at both, track- as well as hit-level. The doubling introduces redundancy while adding to the computational cost. The concerned inputs describe the gas type of the hits, as well as the high threshold and precision hit information. The impact of each input variable on the RNN performance is assessed during the network evaluation by substituting one input at a time with random numbers. If the AOC drops significantly compared to the evaluation with physics values, the variable contains viable information for the RNN and should not be excluded.

Table 5.6(a) shows the AOC as the indicated variable is replaced by random numbers. The comparison against the evaluation based on all physics variables, yields an AOC of 0.866. The redundant track-level variables fHTMB, PHF, fAr, and nXehits do not significantly contribute to the performance, as their randomization results in a reduced AOC of less than 0.5%. Consequently, these variables are excluded from the input parameters[6], and four track-level variables (p, p_T, trkOcc, dEdx) and seven hit-level variables (hit_tot, hit_L, hit_rTrkWire, hit_HitR, hit_HTMB, hit_isPrec, hit_gasType) remain. The selected set of inputs is validated by probing ROC curves in diverse phase-space regions. The example shown in Figure 5.6(b) presents the results based on RNN trainings with the inclusive and the reduced input set in the barrel region. Both curves are in good agreement and exhibit nearly similar performance.

5.5.2 Number of Nodes

The default number of nodes, 64 LSTM nodes & 128 Dense nodes, is generously chosen for the complexity of the task. Since the number of nodes is directly correlated to the mathematical operations

[6] hit_HitZ has no track-related counterpart. It was dropped anyway since it's contribution is with AOC=0.865 negligible.

Model	Dense Nodes	LSTM Nodes	CPU [ms]
0	64	64	158
1	48	48	125
2	32	32	97
3	16	16	72

Table 5.3: Node dependent CPU time for 100 events measured in the TrackCollectionMerger. The sigmoid+tanh activation functions are used across all setups. An uncertainty of ∼2 % can be assumed from repeated measurements.

and thus the evaluation time, a possible reduction of nodes is a suitable approach to reduce the computational load.

The relationship between the complexity of the model and the CPU consumption is given in Table 5.3. The listed values represent the processing of 100 events using Athena release 22.0.37[7]. Within the software framework, the TrackCollectionMerger module is responsible for the RNN evaluation. A constant expense of 38 ms spent in the module in addition to the RNN evaluation was subtracted from the values in Table 5.3 in order to reflect the pure evaluation cost. A significant dependence between the number of nodes and the CPU time is observed.

A compromise between performance and CPU usage is found with 16 nodes in both, the LSTM and Dense layers. Below this threshold, a continuous degradation in performance was observed as the number of nodes decreased, shown in Figure 5.8(a).

5.5.3 Activation Function

The internal structure of a LSTM cell relies on two mathematical functions that moderate the activation of the node. They determine the output of the node and - consequently - the relevance of the provided input. Typically, the hyperbolic tangent and sigmoid function are employed, both of which contain exponential components that significantly contribute to the computational cost.

The hyperbolic tangent and sigmoid functions are defined as follows:

$$\tanh(x) = \frac{\exp(x) - \exp(-x)}{\exp(x) + \exp(-x)} \qquad \text{and} \qquad \mathrm{S}(x) = \frac{1}{1 + \exp(-x)},$$

In contrast, alternative activation functions with linear components require less CPU time. Two such functions, the soft-sign and hard-sigmoid activation functions, are examined for feasibility. They are defined as:

$$\text{soft-sign}(x) = \frac{x}{1 + |x|} \qquad \text{and} \qquad \text{hard-sigmoid}(x) = \max\left(0, \min\left(1, 0.2x + 0.5\right)\right).$$

Figure 5.7 presents the current activation functions alongside their potential replacements. Since the soft-sign function is not available in the lwtnn-framework, which is used to convert neural networks to the required format for use in Athena [8], it was skipped in the Run 3 preparation. Consequently, only the applicability of the hard-sigmoid function is evaluated. Table 5.4 shows the CPU consumption for

[7] `https://gitlab.cern.ch/atlas/athena`

[8] `https://github.com/lwtnn/lwtnn`

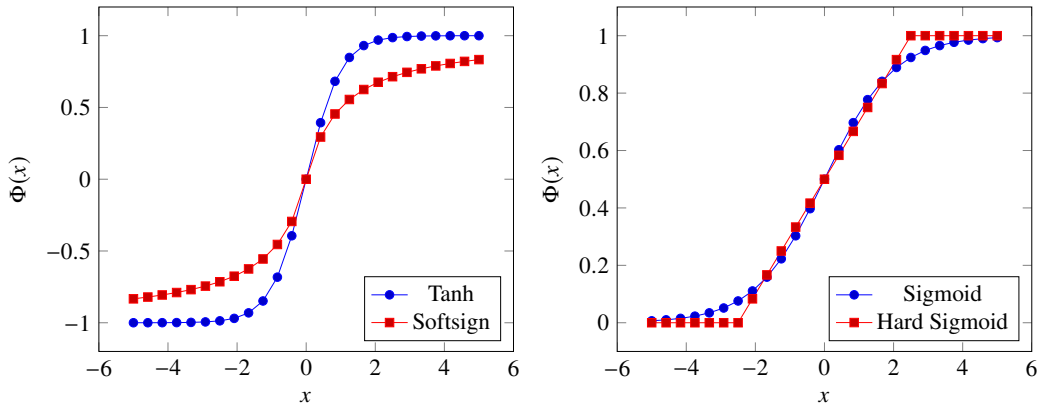
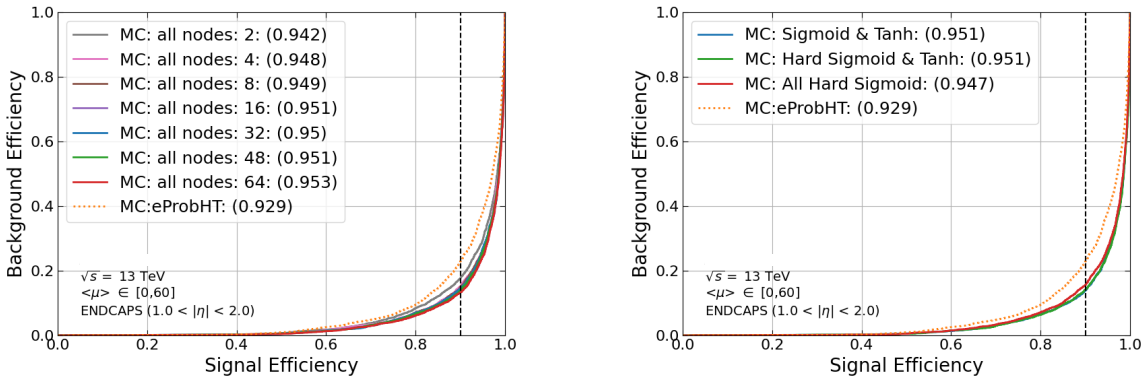


Figure 5.7: Current activation functions in blue and their potential replacements in red.

Model	Activation	CPU [ms]
0	sigmoid+tanh	125
1	hard sigmoid+tanh	110
2	only hard-sigmoid	94

Table 5.4: CPU time dependent on selected activation function for 100 events measured in the TrackCollectionMerger. A total of 48 dense and 48 LSTM nodes are considered. An uncertainty of ~2 % can be assumed from repeated measurements.

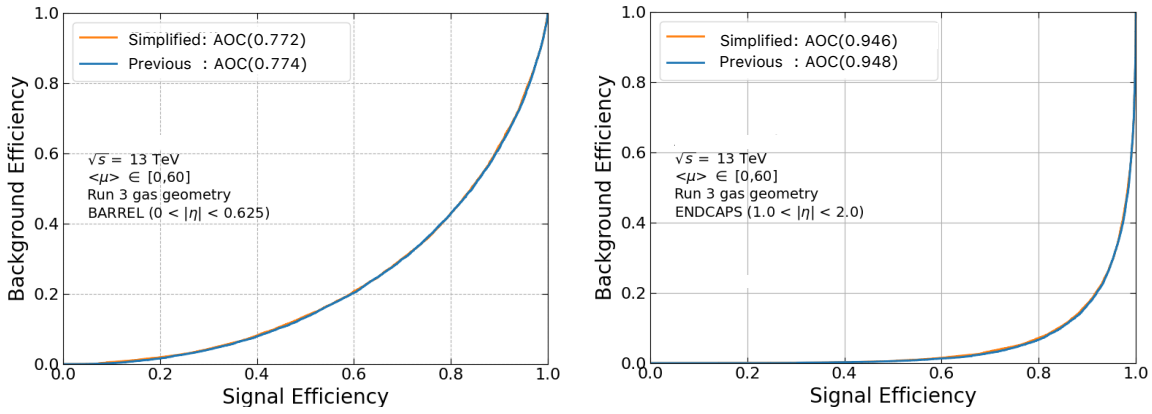
a fixed set of hyper-parameters, with varying configurations of activation functions. While using the double hard-sigmoid activation is the most CPU efficient choice, the best balance between performance and CPU consumption is achieved by replacing only the sigmoid function with the hard-sigmoid function, as documented in Figure 5.8(b).



(a) Node dependent performance

(b) Activation function dependent performance

Figure 5.8: RNN performance depending on the number of nodes or activation functions.



(a) Barrel Region

(b) End-cap Region

Figure 5.9: Performance comparison between the initial RNN setup and the reduced-complexity model. The ROC curves in the barrel region a) and the end-cap region b) are shown. The simplified setting represents the reduced complexity, while the previous setup corresponds to the design of [103].

Setup Validation

Apart from the isolated validation of the individual changes, the full setup incorporating all complexity-reducing measures was tested. A CPU time reduction of up to a factor of 10 was observed [9], without sacrificing the initial performance. This is exemplified in Figure 5.9, which compares ROC curves based on simplified and initial settings.

5.6 Background Validation

The most-frequently hadrons produced in proton-proton collisions at the LHC are consisting of light quarks (u,d). These include charged pions, which represent the main background for electron identification. However, in the training of the neural network, muons instead of pions were used as background reference. Muons provide the advantage of an efficient selection using tag & probe techniques in measured data. Furthermore, their event signature is more isolated, which provides a cleaner training environment for the RNN. Pions ($\sim m_\pi = 140\,\text{MeV}$ [12]), as well as muons ($\sim m_\mu = 105\,\text{MeV}$ [12]), have a similar mass and consequently a similar tendency to emit transition radiation photons for a given momentum.

In order to confirm muons as a pion approximation in the given context, multiple studies were performed on a di-jet sample, introduced in Section 5.4.

5.6.1 Validation Strategy & Results

In order to validate the interchangeability of muon and pion events as background processes, two RNN models are trained - one model based on muons as background and one reference model based on

[9] Different evaluation settings (local measurements compared to the evaluation within ATLAS frameworks) yielded varying gains. The observed CPU reduction ranges from a factor two up to ten.

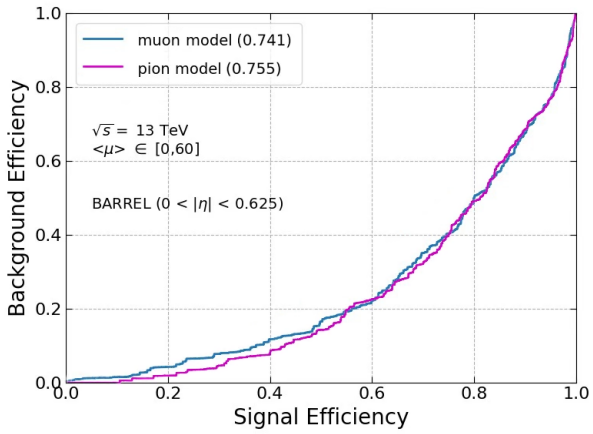


Figure 5.10: Performance comparison of models trained on muon and pion background in the barrel region. Both models are evaluated on the pion background.

the pion background. In a subsequent step, both models are evaluated on the pion background and a performance comparison is conducted.

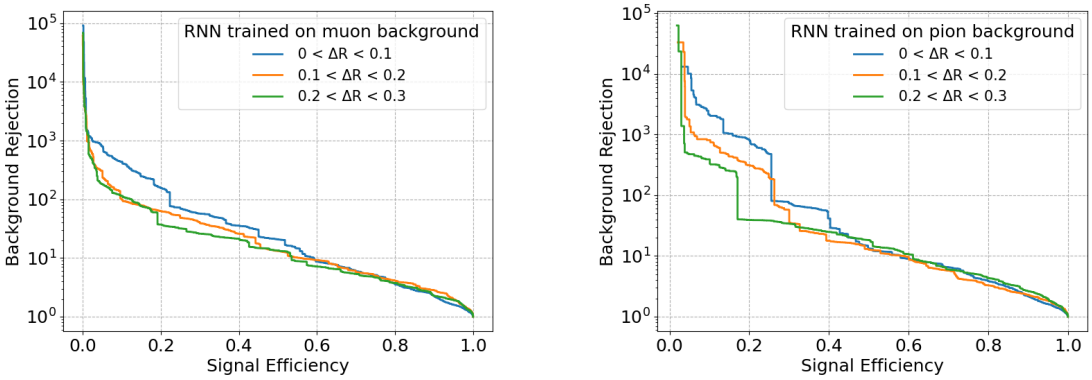
A general evaluation is based on the trend of the ROC curves as depicted in Figure 5.10 for the barrel region. The pion model performs with an AOC-value of 0.755 slightly better than the muon model with AOC = 0.741 since training and evaluation are based on the same particle type. The muon model yields similar separation power across the full signal efficiency range, which is why interchangeability cannot yet be discarded.

An additional investigation of isolation effects provides unbiased comparability between the two backgrounds. The angular difference between the evaluated track and the next closest track, defined in Equation 3.5, is used as figure of merit. Three different ΔR-intervals, [0,0.1], [0.1,0.2] and [0.2,0.3] are explored in Figure 5.11 by investigating the dependence of signal efficiency and background rejection, which is defined as the inverse false positive rate $\frac{1}{\text{FPR}}$. In Figure 5.11(a), the muon model is evaluated on the pion background, whereas in Figure 5.11(b), the pion model is used for evaluation.

Independently of the underlying model, no significant ΔR-dependence is observed in the high signal efficiency region, which is most-relevant for physics analyses. Consequently, isolation effects are negligible and in the context of this study, muons are interchangeable with pions.

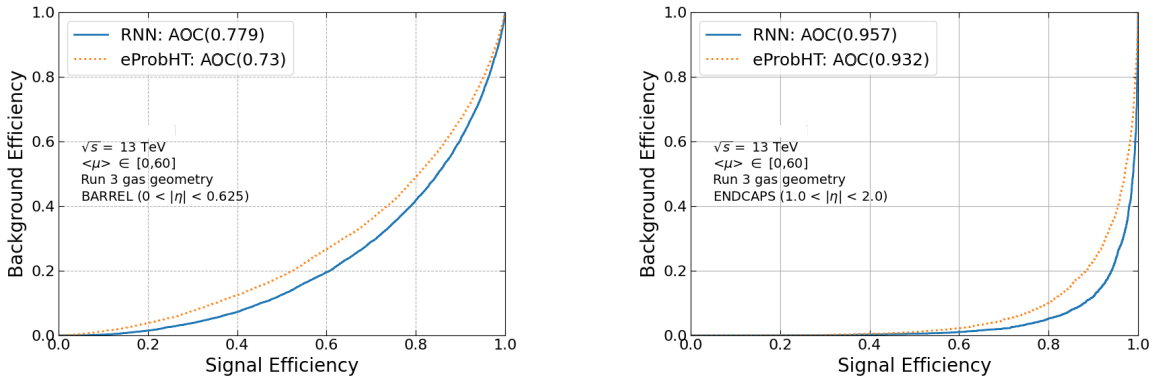
5.7 Run 3 performance on MC

The expected RNN performance in Run 3 is assessed with simulated data and is compared to the established likelihood-based PID approach, previously introduced in Section 4.1. The presented results evaluate electron and muon samples on the optimized network setup, which was developed in Section 5.5. The algorithm's behaviors are investigated in form of inclusive ROC curves as well as phase space dependent background rejection plots to get a full understanding of the expected performance.



(a) Muon Model (b) Pion Model

Figure 5.11: ΔR-dependent ROC curves for models trained on the muon background a) as well as on the pion background b). Both are evaluated on the pion background.



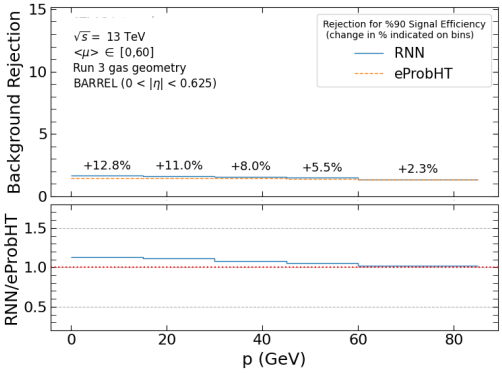
(a) Barrel Region (b) End-cap Region

Figure 5.12: RNN and eProbHT ROC curves based on Run 3 Monte Carlo, barrel region a) and end-cap region b).

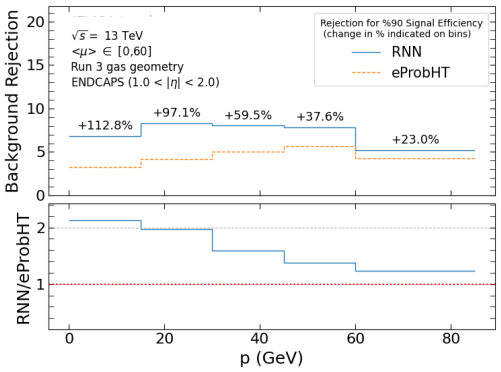
Regional ROC Curves are depicted in Figure 5.12 showing the barrel as well as the end-cap region. The RNN outperforms the likelihood-based approach [10] with a decrease in performance in the barrel due to the utilized Argon mixture, which is less suited for the detection of X-ray photons than Xenon.

Background Rejection Plots are exemplified in Figure 5.13 in dependence of the momentum. The presented background rejection is evaluated at 90% signal efficiency and shows better performance for the RNN than for the likelihood-based eProbHT approach. The deviation between the two outcomes is indicated by the given percentages. The superior PID capabilities of Xenon filled straws are evident regardless of the underlying algorithm.

[10] This gain in performance was already observed in the initial Run 2 studies of the RNN [103]. Other groups, such as EGamma, do not observe the same behavior across all phase-space regions. After a long series of tests excluding different track hypotheses as cause, indications suggest that the discrepancies stem from event selection or missing training in the



(a) Barrel Region



(b) End-cap Region

Figure 5.13: Comparison between the RNN and eProbHT background rejection at 90 % signal efficiency per momentum bin. The deviation is indicated by the given percentage. The plots a) and b) differentiate between the barrel and the end-cap region respectively.

The dependence on pile-up, the occupancy[11] as well as on the number of hits on track are shown in the differential plots of Figure A.3,A.4 and A.5. The results underline the observed RNN performance and provide a detailed assessment of the setup.

5.8 Outlook

The CERN environmental program [113] aims to mitigate its greenhouse gas emissions, which are predominantly caused by the use of gas mixtures in cooling and particle detection. Xenon leaks in combination with high costs in procurement necessitate the adaption of the TRT setup to Argon [114]. While the tracking capabilities of the detector can be retained, the PID performance decreases with the new gas mixture [105]. As part of the ATLAS upgrade in the upcoming shutdown, the Inner Detector will be replaced by an all-silicon Inner Tracker [115]. This measure will also end the operation of the Transition Radiation Tracker. The future ATLAS configuration will achieve electron PID solely based on calorimeter and tracking information.

low-momentum regime.

[11] Occupancy measures the amount of activated straws in an event. The higher the occupancy, the complexer the event, the more challenging accurate reconstruction.

CHAPTER 6

H→ $\tau\tau$ Simplified Template Cross-Section Analysis

The measurement of the $H \rightarrow \tau\tau$ process in ATLAS builds on a decade of experience and success but also on a decade of challenges. With the aim to push the precision frontier, novel analysis techniques need to be developed and be adapted to grow with time and challenges ahead.

In the year 2022, the ATLAS collaboration published a Run 2 $H \rightarrow \tau\tau$ measurement of the inclusive process, of the four main Higgs production modes as well as of nine kinematic regions relevant for searches of phenomena beyond the Standard Model (BSM) [71]. This 2022 analysis provides foundation for the final $H \rightarrow \tau\tau$ analysis of the Run 2 data set, that covers the years 2015-2018. The re-analysis profits from refined techniques as well as the latest theoretical understanding. Since it is the most complete, in-depth exploration of the Run 2 data-set, it serves as reference for future research and will be denoted as *Legacy analysis*. The analysis design and validation is carried out as combined efforts amongst the members of the Legacy analysis team [3] within the ATLAS collaboration. In this chapter, the Legacy analysis design, following the Simplified Template Cross-Section framework [116] and the underlying measurement techniques will be introduced.

6.1 Binned Profile Likelihood Fit

Within the scope of the $H \rightarrow \tau\tau$ analysis, a binned profile likelihood fit is the key technique to extract information from the measured data. The underlying concept of such a fit is a counting experiment with the goal to compare the measured rate of a given process to the expected rate predicted by the underlying Standard Model. At the LHC, events are produced at a rate of $\sim 2\,\text{GHz}$ [1] while the signal process $H \rightarrow \tau\tau$ only occurs once every 30 s [2]. In a counting experiment, the probability to observe a certain number of events is described by a Binomial distribution. At the LHC, the Poisson distribution is used instead, which is a valid approximation since the entire event count is large compared to the probability to observe the targeted process. In a set of n observed events, not only the signal

[1] A bunch spacing of 25 ns [42] corresponds to a collision rate of 40 MHz. The event rate depends additionally on the pile-up, so that the GHz regime is reached.

[2] This rate is estimated from the cross-section of the $H \rightarrow \tau\tau$ production $\sigma_{SM} = 3.17\,\text{pb}$ [71] and the instantaneous luminosity of the Run 2 LHC $\mathcal{L} \sim 10^{34}\,\text{cm}^{-2}\,\text{s}^{-1}$ [11] according to Equation 3.2 $\dot{N} = \mathcal{L}\sigma$

process S is present but also diverse background processes B. Both observables are input to the Poisson probability function, which reads

$$\mathcal{P}(n|S+B) = \exp(-(S+B))\frac{(S+B)^n}{n!} \tag{6.1}$$

The observed events are binned into histograms according to their properties. The yield per bin n_j represents its own counting experiment. The total probability is described by the product of Poisson distributions over all N histogram bins.

$$\mathcal{P}(n_j|S_j+B_j) = \prod_{j=1}^{N} \exp\Big(-(S_j+B_j)\Big)\frac{(S_j+B_j)^{n_j}}{n_j!} \tag{6.2}$$

Based on these principles, parameters of interest (PoIs) can be measured. In this analysis, the amount of Higgs bosons that decay into two τ-leptons, which can be expressed as the product of cross-section and branching ratio $\sigma_H \times BR_{\tau\tau}$, is to be determined. This quantity with respect to the Standard Model prediction is called the signal strength μ

$$\mu = \frac{\sigma_H}{\sigma^{SM}} \cdot \frac{BR_{\tau\tau}}{BR^{SM}_{\tau\tau}}$$

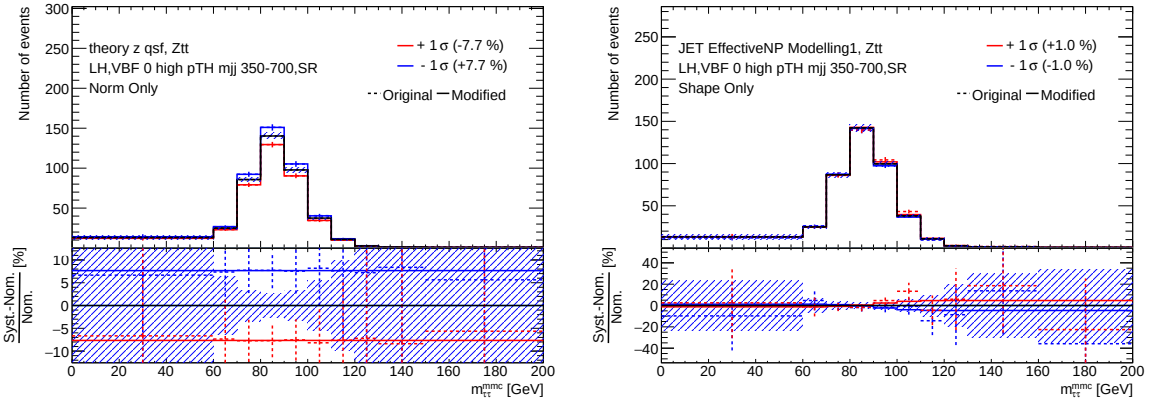
In order to perform this measurement, a degree of freedom needs to be added to the underlying model. The signal strength μ acts as the scaling factor of the signal yield expected in the Standard Model. A measurement of $\mu = 1$ confirms the Standard Model prediction.

$$H = \mu \cdot S + B$$

Probability functions that are interpreted as functions of unknown parameters are called likelihood functions. In a procedure called fitting, the measured data is used to determine the free parameters by maximizing the likelihood function. The underlying model is represented by templates largely built from Monte-Carlo simulations, which are scaled and shaped by the free parameters to match the data best. Not only the parameter of interest is a free parameter of the likelihood function. Additionally, nuisance parameters are required to capture experimental uncertainties in a realistic setting and are also determined in the fitting procedure. Thus, the binned data is profiled by the likelihood fit. The likelihood function is given by

$$\mathcal{L}\left(\vec{n}, \vec{a}|\vec{\theta}, \vec{k}\right) = \prod_{i\in\text{bins}} \text{Pois}\left(n_i|\mu \times S_i(\vec{\theta}) + B_i(\vec{k}, \vec{\theta})\right) \times \prod_{j\in\text{sys}} c_j\left(a_j|\theta_j\right) \tag{6.3}$$

The statistical model includes per histogram bin i the Poisson probability that n_i events are observed when $\mu \cdot S + B$ events are expected. Apart from the measured data $\vec{n}$, the statistical model also depends on systematic uncertainties $\vec{\theta}$. Prior knowledge about the systematic uncertainties is obtained from auxiliary measurements $\vec{a}$, which are used to introduce a gaussian constraint c_j, as detailed in Section 6.1.1. Normalization factors $\vec{k}$ on the other hand represent unconstrained nuisance parameters and take on a similar role as the signal strength μ.



(a) Uncertainty affecting the normalization.

(b) Uncertainty affecting the shape.

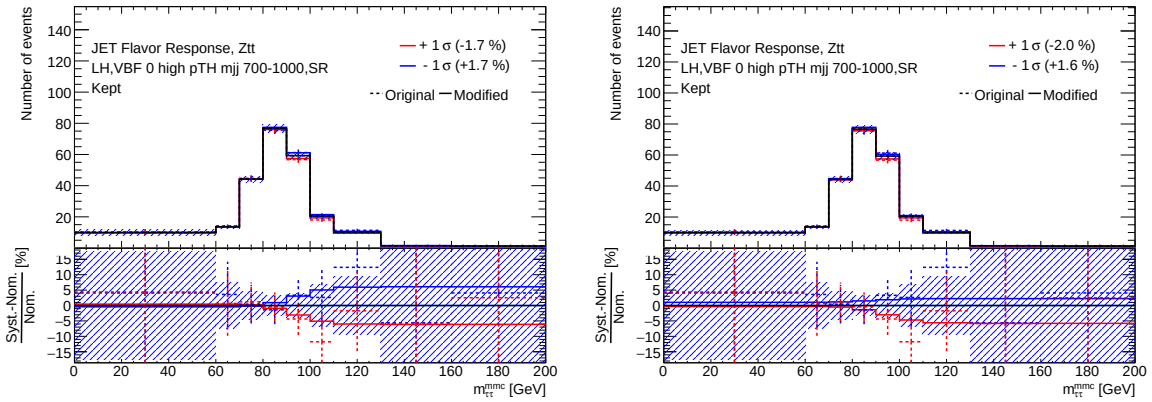
Figure 6.1: Shape and normalization variations of systematic uncertainties. Envelops of the *Ztt theory z qsf* systematic uncertainty in a) as well as the *Ztt JET EffectiveNP Modelling1* systematic uncertainty in b) are shown to illustrate the effect of normalization and shape variations, respectively. The red line depicts the yield of a systematic variation of $+1\sigma$, the blue one of -1σ. The colored solid lines, labeled as *Modified*, show the variation after applying *smoothing* and *symmetrization* algorithms, the dashed line, labeled as *Original*, before. In the bottom panel, the relative difference between the variation and the nominal is shown. This difference is constant if the variation is only affecting the normalization (a) and showing trends if the shape is affected (b).

6.1.1 Nuisance Parameters

Nuisance parameters play an important role when designing a fit model. They can be classified according to their physical origin. Statistical uncertainties describe the random variations that arise when an experiment is repeated and impact both the recorded data as well as the generated Monte-Carlo data. The Monte-Carlo statistical uncertainty is called gamma (γ) and is caused by the limited amount of simulated samples. The second class contains systematic uncertainties of the experiment and of the underlying theory model. Fluctuations caused by systematic uncertainties are estimated from auxiliary measurements. For each source, a variation of $\pm 1\sigma$ with respect to the nominal value are considered by the fitting model. The statistic tool *HistFactory* [117] translates variations into an expected change of yield. A continuous description is achieved by extrapolating between the nominal and the $\pm 1\sigma$ yield. Figure 6.1 shows the expected range of yield variation caused by the resummation[3] scale uncertainty *Ztt theory z qsf* [119], as well as the jet energy scale uncertainty *Ztt JET EffectiveNP Modelling1* [87]. An up-variation of a systematic uncertainty not necessarily translates in an up-variation of the yield.

Both systematic uncertainties show their impact in the same phase-space region, which is defined in Section 6.7. The two sources of uncertainty affect the setup differently. *Ztt theory z qsf*, shown in Figure 6.1(a), only impacts the **normalization**, while *Ztt JET EffectiveNP Modelling1*, shown in Figure 6.1(b), affects the **shape** of the distribution, which is illustrated by the constant and crossing lines in the bottom panel, representing the relative difference between variation and nominal. Systematic uncertainties can also describe the combination of normalization and shape variation.

[3] At high orders of perturbative calculations, terms including large logarithmic contributions, which can cause poor convergence might occur. Resummation techniques account for this effect by reorganizing the critical terms and determining the sum in a stable way [118].



(a) Twosided

(b) Presmocorrect

Figure 6.2: Impact of the Twosided (a) as well as Presmocorrect (b) symmetrisation strategies on the envelop of the Jet Flavor Response systematic. The red line depicts the yield of a systematic variation of $+1\sigma$, the blue one for -1σ. The colored solid lines, labeled as *Modified*, show the variation after applying *smoothing* and *symmetrization* algorithms, the dashed line, labeled as *Original*, before. In the bottom panel, the relative difference between the variation and the nominal is shown.

Smoothing& symmetrization: Smoothing and symmetrization techniques are applied to mitigate statistical fluctuations in order to stabilize the fit. The smoothing algorithm equalizes local spikes and relative sign changes between neighboring bins. In this analysis, the **MaxVariation** algorithm is applied, which limits the number of slope changes in the ratio of systematic uncertainty and nominal. The algorithm relies on the "353QH twice"[120] implementation, which alleviates spikes by replacing the bin content by the average of the bin and its neighboring bins. Afterwards a symmetrization is applied, which corrects up- and down-variations with the same sign. The two dominating approaches used in this analysis are **Twosided** and **Presmocorrect**. In the TrexFitter implementation [121], they are defined as follows:

- **Twosided:** The Twosided symmetrization approach determines the average variation per bin according to

$$\text{var}_{\text{TS}} = \frac{\text{up} - \text{down}}{2} \tag{6.4}$$

  The outcome is used as up-variation and mirrored on the nominal to get a description of the down-variation. Consequently, the variations are fully symmetrized as depicted in Figure 6.2(a).

- **Presmocorrect:** The Presmocorrect algorithm describes a chain of operations starting with a pre-smoothing, which aims to reduce local spikes and to eliminate variations of bins with opposite sign compared to both neighbored bins. Afterwards a symmetrization is applied. Per bin, relative up- and down-variations of the same sign are set to the absolute average of both variations. The smaller variation is set to the negative sign to represent the down-variation. To get rid of artificially introduced spikes, another round of smoothing is applied. The resulting variations are not necessarily fully symmetrized as depicted in Figure 6.2(b).

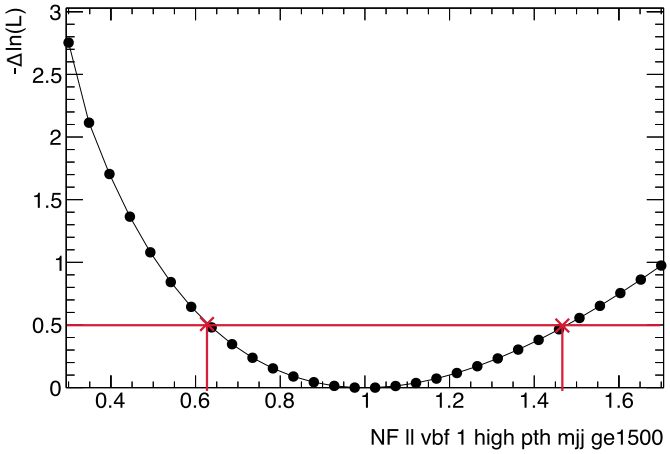


Figure 6.3: Profile likelihood scan of the nuisance parameter ATLAS_norm_ll_vbf_1_high_pth_mjj_ge1500_Ztt. 1σ intervals are defined by an increase of the log-likelihood by 0.5 units with respect to the minimum, which represents the best fit value of the parameter [123].

Pruning Samples in each region with a yield < 0.01 are excluded from the fit since their impact is negligible. The same applies for nuisance parameters with negligible impact. They are removed if their relative contribution is smaller than 1% relative to the yield of a signal sample in a signal enriched region or compared to the total yield of all samples in a background enriched region. The pruning has positive impact on the fit setup's stability [119].

Maximizing the likelihood function requires the nuisance parameters of the fit to be adapted such that the expected model matches the measured data best. Nuisance parameters can be *pulled* and/or *constrained*. A pull is described by the difference between the prior assumption θ_0 and the fitted value $\hat{\theta}$, divided by the uncertainty $\Delta\theta$

$$pull = \frac{\hat{\theta} - \theta_0}{\Delta\theta}. \tag{6.5}$$

A constraint is expressed by a decrease in uncertainty on the nuisance parameter. The increase in parameter accuracy can be driven by the statistical power of the data or correlations of nuisance parameters. If a given nuisance parameter is pulled to change the Poisson probability, the constraint term of Equation 6.3 introduces a penalty for shifting the Nuisance Parameter compared to the auxiliary measurement.

6.1.2 Minimization & Parameter Uncertainties

Fits are performed by finding a set of parameters that maximize the likelihood function $\mathcal{L}$ or minimize the negative logarithm of $-\log\mathcal{L}$. The fit is handled by the $TRexFitter$ [121] framework utilizing the *MINUIT* package of the CERN root data analysis framework [122] for minimization. Apart from the minimum itself, uncertainties as well as correlations between parameters, need to be taken into account. The default minimizer is *MIGRAD* [122], which is based on a gradient descent method.

The minimum of the likelihood curve is defined by a set of parameters $\hat{\hat{\theta}}$. The uncertainty on a parameter μ is defined by the pair of μ-values where the function evaluates to 0.5 when using the profile likelihood ratio as test statistic. The profile likelihood ratio is defined as the ratio of the conditional to the unconditional maximum likelihood estimator of θ [124]. While $\hat{\hat{\theta}}$ maximizes the likelihood for a fixed μ in the conditional likelihood, $\hat{\mu}$ and $\hat{\theta}$ represent the best fit values of parameters in the unconditional case. The employed test statistic is defined as [123]

$$\lambda(\mu) = -2\log\left(\frac{L\left(\mu, \hat{\hat{\theta}}(\mu)\right)}{L\left(\hat{\mu}, \hat{\theta}\right)}\right) = -2\left[\log\Big(L\left(\mu, \hat{\hat{\theta}}(\mu)\right)\Big) - \log\big(L\left(\hat{\mu}, \hat{\theta}\right)\big)\right]. \tag{6.6}$$

The test statistic λ can, in the limit of large sample sizes, be approximated by a χ^2 distribution with one degree of freedom for the "parameter of interest". In this approximation, the 1σ interval, which corresponds to a 68% confidence interval, is reached at $\lambda = 1$. Thus, Equation 6.7 becomes

$$-\Delta\ln(L) = 0.5 \tag{6.7}$$

The likelihood-scan of the normalization factor *ATLAS_norm_ll_vbf_1_high_pth_mjj_ge1500_Ztt*[4] is shown in Figure 6.3. The function exhibits a minimum at $x = 1$. The intersection with $y = 0.5$ yields 0.63 and 1.46 such that the best fit value including the 1σ variation is $1^{+0.46}_{-0.37}$. As illustrated by this example, asymmetric uncertainty intervals can occur in the likelihood-scan method.

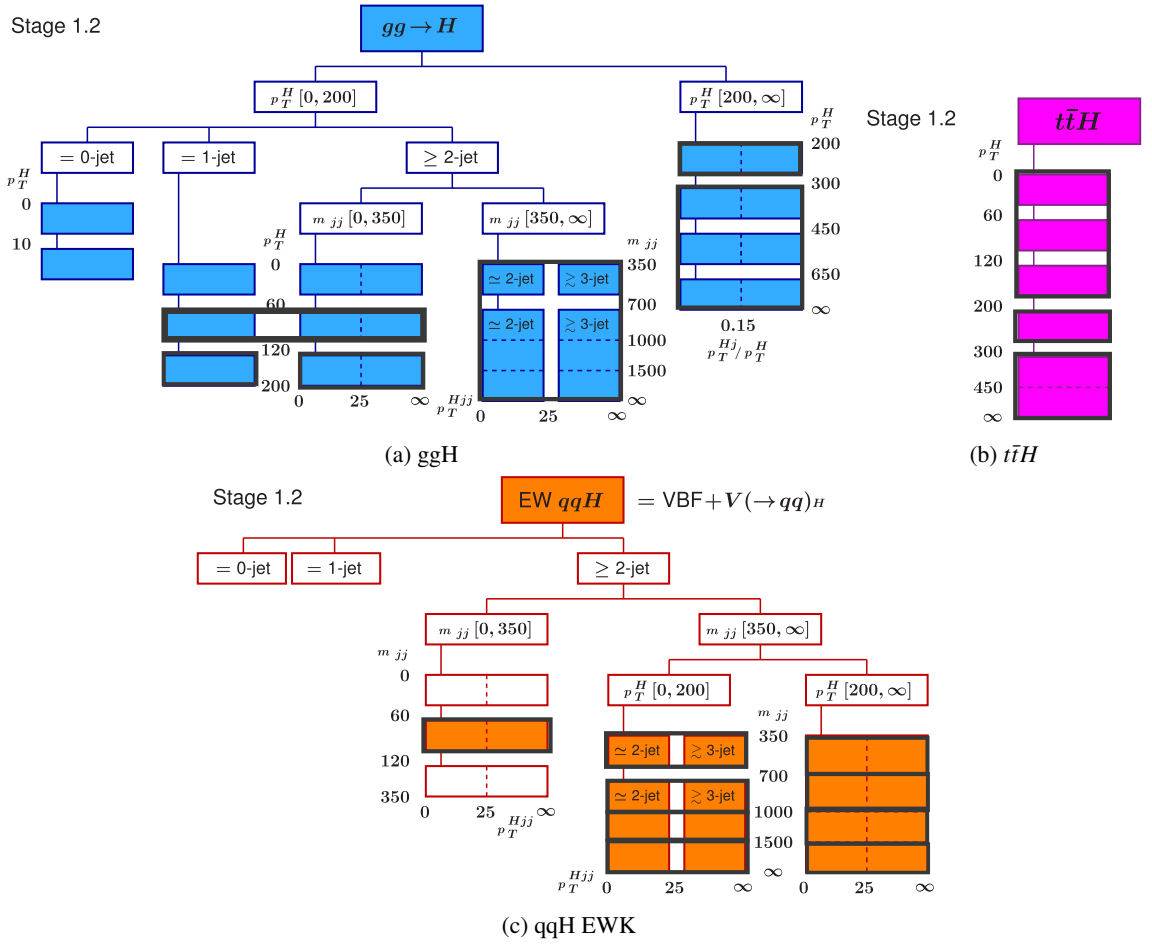
6.2 STXS-Framework

The Simplified Template Cross-Section (STXS) framework gives a guideline to perform measurements in the Higgs sector by providing well-defined phase-space regions with minimum theoretical uncertainties and high sensitivity to BSM physics [116]. By selecting the events according to these criteria and feeding them into the fitting model, a simplified interpretation of the data can be performed. The framework is developed and used in agreement between the ATLAS and CMS collaborations as well as the theory community. The approach allows for the combination of measurements in different decay-channels as well as between experiments. In general, different stages are provided, depending on the coarseness of the proposed binning. While stage 0 mainly distinguishes the different Higgs production modes, stage 1.2 differentiates many phase-space regions per production-mode by splitting different observables, such as the transverse Higgs momentum p_T^H or the number of jets[5].

The Legacy analysis is based on stage 1.2 with the suggested binning depicted in Figure 6.4. The diagrams illustrate the proposed binning for Higgs production from gluon gluon fusion, associated production with a pair of top quarks and electroweak (EWK) Higgs boson production in quark-quark interactions, respectively. The latter describes both, VBF and $qq \rightarrow VH$ production in case of a hadronic decay of the vector-boson V(had)H. The final states of both topologies are equal and follow the same interactions. Consequently, they represent different channels of one physical process. Despite their common grouping, they largely populate different phase-space regions. VBF events are

[4] The definition of analysis phase-space regions and the application of dedicated normalization factors is elaborated on in Section 6.7

[5] Stage 1.1 also describes the differential exploration of different Higgs production mode but got superseded by stage 1.2. The original definition of stage 1.1 is documented in [125].



(a) ggH

(b) $t\bar{t}H$

(c) qqH EWK

Figure 6.4: Definition of stage 1.2 STXS bins [116]. Three groups, split per Higgs production mode are shown, gluon gluon fusion in blue, associated production with a pair of top quarks in pink and electroweak Higgs boson production in quark-quark interactions in orange. Various phase-space regions are explored by differentiating for example intervals of the number of jets, di-jet mass m_{jj} and Higgs transverse momentum p_T^H. The stage 1.2 binning additionally defines phase-space regions for the associated Higgs production in the leptonic vector boson decay (leptonic VH), which are not shown since none are measured in this analysis. The bins that are targeted in the analysis are highlighted by black rectangles. They comprise, six bins in ggH, eight bins in VBF, one bin in V(had)H and three bins in $t\bar{t}H$ resulting in 18 bins in total.

characterized by large di-jet masses[6] due to the large rapidity gap from the hard scattering process in contrast to V(had)H events.

6.2.1 Target Phase-Space

The Legacy analysis design follows the suggestions of the STXS framework. Not all the proposed STXS bins can be feasibly measured due to the limited statistics available and the complexity of the

[6] The di-jet mass describes the invariant mass of a jet pair and can be determined by the energies E_i and the momenta $\vec{p}_i$ according to $m_{jj} = \sqrt{(E_1 + E_2)^2 - (\vec{p}_1 + \vec{p}_1)^2}$.

setup. Consequently, 18 bins are selected for in-depth exploration, highlighted in Figure 6.7. The focus of the analysis design is set on the in-depth exploration of the $t\bar{t}H$ and VBF production mode, which were both measured by a single bin in the 2022 analysis as documented in Figure B.1.

As proposed by the STXS stage 1.2 binning, the main production modes are explored in detail by differentiating phase-space regions depending on the transverse Higgs momentum p_T^H, the di-jet mass m_{jj} or the number of jets. The $p_T^{Hjj} = |\vec{p}_T^{\,H} + \vec{p}_T^{\,j1} + \vec{p}_T^{\,j2}|$ observable, the absolute value of the sum of Higgs and leading jets transverse momenta, is measured inclusively due to its limited resolution in the di-tau final state [119].

$t\bar{t}H$

In this analysis, three bins are explored in $t\bar{t}H$ by splitting the phase-space by the transverse Higgs momentum in $< 200\,\text{GeV}$, $200\,\text{GeV} - 300\,\text{GeV}$ and in $> 300\,\text{GeV}$. The exploration of the high p_T^H regime is motivated by its high sensitivity to BSM physics as shown in theory [13]. These effects would manifest in measurements discrepant to the SM prediction. Furthermore, the $\tau\tau$ final state has high sensitivity in this regime where other final states like $\gamma\gamma$ suffer from a lack of statistics.

VBF

In VBF, eight different STXS-bins are measured. The phase-space is split in a low (<200 GeV) and a high (>200 GeV) p_T^H region, along with four di-jet mass intervals ($350 - 700\,\text{GeV}$, $700 - 1\,000\,\text{GeV}$, $1\,000 - 1\,500\,\text{GeV}$ and $>1\,500\,\text{GeV}$). Similar reasoning as for the p_T^H cut applies for the di-jet mass split. High di-jet mass values are a consequence of a high effective mass of the vector-boson system and consequently sensitive to BSM physics. Additionally, the selection of signal events is simplified by large rapidity gaps between the outgoing jets and the reduction of background cross-sections in this region of phase-space as it is the case for QCD production of Z events [126].

ggH & V(had)H

In the 2022 analysis [71], six bins were measured in ggH and only one in V(had)H (Figure B.1). The same bins are re-evaluated in the Legacy setup.

6.3 Event Selection

The differential investigation of the available phase-space calls for the selection and categorization of event topologies, based on reconstructed particle objects, introduced in Chapter 4. For the $H \to \tau\tau$ channel, light leptons (electrons and muons), visible hadronic τ decay-products, jets as well as missing transverse energy are of interest to identify the target signature in the detector with suppressed background.

Di-tau events are triggered on single-lepton, di-lepton or di-hadronic τ-lepton signatures [127–130]. They are assigned to the corresponding $\tau_e\tau_\mu$, $\tau_{\text{lep}}\tau_{\text{had}}$ or $\tau_{\text{had}}\tau_{\text{had}}$ channel. The double-leptonic mode is restricted to the mixed final state of e and μ since the pure $\tau_e\tau_e$ and $\tau_\mu\tau_\mu$ channels suffer from large background contributions and only offer minimal gain in sensitivity. With respect to the trigger-objects, p_T thresholds are tightened to ensure the evaluation at the trigger efficiency plateau, as listed in Table 6.1.

Trigger signature	Data-taking period	p_T threshold [GeV] used in event selection
Single electron	2015	$p_T(e) > 25$
	2016–2018	$p_T(e) > 27$
Single muon	2015	$p_T(\mu) > 21$
	2016–2018	$p_T(\mu) > 27.3$
One electron, one muon	2015–2018	$p_T(e) > 18$, $p_T(\mu) > 14.7$
Two $\tau_{\text{had-vis}}$	2015–2018	$p_T(\text{leading } \tau_{\text{had-vis}}) > 40$ $p_T(\text{sub-leading } \tau_{\text{had-vis}}) > 30$

Table 6.1: Trigger signatures and the corresponding p_T threshold per data-taking period used in the event selection [3].

During Run 2, the di-tau trigger was extended by an additional jet trigger to achieve manageable rates [131]. The additional jet can for example be produced from the hard-scattering VBF production or initial-state radiation.

The triggered events are further reduced to phase-space regions relevant to the analysis. Electrons are required to meet the 'Loose' identification criterion [132] as well as a transverse momentum larger 15 GeV. They need to be detected within $|\eta| < 2.47$ excluding the transition region $1.37 < |\eta| < 1.52$. Muons are similarly filtered by the 'Loose' identification criterion [84], a transverse momentum > 10 GeV and need to be detected within $|\eta| < 2.5$. Jets are required to fulfill $p_T > 20$ GeV and $|\eta| < 4.5$. Jets with $p_T < 60$ GeV and $|\eta| < 2.5$ are removed, in case the jet vertex tagger does not associate them to the primary vertex. Pile-up jets in the forward region with $|\eta| > 2.5$ and $p_T < 60$ GeV are suppressed by a dedicated algorithm [133]. Jets originating from b-hadrons are tagged by the deep-learning flavour tagging algorithm (DL1r) [134] under the condition that $p_T > 20$ GeV and $|\eta| < 2.5$. Hadronically decaying τ leptons $\tau_{\text{had-vis}}$ are required to have one or three charged tracks with a net charge of $|q| = 1$. In addition, a transverse momentum larger 20 GeV and $|\eta| < 2.47$ needs to be fulfilled, excluding the transition region $1.37 < |\eta| < 1.52$.

The defining properties for analysis channels in the $\tau\tau$ final state are summarized in Table 6.2. The criteria reflect the physical properties and aim to suppress prominent background processes. The latter are introduced in Table 3.1 and are discussed in detail in Section 6.5. Certain object criteria, such as the identification scores, are tightened further to optimize the targeted phase-space selection. Depending on the channel, either one electron and muon, one light lepton and one $\tau_{\text{had-vis}}$ object or two $\tau_{\text{had-vis}}$ objects are required to be reconstructed. In all three cases, opposite particle charge conserves the zero net charge of the Higgs boson. The presence of neutrinos in the τ lepton decay is represented by an E_T^{miss} criterion. Restrictions on the momentum fraction carried by the visible τ decay products have positive impact on the di-tau mass reconstruction. Cuts on the kinematics as well as the b-veto are selected to suppress background contributions like W + jets as well as single Top processes, which both can mimic the signal signature. Kinematic restrictions cut the collinear mass $m_{\tau\tau}$, the invariant mass $m_{e\mu}$ as well as the transverse mass m_T of the lepton + $\tau_{\text{had-vis}}$ system, defined in Equation 7.5. Top processes are especially suppressed by the b-veto, since 96% of decays result in a W + b-quark [12]. B-tagging working points with signal efficiencies of 85% or 70% are applied, depending on the selected channel. The $Z(\rightarrow ee)$ + jets background in the $\tau_e\tau_{\text{1-prong}}$ channel is suppressed by the

	$\tau_e\tau_\mu$	$\tau_{lep}\tau_{had}$ $e\tau_{had}$ | $\mu\tau_{had}$	$\tau_{had}\tau_{had}$
Preselection			
Object counting	# of e = 1, # of μ = 1, # of $\tau_{had,vis}$ = 0	# of e/μ = 1, # of $\tau_{had,vis}$ = 1	# of e/μ = 0, # of $\tau_{had,vis}$ = 2
p_T cut	e/μ : p_T cut 10 to 27.3 GeV	e/μ : p_T cut 21 to 27.3 GeV, $\tau_{had,vis}$: $p_T > 30$ GeV	$\tau_{had,vis}$: $p_T > 40$,30 GeV
ID, Isolation, and eveto	e/μ: Medium e: FCLoose, μ: FCTightTrackOnly	e/μ: Medium, $\tau_{had,vis}$: RNN Medium e: FCLoose, μ: FCTightTrackOnly 1-prong $\tau_{had,vis}$: eleBDT e-veto	$\tau_{had,vis}$: RNN Medium
Charge product	Opposite charge	Opposite charge	Opposite charge
Kinematics	$m_{\tau\tau}^{\text{coll}} > m_Z - 25$ GeV $30 < m_{e\mu} < 100$ GeV	$m_T < 70$ GeV	
b-veto	# of b-jets = 0 wp: DL1r_FixedCutBEff_85	# of b-jets = 0 wp: DL1r_FixedCutBEff_85	# of b-jets = 0 wp: DL1r_FixedCutBEff_70 not applied in tt(0L)$H \to \tau_{had}\tau_{had}$
E_T^{miss}	$E_T^{miss} > 20$ GeV	$E_T^{miss} > 20$ GeV	$E_T^{miss} > 20$ GeV
Leading jet	$p_T > 40$ GeV	$p_T > 40$ GeV	$p_T > 70$ GeV, $\lvert\eta\rvert < 3.2$
Angular	$\Delta R_{e\mu} < 2.0$, $\lvert\Delta\eta_{e\mu}\rvert < 1.5$	$\Delta R_{l\tau_{\text{had, vis}}} < 2.5$, $\lvert\Delta\eta_{l\tau_{\text{had, vis}}}\rvert < 1.5$	$0.6 < \Delta R_{\tau_{\text{had, vis}}\tau_{\text{had, vis}}} < 2.5$ $\lvert\Delta\eta_{\tau_{\text{had, vis}}\tau_{\text{had, vis}}}\rvert < 1.5$
Coll. app. x_1/x_2	$0.1 < x_1 < 1.0$, $0.1 < x_2 < 1.0$	$0.1 < x_1 < 1.4$, $0.1 < x_2 < 1.2$	$0.1 < x_1 < 1.4$, $0.1 < x_2 < 1.4$

Table 6.2: Baseline selection of the three channels $\tau_e\tau_\mu$, $\tau_{\text{lep}}\tau_{\text{had}}$ and $\tau_{\text{had}}\tau_{\text{had}}$[3]. The selected cuts reflect the physical properties of the process and suppress background processes.

electron-veto of the $\tau_{\text{had-vis}}$ object.

6.4 Event Categorization

Event categorization is crucial to separate different production modes and topologies, which enhances signatures of interest. The four main categories are defined by the cuts listed in Table 6.3.

- **VBF**: The topology of a VBF event comprises two high energetic jets separated by a large rapidity gap. Consequently, a high di-jet mass m_{jj} is expected. To suppress the background from $Z(\to \tau\tau)$ + jets, the two jets are required to appear in different hemispheres, $\eta(j_0) \times \eta(j_1) < 0$. Another prominent background are ggF Higgs events including jets. A clean signal selection is the result of a VBF tagger, which is based on a boosted-decision-tree (BDT) and is used to perform a reliable selection. The BDT score, which can be interpreted as a probability measure, is used to split the VBF category in a low, VBF_0, and a high-score, VBF_1, subcategory. The

latter includes events which originate from VBF production with a probability of at least 90%. More details can be found in Section 6.8.

- **tt(0L)$H \rightarrow \tau_{\text{had}}\tau_{\text{had}}$** The topology of $tt(0L)H \rightarrow \tau_{\text{had}}\tau_{\text{had}}$ [7] events is characterized by six jets, two of which originate from he hadronization of a b-quark. The selection requirements allow one observable to be off by one unit to enhance the signal acceptance by requiring at least six jets including at least one b-jet[8] or in case of at least five jets, two jets are required. In addition, a BDT is trained to further separate the signal from background. More details can be found in Section 6.8.

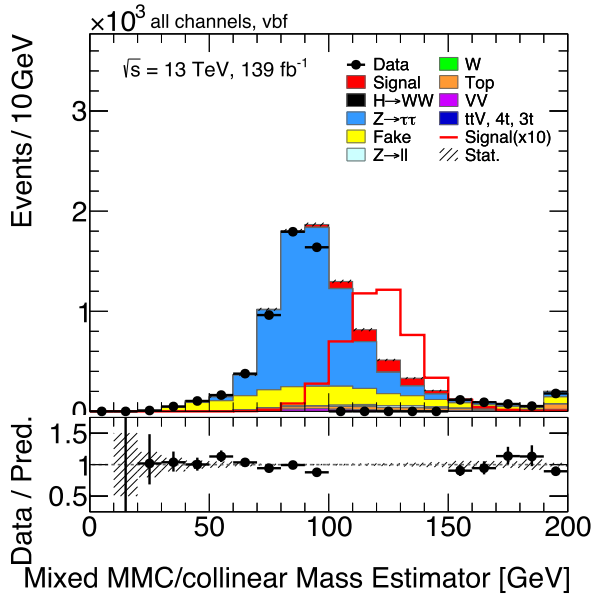
- **V(had)H**: The selection of V(had)H events is characterized by a di-jet mass between 60 GeV and 120 GeV as well as the sub-leading jet $p_T > 30$ GeV. The criteria is identical to the selection of the 2022 analysis [71]. A MVA discriminant is used to split the V(had)H category in a signal enhanced VH_1 region and a VH_0 region enhanced in background (ggH and $Z(\rightarrow \tau\tau)$ +jets). Details are documented in [135].

- **Boost**: The boost category describes reconstructed Higgs events with transverse momenta larger than 100 GeV and which neither fulfill the VBF nor the VH selection. It implements the chosen selection cuts of the 2022 analysis [71].

VBF inclusive	sub-leading jet $p_T > 30$ GeV $m_{jj} > 350$ GeV, $\lvert\Delta\eta_{jj}\rvert > 3$ $\eta(j_0) \times \eta(j_1) < 0$ lepton centrality: visible decay products of the τ leptons between VBF jets
VH inclusive	60 GeV $< m_{jj} <$ 120 GeV sub-leading jet $p_T > 30$ GeV
tt(0L)$H \rightarrow \tau_{had}\tau_{had}$	# of jets $\geq$ 6 and # of b-jets $\geq$ 1 or # of jets $\geq$ 5 and # of b-jets $\geq$ 2
Boost inclusive	Not VBF inclusive Not VH inclusive $p_T(H) > 100$ GeV

Table 6.3: Event categorization in the four dominant Higgs production modes [3].

[7] tt(0L)$H \rightarrow \tau_{\text{had}}\tau_{\text{had}}$: no leptonic top decays and solely hadronic τ decays.
[8] A b-jet originates from a bottom quark.



(a) Ditau-mass distribution

Process	Yield	Contribution
Data	8497	
Signal	475	
Total bkg	8588	
Z→ ττ	6144	71.5%
Fake	1783	20.8%
Top	327	3.8%
VV	174	2.1%
Z→ *ll*	103	1.2%
W	31	0.4%
H→ *WW*	25	0.3%
ttV, 4t, 3t	< 1	8.6‰

(b) Yield Table

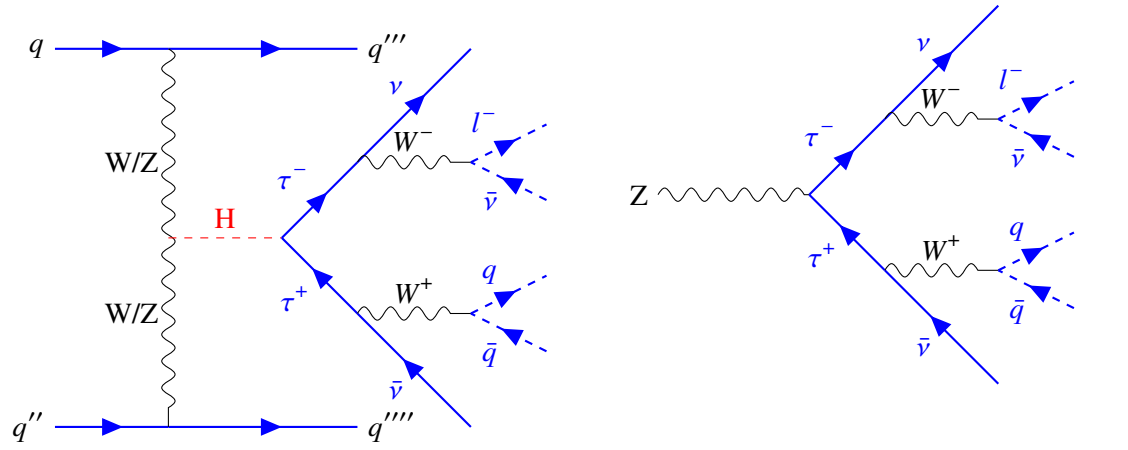
Figure 6.5: Di-tau mass distribution a) and corresponding yield table b) in the VBF production. Signal processes are shown in red, the dominant $Z \rightarrow \tau\tau$ background in blue and misidentified τ objects are depicted in yellow. Various other background processes with minor contribution are present as indicated by the colorful legend.

6.5 Background Estimation

In this Section, the physical processes involved in the analysis are introduced, followed by a discussion of their relevance. Apart from the targeted Higgs processes, various background sources affect the measurement and call for a precise estimation of their contribution to the signal region (SR) [9].

The relative contributions of physical processes are exemplified in Figure 6.5(a) for the VBF category. The di-tau mass distribution is shown. The signal contribution describes events comprising the Higgs boson decaying into two τ leptons. Figure 6.6(a) illustrates the expected signature of a VBF Higgs decay featuring two QCD jets from the hard scattering process, alongside the signature of the τ decays. Depending on the nature of the decay of the heavy lepton, another jet or the observation of a lepton and missing transverse energy define the event topology. The main background of the $H \rightarrow \tau\tau$ processes are $Z \rightarrow \tau\tau$ events. Not only, do those events exhibit a detector signature similar to the signal process, as visualized in Figure 6.6(b), but also exhibit a similar mass. Missing neutrinos from the τ lepton decay complicate the di-tau mass reconstruction and decrease the separation of signal and background. Additionally, misidentified τ leptons or "fakes," constitute the second dominant background, as discussed in Chapter 7. Apart from these primary contributions, various other background processes require additional consideration. The observed yields are quantified in Table 6.5(b) and vary with the defined cuts in each region. Nonetheless, the table serves as a representative indicator of relative contributions.

[9] Defining signal region cuts are elaborated on in Section 6.7



(a) VBF Signal Signature

(b) $Z \rightarrow \tau\tau$ Background Signature

Figure 6.6: Feynman diagram of the expected VBF signal signature in a). Two QCD jets are expected in addition to the signature of the τ decays. Depending on a hadronic or leptonic decay of the heavy lepton, another jet or the observation of a lepton and missing transverse energy define the event topology. In b), the most prominent background source is depicted. The VBF signal signature is mimicked if additional jets or pile-up add to the topology of the Z-decay.

6.5.1 $Z \rightarrow \tau\tau$ Estimation via Parametrized Object Level Embedding

$Z \rightarrow \tau\tau$ events are the dominant source of background in this analysis and consequently require precise modelling. However, shortcomings have been observed in the modelling of simulated Z + jets events [136]. Consequently, the dominant background is affected by two strongly correlated sources of uncertainties, namely Z + jets modelling and τ uncertainties. Pulls and constraints of the τ uncertainties have also large impact on the measured PoI. Due to the similar mass of the Z compared to the Higgs, data based background studies can only be performed by including phase-space regions containing signal events.

Therefore, an **object level embedding** methodology was developed for Run 1 [137]. It utilizes $Z \rightarrow \mu\mu$ data events and replaces the muons at track reconstruction and calorimeter cell-level by simulated τ leptons from $Z \rightarrow \tau\tau$ processes. By this means jet kinematics as well as the Z-boson are extracted from data and only well-understood physics is provided by simulation. This methodology became inaccessible during Run 2 due to conceptual changes in data processing. Therefore, a parametrized embedding version was developed [138], which matches the momentum and efficiencies of selected light leptons to those of a τ lepton. The procedure is performed on NTuple level according to:

1. $Z \rightarrow ll$ *source region*: The source region defines the subset of $Z \rightarrow ll$ events, which are used for the embedding procedure. The selection cuts aim for high statistics and are thus chosen loosely. The dataset is randomly assigned to the three τ decay channels and re-weighted to match the corresponding branching ratios into $\tau_{\text{lep}}\tau_{\text{lep}}$, $\tau_{\text{lep}}\tau_{\text{had}}$ and $\tau_{\text{had}}\tau_{\text{had}}$.

2. *efficiency unfolding*: On particle level, $Z \rightarrow ll$ and $Z \rightarrow \tau\tau$ processes are identical in kinematics, but they are different in reconstruction efficiency and acceptance. An efficiency unfolding mitigates detector effects. $Z \rightarrow ee$ and $Z \rightarrow \mu\mu$ samples are used to determine trigger,

reconstruction and identification efficiencies in p_T and η bins. These efficiencies are accounted for by applying corresponding event weights.

3. *embedding*: The unfolded leptons are subsequently considered to be true τ leptons that have yet to decay. For that purpose the energy carried by the reconstructed visible τ decay products is parametrized as a function of the true τ transverse momentum. This approach directly takes reconstruction efficiencies into account and its calculation is conducted independently for $\tau_{\text{lep}}\tau_{\text{lep}}$, $\tau_{\text{lep}}\tau_{\text{had}}$ and $\tau_{\text{had}}\tau_{\text{had}}$ decays. After selecting and applying a momentum correction factor from this parametrization, observables that depend on the transverse momentum, as the missing transverse energy, are recomputed based on the embedded momenta.

4. *trigger efficiency folding*: So far, weights are only applied on the object-level, while triggers act on event basis. Consequently, the embedded event rate is adapted to the trigger selection efficiency by applying additional event weights.

5. *event selection:* Since the initial $Z \rightarrow ll$ selection was designed to increase statistics, the actual τ signal region selection is applied in the last step of the embedding procedure.

The embedding procedure is inherited from the 2022 analysis design and is further detailed in [71]. It is used to construct control regions for the determination of normalization factors applied to $Z \rightarrow \tau\tau$ MC samples in the SR. Limitations of the approach are for example, the τ spin correlations, which are not taken into account. Their correct treatment would require to model the complete dynamics of τ production and decay. Furthermore, overlap issues might occur in events with a high number of jets since the isolation of surrounding objects is not taken into account.

6.5.2 Estimation of misidentified τ processes

The background from misidentified τ processes, so-called *Fakes*, constitutes the second-largest background, with a relative contribution of up to 25% [71]. Fake events primarily arise from jets misidentified as electrons, muons or hadronically decaying τ leptons. The reconstruction is data-based and relies on CRs with loosened/inverted identification criteria of the falsely identified objects as well as transfer factors to interpolate between CR and SR. In case of a double leptonic decay, the matrix method [139] is employed for reconstruction. The number of expected fake events is determined from efficiencies to observe real or fake leptons. In the $\tau_{\text{lep}}\tau_{\text{had}}$ channel contributions from a faked light lepton and a true τ_{had} are negligible [71]. Thus, only contributions where a jet is misidentified as τ_{had} are estimated with the Fake Factor method [140], which is also applied in the fake estimation of the double hadronic decay channel. Detailed information is provided in Chapter 7, which gives insight into the reconstruction methodology as well as studies beyond the conventional procedure.

6.5.3 Top Background

Especially in the $t\bar{t}H$ selection, the top background plays a non-negligible role. The normalization is determined in control regions as introduced in Section 6.7. The top quark itself typically decays into a b-quark and a W boson, a signature that consists of a QCD jet as well as the decay products of the boson. Thus, a $\tau_{\text{had}}\tau_{\text{had}}$ or $\tau_{\text{lep}}\tau_{\text{had}}$ decay of the di-tau state can be mimicked.

6.5.4 Others

Other background sources such as di-bosons, Z + jets decay into light leptons, W or $H \rightarrow WW$ contribute barely as it is exemplary shown in Table 6.5(b). Their modelling relies directly on simulation with uncertainties assigned to the respective normalization.

6.6 Systematic Uncertainties

Systematic uncertainties implement a variation of the event yield per region as well as the shape of the di-tau mass distribution. In the analysis a total of 352 sources of systematic uncertainties encompass aspects related to detector simulation, such as efficiencies and calibrations, as well as theoretical uncertainties. Dedicated performance groups within ATLAS perform studies to quantify the uncertainties. They are also first contact in question of application or relevance per analysis setting. Detailed information on the systematic uncertainties considered in the analysis can be found in [3].

Experimental Uncertainties: Experimental uncertainties affect the particle reconstruction, identification, isolation and triggers, which in turn impacts the acceptance as well as the event categorization. A central role in the Legacy analysis are jet uncertainties, which describe parameters like the energy scale of the reconstructed object. The experimental uncertainties considered can be assigned to following groups: muon uncertainties, electron uncertainties, tau uncertainties, jet uncertainties, missing transverse energy, luminosity, data-driven fake estimates and embedding.

Theory Background Uncertainties: Theory background uncertainties affect mainly Z + jets with, for example, uncertainties on the renormalization [10] and resummation scale as well as $t\bar{t}$ processes.

Theory Signal Uncertainties have a large impact on the measurement. They cover for example the parton distribution function[11] as well as the strong coupling constant α_s.

6.7 Analysis Design

The targeted STXS bins, introduced in Section 6.2.1, drive the event categorization to perform the measurement. Within the binned profile-likelihood fit, eighteen parameters of interest (PoI) are introduced - one per measurement-bin, illustrated in the left half of Figure 6.7.

6.7.1 Event Sub-Categorization

In order to measure the 18 targeted STXS-bins, dedicated phase-space regions are selected. Regions enriched in either signal or background events are selected through dedicated cuts. The signal regions of the analysis are depicted in the right half of Figure 6.7. Building on the previously defined event categorization into the four Higgs production modes, the targeted phase-space is selected by splitting

[10] The renormalization scale μ_R absorbs infinities that arise from loop correction in perturbative QCD calculations. It serves as reference scale at which the re-normalized parameters such as the strong coupling constant α_S are defined.

[11] Parton distribution functions describe the probability density to find a parton of a certain flavor carrying the momentum fraction x of the hadron.

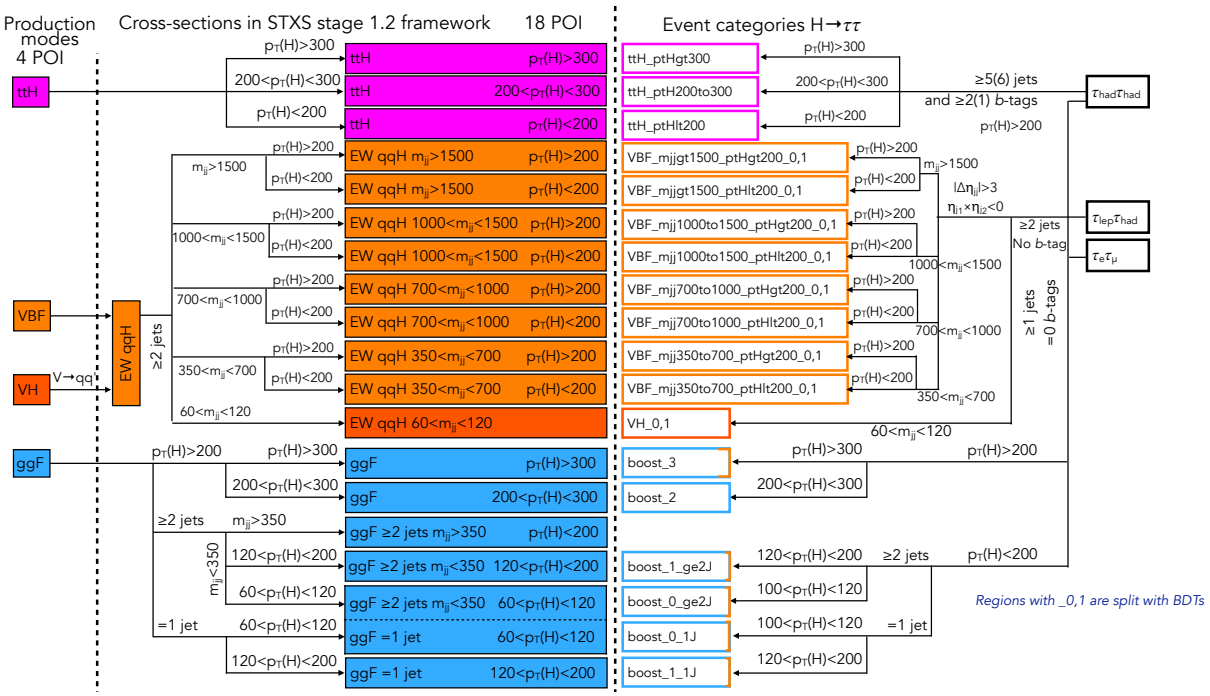


Figure 6.7: Sketch of the event categorization as well as the 18 targeted STXS stage 1.2 bins [119]. The different Higgs production modes are explored in detail. $t\bar{t}H$ related bins are marked in pink, VBF bins in orange, VH bins in red and ggF bins in blue.

in observables like p_T^H or m_{jj}. Under consideration of tagger outputs (further elaborated on in Section 6.8), signal regions are additionally split in a pure and a more diluted region, indicated by the subscripts 1 and 0, respectively. This measure aims to improve the fit-results of the 18 parameters of interest, which represent 18 signal strength parameters, that act on the 18 processes defined via the STXS bins.

The selected signal regions are not purely representative for the targeted signal process and can contain contributions from other STXS processes. The expected signal purity per signal region, derived from MC, is illustrated in Figure 6.8. The bins along the diagonal of the parameter space are strongly populated, indicating that the majority of signal processes are assigned to their corresponding signal region. The case of signal contamination is exemplified by the low p_T^H VBF signal regions where $ggH \geq 2-\text{jet}, m_{jj} \geq 350 p_T^H < 200$ contribute with up to 37%.

Phase-space regions dedicated to background events are defined to determine normalization factors for specific background processes. These control regions are defined for $Z \rightarrow \tau\tau$ and top events.

The $Z \rightarrow \tau\tau$ control regions have the same kinematic requirements as the signal regions but applied to embedded $Z \rightarrow ll$ samples. While signal regions are binned in $m_{\tau\tau}$, $Z \rightarrow \tau\tau$ control regions contain event yields in single-bin histograms. The binning applied in the SRs strongly impacts the stability and precision of the measurement. While a coarse binning is prone to hide physical features in the histograms, a high granularity promotes instabilities due to strong statistical fluctuations. Consequently, an automatic binning across all regions, developed by M. Hübner [98], is applied which provides coarse binning in regions with few physical features and finer binning in more relevant

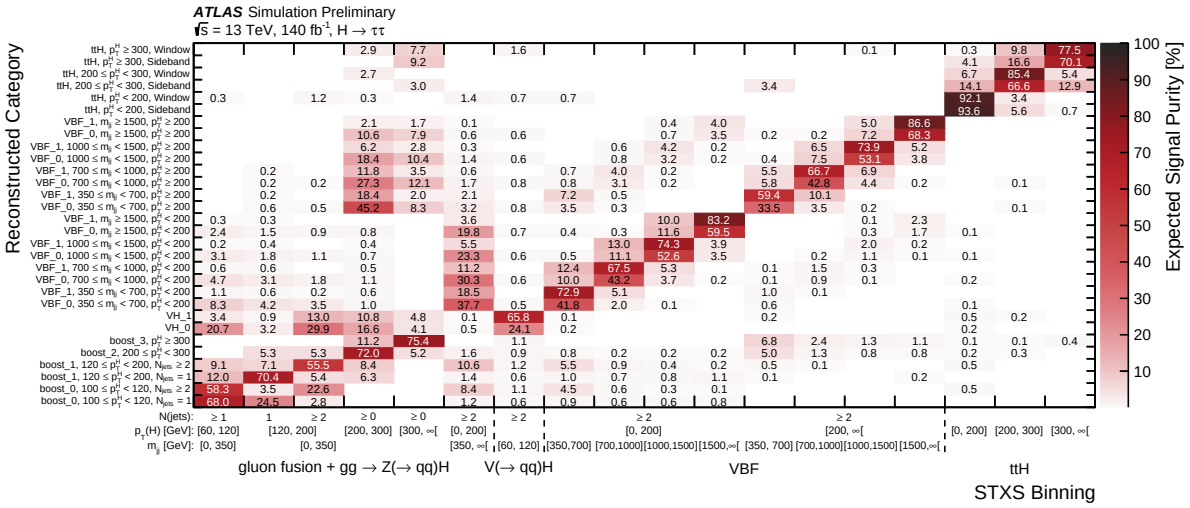


Figure 6.8: Expected signal purity per signal region. A visualization across all τ decay channels is shown. Adapted from [3].

regions. The algorithm merges bins until the relative total uncertainty reaches a pre-defined threshold α_{unc}. In order to guarantee that no physical properties get lost by the binning procedure, the threshold α_{unc} is multiplied by a factor f, if the signal-to-background ratio exceeds another threshold $\alpha_{S/B}$. The same procedure is applied if the statistical uncertainty is smaller than a threshold α_{stat} in order to preserve features of high-statistic bins, such as the $Z \to \tau\tau$ peak. Signal as well as control regions of the ggH and VH category are identical since the focus of the Legacy analysis lies in $t\bar{t}H$ and VBF.

The interplay of control and signal regions is visualized in Figure 6.9. A total of **78 signal regions** are considered, including six signal regions per τ decay channel in the boost topology, two per channel in VH and 16 per channel in VBF. The $t\bar{t}H$ topology is only represented by six signal regions in the $\tau_{\text{had}}\tau_{\text{had}}$ channel, split into three side-band and three window regions, which are characterized by a better signal-to-background ratio.

While each VH, boost & VBF signal regions is supplied by a dedicated $Z \to \tau\tau$ + jets control region, only one control region is defined for the six SRs in $t\bar{t}H$. This results in 73 control regions addressing the dominant background of the analysis. For the top background, seven control regions are introduced, one for the $t\bar{t}H$ SRs in the $\tau_{\text{had}}\tau_{\text{had}}$ channel and one per $\tau_{\text{lep}}\tau_{\text{lep}}$ and $\tau_{\text{lep}}\tau_{\text{had}}$ channel in VBF, boost and VH. The control region associated with $t\bar{t}H$ is defined by reversed BDT cuts, while for the top control region associated to VBF, a b-tagged jet is required.

6.7.2 Alternative Settings

Although the categories of the Legacy analysis setup are designed to measure 18 STXS bins, two alternative measurements are performed on the same setup. All regions remain identical, only the number of parameter of interest changes.

- **Inclusive Measurement:** The inclusive measurement considers only one PoI, which determines the inclusive signal strength of Higgs bosons decaying into two τ leptons.

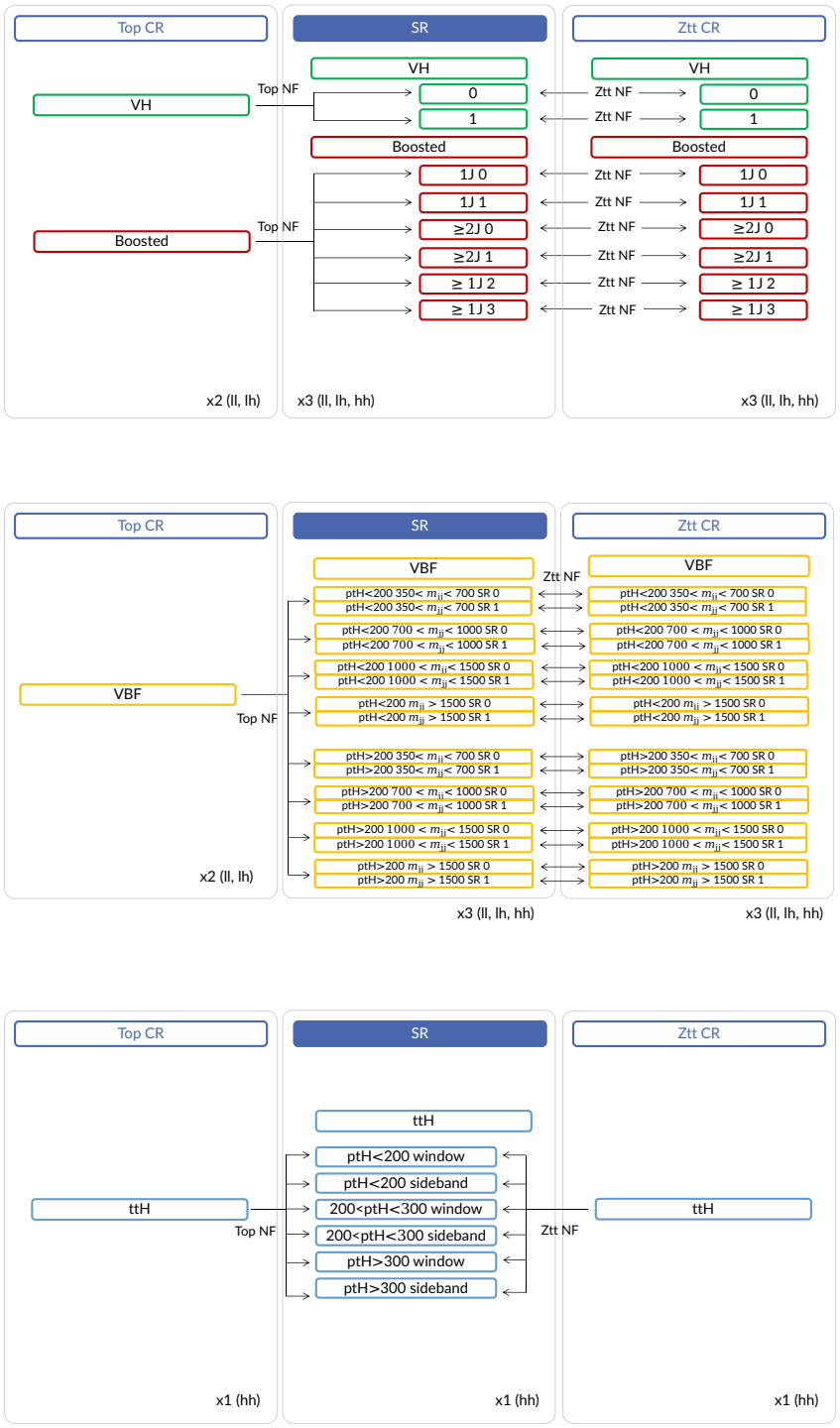


Figure 6.9: Visualization of the Legacy analysis design. Signal regions are grouped in the topologies *Boost, VH, VBF & ttH*.The connecting arrows between CRs and SRs demonstrate the application of normalization factors in the indicated regions [3]. The setup definitions in the VH and boost category are the same as in the 2022 publication [71].

- **Production Mode Dependent Measurement:** The production mode dependent measurement considers four PoIs, one for each production mode.

6.8 Improvements of the Legacy Setup

Compared to the 2022 Run 2 analysis, several changes and improvements have been introduced in the Legacy analysis - design-specific adaptions as well as fundamental changes. Noteworthy advancements are introduced below.

MMC

Instead of only relying on the di-tau mass reconstruction of the MMC, the collinear mass estimation is additionally considered in the mixed approach, *Mixed MMC/collinear Mass Estimator*, introduced in Section 4.6.

p_T^H reconstruction

The transverse momentum of the Higgs boson is an important variable in the definition of various categories in the analysis because of its promising sensitivity to possible BSM physics. The reconstruction is usually based on the MMC techniques. In this analysis, a neural network is used instead which shows improved resolution in the order of $\sim$ 50% for signal and $\sim$ 15% for $Z(\rightarrow \tau\tau)$+jets events [3].

$Z \rightarrow \tau\tau$ EWK Contribution

An underestimation of the electroweak contribution in $Z \rightarrow \tau\tau$ processes was observed for the SHERPA event generation as described in [141]. Therefore a scaling factor of 1.7 is applied to account for the mis-modelling. Furthermore, a scaling uncertainty of the variational range from 1-2.4 is introduced.

VBF tagger

The VBF topology can easily be mimicked by $Z \rightarrow \tau\tau$ events if additional jets are produced. The same applies for Higgs production in gluon gluon fusion if the event is accompanied by jets. In order to differentiate the true VBF events from background, a tagger was already used in the 2022 Run 2 analysis [71]. The tagger is based on a boosted decision tree (BDT), which uses the kinematics of the two leading jets as input. In the training process, VBF $H \rightarrow \tau\tau$ samples are considered as signal while a combination of ggF and $Z \rightarrow \tau\tau$ is used as background. In this analysis, the same training is used as in the 2022 publication but the cuts of the BDT score are optimized for the 8 STXS bins that are measured for VBF. Generally, a low score, VBF_0 and a high score VBF_1 region are differentiated. The cut value is chosen to maximize $\sigma_{\text{tot}} = \sqrt{\sigma_0^2 + \sigma_1^2}$ with $\sigma_i = {}^{S}/\sqrt{S+B}$ [3].

$t\bar{t}H$ tagger

To tag the $t\bar{t}H$ events, two multi-class BDTs were deployed in the 2022 analysis, one for $p_T^H < 200\,\text{GeV}$ and one for $p_T^H > 200\,\text{GeV}$. They discriminate the signal $t\bar{t}H$ events, from $Z \rightarrow \tau\tau$ and $t\bar{t}$ background by providing three different scores - one per targeted process. The variables used for training comprise kinematics of τ_{had}, reconstructed jet properties and missing transverse energy information. The BDT scores are used to define signal as well as control regions of the $t\bar{t}H$ category. SRs solely depend on the p_T^H dependent $t\bar{t}H$ scores while the Z-related score is additionally used for the definition of $t\bar{t}$ and Z CR.

Fake Template Combination

Fake templates, representing the expected fake-background distribution, are combined across different regions to reduce the statistical uncertainty on the shape. Detailed studies are described in Section 7.4.

CHAPTER 7

Studies of the non-τ Background

Misidentified τ leptons, known as *Fakes*, are one of the dominant backgrounds in the $H \rightarrow \tau\tau$ analysis. A common source are QCD jets, which are misidentified as either hadronically or leptonically decaying τ leptons by mimicking the hadronic decay products or light leptons.

The fake contribution to the background of the $H \rightarrow \tau\tau$ analysis varies from 5% in highly boosted categories, up to 25% in less energetic phase-space regions [71].

Improved reconstruction and analysis strategies are promising to increase the sensitivity of the measurement. Starting from the common reconstruction procedure in Section 7.1.2 and 7.2, a more refined τ decay-mode dependent reconstruction is proposed in Section 7.3 targeting the double-hadronic τ decay. Based on the new approach, a re-definition of signal regions becomes feasible, which allows to define regions with reduced background contamination. In addition, the statistical uncertainty on the shape of fake distributions is investigated in Section 7.4 to further improve sensitivity of the measurement.

7.1 Fake Estimation Methods

In the scope of this analysis, two data-driven techniques are applied for fake background estimation. Both methods strive to estimate the contribution of falsely identified lepton candidates in the signal region selection. The modeled distributions are referred to as *fake templates*. The Matrix Method [139] is used to reconstruct the non-τ background in the $\tau_{\text{lep}}\tau_{\text{lep}}$ channel. The Fake Factor Method [140] is applied in the $\tau_{\text{lep}}\tau_{\text{had}}$ and $\tau_{\text{had}}\tau_{\text{had}}$ channel and is discussed in greater detail due to its relevance for this thesis.

7.1.1 Matrix Method

The Matrix Method [139] differentiates two object types, real leptons and fake leptons. By applying either loose or tight (signal-like) cuts on the particle identification score, regions enhanced in either object can be constructed. Dedicated control regions are used to determine efficiencies of real or fake leptons passing the tight selection in addition to the loose requirements, denoted as ϵ_r or ϵ_f. In single-lepton selections, the number of loose leptons observed N^l corresponds to the sum of real N^l_r

and fake leptons N_f^l passing the loose requirements

$$N^l = N_r^l + N_f^l. \tag{7.1}$$

The number of tight leptons N^t is estimated by the sum of real and fake loose leptons, scaled by the corresponding efficiency factors

$$N^t = \epsilon_r N_r^l + \epsilon_f N_f^l. \tag{7.2}$$

Based on these relations, the fake contribution in the tight selection can be estimated. If not one but two leptons are selected, the fake estimation is based on a set of equations [119]. The associated efficiency matrix scales real and fake lepton yields to the expected event count for loose-loose (N_{LL}), loose-tight (N_{LT}), tight-loose (N_{TL}) and tight-tight (N_{TT}) pairs

$$\begin{bmatrix} N_{TT} \\ N_{TL} \\ N_{LT} \\ N_{LL} \end{bmatrix} = \begin{bmatrix} \epsilon_r\epsilon_r & \epsilon_r\epsilon_f & \epsilon_f\epsilon_r & \epsilon_f\epsilon_f \\ \epsilon_r(1-\epsilon_r) & \epsilon_r(1-\epsilon_f) & (1-\epsilon_f)\epsilon_r & \epsilon_f(1-\epsilon_f) \\ (1-\epsilon_r)\epsilon_r & (1-\epsilon_r)\epsilon_f & (1-\epsilon_f)\epsilon_r & (1-\epsilon_f)\epsilon_f \\ (1-\epsilon_r)(1-\epsilon_r) & (1-\epsilon_r)(1-\epsilon_f) & (1-\epsilon_f)(1-\epsilon_r) & (1-\epsilon_f)(1-\epsilon_f) \end{bmatrix} \begin{bmatrix} N_{rr} \\ N_{rf} \\ N_{fr} \\ N_{ff} \end{bmatrix} \tag{7.3}$$

The total fake yield in the signal region includes contributions from events with two misidentified leptons (N_{ff}), as well as events with either one of the two (N_{rf}, N_{fr}) misidentified.

7.1.2 Fake Factor Method

The Fake Factor method is a data-driven approach to estimate the contribution of fake hadronic τ decays. The method aims to estimate the corresponding background in the SR, where direct data-based methods are not feasible due to the presence of signal events. The concepts of the method are developed in $\tau_{\text{lep}}\tau_{\text{had}}$ channel, where the hadronically decaying τ lepton is likely to be misidentified.

The general idea of the method is to extrapolate the fake contribution from a control region to a signal region by applying corresponding transfer factors, also called *Fake Factors* (FF). This control region, called anti-τ region, is defined orthogonal to the SR by inverting the medium τ-ID requirement, which assesses the purity of genuine τ leptons in the sample (see Section 4.5). The CR is populated predominantly by fake events as a result of events failing the medium τ-ID. The fake contribution in the anti-τ region is determined by subtracting the genuine τ events ($N^{\text{anti-tau}}_{\text{genuine }\tau}$), obtained from simulations, from the total events observed in the measurement data ($N^{\text{anti-tau}}_{\text{Data}}$). This procedure is illustrated in the left half of Figure 7.1.

To estimate the fake contribution in the SR, a transfer factor, the Fake Factor, is required to propagate the fake contribution from the CR into the SR, as illustrated in the right half of Figure 7.1. The fake yield $N^{\text{SR}}_{\text{fakes}}$ in the SR is calculated as follows:

$$N^{\text{SR}}_{\text{fakes}} = \left(N^{\text{anti-tau}}_{\text{Data}} - N^{\text{anti-tau}}_{\text{genuine }\tau}\right) \cdot FF \tag{7.4}$$

The FFs need to be determined in a dedicated set of CRs. These separate CRs must be orthogonal to the SR and its anti-τ region by inverting at least one other selection criterion. They are required to exhibit event kinematics similar to the SR to ensure the applicability of the FFs. Additionally, a high

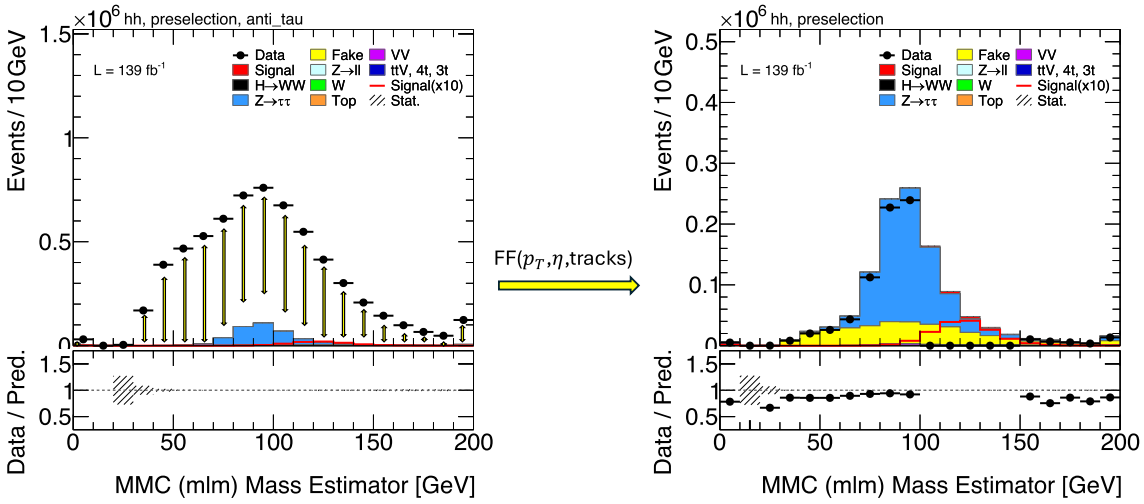


Figure 7.1: Visualization of the Fake Factor method. In the anti-τ region (left) only events failing medium τ-ID are selected. The fake contribution is determined as the difference between the measurement data (black points) and the genuine τ contribution, determined from MC simulation (colored bars). The fake contribution is transferred to the SR by applying a Fake Factor (yellow arrow between the figures), which yields the fake template in the SR, depicted in yellow in the right figure.

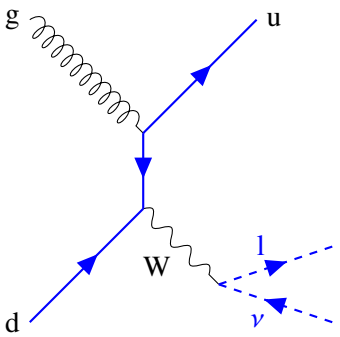


Figure 7.2: Feynman diagram of the W + jet process. The quark initiated jet mimics a hadronically decaying τ lepton. The leptonic τ decay results in the same signature as the leptonic W-decay (lepton and missing energy).

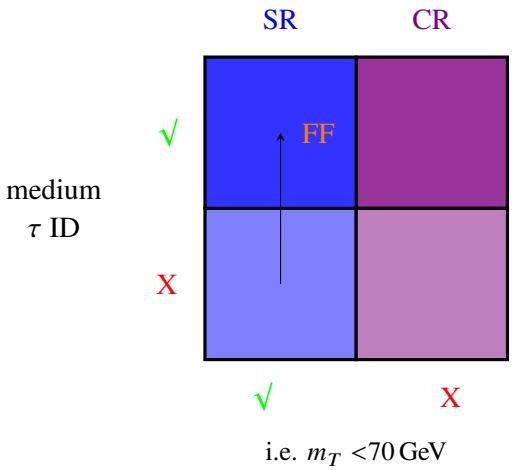


Figure 7.3: Schematic diagram of the Fake Factor method. Four orthogonal regions are defined by either fulfilling (green check mark) or failing (red cross) medium τ-ID and the transverse mass requirement of m_T <70 GeV. Regions marked in violet are used to determine the Fake Factor and those in blue to apply it.

population of jets reliably determines the rate of falsely identified τ_{had} leptons. Such a CR is based on W + jets events, which pass the general $\tau_{\text{lep}}\tau_{\text{had}}$ requirements. The leptonic τ decay is mimicked by the leptonic W decay and the quark initiated jet is misidentified as hadronically decaying τ lepton. The signature of a W + jet event is represented by the Feynman diagram in Figure 7.2.

The transverse mass observable

$$m_T = \sqrt{2p_T^l p_T^\nu (1 - \cos\Delta\Phi)} \tag{7.5}$$

is inverted to differentiate SR from W + jet CR. The angle between the lepton and missing transverse energy vector in the transverse plane is represented by $\Delta\Phi$. In the W + jets CR, the transverse mass is required to be larger than 70 GeV, which includes the W boson mass peak at $\sim$ 80 GeV [12]. In the SR events with transverse masses smaller than 70 GeV are considered. In order to determine a transfer factor between anti-τ and τ-like events, two orthogonal regions are defined within the W + jets CR. τ-like events fulfill the medium τ-ID requirement, anti-τ events fail the requirement. In both regions, the fake contribution is estimated by determining the difference between the observed data and the simulated genuine τ events. The ratio of fake contributions between both regions is defined as the Fake Factor

$$FF = \frac{N_{\text{Data}}^{\tau,\text{CR}} - N_{\text{MC, no jet}\to\tau}^{\tau,\text{CR}}}{N_{\text{Data}}^{\text{anti}-\tau,\text{CR}} - N_{\text{MC, no jet}\to\tau}^{\text{anti}-\tau,\text{CR}}}. \tag{7.6}$$

The Fake Factor method assumes that the ratio of fake contributions in the W + jets CR and the SR is the same. The key aspects of the methodology are illustrated in Figure 7.3. A total of four regions are required: two τ-like regions that fulfill the medium τ-ID and two anti-τ regions that fail it. The two regions per τ-ID requirement are split by transverse mass into two regions, which are utilized to determine and to apply the FFs.

Central to the method is the identification working point of the τ lepton candidate. The fake rejection is however not constant across the full phase-space (see Figure 4.4). It strongly depends on p_T and η as well as the number of reconstructed tracks in the τ decay. Consequently, the Fake Factor is parametrized in p_T and η and is also separately determined for 1- and 3-prong events. The selected binning for calculation in η includes a barrel ($|\eta| < 1.37$) and an end-cap region ($1.37 < |\eta| < 2.5$). The transverse momentum is split into three bins, $30\,\text{GeV} < p_T < 40\,\text{GeV}$, $40\,\text{GeV} < p_T < 60\,\text{GeV}$ and $60\,\text{GeV} < p_T < 500\,\text{GeV}$.

Fake Factors additionally vary with the quark/gluon composition of the selected events and consequently depend on the background source. While the W+jets CR mainly covers quark initiated jets, an additional QCD CR is introduced in the $\tau_{\text{lep}}\tau_{\text{had}}$ channel to describe the fake contribution from QCD multi-jets. The two sets of fake factors, originating from different background sources, are weighted with their expected relative contribution in the anti-τ region used for FF application. The contribution of misidentified light leptons in the $\tau_{\text{lep}}\tau_{\text{had}}$ channel was found to be negligible [71].

7.2 Fake Background Estimation in the $\tau_{\text{had}}\tau_{\text{had}}$ Channel

The fake estimation in the $\tau_{\text{had}}\tau_{\text{had}}$ channel is based on the Fake Factor method, presented in Section 7.1.2. A unique challenge of the $\tau_{\text{had}}\tau_{\text{had}}$ channel is that either one or both $\tau_{\text{had-vis}}$ candidates can be misidentified. The Fake Factors are determined in a W + jets CR, which is based on the $\tau_{\text{lep}}\tau_{\text{had}}$ baseline selection. Additional cuts are applied to mimic the $\tau_{\text{had}}\tau_{\text{had}}$ phase-space, so that the fake factors become applicable. Changes in the selection criteria comprise for example $\Delta\eta(l, \tau_{\text{had-vis}}) > 0.6$. The pseudo-rapidity cut accommodates for a minimum-required spatial separation between the $\tau_{\text{had-vis}}$ candidates imposed by the di-tau trigger.

In order to cope with the immense amount of data provided by the LHC, the stored information is reduced to provide manageable computing time at analysis level. Skimming procedures exclude events in the $\tau_{\text{had}}\tau_{\text{had}}$ channel where both τs fail the loose τ-ID. The Fake Factor determination is however performed in the W+jets CR with not-loose τs included. In the case of two misidentified τ leptons, this Fake Factor cannot be exclusively applied since double not-loose ID events would be covered. Therefore, two sets of Fake Factors are needed to further guarantee a reliable reconstruction. The determination of one set is based on not-medium τs in the anti-τ region (not-loose or loose ID), whereas the other set is based on loose-not-medium (only loose ID) events.

$$FF_{\text{nm}} = \frac{\left(N^{\tau}_{\text{Data}} - N^{\tau}_{\text{MC, genuine }\tau}\right)^{\text{WCR}}_{\text{medium }\tau}}{\left(N^{\text{anti}-\tau}_{\text{Data}} - N^{\text{anti}-\tau}_{\text{MC, genuine }\tau}\right)^{\text{WCR}}_{\text{not medium }\tau}} \tag{7.7}$$

$$FF_{\text{lnm}} = \frac{\left(N^{\tau}_{\text{Data}} - N^{\tau}_{\text{MC, genuine }\tau}\right)^{\text{WCR}}_{\text{medium }\tau}}{\left(N^{\text{anti}-\tau}_{\text{Data}} - N^{\text{anti}-\tau}_{\text{MC, genuine }\tau}\right)^{\text{WCR}}_{\text{loose not medium }\tau}} \tag{7.8}$$

Figure 7.4 shows the 1-prong not-medium and loose-not medium Fake Factors in the barrel and the end-cap region as well as in different transverse momentum bins. Loose-not-medium Fake Factors yield larger values accompanied by larger statistical uncertainties than not-medium Fake Factors. This is caused by low statistics in the loose-not-medium anti-τ region, which is shown in Figures C.1

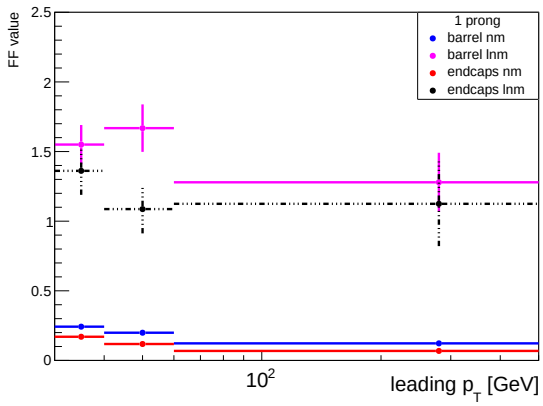


Figure 7.4: Not-medium (nm) and loose-not-medium (lnm) fake factors of the $\tau_{\text{had}}\tau_{\text{had}}$ channel. The transfer factors are shown for 1-prong events and different transverse momentum bins. Barrel (pink and blue) and end-cap region (black and red) are also differentiated.

through C.5. The fake contributions of the loose-not-medium and not-medium CRs enter the Fake Factor calculation in the denominator which is why the Fake Factor value is inversely proportional to the observed statistics.

7.2.1 Application

In the $\tau_{\text{had}}\tau_{\text{had}}$ channel, either one or both τs might be misidentified, which needs to be considered when applying the Fake Factors. The selected τs in the SR τ^P (passed) are a combination of true (τ^T) and fake (τ^F) candidates.

$$\tau_0^P \tau_1^P = \tau_0^T \tau_1^T + \tau_0^T \tau_1^F + \tau_0^F \tau_1^T + \tau_0^F \tau_1^F \tag{7.9}$$

The fake τ^F contribution in the SR is described by the product of Fake Factor and fake contribution in the anti-τ region τ^A:

$$\tau^F = FF\tau^A \tag{7.10}$$

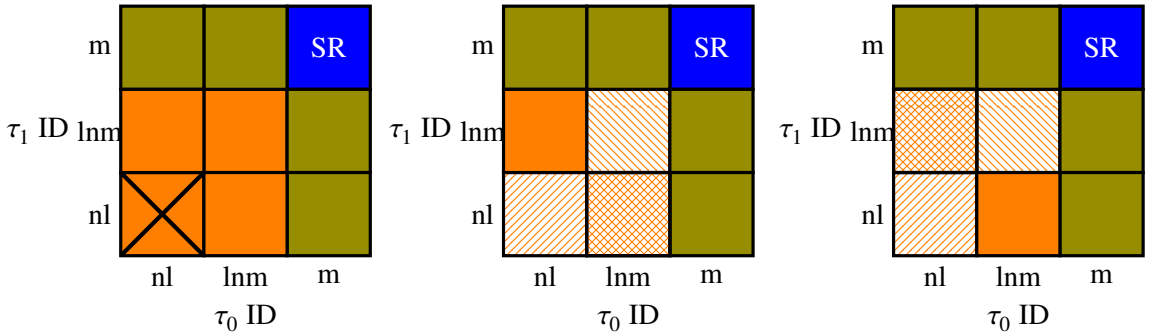
As a consequence, double fake events are estimated by:

$$\tau_0^F \tau_1^F = FF^0 FF^1 \tau_0^A \tau_1^A \tag{7.11}$$

Events where the fake contribution is only assigned to one τ also include cases where the second τ was additionally misidentified.

$$FF^0 \tau_0^A \tau_1^P = \tau_0^F \tau_1^T + \tau_0^F \tau_1^F \tag{7.12}$$

$$FF^1 \tau_0^P \tau_1^A = \tau_0^T \tau_1^F + \tau_0^F \tau_1^F \tag{7.13}$$



(a) τ-ID combinations (b) τ_0-ID: lnm,τ_1-ID: nm (c) τ_1-ID: lnm,τ_0-ID: nm

Figure 7.5: Possible τ-ID combinatorics in the $\tau_{\text{had}}\tau_{\text{had}}$ channel. The signal region is depicted in blue. Medium τ-ID is labelled by *m* and colored in olive. Loose-not-medium and not-loose τ-ID, representing the anti-τ region are colored in orange and labelled by *lnm* and *nl*, respectively. Events, where both τs carry not-loose ID were removed by the skimming procedure, as indicated by the black cross in a). Sub-figures b) and c) show mixed lnm and nm τ-ID configurations. The corresponding Fake Factors cover three out of four orange regions, whereas one region is covered by both contributing templates.

The combination of 7.12 and 7.13 yields

$$\tau_0^F \tau_1^T + \tau_0^T \tau_1^F = FF^0 \tau_0^A \tau_1^P + FF^1 \tau_0^P \tau_1^A - 2 \cdot \tau_0^F \tau_1^F . \tag{7.14}$$

Using expression 7.14 in 7.9 while taking 7.11 into account leads to

$$\tau_0^P \tau_1^P = \tau_0^T \tau_1^T + FF^0 \tau_0^A \tau_1^P + FF^1 \tau_0^P \tau_1^A - FF^0 FF^1 \tau_0^A \tau_1^A . \tag{7.15}$$

Thus, single fake events are summed up, whereas double fake events need to be subtracted. Both cases inform the application strategy for the two sets of Fake Factors, not-medium and loose-not-medium. On event basis, a combination of not-medium and loose-not-medium Fake Factors are applied as event weights, depending on the τ-ID constellation in the anti-τ region. The following explanation is based on Figure 7.5, which shows τ-ID combinatorics in the $\tau_{\text{had}}\tau_{\text{had}}$ channel.

Three different scenarios are possible, leading to different event weights.

Single Fake Events In the case that one of the two τ leptons carries medium τ-ID and the other one carries either not-loose or loose-not-medium ID, the event weight is solely based on the not-medium Fake Factor:

1. τ_0-ID: m, τ_1-ID: nm: $w = FF_{nm}(\tau_1)$
2. τ_1-ID: m, τ_0-ID: nm: $w = FF_{nm}(\tau_0)$

Double Fake Events Double fake events require special treatment. Events where both τ leptons carry not-loose ID were removed. Consequently, a combination of the not-medium and loose-not-medium templates are considered to get an fake estimate.

1. τ_0-ID: lnm, τ_1-ID: nl: $w = -\frac{1}{2}\left(FF_{lnm}(\tau_0) \cdot FF_{nm}(\tau_1)\right)$

2. τ_1-ID: lnm, τ_0-ID: nl: $w = -\frac{1}{2}\left(FF_{lnm}(\tau_1) \cdot FF_{nm}(\tau_0)\right)$
3. τ_1-ID: lnm, τ_0-ID: lnm: $w = -\frac{1}{2}\left(FF_{lnm}(\tau_0) \cdot FF_{nm}(\tau_1) + FF_{nm}(\tau_0) \cdot FF_{lnm}(\tau_1)\right)$

Since the Fake Factors are determined in the $\tau_{\text{lep}}\tau_{\text{had}}$ channel, the contributions from leading and sub-leading $\tau_{\text{had-vis}}$ candidates cannot be differentiated. Double-fake events need to be subtracted, which is represented by a negative event weight. While a loose-not-medium template never covers not-loose contributions, a not-medium template does. The combination of nm and lnm templates in 1. (Figure 7.5(b)) or 2. (Figure 7.5(c)) each cover three out of four anti-τ regions, with both templates overlapping in one of three regions. The entire anti-τ region is covered twice, since the leading and sub-leading τ, and therefore cases 1. and 2. are interchangeable. A factor $\frac{1}{2}$ is introduced to account for this overestimation. The two loose-not-medium τs of case 3. are similarly described by the two templates. Due to the overlap of contributing regions, the sum of case 1. and 2. determines the event weight.

7.2.2 Systematic Uncertainties

Three main sources of systematic uncertainties are considered to provide a suitable Fake Factor estimation in the $\tau_{\text{had}}\tau_{\text{had}}$ channel. The two dominant contributions are the background composition and statistical limitations with an uncertainty of $\sim$ 15% [71], followed by the uncertainty on the parametrization in the order of $\sim$ 5% [71].

Statistical Limitations This source of uncertainty is introduced by the limited statistics in the W + jets CR, which is used to determine the Fake Factors. The uncertainty introduced by the limited sample size is estimated by a 1 σ variation of the determined Fake Factors. Four different variations are considered namely 1-prong, 3-prong, not-medium and loose-not-medium.

Parametrization The applicability of the Fake Factors in the SR, while being determined in the CR is a central assumption of the method. Since the accuracy of the method cannot be directly validated, a parametrization uncertainty is introduced. To get an estimate of the uncertainty extent, the fake estimation procedure is repeated in a fake-enriched environment. To populate the phase-space with non-τ events, a same-sign (SS) requirement is introduced. A dedicated set of Fake Factors is determined and applied to the anti-τ region to get a fake estimate in the SR. Given that the SS SR is fake-enriched, the robustness of the methodology can be probed. Successful background reconstruction in this context provides *closure* for the method. The resulting data/mc ratio is used as weight in the parametrization uncertainty estimation.

Background Composition Jets that originate from gluons or quarks require dedicated Fake Factors. Discrepancies in the background composition between the CR driving the Fake Factor calculation and the region used for application need to be accounted for. To get a handle on this source of uncertainty, another set of Fake Factors is determined besides the W + jets and the SS Fake Factors. This third CR requires high separation between the two τ leptons, $1.5 < \Delta\eta(\tau_{\text{had-vis}}, \tau_{\text{had-vis}}) < 2.0$. The impact of a change in the source region for Fake Factor determination is now covered by two separate uncertainties: one taking the variation based on the same-sign CR and another one one based on the high $\Delta\eta$ CR into account.

7.3 Decay-Mode Dependent Fake Estimation

Precision measurements aim to enhance the sensitivity of the analyzed channel. Improvements can be made by refining the reconstruction of the signal process or by controlling the background processes as well as diverse sources of uncertainty. Mastering all these aspects leads to more advanced analysis setups.

Background Contamination: The kinematic regions of interest, the signal regions, are selected such that the signal-to-background ratio is maximized.

$$R_{\mathrm{sb}} = \frac{\#\mathrm{Signal}}{\sqrt{\#\mathrm{Background}}}$$

While targeting signal-enriched phase-space regions, it is also essential to account for background contamination.

Uncertainties: Eliminating or reducing sources of uncertainty also has a positive impact on the sensitivity.

The following sections present studies towards refined reconstruction techniques of the fake background. The first subject of investigation is a decay-mode dependent fake estimation. The conducted, detailed studies are outlined in order to provide the collected knowledge and expertise for future analyses.

7.3.1 Motivation

The fake background contribution depends on various observables like the transverse momentum of the τ lepton, the pseudorapidity η or the number of charged tracks. Dedicated Fake Factors take these dependencies into account but still leave further dependencies unaccounted for. Not only the number of charged tracks in the τ decay but also the amount of neutral π^0s essentially impacts the fake contribution. The background contribution in the $\tau_{\mathrm{lep}}\tau_{\mathrm{had}}$ channel is shown in relation to the hadronic decay-mode in Figure 7.6. The largest background across all decay-modes is the $Z \rightarrow \tau\tau$ process. The second largest is assigned to fake events. A striking dependency is found in the increase of the fake background contribution with the number of π^0s in the decay.

Considering this dependency in the analysis design carries potential towards an increase in sensitivity. A refined description of the fake background can improve the data/mc agreement, which propagates its positive impact to the fit setup. In addition, increased purity can be achieved by defining decay-mode dependent signal regions.

7.3.2 Fake Factor Calculation

The first step towards a decay-mode dependent fake estimation is the calculation of the corresponding Fake Factors. As outlined in Section 7.1.2 and 7.2, $\tau_{\mathrm{lep}}\tau_{\mathrm{had}}$ W + jets CRs are used for the calculation with additional cuts to mimic a $\tau_{\mathrm{had}}\tau_{\mathrm{had}}$ selection. To determine the Fake Factors in the appropriate phase-space regions, decay-mode cuts are added to the previous settings. Ten W + jets CRs are

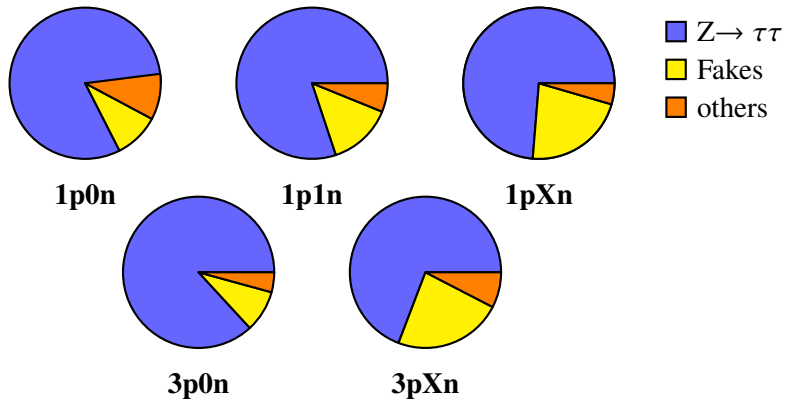


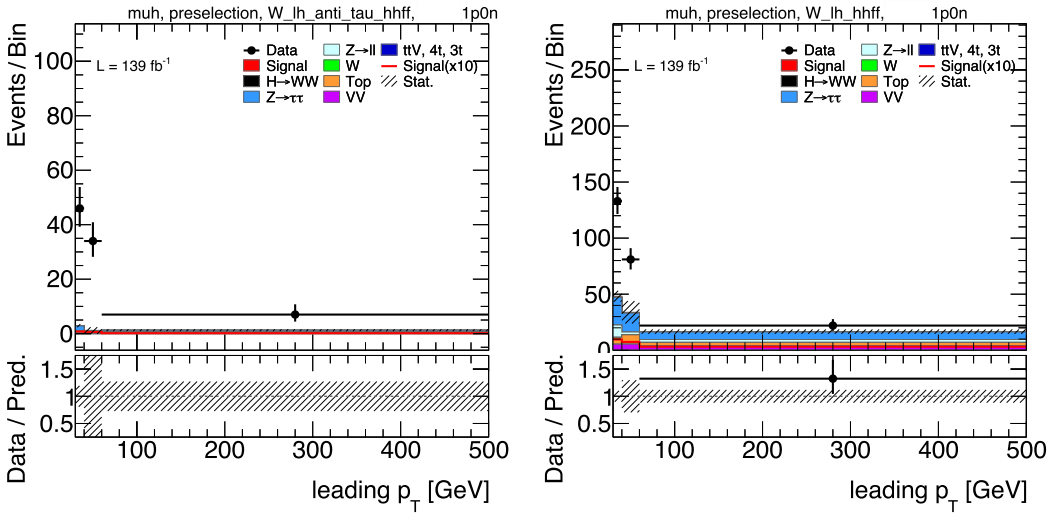
Figure 7.6: Decay-mode dependent background composition in the $\tau_{\text{lep}}\tau_{\text{had}}$ channel at baseline selection. The top row shows decays with one track (1p) and different number of neutral πs (0n, 1n, Xn) while the bottom row represents events with 3 tracks. The dominant contribution arises from $Z \rightarrow \tau\tau$ events depicted in blue, followed by fake events shown in yellow. The remaining background sources are summarized in 'others', depicted in orange.

defined, an anti-τ and a τ-like region for 1p0n, 1p1n, 1pXn, 3p0n and 3pXn decays of the hadronic τ lepton. The CRs are shown in the projection on the transverse momentum in Figure C.1 through C.5. Equation 7.7 and 7.8 yield the Fake Factors, shown in Figure 7.8 in the projection on p_T. The 1p0n Fake Factor calculation of the end-cap region is exemplified for the lnm anti-τ region. The required yields for calculation can be extracted from Figure 7.7. In 7.7(b), the τ-like CR is shown. The fake contribution, which corresponds to the difference between measured data and simulated genuine τ leptons enters the Fake Factor calculation in the nominator. The anti-τ region, whose fake contribution describes the denominator, is depicted in Figure 7.7(a). For each p_T-bin, a dedicated FF can be determined.

$$FF_{\text{lnm, end-cap}}(30\,\text{GeV} < p_T < 40\,\text{GeV}) \approx \frac{133-50}{45-3} \approx 2$$
$$FF_{\text{lnm, end-cap}}(40\,\text{GeV} < p_T < 60\,\text{GeV}) \approx \frac{80-33}{34-2} \approx 1.5$$
$$FF_{\text{lnm, end-cap}}(60\,\text{GeV} < p_T < 500\,\text{GeV}) \approx \frac{25-20}{7-2} \approx 1$$

The extracted values are in line with the corresponding lnm Fake Factors of the 1p0n decay-mode for the end-cap region, shown in Figure 7.8(a).

Through all five plots of Figure 7.8, the loose-not-medium Fake Factors are affected by larger statistical uncertainties than the not-medium Fake Factors, which results from loose-not-medium events being a sub-set of not-medium. Independently of decay-mode or detector region, not-medium FFs tend to decrease with increasing p_T. The behavior is based on the inverse relation between Fake Factor and failed τ-ID. The Fake Factor decreases with increased contributions from the anti-τ region. As the background rejection for medium τ-ID increases with p_T (see Figure 4.4), the yield of events failing medium ID increases which in turn populates the anti-τ region.



(a) lnm WCR anti-τ endcaps

(b) WCR endcaps

Figure 7.7: WCRs used for 1p0n fake factor calculation. The p_T phase space is shown the end-cap region $1.37 < |\eta| < 2.5$. Apart from the τ-like CR, the nm and lnm anti-τ region is depicted.

7.3.3 Validation

The newly defined, decay-mode dependent Fake Factors are applied according to Section 7.2.1 and in accordance with the decay-modes of the τ lepton candidates. In order to validate the new methodology as well as the implementation of the algorithm, validation studies are performed. Fake-enriched phase-space regions are suited for these studies. In the following the high $\Delta\eta$-region is selected, which requires high separation between the two τ leptons, $1.5 < \Delta\eta(\tau_{\text{had-vis}}, \tau_{\text{had-vis}}) < 2.0$.

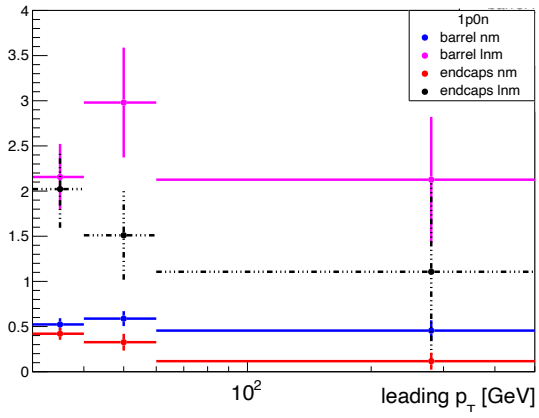
Background Modelling

The validation of the decay-mode dependent fake estimation comprises an investigation of the background modelling in the fake-enriched high $\Delta\eta$-region. The sub-leading p_T observable is shown in Figure 7.9(b) for 1-prong events, which comprise the 1p0n, 1p1n and 1pXn decay-mode. Fakes are the dominant background. Within the uncertainties, a good data/MC agreement is achieved across the whole distribution, which validates the methodology as well as the implementation of the algorithm up to this point.

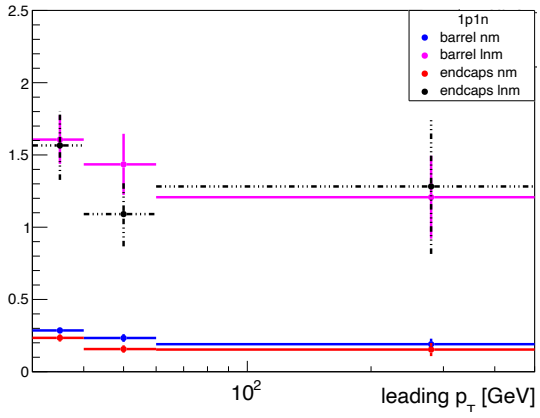
Template Comparison

The comparison of fake templates based on the inclusive approach, disregarding the decay-mode dependence, and the one considering the split, offer another opportunity for a cross-check.

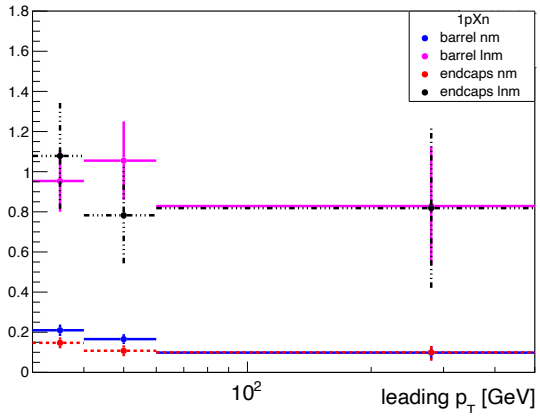
Figure 7.9(a) and 7.9(b) show a data/MC comparison considering fake templates based on the inclusive and decay-mode dependent Fake Factors, respectively. The reconstructed background describes the data within the uncertainties in both cases. The direct comparison of both fake templates, visualized in Figure 7.9(c), confirms their compatibility in shape and normalization.



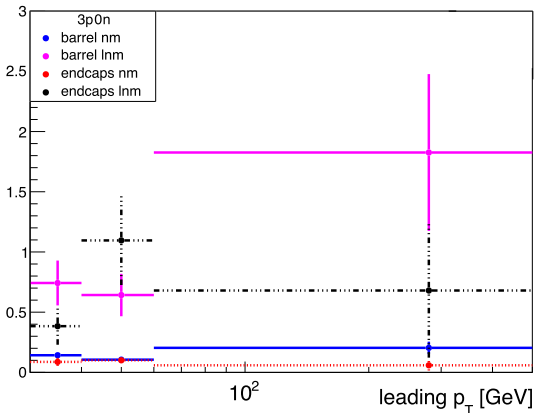
(a) 1p0n



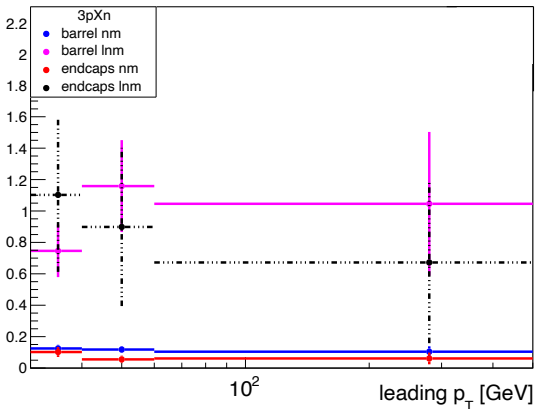
(b) 1p1n



(c) 1pXn

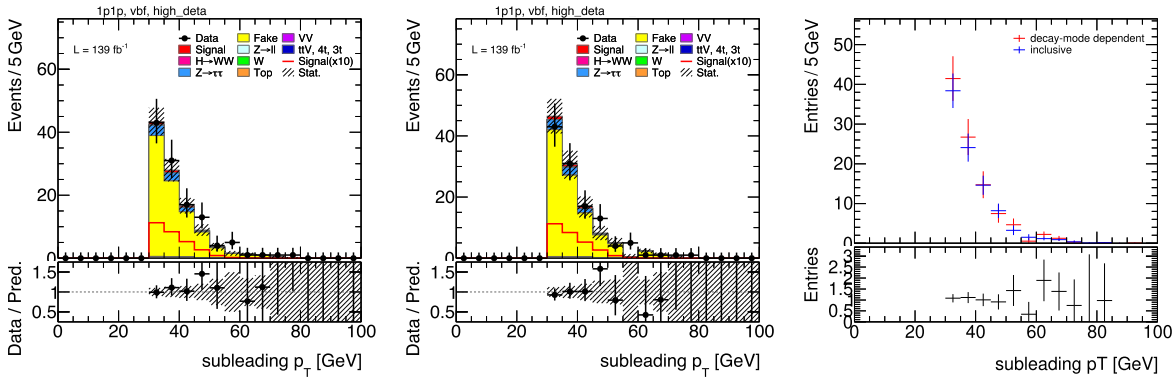


(d) 3p0n



(e) 3pXn

Figure 7.8: Decay-mode dependent Fake Factors projected on the transverse momentum p_T. Nm as well as lnm Fake Factors are shown for the barrel as well as the end-cap region.



(a) Inclusive fake template, yield 92.47 (b) Decay-mode fake template, yield 99.36 (c) Comparison of fake templates

Figure 7.9: Comparison of inclusive and decay-mode dependent fake template in the high $\Delta\eta$-region. Inclusive means the absence of the decay-mode split. A separation in p_T, η, and the number of tracks is still present. The two templates are separately compared to data in a) and b). In c) they are directly compared to each other.

τ / τ	1p0n	1p1n	1pXn	3p0n	3pXn
1p0n	3.3%	14.8%	6%	5.6%	3%
1p1n		16.8%	14%	12.6%	6.8%
1pXn			2.9%	5.2%	2.8%
3p0n				2.4%	2.6%
3pXn					0.7%

Table 7.1: Decay-mode grouping in the $\tau_{\text{had}}\tau_{\text{had}}$ channel. 15 possible decay-mode combinations are possible. Channels of low statistics and/or low contribution of neutral decay-products are combined to new SRs, as indicated by the color scheme. The percentages give the relative yield in the VBF channel.

7.3.4 Signal Region Split

Signal regions are selected such that they are as pure in signal as possible, which can be reached by a high signal yield in combination with low background contamination. In the following, a signal region split is discussed, which targets a differentiation in decay-modes. Starting point of the discussion is the inclusive VBF phase-space introduced in Chapter 6, which is not yet separated in p_T^H or m_{jj}.

The fake contribution increases with the number of π^0s involved in the τ decay. Low-background regions are formed by including as few π^0 contributions as possible. Within these low-background regions, loosening the τ-ID working point becomes a viable option to improve the signal efficiency while lowering the fake rejection. Loosening the τ-ID working point means that loose τ-ID is sufficient to pass the SR selection instead of medium τ-ID. The anti-τ region used for fake estimation consequently requires not loose ID. Because of the low fake contribution by design, the change might, in terms of sensitivity, add more to the signal than it does to the background.

The strategy of the signal region split is discussed in the double hadronic channel in Table 7.1. With two τ leptons decaying in one of five possible modes, 15 combinations can be formed. However,

not every single decay-mode combination is worth a standalone region. On the one hand, numerous narrow decay-mode dependent regions artificially add to the complexity of the setup and on the other hand sensitivity can only be maximized if statistical uncertainties remain moderate. Consequently, a compromise between statistics and low contribution of π^0s needs to be found. The MC relative yield per decay-mode combination in the VBF category is indicated in Table 7.1. A total of eight regions are proposed. The grouping prioritizes regions with few π^0 contributions before statistics and still ensures a reasonable total count of regions in order to provide good fit stability. Decay-mode pairs of high purity are for example 1p0n_1p0n or 3p0n_3p0n, which represent a low-statistic subset of data that amounts to less than 5% of the full dataset. The highest occurrence are 1p1n events, which get a standalone region assigned.

The di-tau mass distributions in the newly defined SRs are investigated in Figure 7.10. In the following discussion, focus is set on the fake background contamination, the available statistics as well as the background modelling achieved with the new decay-mode dependent fake reconstruction. As indicated by Table 7.1, the available statistics varies across the different decay-mode groupings. Especially, the regions of low-background contamination as 3p0n_3p0n are characterized by low statistics. While this is not an issue at pre-selection level, statistical uncertainties might rise significantly when splitting the phase-space further to target different STXS-bins. Because of the nearly negligible fake contribution in regions like 3p0n_3p0n, a looser τ-ID working point might be feasible and might also mitigate the issue of low statistics.

Through all regions, data/MC agreement is largely achieved within the uncertainties. The only exceptions with shortcomings in the normalization occur in decay-mode groupings where many neutral products are involved in the decay. Such regions are the groups 1pXn_1p, 3pXn_1p and 3pXn_3p, depicted in the sub-figures 7.10(d), 7.10(f) and 7.10(h), respectively. The mis-modelling can be caused by the decreasing decay-mode reconstruction efficiencies for decay-modes containing more than one π^0, as visualized in Figure 4.5. Consequently, an increased fraction of events is scaled by the wrong Fake Factors. This effect can be accounted for by determining τ decay-mode efficiency correction factors as nuisance parameters in the fit.

7.3.5 Decay-Mode Efficiency Correction Factors

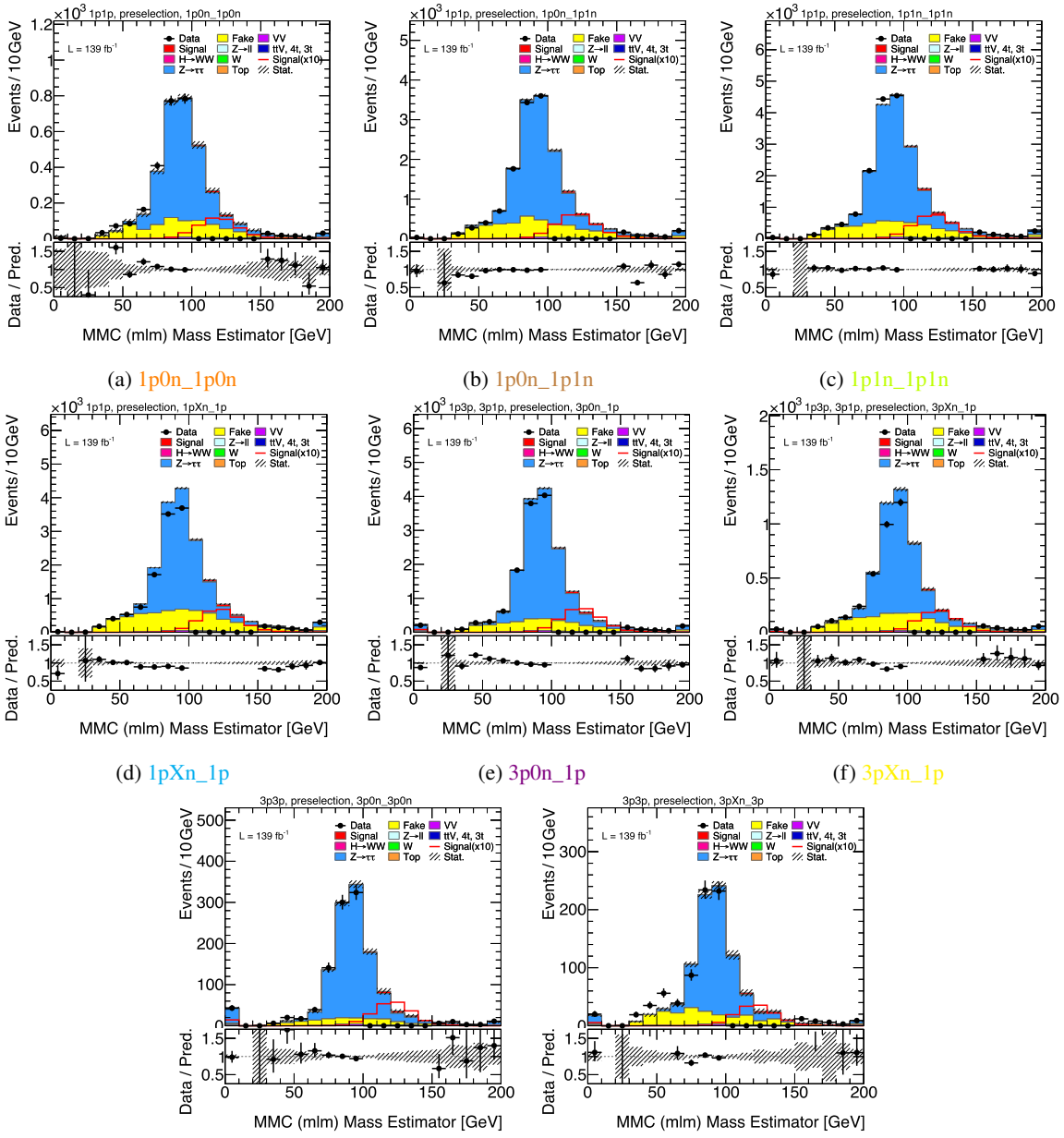
A suitable observable for the decay-mode dependent efficiency correction factor measurement is found in the visible τ mass $m(\tau_{\text{had-vis}})$, which is determined from the reconstructed four-momenta of charged (subscript c) and neutral (subscript n) τ decay products.

$$m(\tau_{\text{had-vis,0}}) = \sqrt{(E_{0,c} + E_{0,n})^2 - (Px_{0,c} + Px_{0,n})^2 - (Py_{0,c} + Py_{0,n})^2 - (Pz_{0,c} + Pz_{0,n})^2} \quad (7.16)$$

Depending on the τ decay-mode, events populate different $m(\tau_{\text{had-vis}})$ ranges, as illustrated in Figure 7.11, which shows the visible τ mass of the leading τ lepton of the $Z \rightarrow \tau\tau$ process.

The 1p0n peak is located at the invariant mass of the neutral pion $m_{\pi^0} = 135\,\text{MeV}$ [12]. As explained in Section 2.3.1, 1p1n events peak at a mass close to the ρ resonance at $m_\rho = 775\,\text{MeV}$ [12] and 3p0n events have their maximum close to the a_1 resonance at $m_{a_1} = 1\,250\,\text{MeV}$ [34]. 1-prong systems tend to peak at lower $m(\tau_{\text{had-vis}})$, whereas 3-prong systems are shifted to higher values. The distinct decay-mode dependent peaks favor an extraction of the correction factor estimation in the fit.

In order to introduce the measurement to the fit setup, another control region is required. The CR is



(a) 1p0n_1p0n (b) 1p0n_1p1n (c) 1p1n_1p1n

(d) 1pXn_1p (e) 3p0n_1p (f) 3pXn_1p

(g) 3p0n_3p0n (h) 3pXn_3p

Figure 7.10: Di-tau mass distributions of the VBF category in the decay-mode grouping defined in Table 7.1. The decay-mode considered per sub-figure can be extracted from Table 7.1 by following the color code of the sub-captions. The fake estimation is based on the decay-mode dependent Fake Factors shown in Figure 7.8.

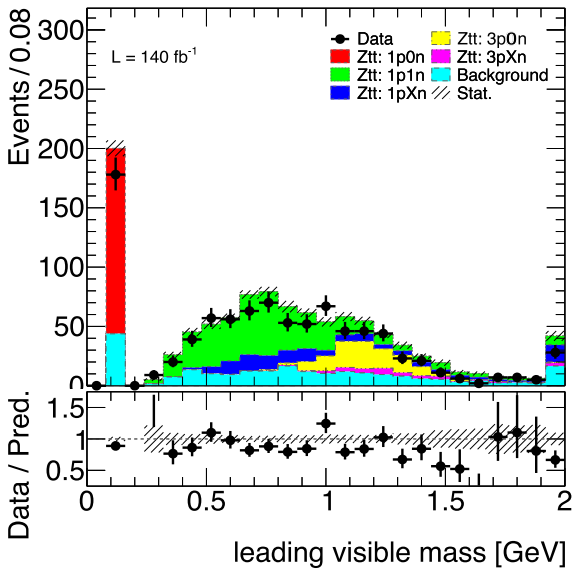


Figure 7.11: Leading visible τ mass of the $Z \rightarrow \tau\tau$ process. Contributions per decay-mode are separately shown. All remaining processes are marked as background. The decay-mode contributions are visualized by different colors. The illustrated phase-space corresponds to the tau_m_vis_CR introduced in Table 7.2.

based on the VBF baseline cuts (Table 6.2 and 6.3) in the $\tau_{\text{had}}\tau_{\text{had}}$ channel [1].

The CR exploits the sub-leading jet p_T window from 30 GeV$< p_T(j_1) <$ 40 GeV as well as a di-tau mass cut on the Z - peak, 60 GeV$<$ MMC(mlm)$<$ 95 GeV, to avoid cutting the signal. For a selection orthogonal to the VBF region, which originally included events with 30 GeV$> p_T(j_1)$, the VBF cuts need to be adapted. The p_T threshold is shifted to $p_T(j_1) >$ 40 GeV or in cases where $p_T(j_1) <$ 40 GeV, the condition MMC(mlm) >95 GeV is applied. A loss in signal events is monitored by a comparison between the original VBF definition, see Figure 7.17(a), and the newly defined region, see Figure 7.12(b). In the new setting, statistics is not significantly reduced so that shape information is still maintained. The signal yield decreases from 322.1 to 319.2, so that only 3 signal events are lost to the CR, which corresponds to less than 1%.

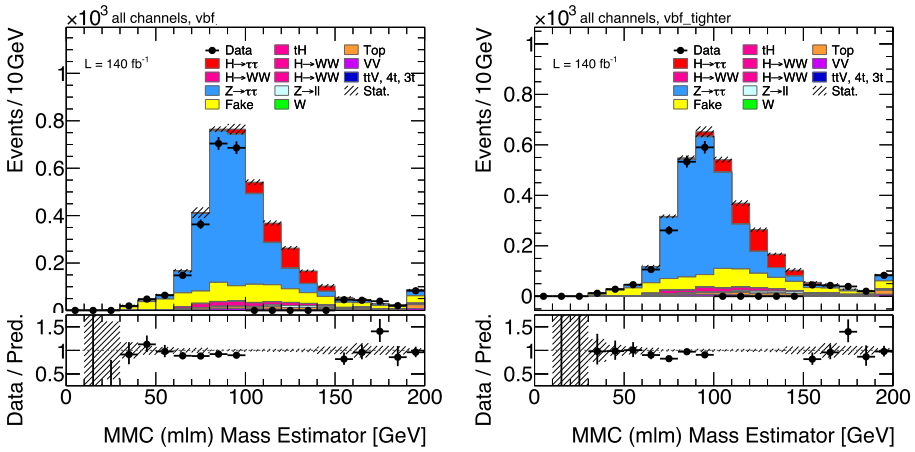
The lower di-τ mass tail MMC(mlm) $<$ 60 GeV in combination with the sub-leading jet p_T requirement $pT(j_1) <$ 40 GeV is reserved for a validation region. This region can be used to probe the method in another fake enriched phase-space. The newly defined cuts are summarized in Table 7.2.

7.3.6 Systematic Uncertainties

In Section 7.2.2, sources of fake related uncertainties in the $\tau_{\text{had}}\tau_{\text{had}}$ channel were discussed and need to be re-evaluated in the decay-mode dependent fake estimation.

Statistical Limitations Due to the decay-mode dependent phase-space cut, statistics was further reduced in the W + jets CR and thus increases the statistical uncertainties on the Fake Factors.

[1] The $\tau_{\text{had}}\tau_{\text{had}}$ channel is used as starting point since the corresponding NTuples are the only ones with the τ sub-structure information included. The charged and neutral four-momenta of the τ decay-products are needed to determine $m(\tau_{\text{had-vis}})$ used for the CR definition.



(a) common VBF SR, signal yield: 322.1 (b) new VBF SR, signal yield: 319.2

Figure 7.12: Di-tau mass distribution for common and newly defined VBF pre-selection with focus on the signal yield. The selection cuts are defined in Table 6.2 and 7.2, respectively.

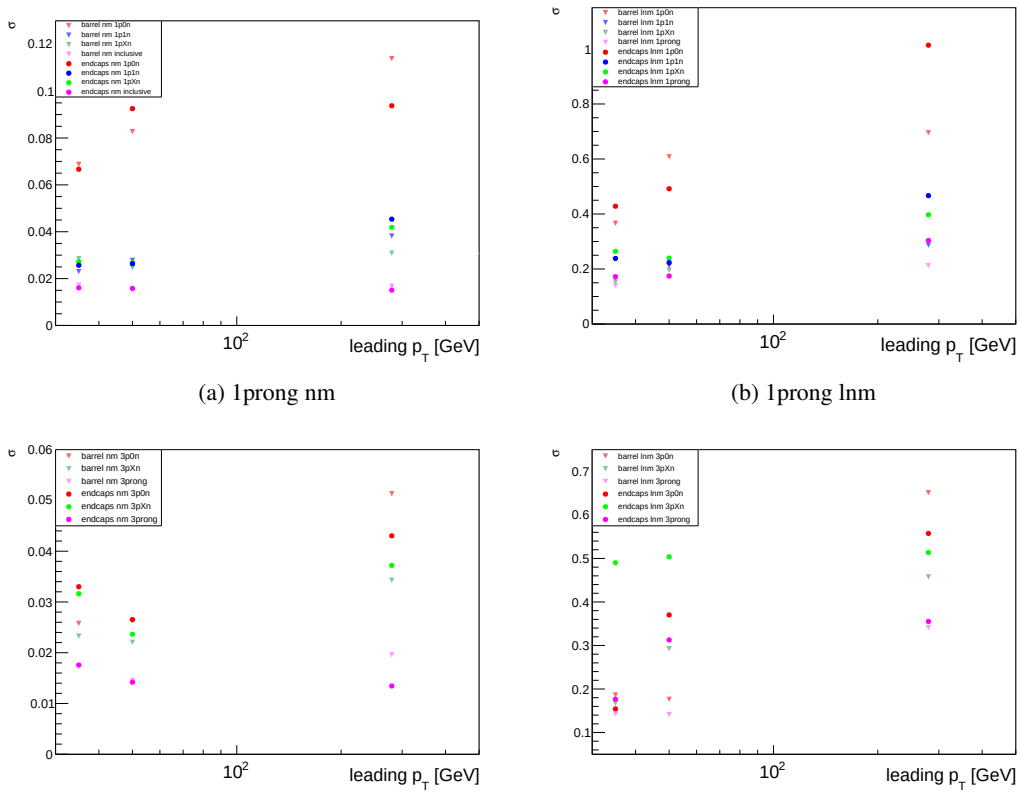
region	general	additionally
tau_m_vis_CR	pre-selection	30 GeV< $pT(j_1)$ <40 GeV & 60 GeV< MMC(mlm)<95 GeV
tau_m_vis_VAL	pre-selection	$pT(j_1)$ < 40 GeV & MMC(mlm)<60 GeV
vbf_new	VBF	$pT(j_1)$ > 40 GeV or ($pT(j_1)$ < 40 GeV & MMC(mlm) >95 GeV)

Table 7.2: Selection cuts for the introduction of a decay-mode dependent efficiency correction factor measurement in the fit. A control, as well as a validation region are newly introduced. In addition, the VBF pre-selection cuts are adapted.

Figure 7.13 compares the inclusive 3-prong and 1-prong statistical Fake Factor uncertainties to the decay-mode related statistical uncertainties. In distinct cases, an increase of $\sim 300\%$ is observed as for example the 1p0n end-caps lnm uncertainty in comparison to the 1-prong end-cap lnm uncertainty in the high p_T bin.

Parametrization The decay-mode dependent fake estimation strategy features improved background modelling due to more detailed reconstruction. This effect can be tested by estimating the parametrization uncertainty following the strategy of Section 7.2.2. For this purpose, a separate decay-mode dependent set of Fake Factors needs to be determined in the fake-enriched same-sign CR. Applying these Fake Factors to the same-sign anti-ID region provides insight into closure. The resulting data/mc ratio is used as a weight in the determination of the parametrization uncertainty.

Background Composition The uncertainty associated with the background composition also needs to be re-evaluated for the decay-mode dependent approach. Therefore, Fake Factors need to be additionally determined in the third fake enriched CR, the high $\Delta\eta$ region.



(a) 1prong nm

(b) 1prong lnm

(c) 3prong nm

(d) 3prong lnm

Figure 7.13: Comparison of 1σ statistical uncertainties on Fake Factors due to limited sample size in W + jets CR. The uncertainties on the decay-mode dependent Fake Factors are shown together with the inclusive 1-prong and 3-prong Fake Factors.

.

7.3.7 Outlook

In-depth studies have been successfully conducted to collect the necessary expertise for a decay-mode dependent fake estimation in future $H \rightarrow \tau\tau$ analysis. In order to facilitate future work, open points of research as well as interesting aspects of study are outlined in this section.

Signal Region Split: The signal region split needs to be validated and adapted in fit studies where the interplay of fit stability, statistical uncertainties and signal purity can be assessed. Furthermore, the gain of loosened τ−ID working points can be investigated.

Decay-Mode Efficiency Correction Factors: The concepts and ideas for decay-mode efficiency correction factor measurements in the fit setup have been prepared but need to be validated and fine-tuned in the fit setup.

Systematic Uncertainties: The Fake Factor Calculation in the W + jets region is limited to the $\mu\tau_{\text{had}}$ channel and can be extended to the $e\tau_{\text{had}}$ channel to improve the available statistics. Other sources of uncertainty like the parametrization or background composition uncertainty need to be determined in future studies in order to assess the full potential of the decay-mode dependent fake estimation in the $H \rightarrow \tau\tau$ measurement.

7.4 Fake Template Combination

In the STXS analysis, signal strength measurements across several kinematic regions are performed to achieve a detailed understanding of the VBF phase-space. As outlined in Section 6.7, cuts are applied to define four different di-jet mass intervals, a low and a high p_T^H region as well as a VBF 0 and VBF 1 category. These splits introduce a higher uncertainty to the shape of individual fake templates. The decrease in precision, however, is not entirely justified since the kinematics of these groups are well established. Concepts and strategies of combined fake templates were developed to counteract the increase in uncertainty introduced by the cuts. The impact on the fit including the discussion of sensitivity and nuisance parameters is elaborated on in Chapter 8.

7.4.1 Combination Strategy

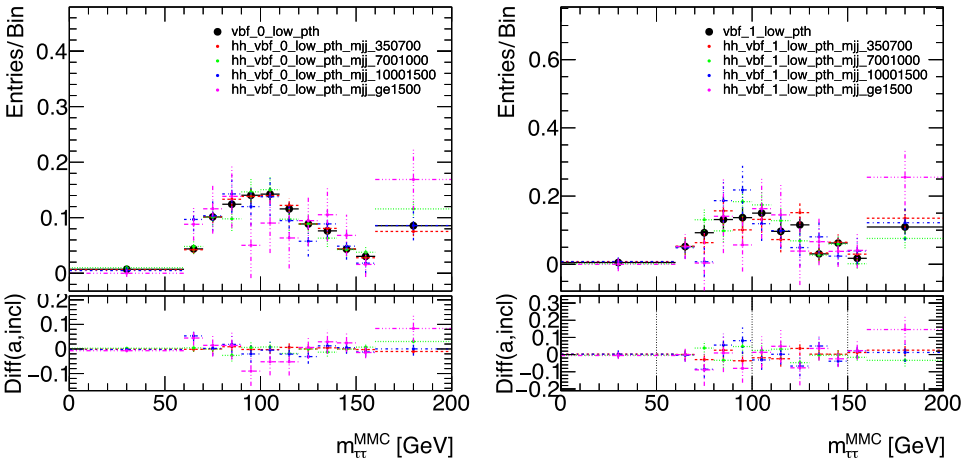
Fake templates can be combined across regions if their kinematic distributions follow the same shape. Different shapes are expected for low and high p_T^H events since the kinematic properties of the Higgs boson directly influence its decay products - the τ leptons. Consequently, a correlation between the Higgs momentum and the fake template shape is expected.

Building on these thoughts, a grouping is determined through a visual assessment of the kinematic distributions, which results in four units in the $\tau_{\text{had}}\tau_{\text{had}}$ channel, as illustrated in Figure 7.14.

Four groups, differentiating between low and high p_T^H as well as low and high VBF purity (VBF 0 and VBF 1) are found. Each plot shows events across the four di-jet mass intervals as well as the kinematic distribution of the combined template of all m_{jj} intervals within one group. All histograms are normalized to unity. Within each plot, the fake template shapes are compatible with the combined inclusive version.

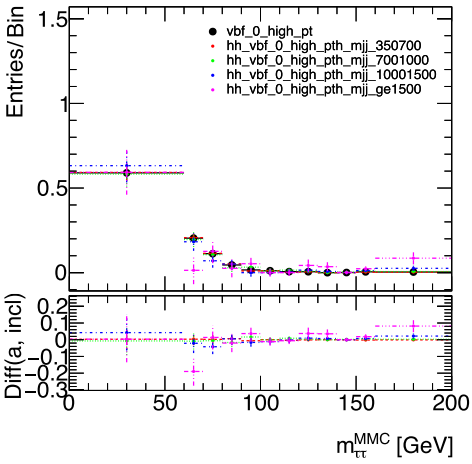
An analogous comparison was performed in the $\tau_{\text{lep}}\tau_{\text{had}}$ and $\tau_{\text{lep}}\tau_{\text{lep}}$ channel, presented in Figure 7.15 and 7.16, respectively. In the $\tau_{\text{lep}}\tau_{\text{lep}}$ channel, the same grouping is found as in the $\tau_{\text{had}}\tau_{\text{had}}$ channel (four combinations: vbf_0_low_pth, vbf_1_low_pth, vbf_0_high_pth and vbf_1_high_pth). The $\tau_{\text{lep}}\tau_{\text{had}}$ channel additionally combines VBF 0 and VBF 1, resulting in two groups vbf_low_pth and vbf_high_pth.

To validate the compatibility of the combined normalized distribution to the individual distributions, a χ^2-test was performed, where each bin corresponds to one degree of freedom. The test is based on the implemented CERN ROOT function [142], with χ^2/ndf-values close to 1 indicating a good agreement. The χ^2-test has shortcomings when dealing with histograms of low statistics and is also sensitive to the chosen binning. A Kolmogorov-Smirnov test is not taken into account since it is designed to process unbinned data. Table 7.3 provides an overview of the selected combinations and test results. The tests are performed between the fake templates of the individual sub-templates and the combined template. The data is found to be compatible within the chosen combinations, which justifies the tested combination strategy.

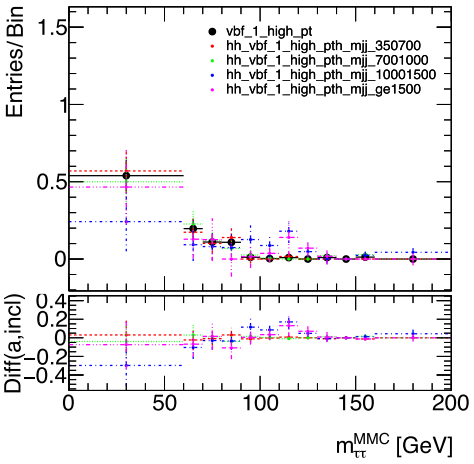


(a) vbf_0_low_pth

(b) vbf_1_low_pth

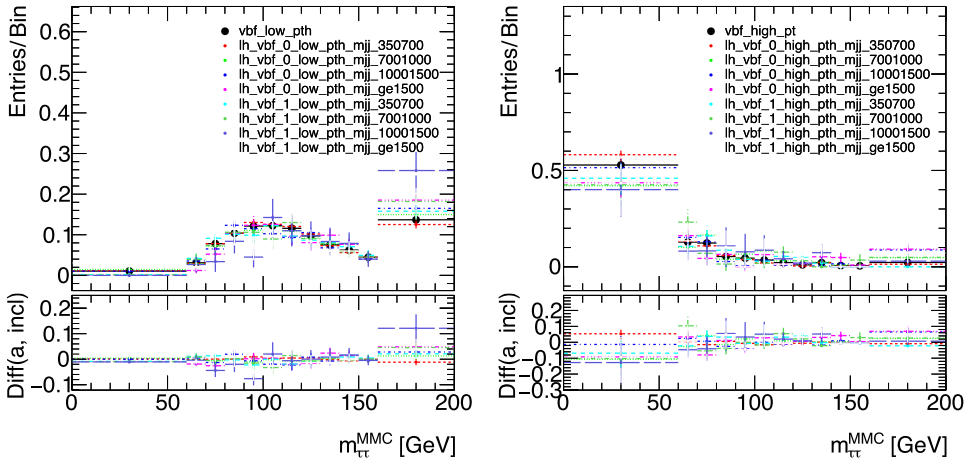


(c) vbf_0_high_pth



(d) vbf_1_high_pth

Figure 7.14: Fake templates of the $\tau_{\text{had}}\tau_{\text{had}}$ channel. Four groups, differentiating low and high p_T^H in the top and bottom row as well as low and high VBF purity (VBF 0 and VBF 1) in the left and right column, are shown. Each plot shows events of the four di-jet mass intervals in color as well as the kinematic distribution of the combined events in black. All histograms are normalized to unity. In the bottom panel, the difference between the individual and the combined template is shown.

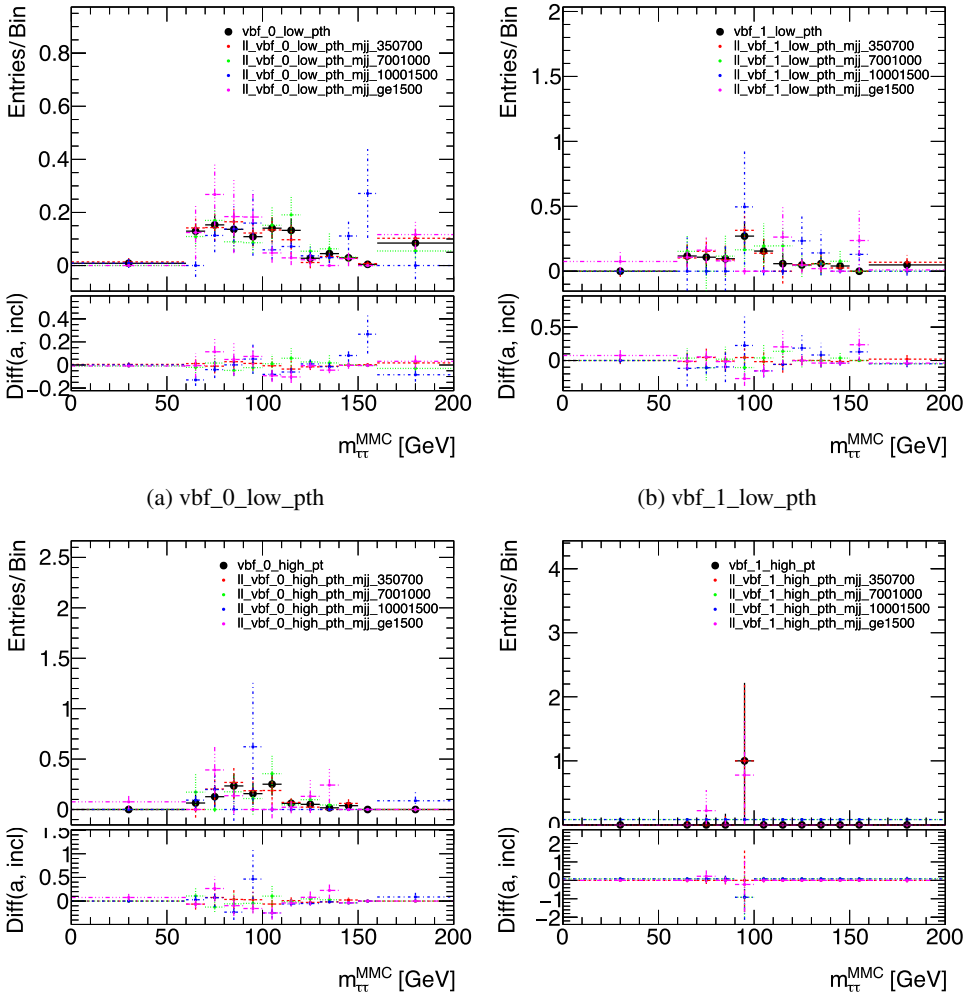


(a) vbf_low_pth (b) vbf_low_pth

Figure 7.15: Fake templates of the $\tau_{\text{lep}}\tau_{\text{had}}$ channel. Two groups, differentiating low and high p_T^H are shown in the left and right column, respectively. Each plot shows events of the four di-jet mass intervals per VBF region (VBF 0 and VBF 1) in color as well as the kinematic distribution of the combined events in black. All histograms are normalized to unity. In the bottom panel, the difference between the individual and the combined template is shown.

	Groups		χ^2/ndf		
region	hh & ll	lh	hh	lh	ll
vbf_0_low_pth_mjj_350700	vbf_0_low_pth	vbf_low_pth	0.14	0.93	0.12
vbf_0_low_pth_mjj_7001000			0.55	1.58	0.42
vbf_0_low_pth_mjj_10001500			0.78	1.62	1.54
vbf_0_low_pth_mjj_ge1500			0.98	1.83	1.17
vbf_1_low_pth_mjj_350700	vbf_1_low_pth		0.31	3.27	0.06
vbf_1_low_pth_mjj_7001000			0.63	2.48	0.25
vbf_1_low_pth_mjj_10001500			0.83	1.38	0.83
vbf_1_low_pth_mjj_ge1500			0.58	1.57	1.27
vbf_0_high_pth_mjj_350700	vbf_0_high_pth	vbf_high_pth	0.11	0.93	0.16
vbf_0_high_pth_mjj_7001000			0.23	1.58	0.43
vbf_0_high_pth_mjj_10001500			0.54	1.62	1.28
vbf_0_high_pth_mjj_ge1500			1.41	1.83	1.09
vbf_1_high_pth_mjj_350700	vbf_1_high_pth		0.45	3.27	-
vbf_1_high_pth_mjj_7001000			0.2	2.48	-
vbf_1_high_pth_mjj_10001500			1.21	1.38	-
vbf_1_high_pth_mjj_ge1500			0.6	1.57	-

Table 7.3: χ^2-compatibility test per combination group. Whereas in $\tau_{\text{had}}\tau_{\text{had}}$ and $\tau_{\text{lep}}\tau_{\text{lep}}$, four groups are formed, $\tau_{\text{lep}}\tau_{\text{had}}$ only takes two groups into account. The χ^2-test is performed between the fake templates of the individual regions and the combined template.



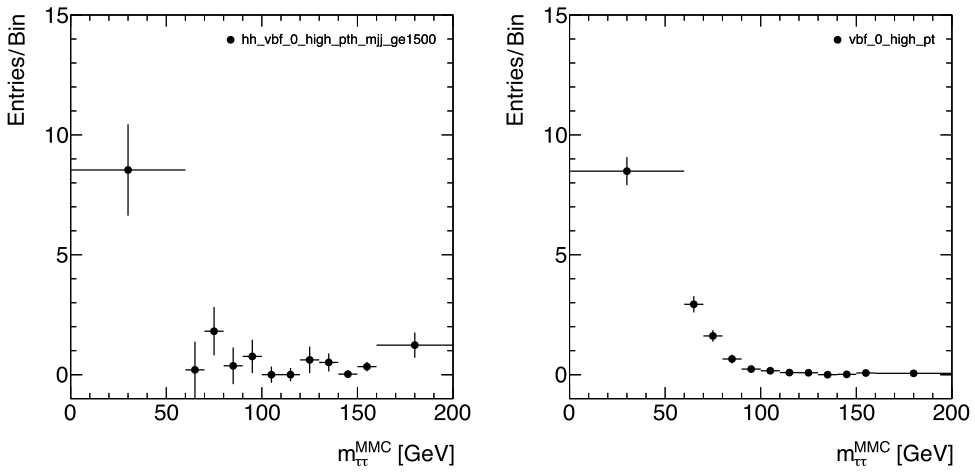
(a) vbf_0_low_pth

(b) vbf_1_low_pth

(c) vbf_0_high_pth

(d) vbf_1_high_pth

Figure 7.16: Fake templates of the $\tau_{\text{lep}}\tau_{\text{lep}}$ channel. Four groups, differentiating low and high p_T^H in the top and bottom row as well as low and high VBF purity (VBF 0 and VBF 1) in the left and right column are shown. Each plot shows events of the four di-jet mass intervals in color as well as the kinematic distribution of the combined events in black. All histograms are normalized to unity. In the bottom panel, the difference between the individual and the combined template is shown.



(a) original (b) replacement

Figure 7.17: Original fake template hh_vbf_0_high_pth_ge1500 in a) and its combined template b) as replacement.

In order to reduce the statistical uncertainty on the shape, each individual fake template is replaced by the combined template of its respective group, scaled to the corresponding yield. The original template of the hh_vbf_0_high_pth_ge1500 region is exemplified in Figure 7.17(a). The associated combined template with identical yield is shown in 7.17(b). The combined template exhibits a smoother, well-defined shape as well as small uncertainties within the individual bins.

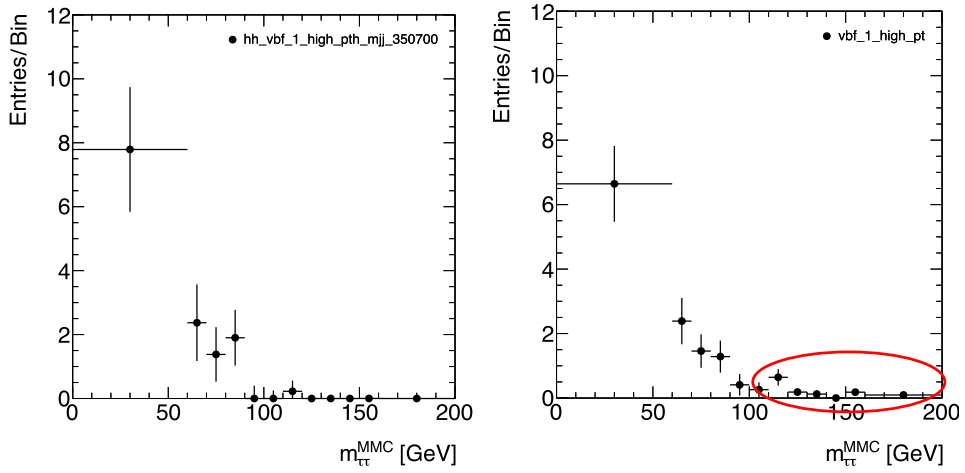
The combined template exclusively incorporates fake templates from high-statistics m_{jj} regions of 300–700 GeV and 700–1 000 GeV. Low-statistics regions (1 000–1 500 GeV and >1 500 GeV) exhibit outliers that alter the shape. The impact of these low-statistics regions on the combined $m_{\tau\tau}$ shape is illustrated in Figure 7.18. While the original fake template has very low fake contribution in $m_{\tau\tau} > 100$ GeV, the combined template shows a non-negligible fake contribution in that phase-space region, where also the signal peak is located. This up-fluctuation has therefore negative impact on the sensitivity due to its adverse effect on the signal-to-background ratio. Consequently, the combined fake template is only determined from templates with high statistics. The resulting shape is then applied to all sub-templates of the group, including the low-statistics regions. This combination procedure was also applied in Figure 7.14, 7.15 and 7.16.

7.4.2 Systematic Uncertainties

The combination of templates introduces new sources of uncertainty. In addition, strategies need to be developed that describe the handling of other fake-related uncertainties.

Normalization Uncertainty

Normalization uncertainties are a newly introduced source of systematic uncertainty arising from the combination procedure. The combined template is scaled to match the yield of each individual sub-template. The uncertainty on the normalization factor is driven by the uncertainty on the yield



(a) original (b) replacement

Figure 7.18: Original fake template hh_vbf_1_high_pth_350700 in a) and its combined replacement scaled to the corresponding yield in b). For the combination, all four fake templates of the corresponding group were considered.

observable N. Since the events are weighted, a Poissonian uncertainty estimation $\sqrt{N}$ is not accurate. Instead, the uncertainty is estimated by considering bin errors Δo_i of the original template and normalizing the entire expression to the nominal yield.

$$\sigma_N = \frac{\sqrt{\sum(\Delta o_i)^2}}{\sum o_i} \tag{7.17}$$

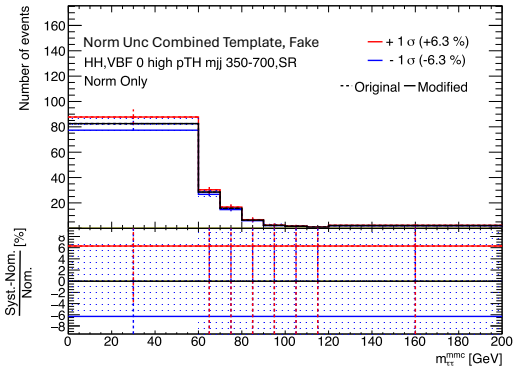
The factor covering the variation is global per given region and the relative uncertainty is the same for all bins.

The corresponding up- and down-variation in the vbf_0_high_pth group is shown in Figure 7.19. Conservative uncertainty estimates, with variations up to 20% of the nominal value, can get further constrained in the fit. The envelops of the remaining templates can be found in Figure C.6 through C.11. Missing envelops got pruned and are consequently not considered in the fit.

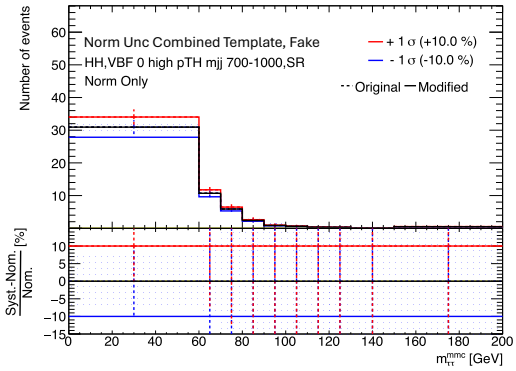
Fake-Related Uncertainties

Systematic uncertainties, such as those related to the Fake Factor Method, require the nominal template as a reference. For instance, the down-variation is determined as a mirrored version of the up-variation.

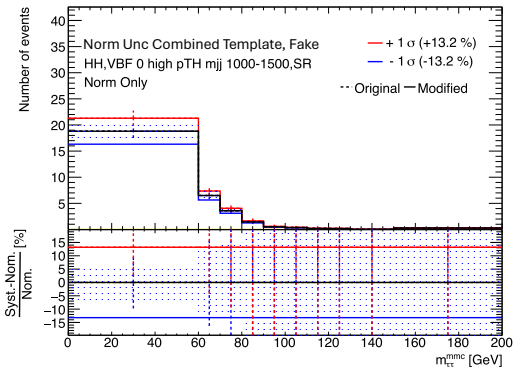
To maintain consistency, fake related uncertainties use the original template as reference instead of the combined template. Otherwise, it would be necessary to combine and re-determine the uncertainties. These fake-related uncertainties include those stemming from the Fake Factor Method itself, as discussed in Section 7.2.2, as well as other uncertainties affecting fake samples, such as τ or jet related uncertainties, which are determined with respect to the original nominal fake template.



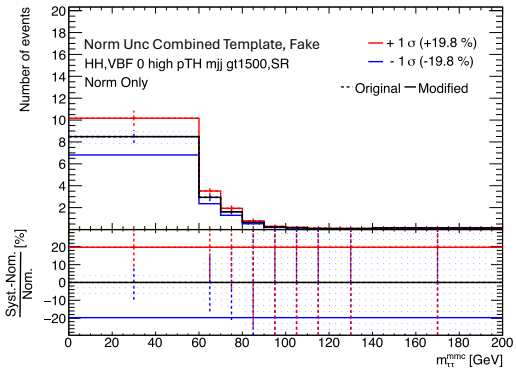
(a) 300 GeV< m_{jj} <700 GeV



(b) 700 GeV< m_{jj} <1 000 GeV



(c) 1 000 GeV< m_{jj} <1 500 GeV



(d) m_{jj} >1 500 GeV

Figure 7.19: Up- and down-variation of the Normalization Uncertainty in the vbf_0_high_pth group. The relative uncertainty estimate is constant across all bins as described in Equation 7.17.

CHAPTER 8

Fit Results

The highly complex Legacy fit setup features a multitude of correlated nuisance parameters and encompasses diverse regions that allow to control a wide range of physical processes. A comprehensive understanding of the interplay between these fit parameters is of fundamental importance for the following discussions, as their interaction can significantly impact the results. Therefore, scrutinizing studies are outlined, which build confidence in the outcome of the result. Many of these studies validate the setup and demonstrate its intentional design. An extensive understanding of the fit beyond the notion of a black box prevents bugs or inadequate modelling. The detailed examination of pulls and constraints of nuisance parameters is accompanied by the investigation of uncertainty envelops or correlations of parameters. The following sections aim to provide a fundamental understanding of the central aspects of the fit while focusing on studies at the heart of this thesis. The presented plots are based on a non-final version of the fit setup [1]. With respect to the final settings used for the publication, only small quantitative changes are expected while the qualitative statements made in this thesis remain valid.

8.1 Asimov Studies

Asimov data is used to conduct studies of the analysis setup. It is a set of pseudo-data designed such that parameter estimators evaluated on this very data-set correspond to the true parameters of the underlying model. The model parameters used to generate the pseudo-data are the best-fit values of the profile-likelihood fit. Instead of using an ensemble of simulated toy-data sets, which would be computationally expensive, the Asimov data set is used in place of toy data and as a representative, which corresponds to the *average* of the ensemble [143]. The concept is motivated in the short story *Franchise* by Isaac Asimov [144], where a single most representative voter is selected to replace the entire electorate. Asimov data can be used to obtain unbiased insight into the expected sensitivity of the measurement and also helps to reveal shortcomings of the setup. In place of measurement data, Asimov data prohibits that the analysis design is unintentionally skewed towards desired results.

[1] The plots rely on input version v15 [121]. The luminosity update to 140 fb^{-1} is not yet considered.

8.1.1 Setting 18 Parameters of Interest

The analysis is designed to measure 18 STXS-bins. The expected sensitivity per targeted phase-space region is determined in Asimov studies and documented in Figure 8.1. The differences between the *combined* and *reference* setup are the topic of Section 8.1.2.

The six ggH related PoIs, the one VH measurement, the eight VBF related bins and the three $t\bar{t}H$ measurements are evaluated. All best fit values equal one by construction of the Asimov dataset. The 1σ uncertainty intervals per measured STXS bins are shown inclusively, as well as separately for statistical and systematic contributions. The latter distinction disentangles the individual impact to the measurements sensitivity. The statistic-only contribution is determined by fitting the data with all NPs fixed to their post-fit value without their individual uncertainties. The systematic contribution for a given systematic variation is calculated as follows

$$\Delta\text{sys}_{\text{down/up}} = \sqrt{\Delta\text{full}^2_{\text{down/up}} - \Delta\text{stat}^2_{\text{down/up}}}. \tag{8.1}$$

The expected sensitivity of the ggH and VH bins was investigated in the 2022 analysis and is not further optimized in the Legacy analysis. The focus of the Legacy analysis is placed on the VBF and $t\bar{t}H$ related PoIs. Despite the detailed split of the VBF phase-space to explore eight parameters of interest, reasonable sensitivity is achieved while providing an extensive insight in this very production mode. Sensitivity improves with increasing m_{jj} regions since the signal to background ratio improves. Large uncertainties in the order of 150-250% are measured in Asimov studies for the $t\bar{t}H$ STXS-bins. The fine subdivision of the $t\bar{t}H$ phase-space into three bins dilutes the informative value of the cross-section measurement. The aim of these three STXS-bins is to provide limits on the measurement. The specification of per-bin limits is interesting for the high p_T^H regions, which are especially sensitive to beyond the Standard Model physics.

Statistical uncertainties dominate the systematic uncertainties in most STXS bins. In the VBF measurements high m_{jj} bins are predominantly limited by statistics. Systematic uncertainties drive the result in case of ggH related measurements, which profit from their high production rate at the LHC. The contributions from systematic uncertainties are diverse. In order to get a more granular view, systematic uncertainties are assigned to groups according to their nature, such as introduced in Section 6.6.

The share of a given systematic uncertainty group with respect to the total uncertainty is summarized in grouped impact tables. The total uncertainty on a PoI is described by the 1σ uncertainty interval $\Delta\mu$. To determine the impact of a certain NP group, the given group is removed from the fit and a new uncertainty on the PoI $\Delta\mu'$ is determined. The impact is defined as

$$\text{impact} = \sqrt{(\Delta\mu)^2 - (\Delta\mu')^2}.$$

The summed square of all contributions might differ from the total uncertainty due to correlations. The grouped impact tables of the eight VBF related PoIs are shown in the *Combined* column of Table 8.1 and 8.2.

While the order of the low impact systematic uncertainties varies with the PoI, the driving systematics are the same across all measured bins. The dominant groups are signal theory nuisance parameters, statistical uncertainty on the simulated sample size and jet/MET systematic uncertainties. The latter can cause shape variations, which explains their large impact in the fit setup. Statistical uncertainties

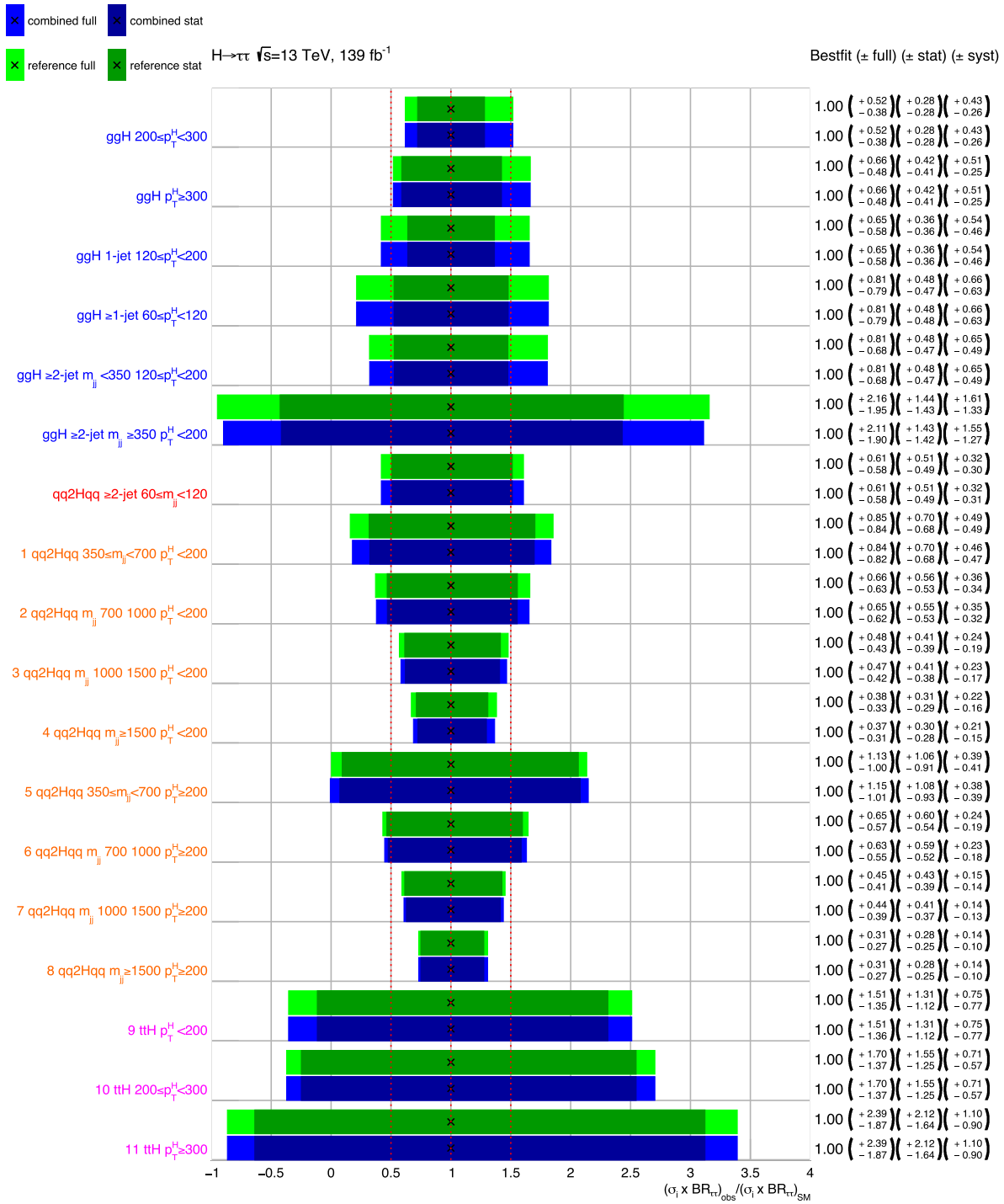


Figure 8.1: Expected sensitivity per measured STXS bin in Asimov studies. From top to bottom, the six ggH related PoIs are marked in blue, the one VH bin in red, the eight VBF related measurements in orange and the three $t\bar{t}H$ bins are labeled in pink. The best fit value is represented by a black cross, the coloured bars indicate 1σ uncertainty intervals. The full uncertainty is depicted in bright color whereas the statistic only contribution is depicted in muted colors. The *combined* setup, shown in blue, is based on combined fake templates. The *reference* setup, shown in green, uses the original fake templates.

POI	mjj_350700_ptH_0_200		mjj_7001000_ptH_0_200		mjj_10001500_ptH_0_200		mjj_ge1500_ptH_0_200	
Fake Template	Reference	Combined	Reference	Combined	Reference	Combined	Reference	Combined
Full Syst	0.535	0.513	0.388	0.377	0.241	0.224	0.209	0.194
Gammas	0.376	0.335	0.263	0.240	0.153	0.116	0.108	0.079
SigTheory	0.191	0.191	0.141	0.140	0.121	0.120	0.140	0.141
JETMET	0.147	0.148	0.117	0.115	0.067	0.069	0.042	0.040
TopTheory	0.086	0.081	0.029	0.029	0.012	0.01	0.013	0.015
Lepton	0.086	0.078	0.052	0.049	0.024	0.022	0.024	0.020
Tau	0.079	0.071	0.060	0.057	0.028	0.028	0.024	0.022
Fake	0.06	0.105	0.051	0.087	0.017	0.056	0.022	0.044
ZttTheory	0.042	0.041	0.023	0.022	0.014	0.013	0.015	0.014
BTag	0.031	0.031	0.015	0.014	0.006	0.007	0.014	0.0119
Lumi	0.017	0.017	0.015	0.015	0.017	0.017	0.016	0.016

Table 8.1: Grouped impact for low p_T^H VBF related PoIs in an original (reference) setting as well as in a fit based on combined fake templates. The selected color scheme in the reference column follows a heat map, where orange indicates a large impact and cyan a small impact. The color gradient from cyan to orange represents values in the range from 0 to 0.2. Values above the threshold are also depicted in orange.

POI	mjj_350700_ptH_gt200		mjj_7001000_ptH_gt200		mjj_10001500_ptH_gt200		mjj_ge1500_ptH_gt200	
Fake Template	Reference	Combined	Reference	Combined	Reference	Combined	Reference	Combined
Full Syst	0.448	0.437	0.239	0.228	0.163	0.153	0.128	0.125
Gammas	0.307	0.287	0.136	0.121	0.093	0.076	0.048	0.042
SigTheory	0.236	0.232	0.155	0.154	0.109	0.115	0.103	0.099
JETMET	0.124	0.124	0.052	0.051	0.035	0.033	0.021	0.022
TopTheory	0.024	0.03	0.021	0.031	0.009	0.009	0.009	0.009
Lepton	0.020	0.018	0.025	0.012	0.01	0.010	0.009	0.009
Tau	0.050	0.049	0.018	0.018	0.014	0.015	0.015	0.016
Fake	0.023	0.044	0.014	0.025	0.007	0.020	0.006	0.014
ZttTheory	0.026	0.026	0.014	0.013	0.01	0.006	0.007	0.006
BTag	0.014	0.005	0.017	0.017	0.005	0.005	0.004	0.004
Lumi	0.019	0.032	0.019	0.019	0.018	0.018	0.018	0.018

Table 8.2: Grouped impact for high p_T^H VBF related PoIs in an original setting as well as in a fit based on combined fake templates. The selected color scheme in the reference column follows a heat map, where orange indicates a large impact and cyan a small impact. The color gradient from cyan to orange represents values in the range from 0 to 0.2. Values above the threshold are also depicted in orange.

cannot be easily mitigated since immense computational resources are required to increase the number of simulated events in the required phase-space region.

8.1.2 Combined Fake Templates

The role of the combined fake templates, previously introduced in Section 7.3, in the analysis setting is addressed in this Section. Fit results of a reference run using the original fake templates are compared with results from combined fake templates along with the introduction of normalization uncertainties.

The sensitivities determined with Asimov data are compared in Figure 8.1 for both setups, using the combined and the original fake templates, respectively. Marginal improved sensitivity is observed in the fit based on combined templates in all VBF related STXS bins except the VBF related PoI with $350\,\text{GeV} < m_{jj} < 700\,\text{GeV}$, $p_T^H > 200\,\text{GeV}$. For this PoI, the fit based on the conventional fake template performs marginally better. Improved performance of the fit based on the combined templates in the VBF regions is also observed in the ggH ≥ 2 jet, $m_{jj} \geq 350\,\text{GeV}$, $p_T^H < 200\,\text{GeV}$ PoI, although the fake templates of the boost category are not adapted.

In the context of precision measurements, improvements in the per mille level, as those caused by the combined fake templates, are noteworthy progress. The one exceptional VBF PoI does not diminish the previous statement. The performance difference of the compared templates in the order of 1% can originate from a difference in the two sets of Asimov data, which were separately generated. A noticeable performance difference is observed in the aforementioned ggH related PoI, which has a non-negligible contribution in the VBF-like SR as discussed in Figure 6.8. Following this correlation, the benefits of the combined templates propagate to the ggH related PoI.

The influence of the two settings is quantified in the grouped impact Tables 8.1 and 8.2. In comparison, the impact of Gammas, as one of the leading systematic contributions, decreases in the combined setting. The remaining groups show compatible impact across the two setups despite the Fake uncertainties. The impact of the setup based on combined fake templates increases due to the introduction of normalization uncertainties. They add to the Fake uncertainty group and are not included in the original setup. The full uncertainties are, however, still smaller in the combined fake template setting due to the larger impact of the Gammas.

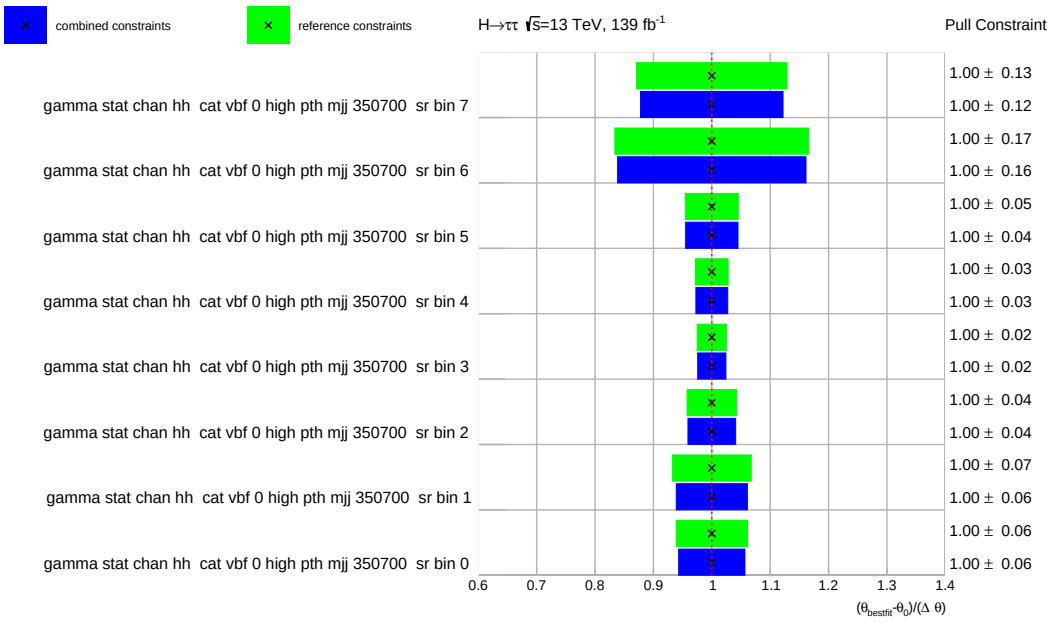
In conclusion, the combined template positively impacts the sensitivity of the measurements as well as the stability of the fit setup. Consequently, the combination strategy is implemented in the final Legacy analysis setup.

Statistcal MC Uncertainties: Gammas

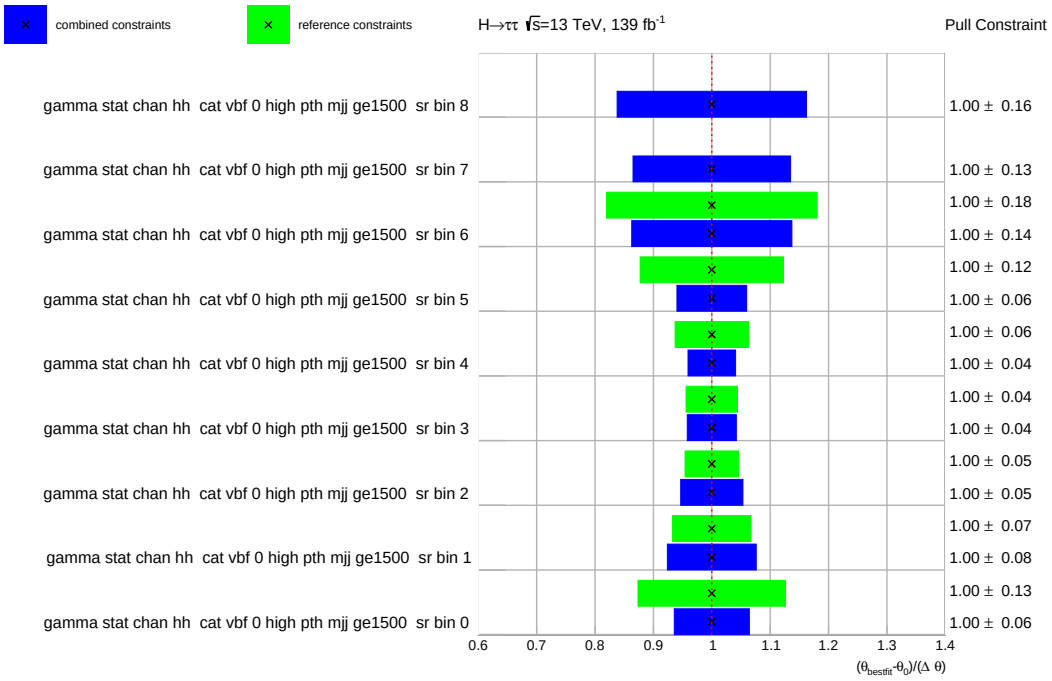
The statistical MC uncertainties are determined for each individual bin of the di-tau mass histograms that enter the fit. The concept of combining fake templates across regions aims to reduce this source of uncertainty, as elaborated on in Section 7.4. Previous studies have shown a positive effect of the template combination strategy on the STXS-bin wide impact. In this Section, the individual Gamma contributions in the fit are investigated.

In order to confirm the effectiveness of the combination approach, individual Gamma uncertainties are compared between the original and the combined fake template settings.

Figure 8.2 shows the bin-wise Gamma contribution in the lowest 8.2(a) and highest 8.2(b) m_{jj} regions of the VBF 0, high p_T^H category. The automated binning algorithm, introduced in Section 8, is applied in all setups. Furthermore, Asimov data was generated separately. These two aspects can

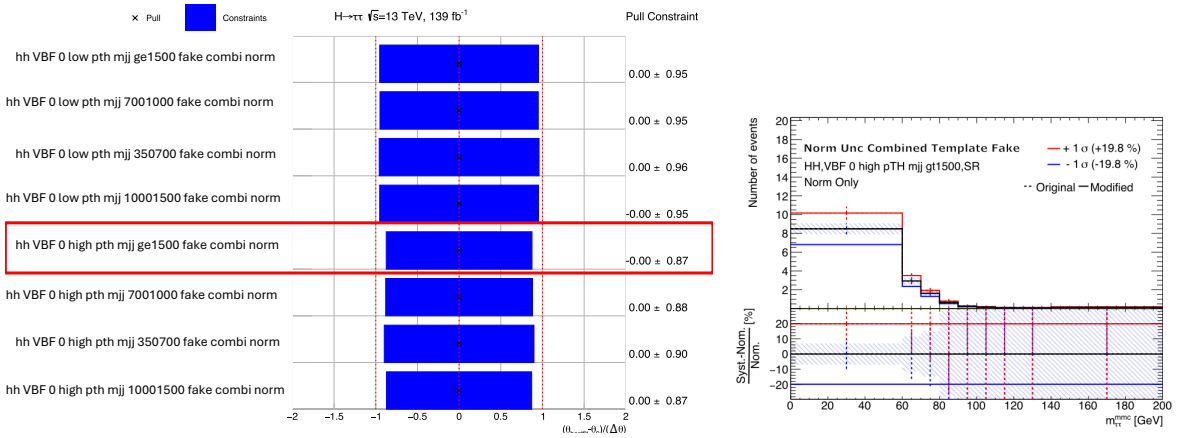


(a) $350\,\text{GeV} < m_{jj} < 700\,\text{GeV}$



(b) $m_{jj} \geq 1\,500\,\text{GeV}$

Figure 8.2: Comparison of statistical uncertainties on the MC prediction per histogram bin for setups based on the original (reference) and the combined fake templates depicted in green and blue, respectively. The lowest and the highest m_{jj} region of the VBF 0, high p_T^H phase-space are discussed.



(a) Constraints

(b) Envelop of high p_T^H $m_{jj} \geq 1\,500\,\text{GeV}$

Figure 8.3: Constraints on the normalization uncertainties in the $\tau_{\text{had}}\tau_{\text{had}}$ VBF 0 regions are shown in a). The red rectangle highlights the normalization uncertainty whose envelop is depicted in b).

cause different behavior in the fit, which is why a quantitative comparison needs careful consideration. Two qualitative statements can be reliably made:

- The uncertainty per bin predominantly decreases for the setup using combined templates or remains unchanged with respect to the original setup. This is shown by Figure 8.2(a), which represents the low m_{jj} region from 350 GeV to 700 GeV in the VBF 0, high p_T^H phase-space.

- In other cases, the combined fake templates allow an increased binning granularity per histogram, which intensifies physical effects in the shape of the distributions. Such a case is exemplified in Figure 8.2(b), representing the highest m_{jj} region of the VBF 0, high p_T^H phase-space. The increase of bins is facilitated by the binning algorithm, which splits the bins depending on the available statistics. As expected, regions of low statistics, as $m_{jj} \geq 1\,500\,\text{GeV}$ profit from the combined templates.

Normalization Uncertainties

The normalization uncertainties, introduced in Section 7.4.2, are included to compensate for uncertainties on the total yield in a given region. Figure 8.3(a), shows $\tau_{\text{had}}\tau_{\text{had}}$ VBF 0 related uncertainties and demonstrates that the fit can tighten the initially assumed constraint in the high p_T^H phase-space. This gain in knowledge compared to the prior assumption can be provided by data or through correlations between NPs. For example, the uncertainty envelop of the most pronounced constraint of the $m_{jj} \geq 1\,500\,\text{GeV}$ region is depicted in Figure 8.3(b). The statistical uncertainty in the first bin is smaller than the primarily assumed normalization uncertainty, which narrows in on the corresponding constraint. The normalization uncertainties in the $\tau_{\text{lep}}\tau_{\text{had}}$ and $\tau_{\text{lep}}\tau_{\text{lep}}$ channel behave similarly under Asimov data and are documented in Figure C.12. The corresponding envelops are shown in Figure C.6 through C.11 . In summary, the normalization uncertainties are expected to cover the fluctuations in yield appropriately.

8.2 Partially Unblinded Fits

Asimov data is a powerful tool for detailed cross checks during the development of the analysis setup. Once a robust configuration is found, partially unblinded techniques are used as another validation step of the setup. Other than the artificial Asimov dataset, partially unblinded setups rely on measurement data but with diluted signal contribution, so that the analysis design cannot be manipulated towards desired outcomes. By these means, pulls or the background modelling can be investigated. PoIs or their correlations with other parameters cannot be studied in this stage. In the partially unblinded phase, two analysis strategies are applied in analogy to the 2022 analysis: the random scaling setup as well as sideband fits [2]. Due to the focus on personal contributions, random scaling fits will be elaborated on, other than sideband fits. The studies of this Section are based on 4PoI fits, which measures the four dominant Higgs production modes, like introduced in Section 6.7.2.

8.2.1 Random Scaling

The random scaling approach hides the true signal values by applying a random scaling factor μ to the MC signal samples. The scaling factor is drawn in an adequate range, which was determined in the 2022 analysis [135], by using a gaussian distribution of mean 1.5 and width 0.3. In that way the statistical properties and stability of the fit are maintained. Pulls and constraints of Normalization Factors and Nuisance Parameters can be studied in a random scaling setup since their fit results are expected to align with those of a fully unblinded setup. In this approach, it is not forseen to look into pre- and post-fit plots, which could provide hints on the random scaling factor μ.

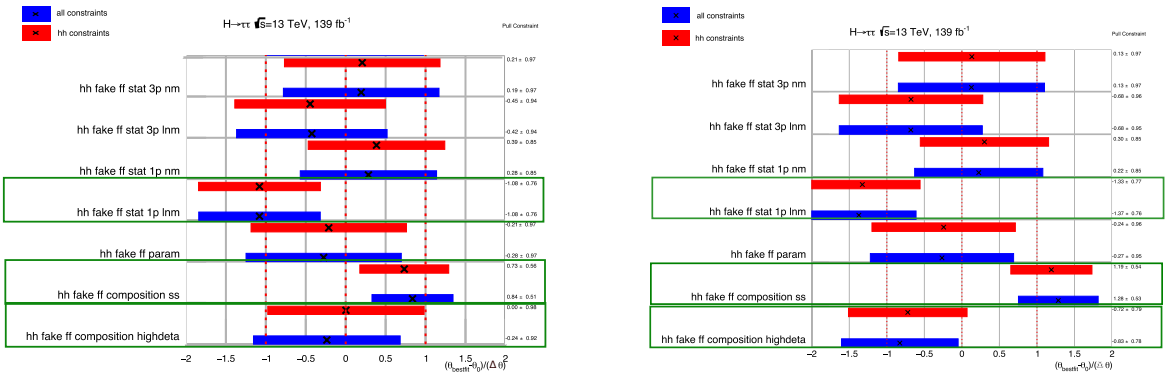
Fake Systematic Studies in the $\tau_{\text{had}}\tau_{\text{had}}$ Channel

With the introduction of partially unblinded data, parameter pulls can be investigated. Since the discussion of all 352 systematic uncertainties exceeds the scope of a thesis, a case study specific to the fake-related nuisance parameters is conducted. The discussion provides insight into key aspects that are necessary for the interpretation of fit results. The highlighted aspects of this case study form the corner stones for most tests relevant for the validation of the fit setup.

The presented study focuses on $\tau_{\text{had}}\tau_{\text{had}}$ fake systematic uncertainties, introduced in Section 7.2.2. Their pulls and constraints in the random scaling fit are depicted in Figure 8.4(b) for the Legacy analysis. The corresponding results of an equivalent study in the 2022 analysis are depicted in 8.4(a). In both analyses, a standalone fit in the $\tau_{\text{had}}\tau_{\text{had}}$ phase-space as well as a combined fit using the full available phase-space are performed.

Observation: The standalone fit results are compatible with the combined fit over all channels. Pulls are distributed with adequate fluctuations around zero. In the Legacy analysis, two sources of uncertainty **hh fake ff stat 1p lnm**, and **hh fake ff composition ss** stand out with pulls of $\sim 1.7\sigma$ and $\sim 2\sigma$, respectively. While the direction of pull follows the trend of the 2022 analysis, noticeable differences occur in the absolute values. Although the central pull value is still covered by the

[2] In the sideband fit setup, signal enriched bins are excluded from the fit. In order to match signal-like properties, a bin must fulfill $110\,\text{GeV} < m_{\tau\tau} < 150\,\text{GeV}$ and $\frac{\#\text{ signal events}}{\#\text{ background events}} > 0.05$.



(a) 2022 Analysis.

(b) Legacy analysis

Figure 8.4: Pulls and constraints of $\tau_{\text{had}}\tau_{\text{had}}$ fake systematic uncertainties in 4PoI random scaling fits. The inclusive fit considering all channels is depicted in blue, the $\tau_{\text{had}}\tau_{\text{had}}$ standalone fit in red. Systematic uncertainties that are discussed in the text are highlighted by a green rectangle. Results of the 2022 analysis are shown [135] in a), which were produced with a non-final setup. Results of the Legacy analysis are depicted in b).

uncertainty interval of the 2022 analysis result, scrutinizing tests are performed to confirm the observed differences.

Correlations: An understanding of the interplay of nuisance parameters is accessible through correlation matrices. The correlations of the $\tau_{\text{had}}\tau_{\text{had}}$ fake systematic uncertainties are shown in Figure 8.5. The two uncertainties **hh fake ff composition ss** and **hh fake ff stat 1p lnm** are anti-correlated by $-30\,\%$, which relates to relative opposite pull directions. The **hh fake ff composition ss** nuisance parameter exhibits an even stronger correlation with other nuisance parameters. An example is its anti-correlation of $-44\,\%$ with **hh fake ff composition highdeta**. Even these strong correlations do not contradict the observed configuration of nuisance parameter pulls. A pull of **hh fake ff composition ss** towards positive values causes the other two exemplified uncertainties to shift in the opposite direction.

Phase-Space Restrictions: In a next step, an attempt is made to attribute the differences between the two analysis results to specific phase-space regions. For this purpose, four standalone random-scaling fits are performed, which only consider regions corresponding to one of the four targeted production modes: boost, VH, VBF or $t\bar{t}H$ [3]. The corresponding fit results for the $\tau_{\text{had}}\tau_{\text{had}}$ fake systematic uncertainties are depicted in Figure 8.6.

The phase-space region with the largest effect on most fake uncertainties is boost. Since the corresponding inputs to the fit are adopted from the 2022 analysis, as it is the case for VH, their impact is unlikely to be influenced by the Legacy analysis design. A fundamental difference between the settings of the two analyses is the VBF categorization. The standalone fit in the corresponding VBF phase-space results in non-negligible nuisance parameter pulls in **hh fake ff composition highdeta** and **hh fake ff stat 1p lnm** with central values of ~ -0.7 and ~ -0.5, respectively.

[3] To ensure consistency across all fits, the same seed was used to draw the random scaling value.

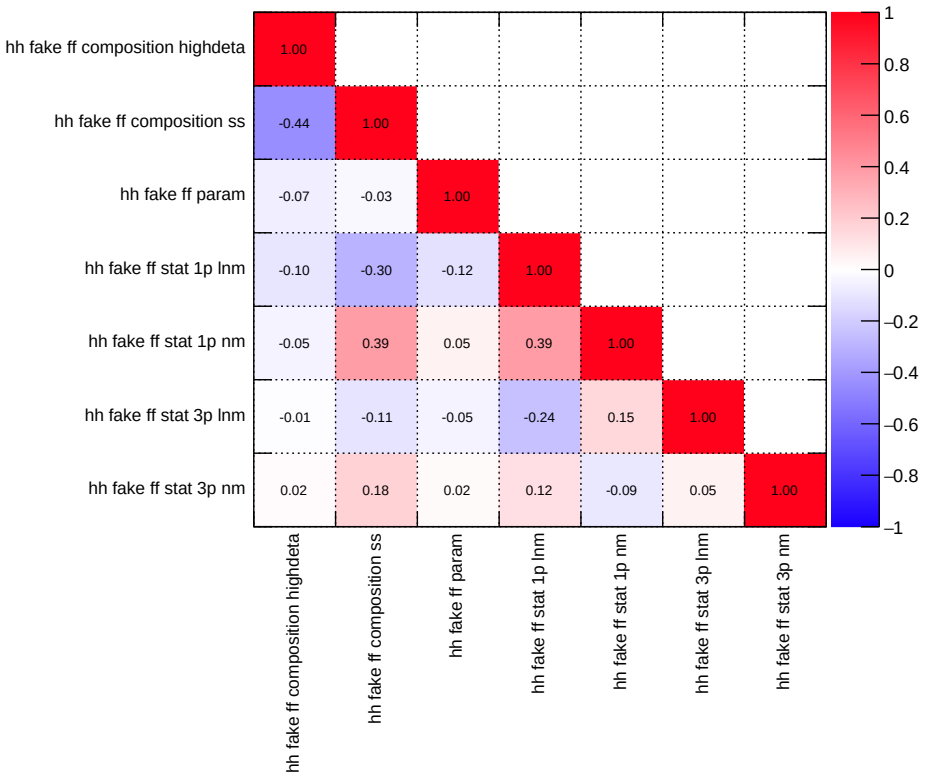


Figure 8.5: Correlation of the $\tau_{\text{had}}\tau_{\text{had}}$ fake systematic uncertainties in a $\tau_{\text{had}}\tau_{\text{had}}$ standalone 4PoI random scaling fit. The color scheme follows a heat map where fields colored in blue shades indicate an anti-correlation of parameters and fields colored in a red shade indicate a correlation.

A possible cause for such a pull in the Legacy analysis setup is the inclusion of data/MC mis-modelling in a newly defined VBF signal region. Such a mis-modelling can most frequently be observed in the first or last bins of the $m_{\tau\tau}$ distributions, retraceable in Figure D.4 - D.15. In order to balance the data/MC disagreement, the aforementioned nuisance parameters might be pulled by the fit to match the observed yields.

Cross-Checks: To test the hypothesis, a fit setup was designed that de-correlates the two systematic uncertainties in question across the VBF regions. In this way, the origin of the pull can be constricted further to specific VBF phase-space regions. The **hh fake ff composition highdeta** as well as the **hh fake ff stat 1p lnm** parameter are replaced by 16 standalone systematic uncertainties, which originate from the 2 VBF $\times$ 2 p_T^H $\times$ 4 m_{jj} regions, sketched in Figure 8.7.

The $\tau_{\text{had}}\tau_{\text{had}}$ fake systematic nuisance parameter pulls in the modified Legacy fit design are shown in Figure 8.8 together with the original Legacy fit results. Both settings are based on standalone fits in the VBF category since the nuisance parameter pulls were pinpointed to this very channel.

Contrary to the hypothesis, strong pulls pointing to specific VBF regions are not observed in the de-correlated setup. The 16 standalone **hh fake ff stat 1p lnm** parameters deviate by an average of

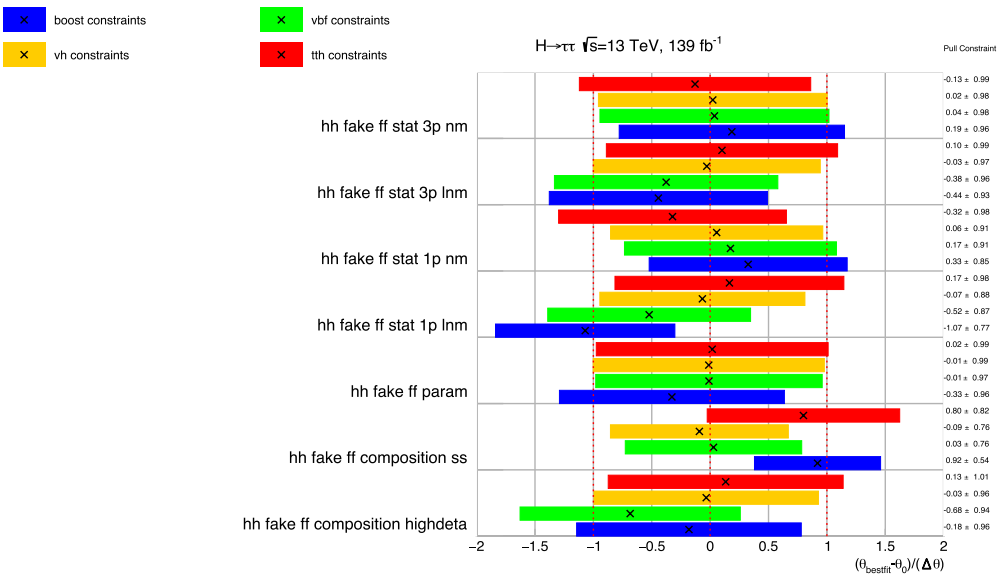


Figure 8.6: $\tau_{\text{had}}\tau_{\text{had}}$ fake systematic uncertainties in production mode dependent standalone 4PoI random μ fits. The standalone fit in the boost category is shown in blue, VBF in green, VH in yellow and $t\bar{t}H$ in red.

-0.042 from the nominal. In case of 16 standalone **hh fake ff composition highdeta** parameters the average deviation yields -0.05. In comparison, the two original Legacy analysis parameters yield central values of -0.53 and -0.69, respectively. To 'compensate' for the missing pull, the remaining $\tau_{\text{had}}\tau_{\text{had}}$ fake systematics react and show shifted pulls with respect to the original setup, such as **hh fake ff composition ss** with a pull of -0.34 compared to 0.03. Despite the de-correlated nuisance parameters not showing any strong pulls, their interplay does not contradict the expectation. While the entirety of **hh fake ff composition highdeta** is pulled towards more positive values compared to the reference setup, **hh fake ff composition ss** is pulled towards more negative values, which is in line with their anti-correlation of -23% (see Figure D.1). Similarly, the entirety of **hh fake ff stat 1p lnm** is pulled towards the right, which is anti-correlated with **hh fake ff composition ss** by -41%. Apart from the $\tau_{\text{had}}\tau_{\text{had}}$ fake systematic uncertainties, no other nuisance parameters show discrepancies across the two setups. In Asimov studies (Figure D.2) an identical sensitivity on the PoIs was shown for both setups. Since the $\tau_{\text{had}}\tau_{\text{had}}$ fake systematics are not estimated per signal region, the more inclusive, correlated approach is selected.

In conclusion, no irregularities are found in the $\tau_{\text{had}}\tau_{\text{had}}$ fake systematic uncertainties. The observed parameter pulls can be explained by correlations.

Generally, for all 352 nuisance parameters of the Legacy analysis setup, the majority of observed nuisance parameter pulls do not extend beyond 1 σ and are not observed to be strongly constrained. Observed discrepancies were treated as exemplified by this walk through.

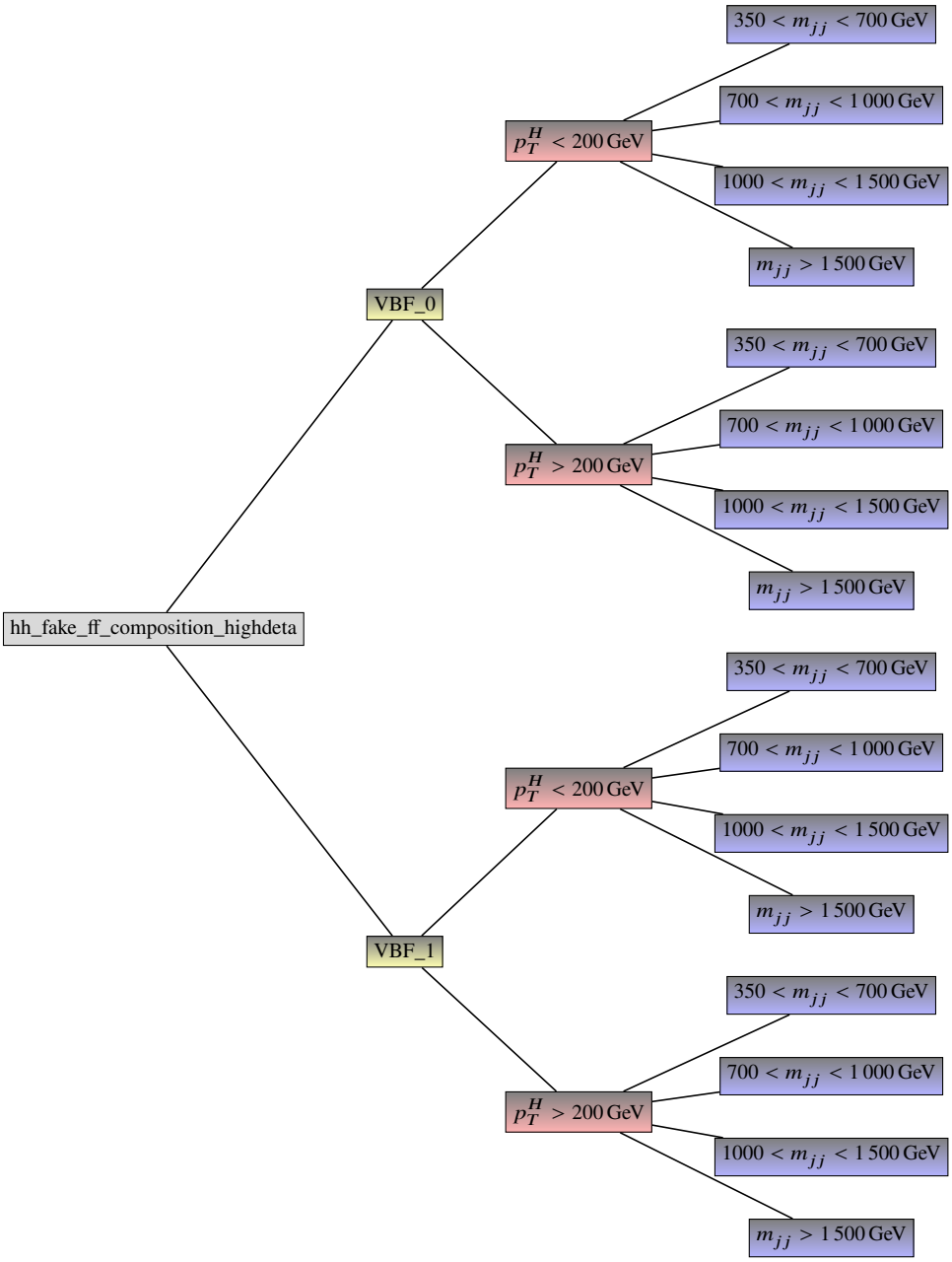


Figure 8.7: De-correlation of the **hh fake ff composition high-deta** nuisance parameter across VBF regions yields in 16 nuisance parameters. Different colors indicate different cut variables.

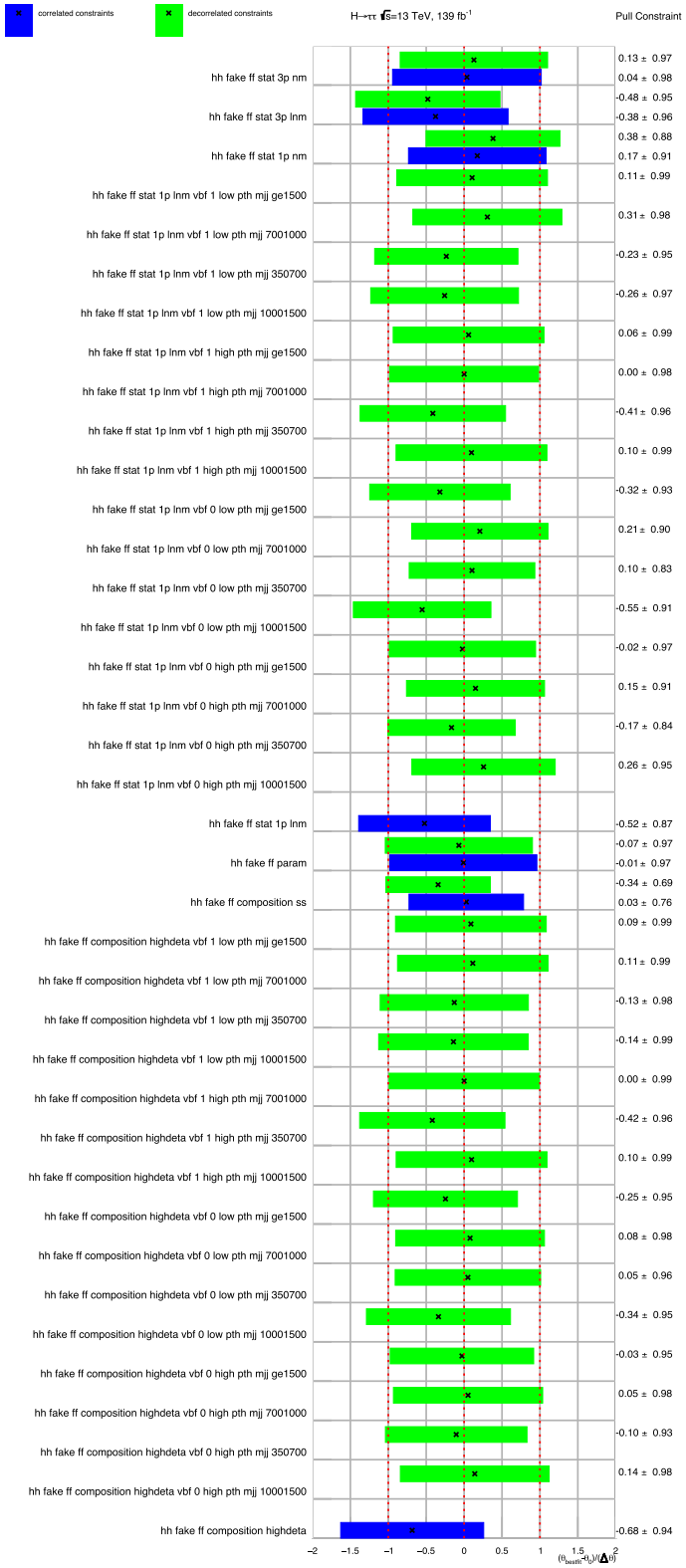


Figure 8.8: $\tau_{\text{had}}\tau_{\text{had}}$ fake systematics in a random μ 4PoI standalone fit in VBF. In blue, the reference setup is shown. In the green setup, **hh fake ff composition highdeta** and **hh fake ff stat 1p lnm** are de-correlated across VBF regions.

8.3 Unblinded STXS Results

After the detailed validation of the Legacy analysis setup, the full unblinded Run 2 dataset can be explored. The signal strength measurements comprise the inclusive measurement, the measurement per Higgs production mode as well as in the 18 STXS bins.

8.3.1 Post-Fit Studies of the Background

Before focusing on the measured PoIs and their correlations, the background modelling is investigated at post-fit level, which opens the possibility to gain further insight into nuisance parameter pulls. Due to the immense amount of free parameters and their correlations, the interplay cannot be easily understood. Significant changes with respect to the pre-fit plots can however be spotted. Furthermore, an investigation of MC mis-modelling effects can be conducted. This Section takes the opportunity to discuss pre- and post-fit plots and to trace the effect of normalization factors [4].

In Figure 8.9, pre- and post-fit plots of three different VBF regions are shown:

- **Region A**: $\tau_{\text{had}}\tau_{\text{had}}$, VBF 0, high p_T^H, 350 GeV < m_{jj} < 700 GeV
- **Region B**: $\tau_{\text{had}}\tau_{\text{had}}$, VBF 1, high p_T^H, 350 GeV < m_{jj} < 700 GeV
- **Region C**: $\tau_{\text{lep}}\tau_{\text{had}}$, VBF 0, low p_T^H, m_{jj} > 1 500 GeV

In addition to the signal regions, the corresponding $Z \rightarrow \tau\tau$ control regions are shown. The latter is used to determine a normalization factor for the dominant background. No shape information is needed and a singular, inclusive bin is considered.

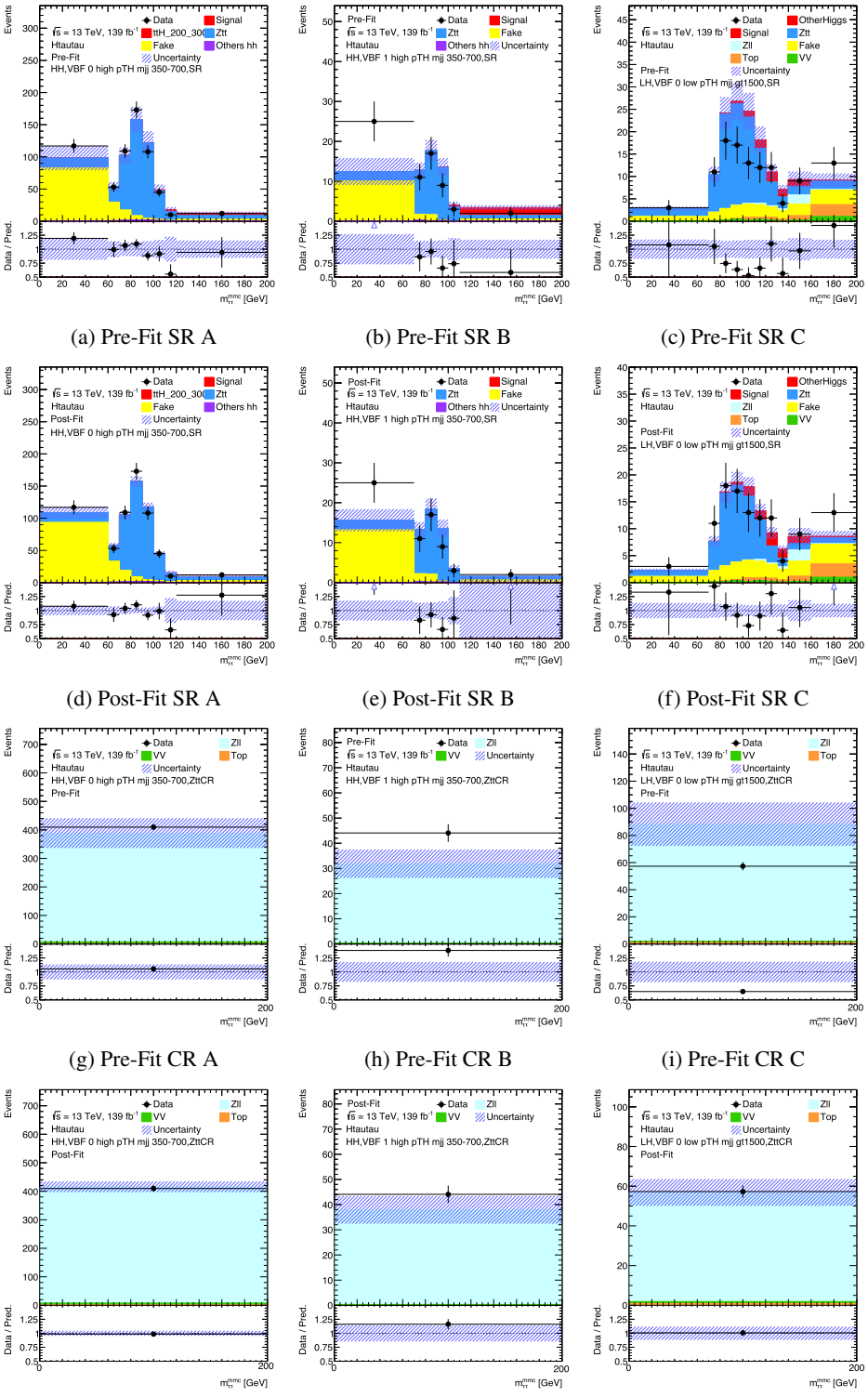
Region A visualizes the improvement in data/MC agreement following the change of nuisance parameters. In the pre-fit plots, Figures 8.9(a) and 8.9(g), the recorded data does not match the background but still falls within the uncertainty bands. A comparison with post-fit plots shows smaller uncertainty bands as a result of constrained nuisance parameters. In the first bin, a noticeable change in fake yield indicates a pull of fake systematics.

The region B exhibits a significant data/MC mis-modelling in the first $m_{\tau\tau}$ bin. Since the $Z \rightarrow \tau\tau$ contribution is low, the observed effect is not compensated by the scaling factor of this specific background, which is determined in the corresponding CR. Instead, the fake background is increased, which goes along with a penalty contribution in the likelihood product. Since the signal contribution is small in fake-enriched bins, strong pulls only have a small impact on the overall sensitivity of the PoIs.

The region C exemplifies the necessity for a down-scaling of the $Z \rightarrow \tau\tau$-background to improve the data/MC agreement. The observations made are reflected in the determined normalization factor depicted in Figure 8.10. In general, the $Z \rightarrow \tau\tau$ norm factors are a powerful tool to account for MC mis-modelling. The high m_{jj} regions exhibit stronger NF pulls accounting for mis-modelling than low m_{jj} regions. VBF 0 NFs and VBF 1 NFs often are compatible with each other, which indicates a good modelling of the BDT used for the event split.

At post-fit level, the MC data and measurement data are in predominant agreement within uncertainties. Outliers and their effects are separately discussed in Section 8.3.3.

[4] This background related study can also be performed on a reduced phase-space in side-band fits.



(a) Pre-Fit SR A (b) Pre-Fit SR B (c) Pre-Fit SR C

(d) Post-Fit SR A (e) Post-Fit SR B (f) Post-Fit SR C

(g) Pre-Fit CR A (h) Pre-Fit CR B (i) Pre-Fit CR C

(j) Post-Fit CR A (k) Post-Fit CR B (l) Post-Fit CR C

Figure 8.9: Collection of pre- and corresponding post-fit plots. SRs as well as the corresponding $Z \to \tau\tau$ CRs are shown for three different regions: **A**: $\tau_{\text{had}}\tau_{\text{had}}$, VBF 0, high p_T^H, 350 GeV < m_{jj} < 700 GeV; **B**: $\tau_{\text{had}}\tau_{\text{had}}$, VBF 1, high p_T^H, 350 GeV < m_{jj} < 700 GeV; **C**: $\tau_{\text{lep}}\tau_{\text{had}}$, VBF 0, low p_T^H, m_{jj} > 1 500 GeV.

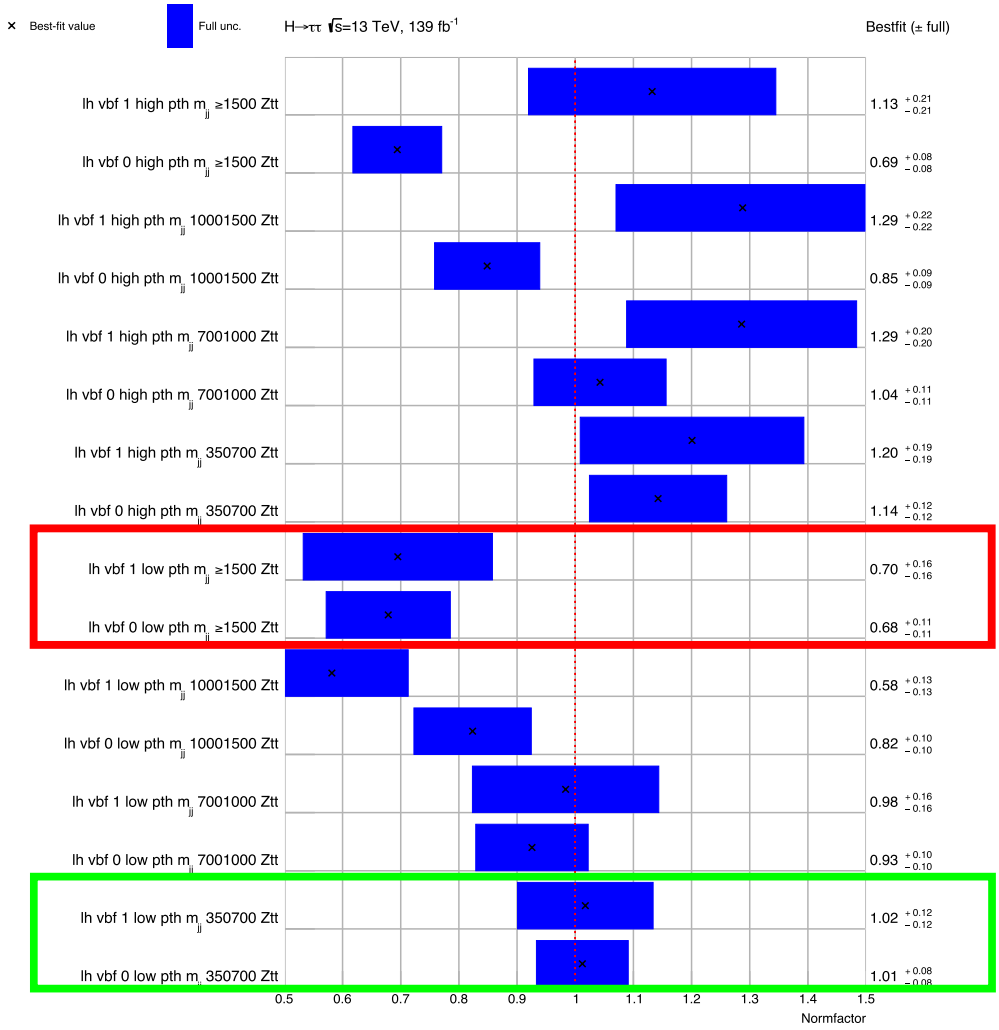


Figure 8.10: $Z \to \tau\tau$ normalization factors for the VBF SRs in the unblinded 18PoI fit. The red and green rectangle highlight the differences observed in high and low m_{jj} regions, respectively.

		2022 Analysis		Legacy Analysis	
		Asimov	Unblinded	Asimov	Unblinded
Inclusive	Full	$1.00^{+0.14}_{-0.13}$	$0.93^{+0.13}_{-0.12}$	$1.00^{+0.12}_{-0.11}$	$0.93^{+0.12}_{-0.11}$
	Stat	$^{+0.07}_{-0.07}$	$^{+0.07}_{-0.07}$	$^{+0.06}_{-0.06}$	$^{+0.07}_{-0.06}$
	Syst	$^{+0.12}_{-0.11}$	$^{+0.12}_{-0.10}$	$^{+0.10}_{-0.09}$	$^{+0.10}_{-0.09}$
ggH	Full	$1.00^{+0.36}_{-0.29}$	$0.96^{+0.34}_{-0.28}$	$1.00^{+0.30}_{-0.26}$	$0.94^{+0.32}_{-0.27}$
	Stat	$^{+0.15}_{-0.15}$	$^{+0.15}_{-0.15}$	$^{+0.14}_{-0.14}$	$^{+0.15}_{-0.15}$
	Syst	$^{+0.33}_{-0.25}$	$^{+0.31}_{-0.23}$	$^{+0.27}_{-0.22}$	$^{+0.28}_{-0.22}$
VBF	Full	$1.00^{+0.20}_{-0.17}$	$0.90^{+0.20}_{-0.17}$	$1.00^{+0.16}_{-0.15}$	$0.93^{+0.17}_{-0.15}$
	Stat	$^{+0.13}_{-0.13}$	$^{+0.13}_{-0.12}$	$^{+0.11}_{-0.11}$	$^{+0.12}_{-0.11}$
	Syst	$^{+0.15}_{-0.12}$	$^{+0.15}_{-0.12}$	$^{+0.12}_{-0.10}$	$^{+0.12}_{-0.10}$
VH	Full	$1.00^{+0.60}_{-0.58}$	$0.98^{+0.61}_{-0.58}$	$1.00^{+0.60}_{-0.57}$	$0.91^{+0.63}_{-0.60}$
	Stat	$^{+0.50}_{-0.48}$	$^{+0.50}_{-0.48}$	$^{+0.50}_{-0.48}$	$^{+0.53}_{-0.51}$
	Syst	$^{+0.34}_{-0.33}$	$^{+0.34}_{-0.33}$	$^{+0.32}_{-0.31}$	$^{+0.35}_{-0.33}$
$t\bar{t}H$	Full	$1.00^{+1.24}_{-1.06}$	$1.06^{+1.28}_{-1.08}$	$1.00^{+0.92}_{-0.79}$	$0.77^{+1.01}_{-0.92}$
	Stat	$^{+1.06}_{-0.93}$	$^{+1.07}_{0.94-}$	$^{+0.80}_{-0.71}$	$^{+0.87}_{-0.77}$
	Syst	$^{+0.64}_{-0.52}$	$^{+0.70}_{-0.53}$	$^{+0.45}_{-0.35}$	$^{+0.52}_{-0.50}$

Table 8.3: Measured $\sigma_H \times B(H \to \tau\tau)$ relative to SM expectation, inclusive as well as in the four dominant Higgs production modes. The indicated uncertainties cover systematic as well as statistical uncertainties. Values of the 2022 analysis are extracted from [71], [145]. The statistics only contribution is determined in a separate fit as described in Section 8.1.1. Outstanding improvements in the final fit results are highlighted in color.

8.3.2 Inclusive & Production Mode Dependent Measurement

The inclusive and production mode dependent measurement results of the PoIs are summarized in Table 8.3 together with the expectation from Asimov studies. In addition to the Legacy analysis, the results of the 2022 analysis are shown to illustrate the accomplished improvements in the Legacy setup.

Inclusive Measurement: The inclusive measurement of $\sigma_H \times B(H \to \tau\tau)$ relative to the SM expectation yields $0.93^{+0.12}_{-0.11}$, which agrees with the expectation from Asimov studies. Compared to the previous measurement, a slightly improved sensitivity is reached as a result of an updated uncertainty scheme. Incorporated updates entail for example improved theoretical uncertainties on the ggH signal [146], which are one of the dominant uncertainty sources, as shown in Table 8.1. Furthermore, changes in the VBF and $t\bar{t}H$ categorization are expected to yield differences with respect to the 2022 analysis.

Production Mode Dependent Measurement: The four production modes are measured in a fit with four parameters of interest. All results are within their uncertainties in agreement with the SM. The most sensitive production-mode measurement is performed in VBF. The second best sensitivity is measured in the ggH production channel, which profits from the improved $m_{\tau\tau}$ resolution in the boosted regime of the Higgs boson. VH and $t\bar{t}H$ follow behind. The design of the Legacy analysis is

focused on VBF and $t\bar{t}H$, which is why the most significant improvements are expected and observed in these channels. Compared to the previous measurement, the result of $0.93^{+0.17}_{-0.15}$ in the VBF production mode shows a slight improvement based on the novel categorization strategy. A larger difference can be observed in $t\bar{t}H$, where optimized MVA strategies are applied. Compared to the previous result, the central value shifts further away from the SM expectation, is however still within the large uncertainty bands.

8.3.3 18 PoI Result

The differential exploration of diverse phase-space regions to find hints of beyond the Standard Model physics has shaped the design of the analysis setup. The fit results for the 18 parameters of interest are visualized in Figure 8.11. The compatibility of the measurement with the Standard Model prediction yields a p-value of 6% [3]. The p-value describes the probability of obtaining the observed or more discrepant data assuming the Standard Model hypothesis is correct.

VH and ggH

The ggH and VH PoIs are in good agreement with the SM and the results of the 2022 analysis. Matching results are expected due to identical selection criteria. The $\boldsymbol{ggH \geq 2jet, m_{jj} \geq 350\,\text{GeV}, p_T^H < 200\,\text{GeV}}$ channel forms an outlier that is discussed in the following.

$t\bar{t}H$

As already revealed by studies based on Asimov data, statistical uncertainties strongly affect the $t\bar{t}H$ measurement. Therefore, the measurements are used to set upper cross-section limits at 95% confidence level using the CL_s method [147]. The corresponding plots are documented in the publication [3].

VBF

The VBF production mode demonstrated good sensitivity in studies based on Asimov data. Therefore, some noteworthy observations in the unblinded setting need to be highlighted:

- Improved precision in the high p_T^H / m_{jj} phase-space due to reduced background contamination.
- VBF low p_T^H related PoIs tend to yield values below the SM prediction.
- The most pronounced deviations that yield results below the SM expectation are
  - qq2Hqq 350 GeV $< m_{jj} <$ 700 GeV, $p_T^H >$ 200 GeV with $\sim 2.5\sigma$
  - qq2Hqq $m_{jj} \geq$ 1 500 GeV, $p_T^H <$ 200 GeV with $\sim 3\sigma$

Discussion

Correlations play a critical role in the observed results. The decisive measurement is the ggH PoI $\boldsymbol{ggH \geq 2jet, m_{jj} \geq 350\,\text{GeV}, p_T^H < 200\,\text{GeV}}$, which has strong impact on the other measurements. It will be denoted as *VBF-like* since the low p_T^H VBF STXS-bins have analogous STXS-bins in the

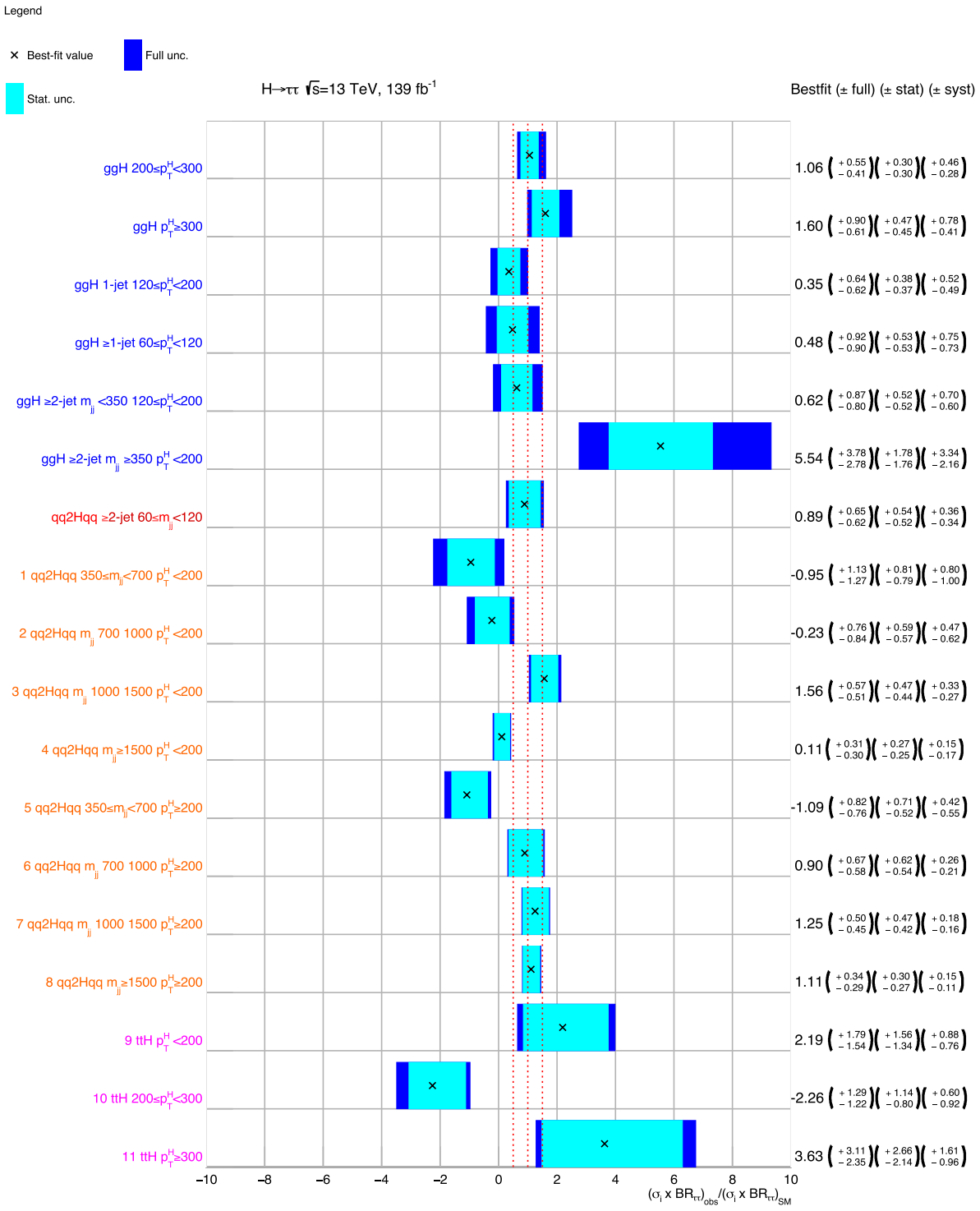


Figure 8.11: Fit results of the 18 parameters of interest using the full Run 2 data set. The six ggH related PoIs are marked in blue, the one VH bin in red, the eight VBF related measurements in orange and the three $t\bar{t}H$ bins are shown in pink. The best fit value is visualized by the black cross, the coloured bars indicate the 1σ uncertainty interval. The full uncertainty is depicted in dark blue whereas the statistic only contribution is depicted in cyan.

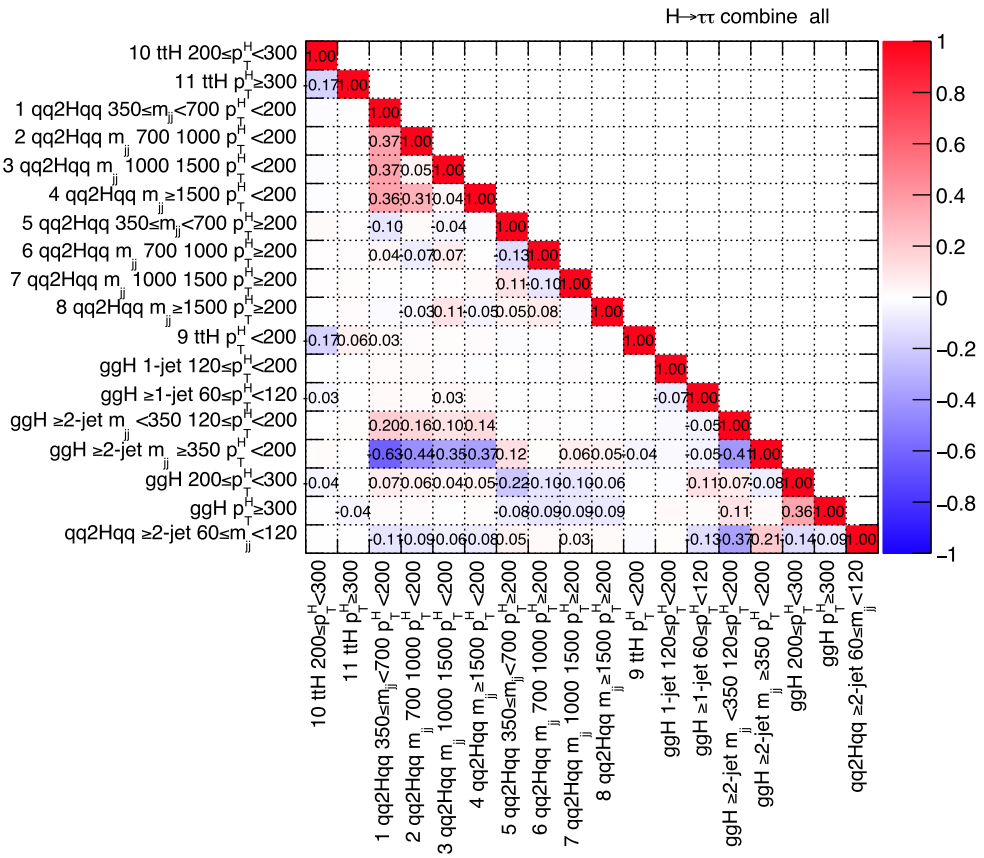
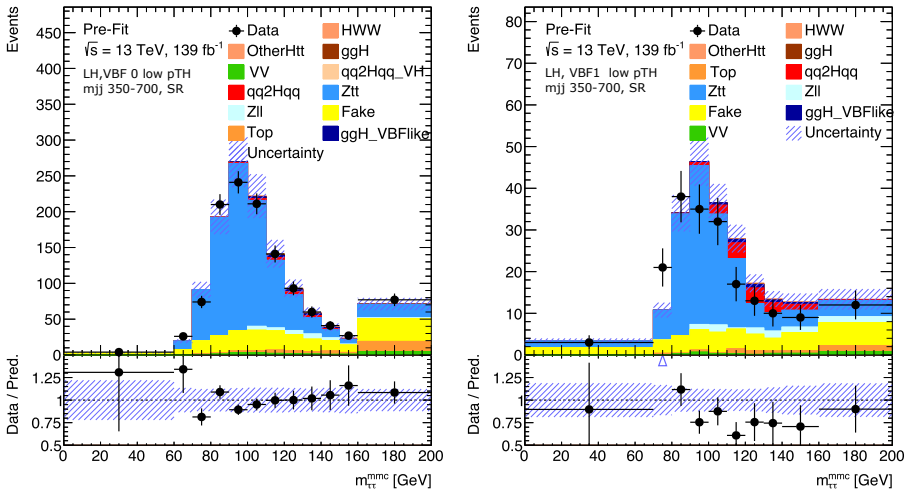


Figure 8.12: Correlations of the 18 PoIs measured in the unblinded setup. The color scheme follows a heat map that transitions from blue fields indicating an anti-correlation of parameters to red fields indicating a correlation. Correlations > 0.02 and anti-correlations < −0.02 are given by value.

ggH sector, which share the same phase-space splitting in terms of their number of jets and m_{jj} value, as visualized in Figure 6.4. Despite the low sensitivity of the VBF-like bin, it strongly impacts the measurement in more sensitive bins due to strong anti-correlations with low p_T^H related VBF PoIs of up to 60% as indicated in Figure 8.12.

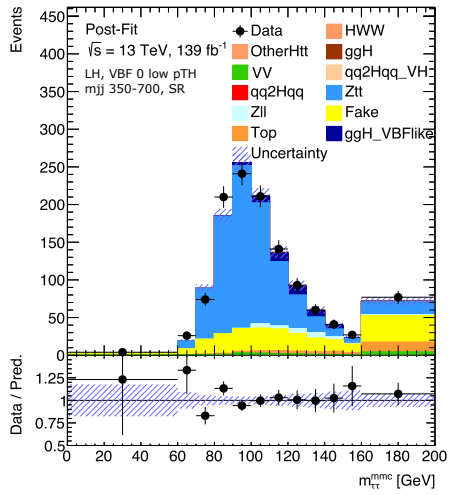
The anti-correlation is caused by a contamination of ggH events in the background enriched VBF 0 SRs, previously shown in Figure 6.8. The VBF 1 SR is by construction more signal-enriched (VBF tagger). Still, it is not sufficient to guide the fit, which needs to maximize the likelihood in the complex interplay of parameters. The most severe mis-modelling within the 158 regions is shown in Figure 8.13 and is representative for the observed pull.

The pre- and post-fit distributions of the **low p_T^H, 350 GeV < m_{jj} < 700 GeV** SR are shown for VBF 0 and VBF 1, respectively. In the VBF 1 SR (see Figure 8.13(b)), a mis-modelling of the SM background can be observed, which has a large impact on the PoIs. While the resulting down-fluctuation of data in the VBF 1 region is compensated by scaling down the VBF signal PoI, the data/MC agreement is maintained in VBF 0 by increasing the contaminating VBF-like ggH

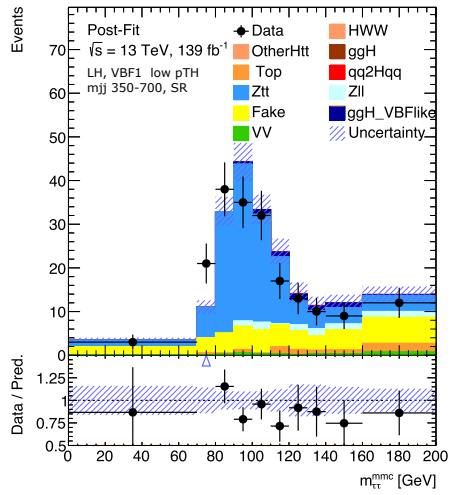


(a) Pre-fit VBF 0

(b) Pre-fit VBF 1



(c) Post-fit VBF 0



(d) Post-fit VBF 1

Figure 8.13: Comparison of pre and post-fit distributions of the **low p_T^H, 350 GeV<m_{jj} < 700 GeV** SR in the VBF 0 and VBF 1 selection, respectively.

contribution. Scaling the PoIs to account for mis-modelling is more convenient than pulling systematic uncertainties since no penalty is introduced by parameters of interest. Several tests were performed in order to guarantee that no setup design choices have effect on the observed pulls.

Fake Templates: A novelty within the analysis are the inclusive fake templates. In order to rule out, that the fit is missing degrees of freedom due to the combination of fake templates, the unblinded fit was additionally performed with the original fake templates. Between the two settings, no discrepancies are observed, as documented in Figure D.16.

Mis-calibration: The mis-modelling observed in Figure 8.13(b) is interpreted as a down-fluctuation of data. An alternative interpretation argues with a shifted Z-peak, plausibly caused by mis-calibrated τ leptons. The τ reconstruction is a complex task folding different sources of uncertainty like uncertainties on tracking and jet finding algorithms (see Section 2.3.1). In case of mis-calibration, phase-space regions with better $m_{\tau\tau}$ resolution provide visible indications, that can be diluted for broader Z-peak distributions. This assumption does not hold since no severe Z-peak mis-modelling is observed in regions other than the one discussed in Figure 8.13[5].

In addition to the $m_{\tau\tau}$ distributions, ranking plots can reveal a possible mis-calibration. Ranking plots illustrate the impact of single sources of uncertainty on the parameter of interest by fixing a given nuisance parameter to the $\pm 1\sigma$ pre- and post-fit variation at pre- and post-fit level. This results in four separate fits per nuisance parameter. The impact on the parameter of interest is shown as the difference $\Delta\mu$ between the measurement achieved with the nominal and the setup relying on fixed nuisance parameters. All remaining nuisance parameters and norm factors remain free floating. The twenty nuisance parameters that case the largest impacts on the VBF PoI $\mathbf{350\,GeV < m_{jj} < 700\,GeV, p_T^H < 200\,GeV}$ are shown in Figure 8.14. They belong to the three dominating groups - signal theory, JET/MET and MC statistical nuisance parameters, respectively.

In case of a fit result being manipulated by a τ mis-calibration, shape varying uncertainties related to the τ reconstruction would dominate the ranking plots. Such shape varying uncertainties are related to missing transverse energy (MET) or jet properties (JET). Figure 8.14 shows the rankings for the PoI that is targeted by the signal region, which is affected by mis-modelling (Figure 8.13(b)). Although systematic uncertainties affecting the jet energy resolution (JER) are well-represented in the ranking, the impact on the signal strength does not show any striking features that indicate a τ lepton mis-calibration.

The same applies to the ranking plots representing the remaining parameters of interest depicted in Figure D.19 through D.17. Together with the fact that the mis-modelling is not consistently observed across different regions, the initial interpretation of a down-fluctuation of data being responsible remains credible.

Miscellanious Other tests were performed as part of the collaborative effort in the analysis working group. Fixing the VBF-like ggH PoI to the SM expectation, looking into the measurements of channel dependent stand-alone fits or merging low p_T^H VBF bins with the ggH counterpart [6], all yield results that do not contradict the aforementioned explanation of the observed outcome.

[5] The $m_{\tau\tau}$-distributions of other phase-space regions are documented in Figure D.4-D.15

[6] Since these checks were performed by other members of the analysis team, no plots are shown. For more details see [119].

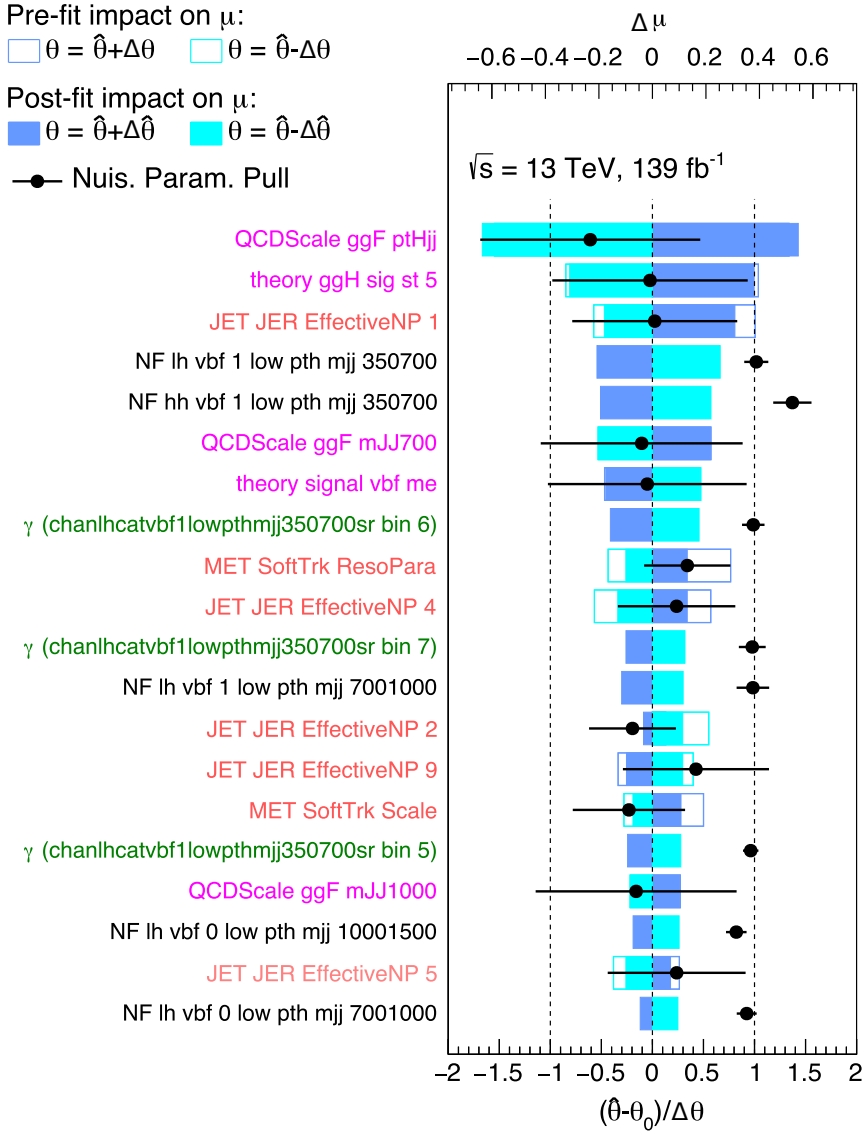


Figure 8.14: Ranking of systematic uncertainties for the VBF PoI with 350 GeV $< m_{jj} <$ 700 GeV and $p_T^H <$ 200 GeV. The colored bands indicate the impact on μ when fixing the indicated nuisance parameter to its pre-/post fit values. The nuisance parameter pulls themselves are shown by black data points. Pink, orange and green colored uncertainties belong to signal theory, JET/MET and MC statistical nuisance parameters, respectively.

8.4 Analysis Landscape & Perspectives

Precision measurements like the $H \to \tau\tau$ measurements will be improved across future iterations of the analysis approach and setup. With this perspective it is important to acknowledge alternative approaches as well as the lessons learned.

8.4.1 CMS Run 2 Results

The final validation of results from precision measurements is ultimately achieved through cross-checks between the two multi-purpose detectors ATLAS and CMS. The STXS approach is designed to facilitate combinations across channels and experiments.

In this spirit, the $H \to \tau\tau$ Run 2 STXS publication of the CMS collaboration in the year 2023 [148] provides the analogous results. With an integrated luminosity of 137 fb^{-1} similar data set sizes were recorded in both experiments. CMS follows a slightly different analysis design by measuring a ggF, EW qqH (VBF+V($\to$ qq)H) and V($\to$ leptons)H category and exploring up to 16 different kinematic regions. Although the general analysis idea is consistent within the two experiments, fundamental differences to the ATLAS Legacy analysis need to be considered when comparing the results. These comprise

- the exploration of different phase-space regions as for example a 0-jet category in the ggH phase-space.
- the exploration of a neural network based categorization for the ggF and qqH related analysis. Input distributions to the fit are designed as a function of the networks score.
- a full embedding [149] for $Z \to \tau\tau$ background estimation implicating smaller uncertainties as for the object level-embedding[7].

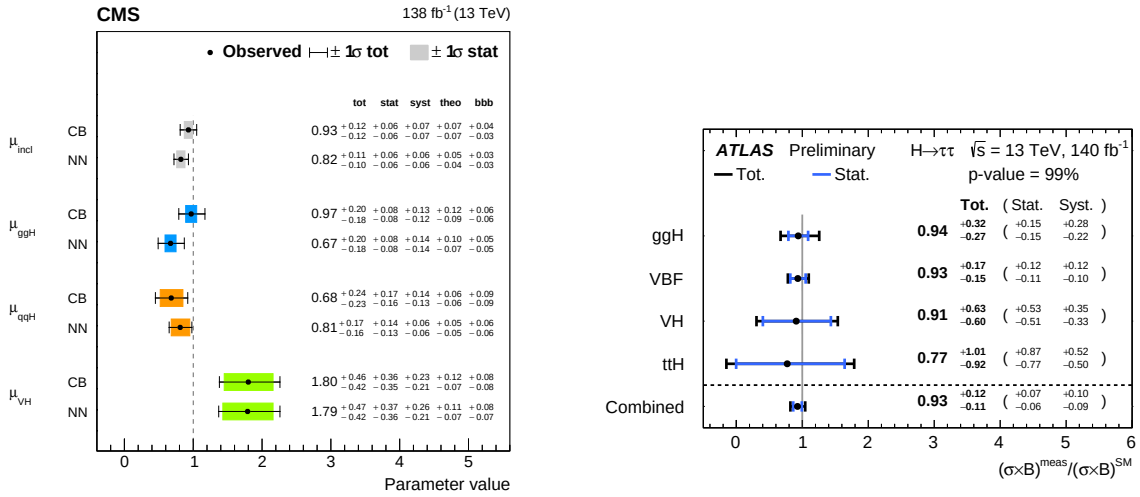
Based on the differences between both analyses, the comparison focuses on the production-mode level. The corresponding results of both experiments are depicted in Figure 8.15.

In the inclusive measurement both experiments reach comparable sensitivity in the regime of ~ 0.12. For ggH, CMS outperforms the ATLAS measurement with an uncertainty of ~ 0.19 compared to ~ 0.3. Since ggH is the only production-mode dependent measurement that is dominated by systematic uncertainties, the difference might be caused by the reduced uncertainties on the embedding technique. The published information is however not detailed enough to judge the impact of individual nuisance parameters. The ATLAS VBF category does not represent the same phase-space as qqH, which additionally takes V($\to$ qq)H into account. Nevertheless, a similar sensitivity of ~ 0.17 can be achieved in both analyses. Both experiments show consistent results and confirm the SM predictions with slightly deviating sensitivity per measured phase-space.

8.4.2 Lessons learned & Consequences for Future Measurements

The Legacy analysis did provide convincing physics results and was able to accumulate extensive knowledge to impact future analysis setups. In perspective of Run 3, analysis choices like signal separation, $Z \to \tau\tau$ background modelling or fake estimation need to be reconsidered.

[7] In the full embedding approach, di-muon events are selected in data and their energy depositions are replaced by simulated τ decays with identical properties.



(a) CMS (b) ATLAS

Figure 8.15: Signal strength measurements of the CMS [148] and the ATLAS [3] collaboration. While CMS performs a V(→ leptons)H measurement, the VH measurement of the ATLAS plot corresponds to V(→ qq)H. The CMS analysis follows a cut- as well as a neural network based analysis, labeled as CB and NN, respectively. For more information see [148].

Signal Separation: In the detailed exploration of the VBF phase-space, a strong anti-correlation with the VBF-like ggH events did reveal shortcomings of the setup. This anti-correlation was already observed in studies using Asimov data. Its impact was however underestimated due to the the low sensitivity of the VBF-like PoI. As a result of the BDT design, responsible for the separation of the VBF phase-space, the contamination of the VBF SRs with ggH events is larger in the VBF 0 selection than in VBF 1. This aspect of the analysis design is not unique to the $H \rightarrow \tau\tau$ analysis. Strong anti-correlations between VBF and VBF-like ggH bins have also been observed in $H \rightarrow \gamma\gamma$ [150] as well as in $H \rightarrow WW$ [151]. These effects put the feasibility of a detailed exploration of the VBF phase-space based on the STXS framework in question. Several approaches are applicable in the development for future setups.

- Improved MVA techniques as a multi-class BDT for improved signal separation.
- The MMC $m_{\tau\tau}$ observable does not provide the possibility to separate ggF from VBF events since both processes produce a real Higgs boson. Other variables, like the neural network output used in the CMS publication [148], are a promising alternative to perform the fit.
- An optimized STXS binning can resolve overarching correlations.

$Z \rightarrow \tau\tau$ background: Despite the applied object-level embedding as a suitable candidate to overcome challenges in the Sherpa normalization, extreme phase-space regions as the low p_T^H / m_{jj} region suffer from insufficient background modelling. Possible future alternatives are found in extended embedding techniques. Apart from the normalization, the shape of the Z background can be extracted from embedding. Another approach splits the CRs used for the extraction of normalization

factors into several bins. Although this would guarantee a more detailed description, its realization heavily depends on available statistics.

Fake Background: A sophisticated event classification strategy is important to defined signal-enriched phase-space regions. As outlined in Chapter 7, a decay-mode dependent fake estimation not only provides a more detailed background description but also presents the opportunity to define signal regions with decreased fake contribution. The selected granularity of the defined regions has however a large impact on the statistical uncertainties as well as on the complexity and stability of the fit setup. The current Legacy analysis setup comprises a total of 78 signal regions and 80 CRs. In Chapter 7, a SR split into eight decay-mode configurations was suggested such as 1p0n_1p0n, 1p0n_1pXn, etc. Consequently, when only applied to the 48 VBF SRs, a total of $48 \cdot 8 + 30 = 414$ SRs and $48 \cdot 8 + 16 + 30 = 430$ CRs is needed. Loosened τ-ID working points in signal enriched regions might mitigate the statistical limitations. In conclusion, a compromise between complexity, statistics and physics gain, needs to be found.

τ-Lepton Reconstruction: As key player in the analysis, the τ-lepton reconstruction, calibration and identification carries much potential towards more precise measurements. An exciting development are so-called end-to-end approaches where a singular multi-variate algorithm replaces multiple state-of-the art reconstruction algorithms. The optimized strategy simplifies calibration and fine-tuning. Applications in flavor tagging are under investigation and can be extended to various other reconstruction chains, such as for particle flow objects in τ-lepton reconstruction. In general, synergies with other working groups might have positive effects by developing common strategies and tools.

CHAPTER 9

Conclusion

The quest for precision in Standard Model measurements necessitates the development of advanced analysis strategies. The need arises from the incomplete description of nature, which requires extensions of the theory. The Higgs being the most recently discovered and central particle of the model leaves many of its properties to be determined at the lowest possible uncertainty.

The $H \rightarrow \tau\tau$ measurement provides prominent access to the Yukawa-coupling and is central to the Standard Model theory. Apart from its relevance for the Yukawa coupling, the di-tau channel is suited to explore Higgs properties, such as production cross-sections, due to the high branching ratio into two τ-leptons and their distinguished signature in the detector. Another suited measurement in the di-tau channel are CP observables due to the sensitivity to spin correlations. The exploration of the di-tau channel is currently based on the ATLAS Run 2 data-set, which accesses 140 fb^{-1} [11] of collisions.

The Legacy analysis results [3] comprise the most detailed cross-section measurements of the channel, applying state-of-the-art analysis strategies and superseding previous publications. The most precise cross-section measurement in the Vector-Boson-Fusion (VBF) production mode yields a value of $0.93^{+0.17}_{-0.15}$ relative to the SM prediction. Following the STXS-analysis approach, 18 phase-space regions are measured and result in a p-value of 6%, which describes the compatibility with the Standard Model prediction. The eight VBF-related regions comprise the first measurements of the high $p_T^H > 200\,\text{GeV}$ and high $m_{jj} > 1.5\,\text{TeV}$ phase-space region ($1.29^{+0.39}_{-0.34}$) [3], as well as the most precise exploration of the low $p_T^H < 200\,\text{GeV}$ region in combination with a high $m_{jj} > 1.5\,\text{TeV}$ selection ($0.12^{+0.34}_{-0.33}$) [3]. One novelty that contributes to these results is the combination of fake templates across specific phase-space regions. These more inclusive fake templates have reduced statistical shape uncertainties on and add to the fit setup stability. Despite their successful reduction, the MC statistical uncertainties are still the limiting source of measurement uncertainty in addition to the signal theory uncertainty as well as JET/MET related uncertainty contributions.

In addition to the stand-alone channel-dependent analyses, ATLAS publishes combined performance studies. Each flavor of Higgs analysis faces individual challenges and benefits from unique advantages. Their complementary findings provide an extended picture of Higgs physics across all decay-channels in a combined fit setup.

The latest combined performance study is based on the 2022 $H \rightarrow \tau\tau$ analysis [9]. In a following publication round, improved performance from the Legacy analysis setup is expected. The updated

analysis will have a large impact on the production-mode cross-section measurements in VBF and $t\bar{t}H$, as well as a gain in global signal strength.

The credibility of the Legacy results is supported by a long series of validation studies. The studies reveal a strong anti-correlation between VBF and VBF-like ggH bins. These effects put the feasibility of a detailed exploration of the VBF phase-space based on the STXS framework in question and require a change of strategy in future analyses. Apart from improved MVA techniques for better signal selection, optimized STXS binning is a promising approach to resolve the strong correlations. Another interesting aspect of study is the observable used for the fit. The correlation is introduced by the imperfect categorization of Higgs events into separate production-modes through application of analysis cuts and MVA algorithms. The current fit relies on the reconstructed di-tau mass, which is not sensitive to the various Higgs production modes. Alternative neural network outputs are an interesting approach to break this correlation.

Potential for improvement within the reconstructed di-tau mass lies in the resolution. Alternative neural-network based algorithms in place of the likelihood-based Missing Mass Calculator can improve separation between the Higgs signal and the dominant $Z \rightarrow \tau\tau$ background.

The latter is reconstructed employing the embedding method, which exhibits subpar modelling in extreme phase-space regions (low p_T^H/m_{jj}). Consequently, developments in extended embedding techniques are promising to improve the background description.

The second largest background, the misidentified τ leptons, provide an anchor point for future analysis setups. A decay-mode dependent fake estimation enables the definition of phase-space regions with improved signal over background ratio. The decay-mode dependent estimation is found to agree with the inclusive approach within the uncertainties. A re-definition of signal regions has been proposed and is balancing signal purity against available statistics and fit stability. Statistical limitations are mitigated by loosened τ-ID working points in signal enriched regions in exchange for signal purity. In the decay-mode reconstruction, events migrate between different decay-modes due to complex τ-substructure signatures. To account for that effect, individual efficiency correction factors per decay-mode need to be introduced. A suited observable for their measurement is the visible τ-lepton mass $m_{\tau\text{-had-vis}}$ due to distinct mass-peaks per decay-mode. To measure the efficiency correction factors in the fit setup, suited CRs are defined. Validation and adaptation in fit studies is still pending.

In the high-luminosity LHC era, an extended version of the presented Run 2 Legacy $H \rightarrow \tau\tau$ setup will be able to overcome the current limitation in statistics. The presently limiting factor will be mitigated by the additional order of magnitude in collisions provided by the HL-LHC. The expected integrated luminosity of 3 000 fb^{-1} [45] is also a promising perspective for the decay-mode dependent, signal enriched phase-space selection.

In preparation for accelerators operating at the highest-possible luminosity, reliable and computationally efficient reconstruction is a core-requirement. The presented development of a recurrent neural network for electron PID bridges the current reconstruction algorithms to the future of object reconstruction in high-energy physics.

APPENDIX A

Auxiliary Material for Chapter 5

Training Samples

Signal Samples:

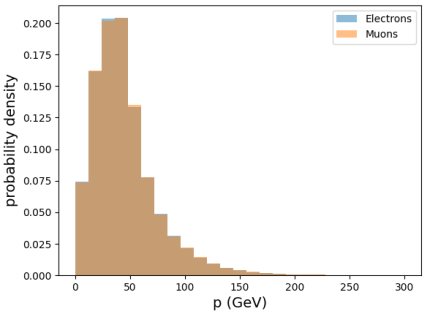
- MC:
  1. Run 3: `group.det-indet.361106.PowhegPythia8EvtGen_AZNLOCTEQ6L1_Zee.simul.TRTxaod_run3baseline_geom_trt119_EXT0`
  2. Run 2: `group.det-indet.mc15_13TeV.361106.PowhegPythia8EvtGen_AZNLOCTEQ6L1_Zee.TRTxAOD.e3601_s2876_trt117-02_EXT0`

Background Samples:

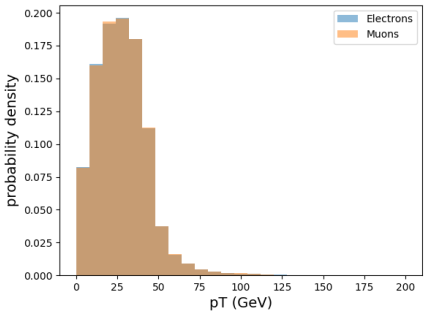
- MC:
  1. Run 3: `group.det-indet.361107.PowhegPythia8EvtGen_AZNLOCTEQ6L1_Zmumu.simul.TRTxaod_run3baseline_geom_trt119-01_EXT0`
  2. Run 3: `group.det-indet.423300.Pythia8EvtGen_A14NNPDF23LO_perf_JF17.TRTxAOD.e3869_e5984_s3126 _trt124_EXT0`
  3. Run 2: `group.det-indet.mc15_13TeV.361107.PowhegPythia8EvtGen_AZNLOCTEQ6L1_Zmumu.TRTxAOD.e3601_s2876_trt117-02_EXT0`

RNN Input Variables

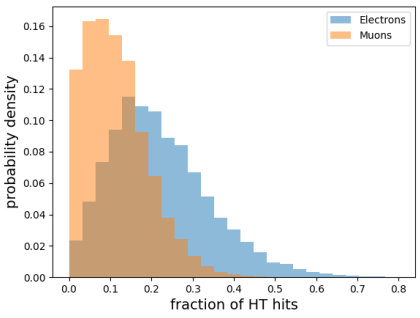
The following pages contain distributions of the RNN input variables.



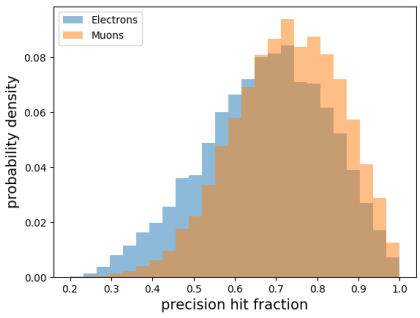
(a) momentum



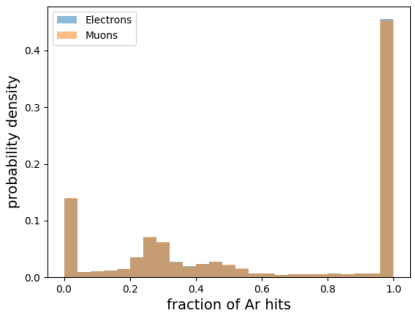
(b) p_T



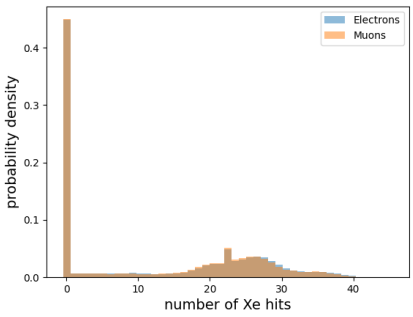
(c) Fraction of High Threshold Hits



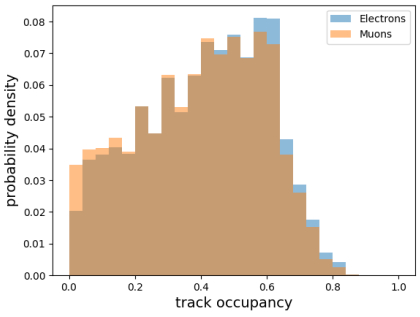
(d) Precision Hit Fraction



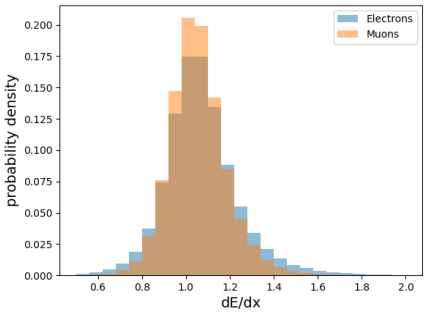
(e) Fraction of Argon Hits



(f) Number of Xenon Hits

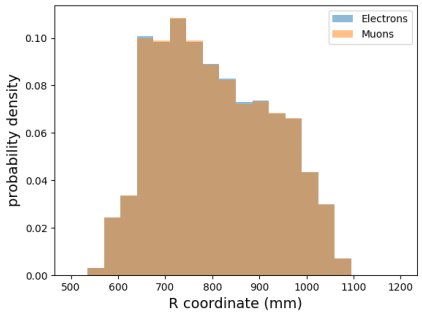


(g) Track Occupancy

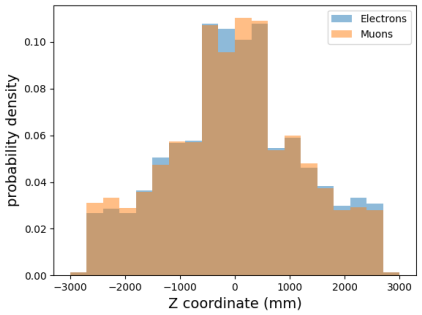


(h) dE/dx

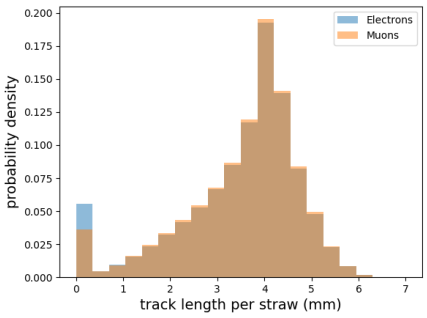
Figure A.1: Track-level variables after re-weighting to achieve a similar p_T and η phase-space for signal and background. Signal and background distributions are mostly congruent, except for high-threshold observables.



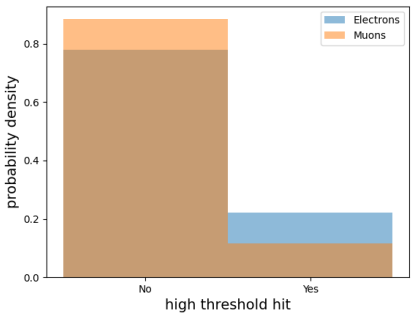
(a) R coordinate



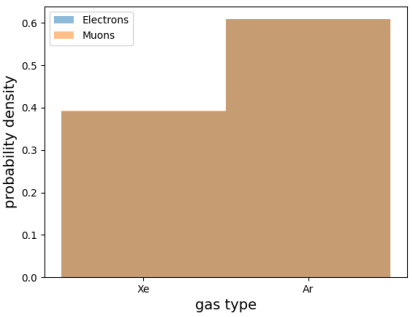
(b) Z coordinate



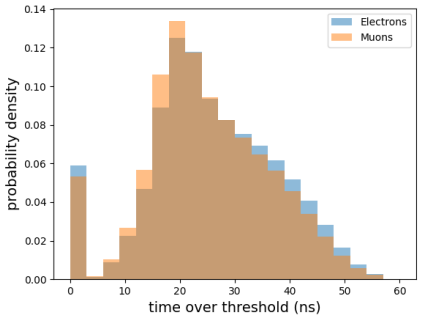
(c) Track length per straw



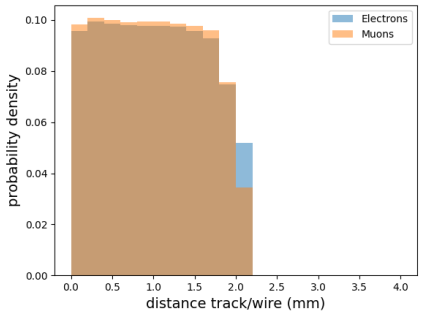
(d) High threshold information



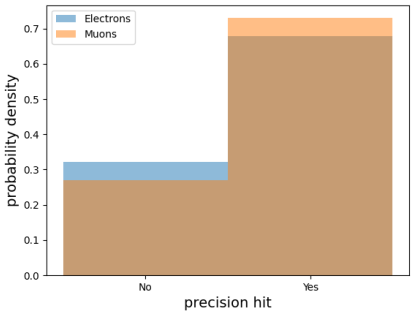
(e) Hit gas type



(f) Time over threhold



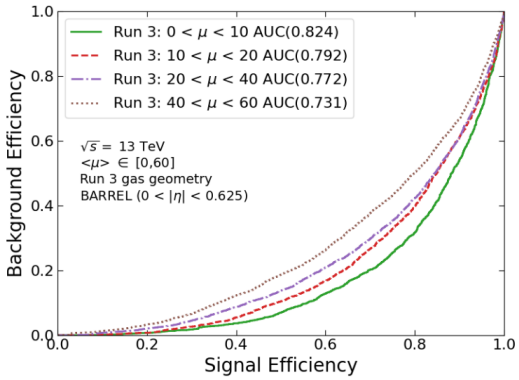
(g) Distance between wire and track



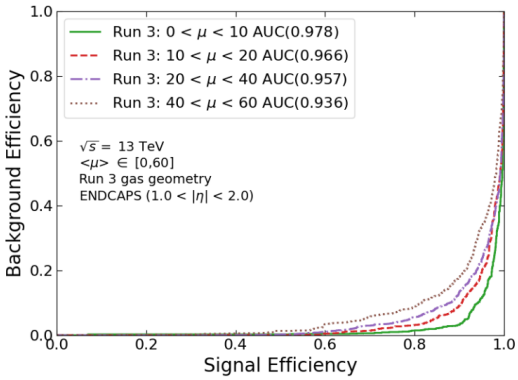
(h) Precision hit information

Figure A.2: Hit-level variables after re-weighting to achieve a similar p_T and η phase-space for signal and background. Signal and background distributions are mostly congruent, except for high-threshold observables.

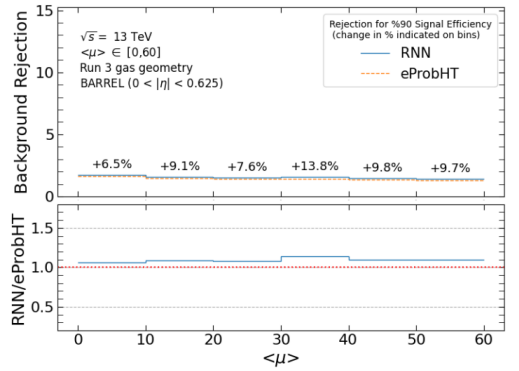
RNN Performance Plots



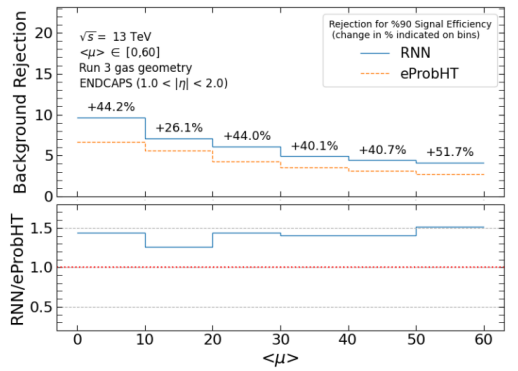
(a) ROC: Barrel Region



(b) ROC: End-cap Region

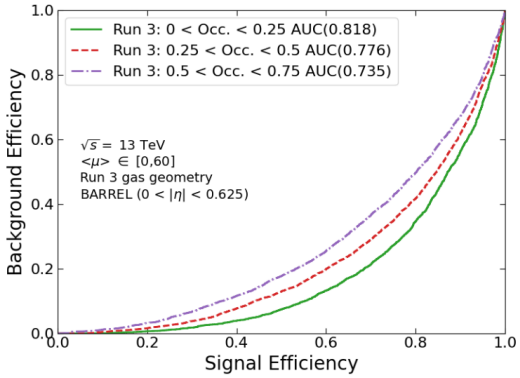


(c) Rejection: Barrel Region

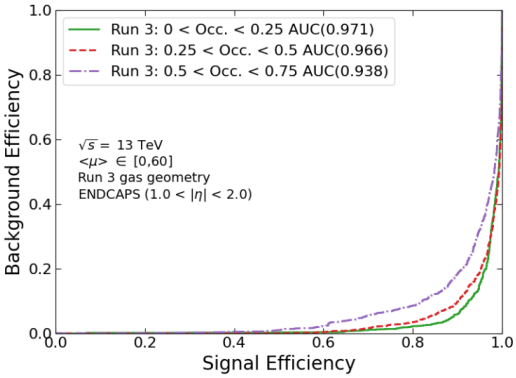


(d) Rejection: End-cap Region

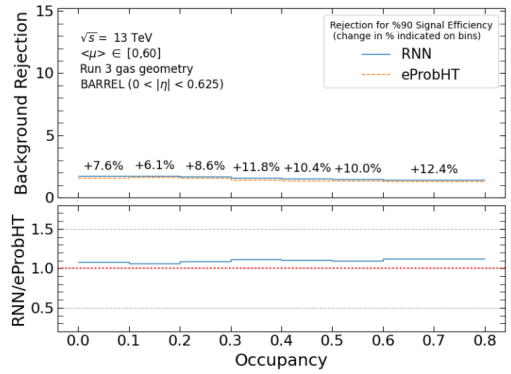
Figure A.3: Performance comparison between the Run 3 RNN and the likelihood-based approach in different pile-up regions. ROC curves as well as the background rejection at 90% signal efficiency are probed in the barrel and the end-cap region.



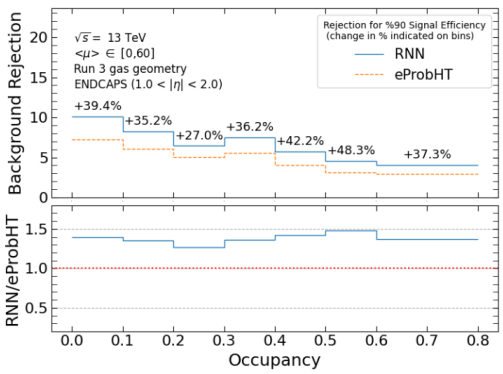
(a) ROC: Barrel Region



(b) ROC: End-cap Region

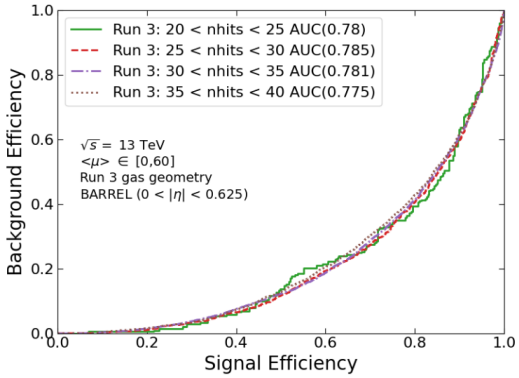


(c) Rejection: Barrel Region

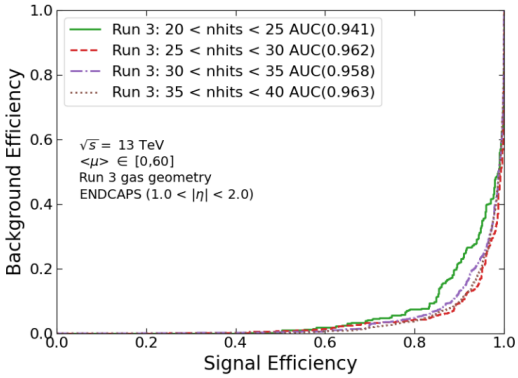


(d) Rejection: End-cap Region

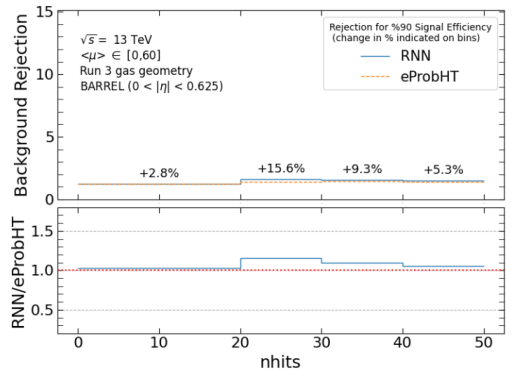
Figure A.4: Performance comparison between the Run 3 RNN and the likelihood-based approach in different occupancy regions. ROC curves as well as the background rejection at 90% signal efficiency are investigated in the barrel and the end-cap region.



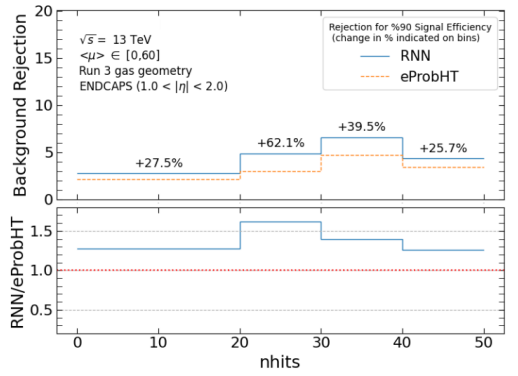
(a) ROC: Barrel Region



(b) ROC: End-cap Region



(c) Rejection: Barrel Region



(d) Rejection: End-cap Region

Figure A.5: Performance comparison between the Run 3 RNN and the likelihood-based approach in dependence on the number of hits. ROC curves as well as the background rejection at 90% signal efficiency are investigated in the barrel and the end-cap region.

APPENDIX B

Auxiliary Material for Chapter 6

Analysis Design of the 2022 Setup

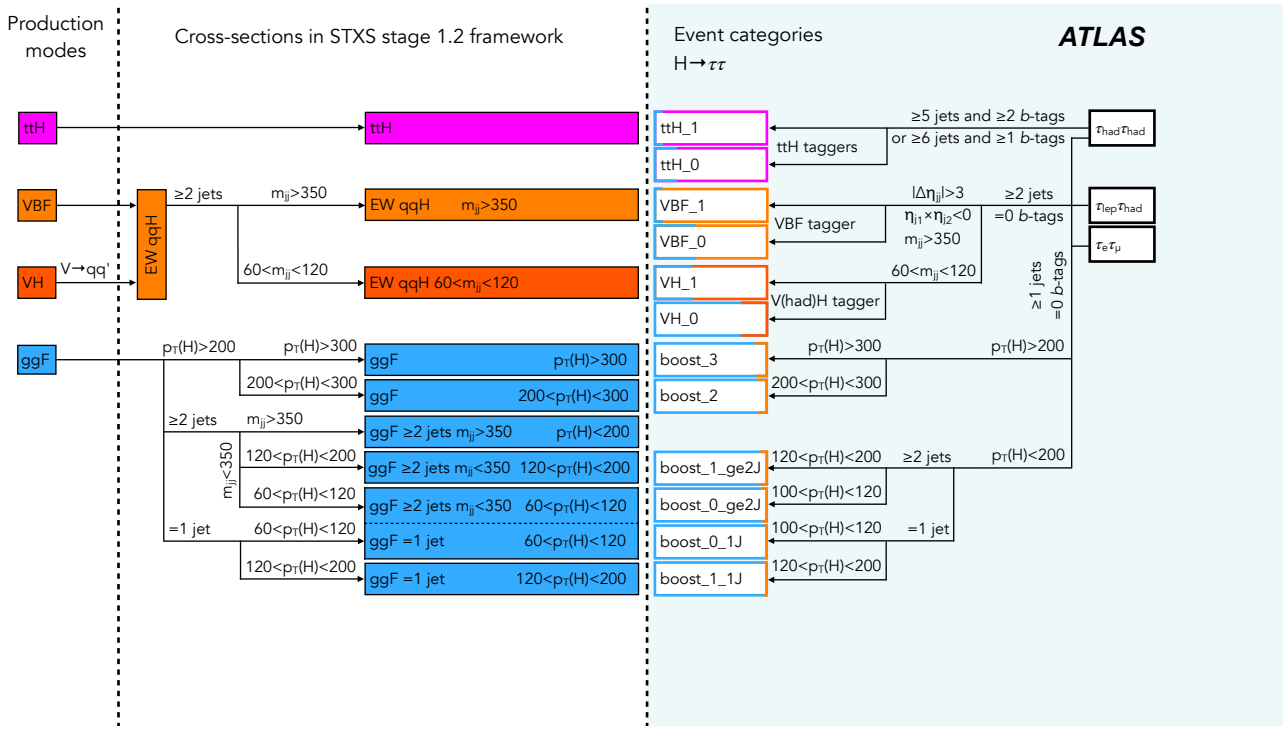
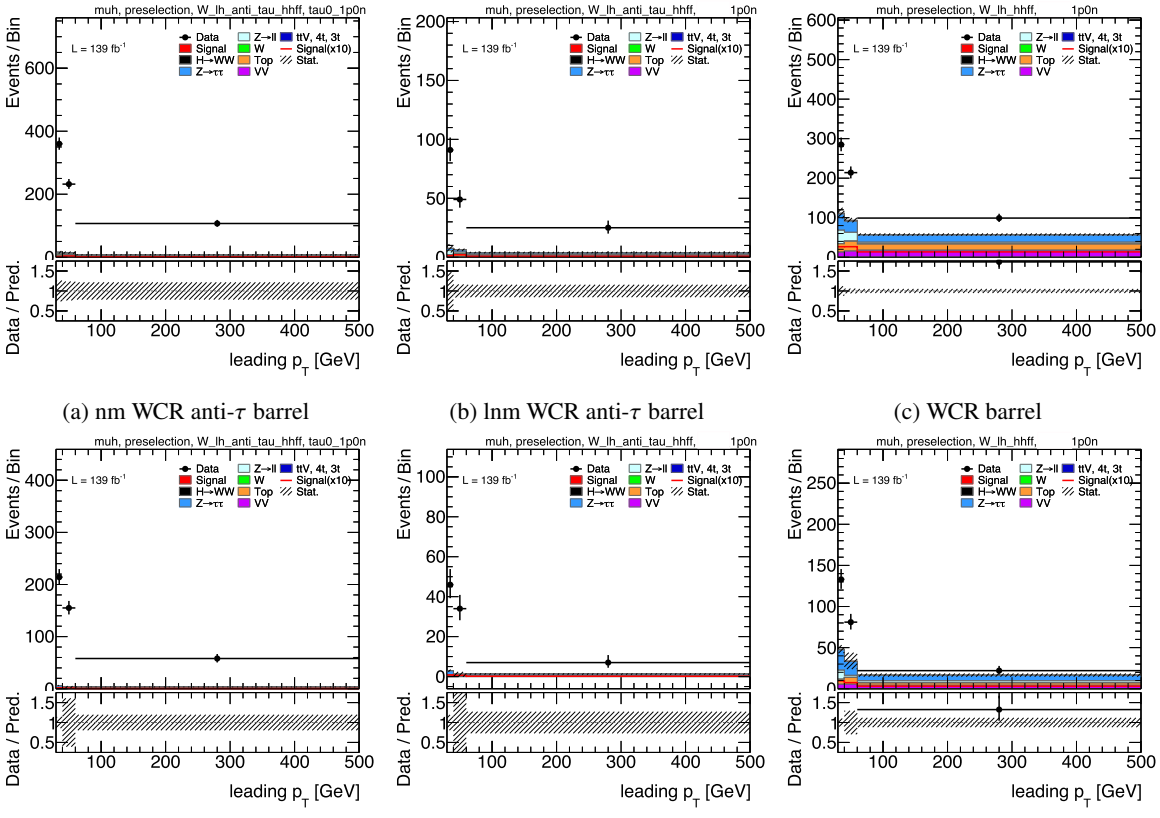


Figure B.1: Targeted cross-sections and the event categorization in the 2022 analysis [71]. Relative contributions from the main STXS bins are indicated by the colors along the category boxes [71].

APPENDIX C

Auxiliary Material for Chapter 7

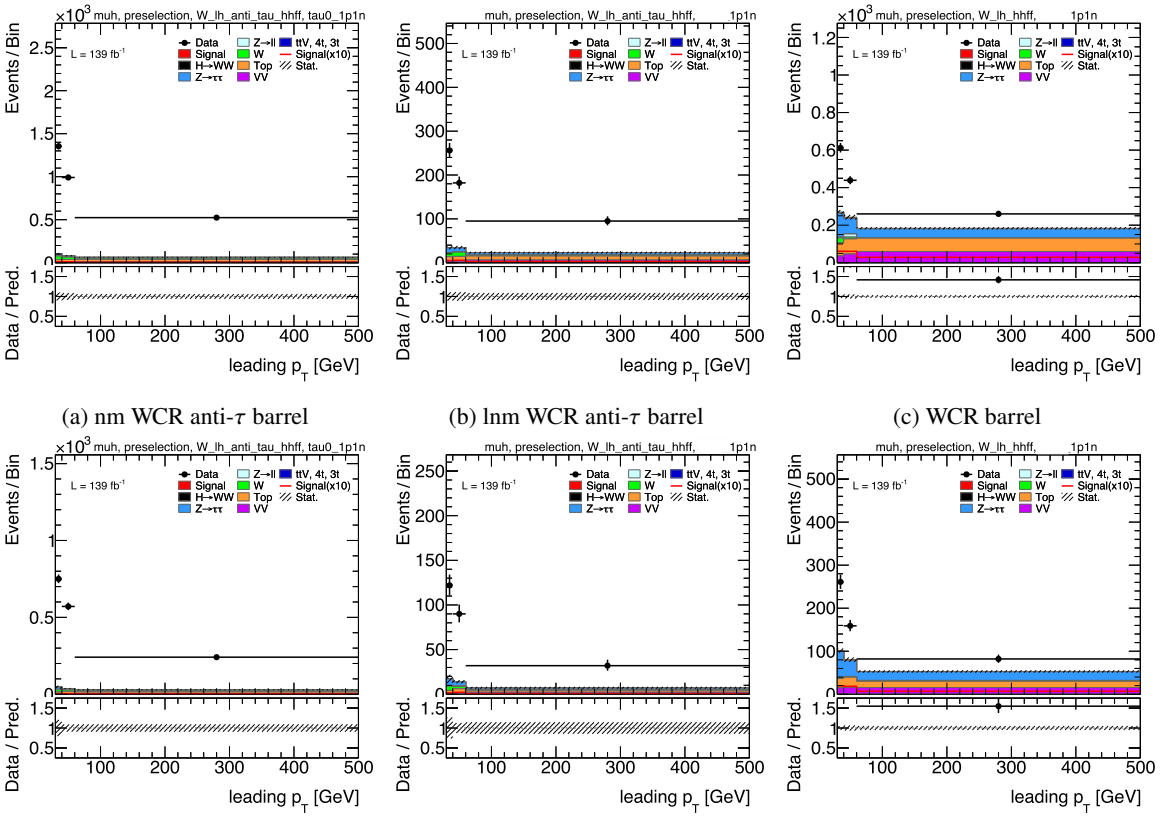
Phase-Space Regions Relevant for Fake Factor Calculation



(a) nm WCR anti-τ barrel (b) lnm WCR anti-τ barrel (c) WCR barrel

(d) nm WCR anti-τ endcaps (e) lnm WCR anti-τ endcaps (f) WCR endcaps

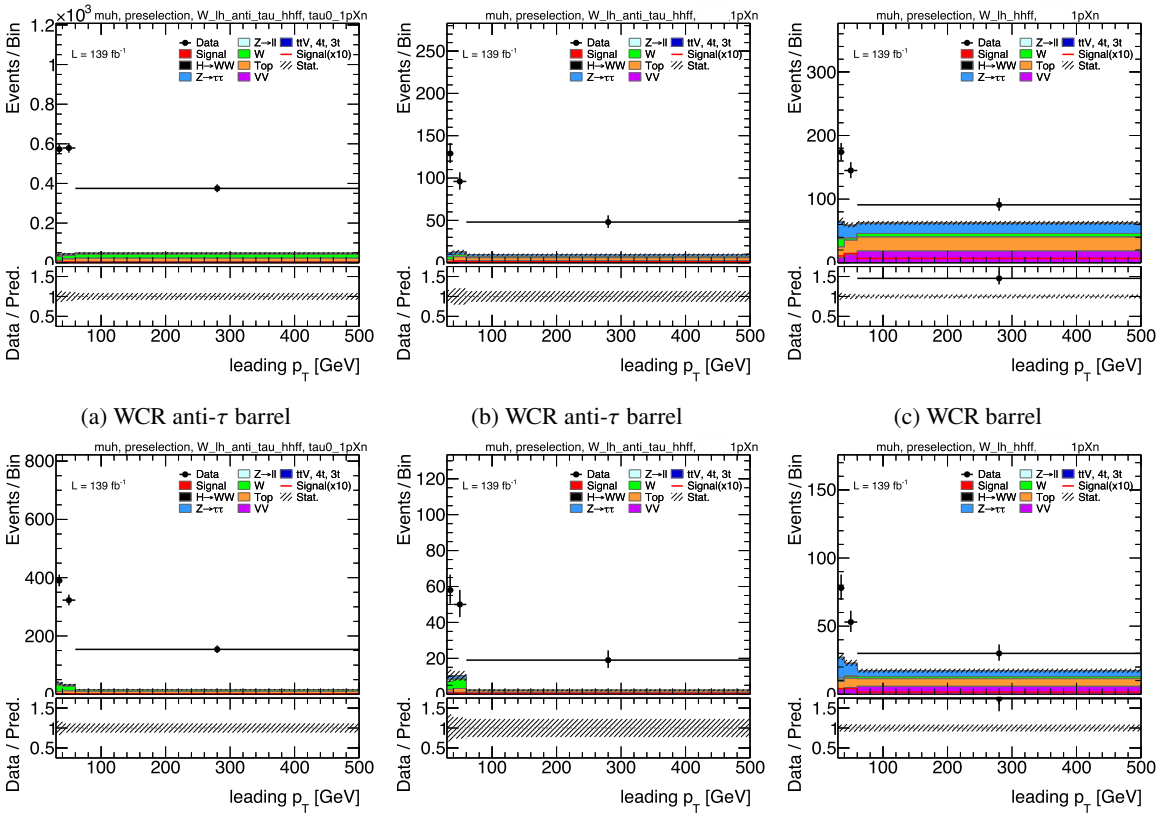
Figure C.1: WCRs used for 1p0n fake factor calculation. The p_T phase space is shown separately for the barrel, $|\eta| < 1.37$ and the end-cap region $1.37 < |\eta| < 2.5$. In addition to the τ-like CR, the nm and lnm anti-τ region is shown.



(a) nm WCR anti-τ barrel (b) lnm WCR anti-τ barrel (c) WCR barrel

(d) nm WCR anti-τ endcaps (e) lnm WCR anti-τ endcaps (f) WCR endcaps

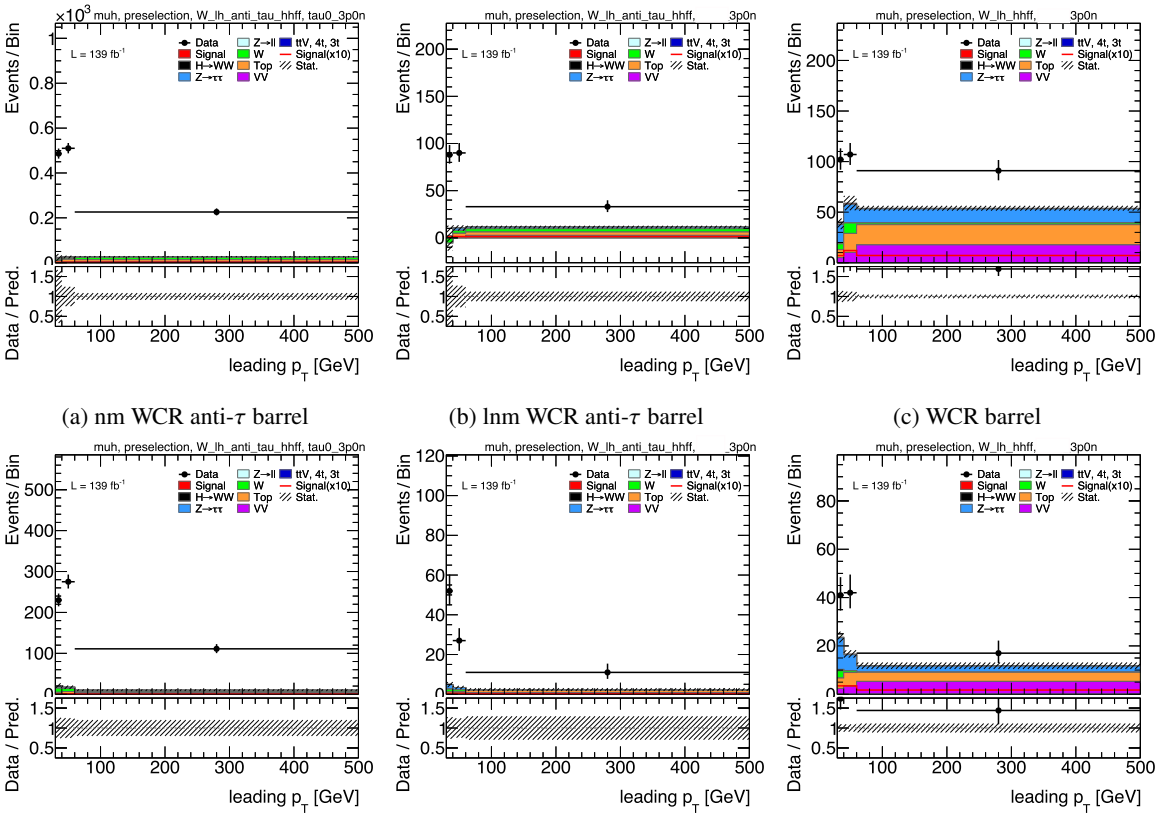
Figure C.2: WCRs used for 1p1n fake factor calculation. The p_T phase space is shown separately for the barrel, $|\eta| < 1.37$ and the end-cap region $1.37 < |\eta| < 2.5$. In addition to the τ-like CR, the nm and lnm anti-τ region is shown.



(a) WCR anti-τ barrel (b) WCR anti-τ barrel (c) WCR barrel

(d) WCR anti-τ endcaps (e) WCR anti-τ endcaps (f) WCR endcaps

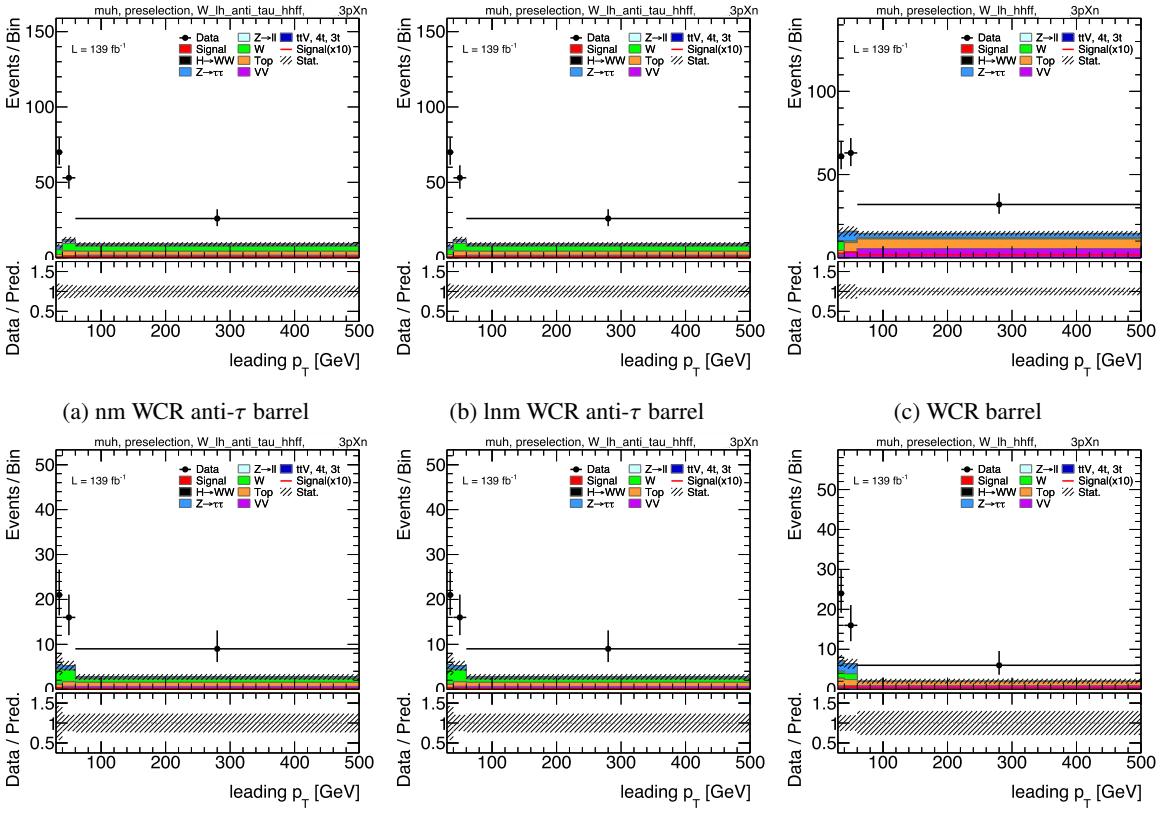
Figure C.3: WCRs used for 1pXn fake factor calculation. The p_T phase space is shown separately for the barrel, $|\eta| < 1.37$ and the end-cap region $1.37 < |\eta| < 2.5$. In addition to the τ-like CR, the nm and lnm anti-τ region is shown.



(a) nm WCR anti-τ barrel (b) lnm WCR anti-τ barrel (c) WCR barrel

(d) nm WCR anti-τ endcaps (e) lnm WCR anti-τ endcaps (f) WCR endcaps

Figure C.4: WCRs used for 1p0n fake factor calculation. The p_T phase space is shown separately for the barrel, $|\eta| < 1.37$ and the end-cap region $1.37 < |\eta| < 2.5$. In addition to the τ-like CR, the nm and lnm anti-τ region is shown.

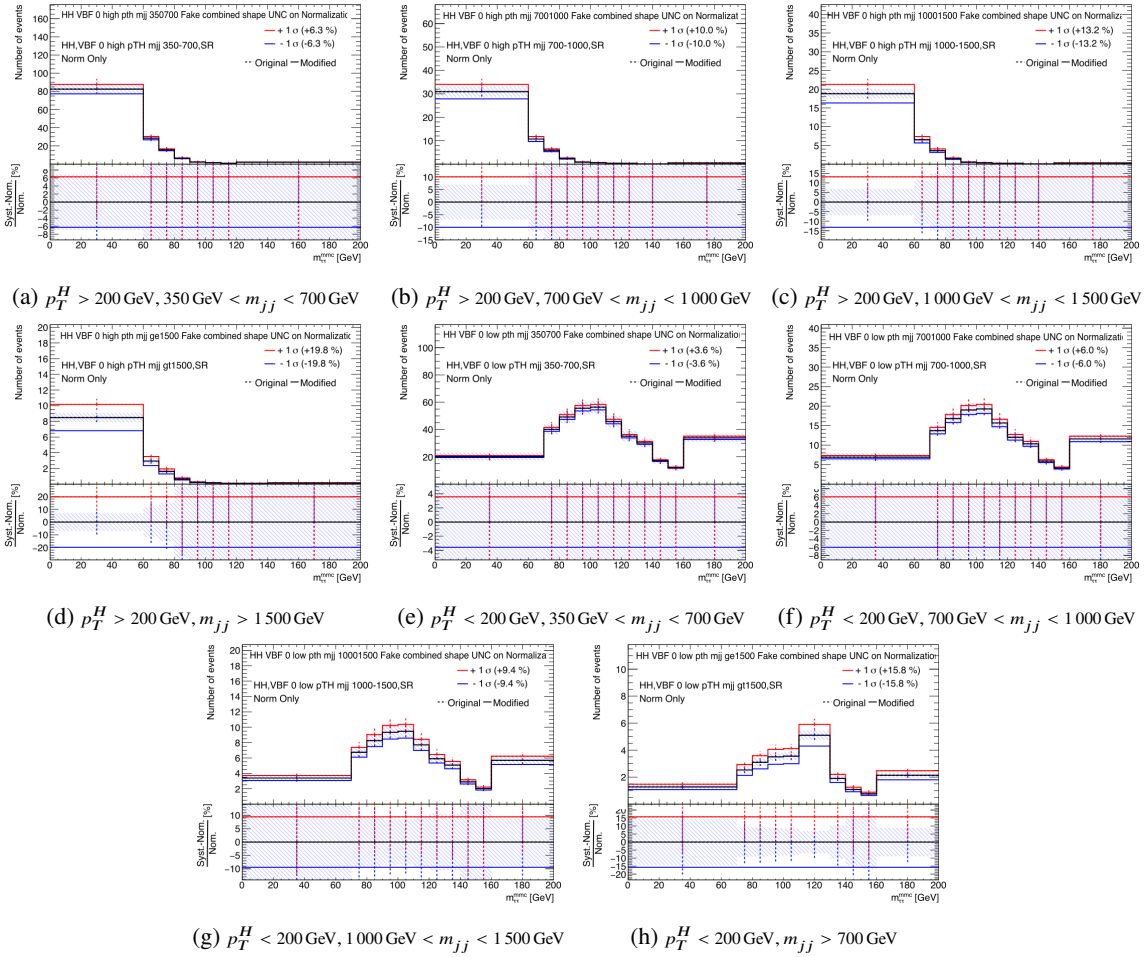


(a) nm WCR anti-τ barrel (b) lnm WCR anti-τ barrel (c) WCR barrel

(d) nm WCR anti-τ endcaps (e) lnm WCR anti-τ endcaps (f) WCR endcaps

Figure C.5: WCRs used for 3pXn fake factor calculation. The p_T phase space is shown separately for the barrel, $|\eta| < 1.37$ and the end-cap region $1.37 < |\eta| < 2.5$. In addition to the τ-like CR, the nm and lnm anti-τ region is shown.

Normalization Uncertainty Envelops

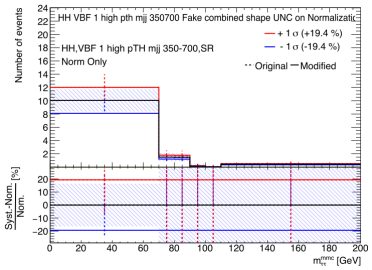


(a) $p_T^H > 200\,\text{GeV}, 350\,\text{GeV} < m_{jj} < 700\,\text{GeV}$ (b) $p_T^H > 200\,\text{GeV}, 700\,\text{GeV} < m_{jj} < 1\,000\,\text{GeV}$ (c) $p_T^H > 200\,\text{GeV}, 1\,000\,\text{GeV} < m_{jj} < 1\,500\,\text{GeV}$

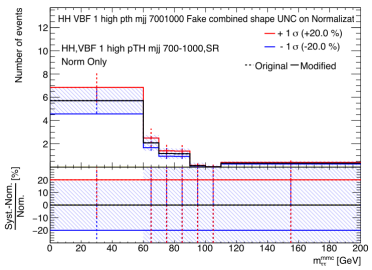
(d) $p_T^H > 200\,\text{GeV}, m_{jj} > 1\,500\,\text{GeV}$ (e) $p_T^H < 200\,\text{GeV}, 350\,\text{GeV} < m_{jj} < 700\,\text{GeV}$ (f) $p_T^H < 200\,\text{GeV}, 700\,\text{GeV} < m_{jj} < 1\,000\,\text{GeV}$

(g) $p_T^H < 200\,\text{GeV}, 1\,000\,\text{GeV} < m_{jj} < 1\,500\,\text{GeV}$ (h) $p_T^H < 200\,\text{GeV}, m_{jj} > 700\,\text{GeV}$

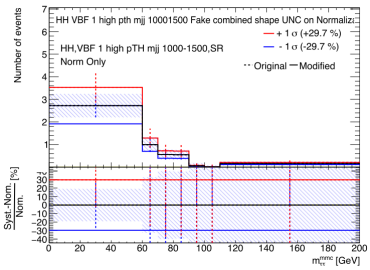
Figure C.6: Envelops of the fake shape combination normalization uncertainty in the $\tau_{\text{had}}\tau_{\text{had}}$ VBF 0 channel.



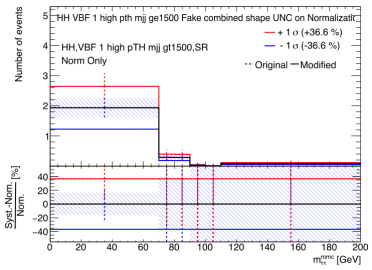
(a) $p_T^H > 200\,\text{GeV}, 350\,\text{GeV} < m_{jj} < 700\,\text{GeV}$



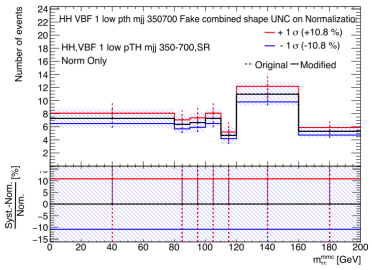
(b) $p_T^H > 200\,\text{GeV}, 700\,\text{GeV} < m_{jj} < 1\,000\,\text{GeV}$



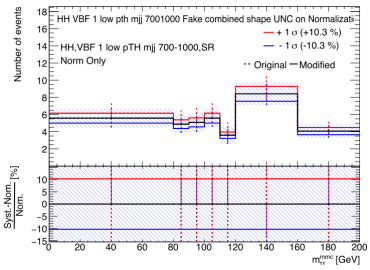
(c) $p_T^H > 200\,\text{GeV}, 1\,000\,\text{GeV} < m_{jj} < 1\,500\,\text{GeV}$



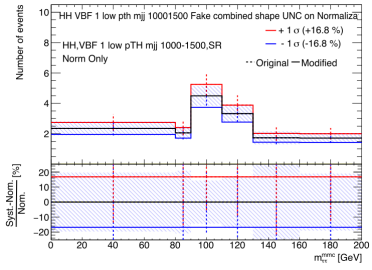
(d) $p_T^H > 200\,\text{GeV}, m_{jj} > 1\,500\,\text{GeV}$



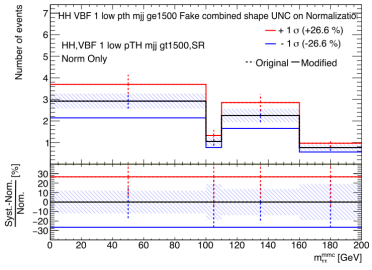
(e) $p_T^H < 200\,\text{GeV}, 350\,\text{GeV} < m_{jj} < 700\,\text{GeV}$



(f) $p_T^H < 200\,\text{GeV}, 700\,\text{GeV} < m_{jj} < 1\,000\,\text{GeV}$

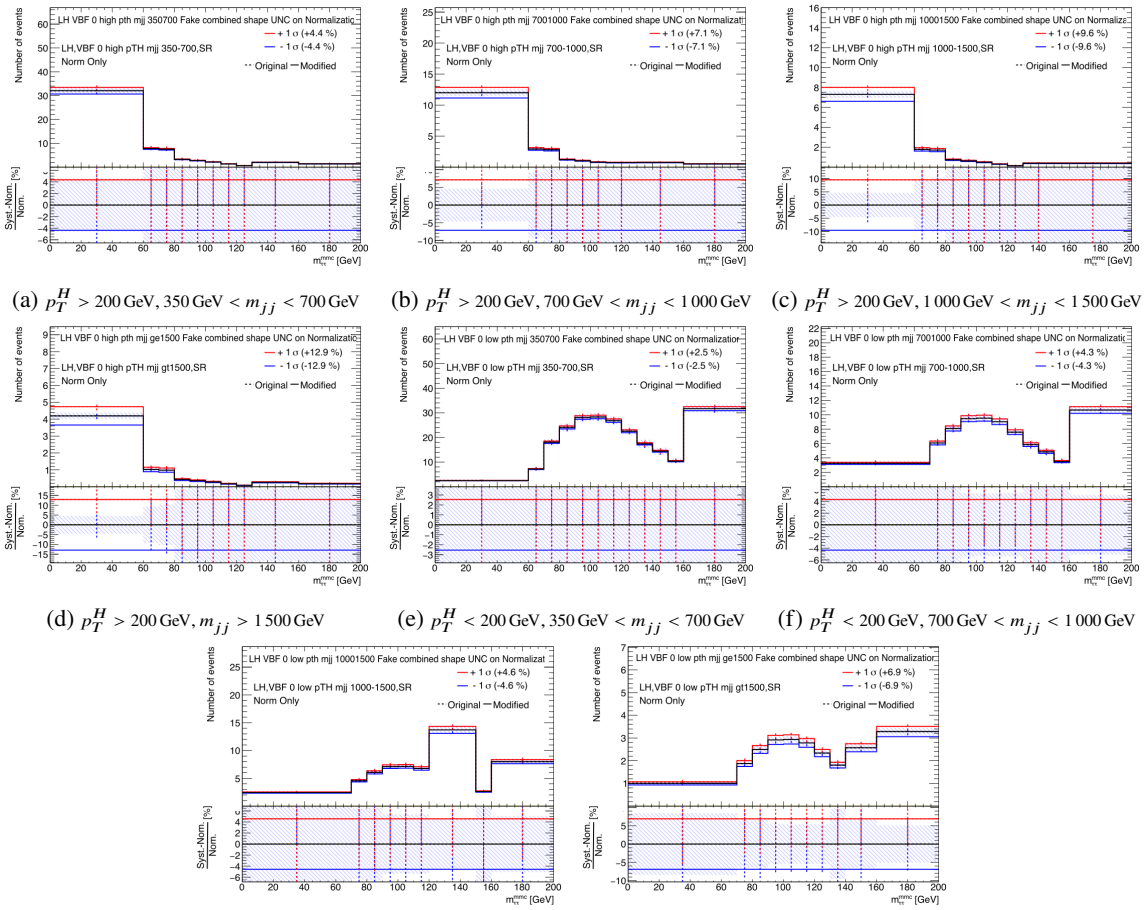


(g) $p_T^H < 200\,\text{GeV}, 1\,000\,\text{GeV} < m_{jj} < 1\,500\,\text{GeV}$



(h) $p_T^H < 200\,\text{GeV}, m_{jj} > 1\,500\,\text{GeV}$

Figure C.7: Envelops of the fake shape combination normalization uncertainty in the $\tau_{\text{had}}\tau_{\text{had}}$ VBF 1 channel.

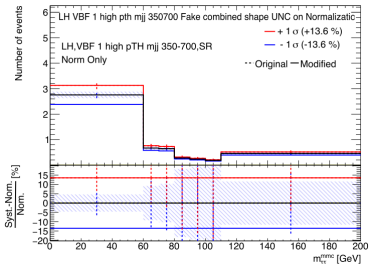


(a) $p_T^H > 200\,\text{GeV}, 350\,\text{GeV} < m_{jj} < 700\,\text{GeV}$ (b) $p_T^H > 200\,\text{GeV}, 700\,\text{GeV} < m_{jj} < 1\,000\,\text{GeV}$ (c) $p_T^H > 200\,\text{GeV}, 1\,000\,\text{GeV} < m_{jj} < 1\,500\,\text{GeV}$

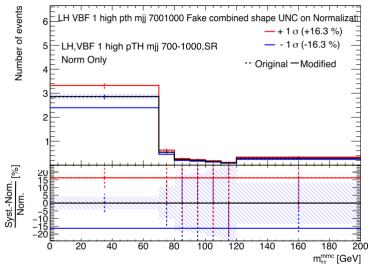
(d) $p_T^H > 200\,\text{GeV}, m_{jj} > 1\,500\,\text{GeV}$ (e) $p_T^H < 200\,\text{GeV}, 350\,\text{GeV} < m_{jj} < 700\,\text{GeV}$ (f) $p_T^H < 200\,\text{GeV}, 700\,\text{GeV} < m_{jj} < 1\,000\,\text{GeV}$

(g) $p_T^H < 200\,\text{GeV}, 1\,000\,\text{GeV} < m_{jj} < 1\,500\,\text{GeV}$ (h) $p_T^H < 200\,\text{GeV}, m_{jj} > 1\,500\,\text{GeV}$

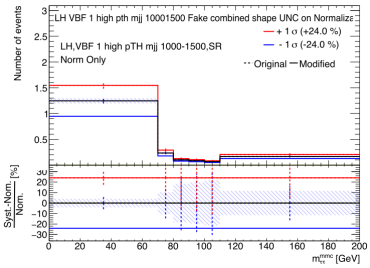
Figure C.8: Envelops of the fake shape combination normalization uncertainty in the $\tau_{\text{lep}}\tau_{\text{had}}$ VBF 0 channel.



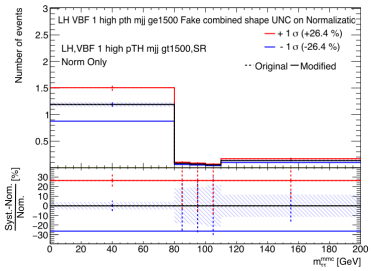
(a) $p_T^H > 200\,\text{GeV}, 350\,\text{GeV} < m_{jj} < 700\,\text{GeV}$



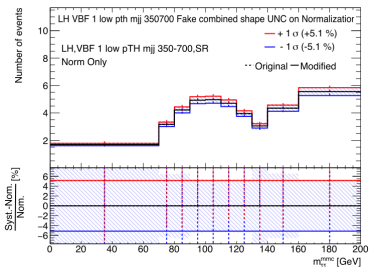
(b) $p_T^H > 200\,\text{GeV}, 700\,\text{GeV} < m_{jj} < 1\,000\,\text{GeV}$



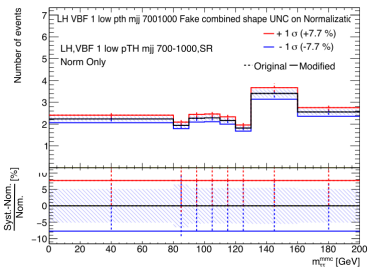
(c) $p_T^H > 200\,\text{GeV}, 1\,000\,\text{GeV} < m_{jj} < 1\,500\,\text{GeV}$



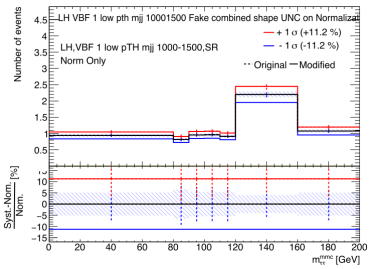
(d) $p_T^H > 200\,\text{GeV}, m_{jj} > 1\,500\,\text{GeV}$



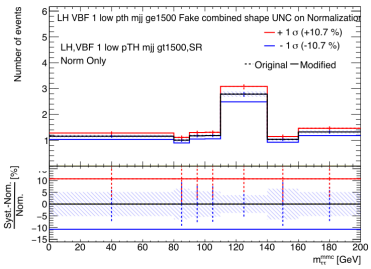
(e) $p_T^H < 200\,\text{GeV}, 350\,\text{GeV} < m_{jj} < 700\,\text{GeV}$



(f) $p_T^H < 200\,\text{GeV}, 700\,\text{GeV} < m_{jj} < 1\,000\,\text{GeV}$

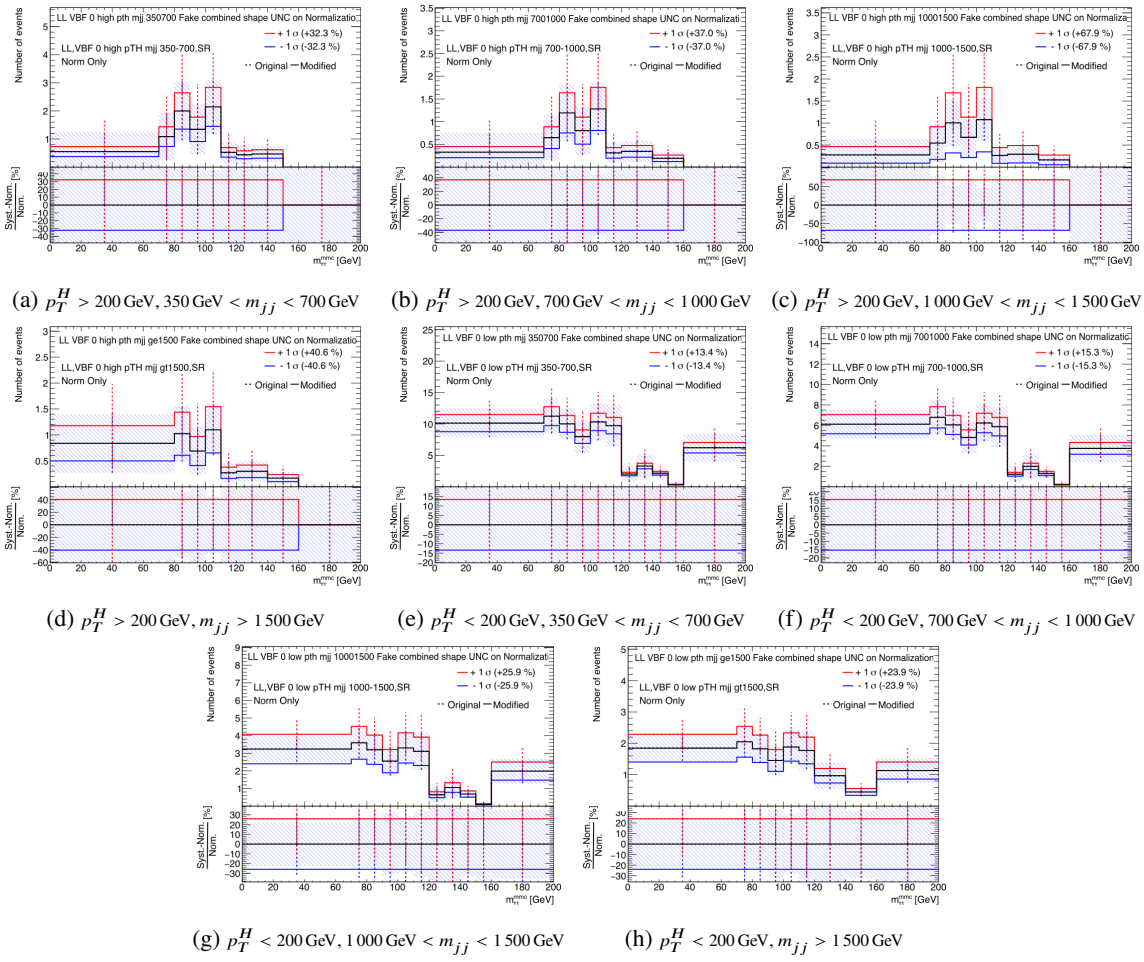


(g) $p_T^H < 200\,\text{GeV}, 1\,000\,\text{GeV} < m_{jj} < 1\,500\,\text{GeV}$



(h) $p_T^H < 200\,\text{GeV}, m_{jj} > 1\,500\,\text{GeV}$

Figure C.9: Envelops of the fake shape combination normalization uncertainty in the $\tau_{\text{lep}}\tau_{\text{had}}$ VBF 1 channel.

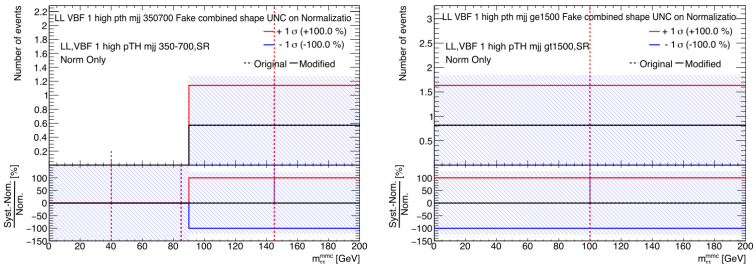


(a) $p_T^H > 200\,\text{GeV}, 350\,\text{GeV} < m_{jj} < 700\,\text{GeV}$ (b) $p_T^H > 200\,\text{GeV}, 700\,\text{GeV} < m_{jj} < 1\,000\,\text{GeV}$ (c) $p_T^H > 200\,\text{GeV}, 1\,000\,\text{GeV} < m_{jj} < 1\,500\,\text{GeV}$

(d) $p_T^H > 200\,\text{GeV}, m_{jj} > 1\,500\,\text{GeV}$ (e) $p_T^H < 200\,\text{GeV}, 350\,\text{GeV} < m_{jj} < 700\,\text{GeV}$ (f) $p_T^H < 200\,\text{GeV}, 700\,\text{GeV} < m_{jj} < 1\,000\,\text{GeV}$

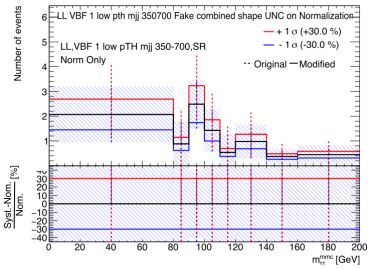
(g) $p_T^H < 200\,\text{GeV}, 1\,000\,\text{GeV} < m_{jj} < 1\,500\,\text{GeV}$ (h) $p_T^H < 200\,\text{GeV}, m_{jj} > 1\,500\,\text{GeV}$

Figure C.10: Envelops of the fake shape combination normalization uncertainty in the $\tau_{\text{lep}}\tau_{\text{lep}}$ VBF 0 channel.

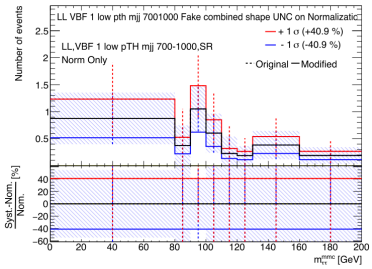


(a) $p_T^H > 200\,\text{GeV}, 350\,\text{GeV} < m_{jj} < 700\,\text{GeV}$

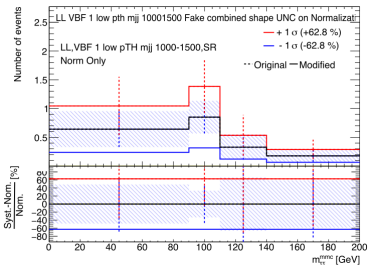
(b) $p_T^H > 200\,\text{GeV}, m_{jj} > 1\,500\,\text{GeV}$



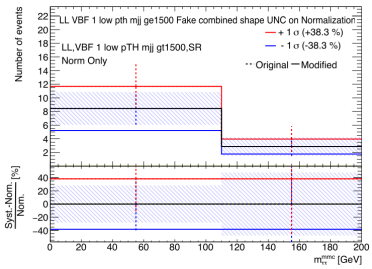
(c) $p_T^H < 200\,\text{GeV}, 350\,\text{GeV} < m_{jj} < 700\,\text{GeV}$



(d) $p_T^H < 200\,\text{GeV}, 700\,\text{GeV} < m_{jj} < 1\,000\,\text{GeV}$



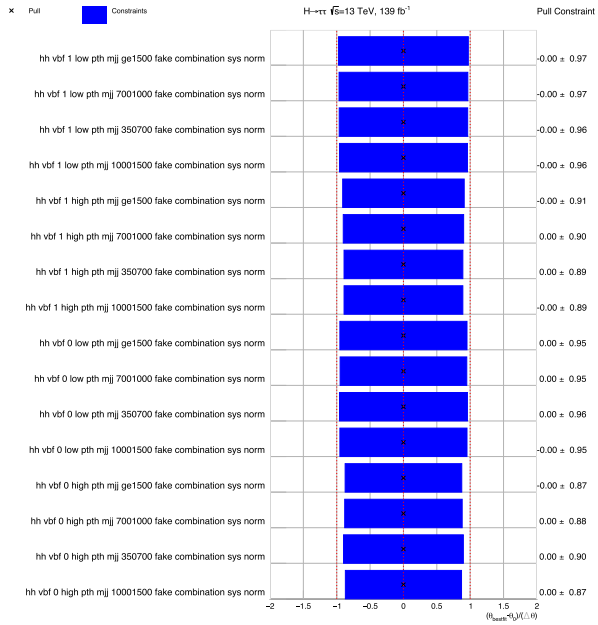
(e) $p_T^H > 200\,\text{GeV}, 1\,000\,\text{GeV} < m_{jj} < 1\,500\,\text{GeV}$



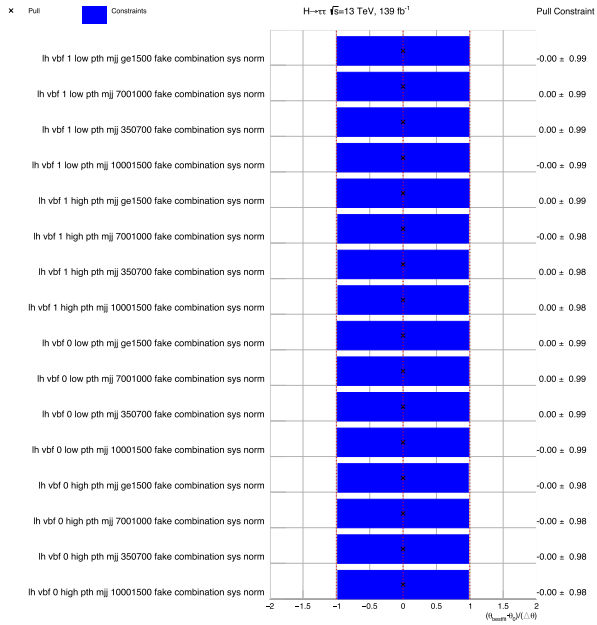
(f) $p_T^H > 200\,\text{GeV}, m_{jj} > 1\,500\,\text{GeV}$

Figure C.11: Envelops of the fake shape combination normalization uncertainty in the $\tau_{\text{lep}}\tau_{\text{lep}}$ VBF 1 channel.

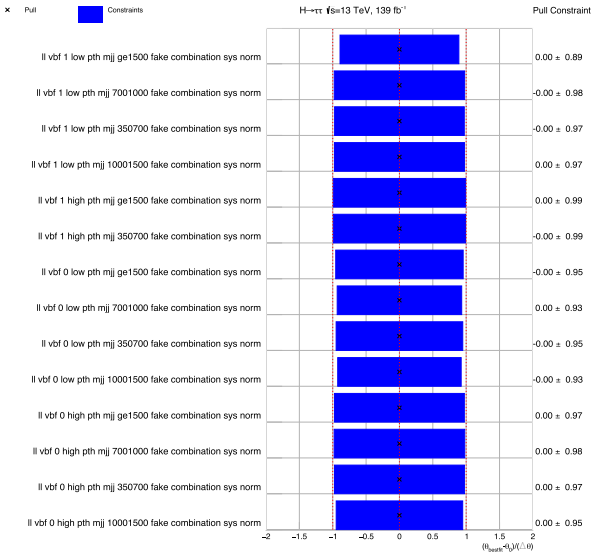
Normalization Uncertainty Constraints



(a) $\tau_{\text{had}}\tau_{\text{had}}$



(b) $\tau_{\text{lep}}\tau_{\text{had}}$



(c) $\tau_{\text{lep}}\tau_{\text{lep}}$

Figure C.12: Constraints on the Normalization Uncertainty in all channels (Asimov fit).

APPENDIX D

Auxiliary Material for Chapter 8

Correlation Studies

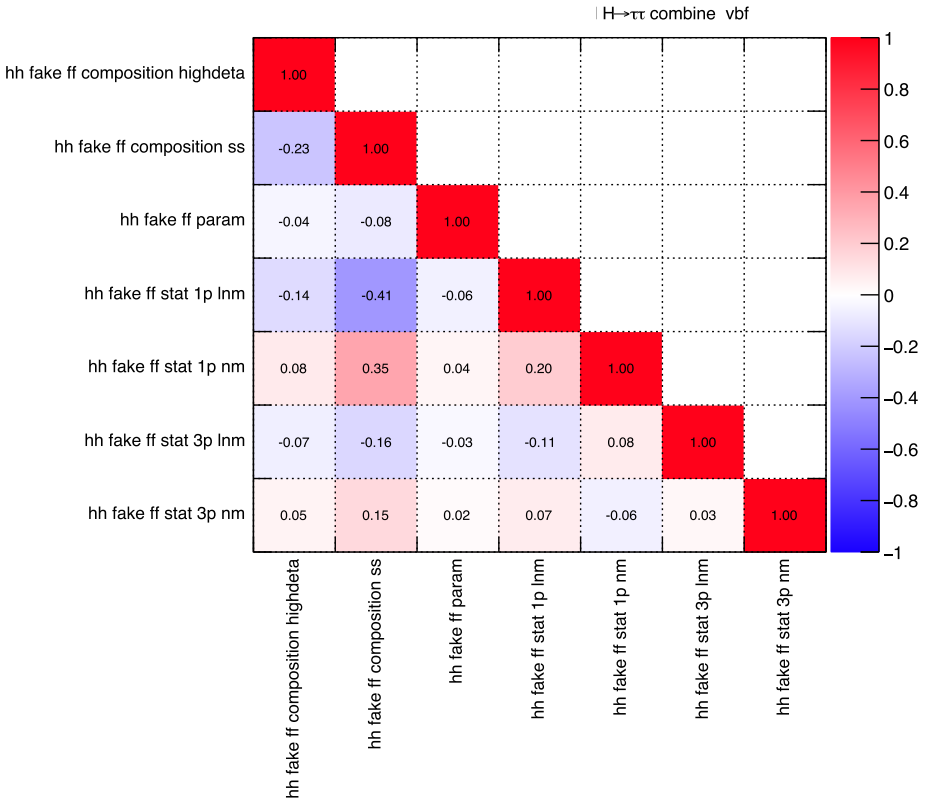


Figure D.1: Correlation of the $\tau_{\text{had}}\tau_{\text{had}}$ fake systematics in a VBF standalone 4PoI random scaling fit.

Asimov De-correlation Studies

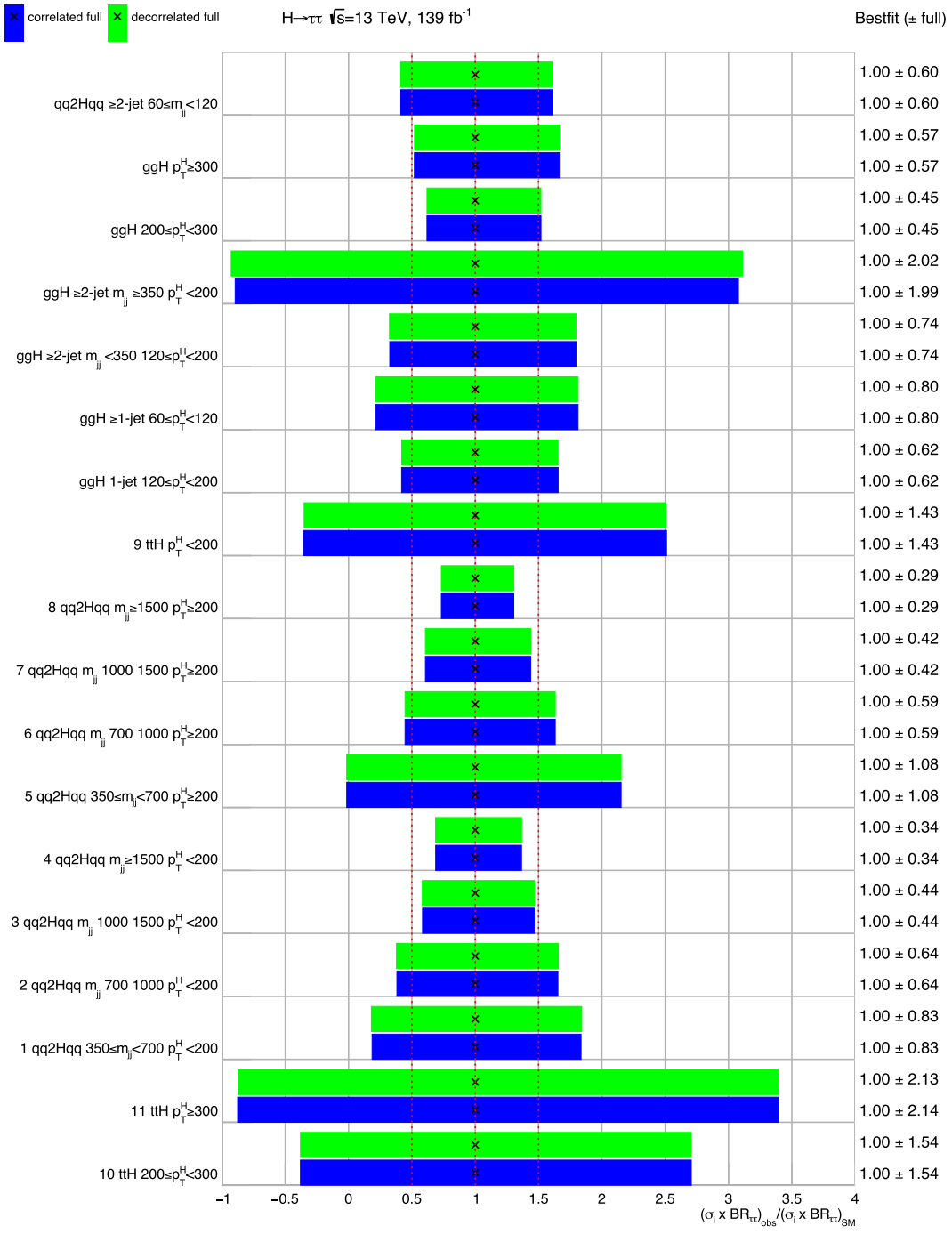
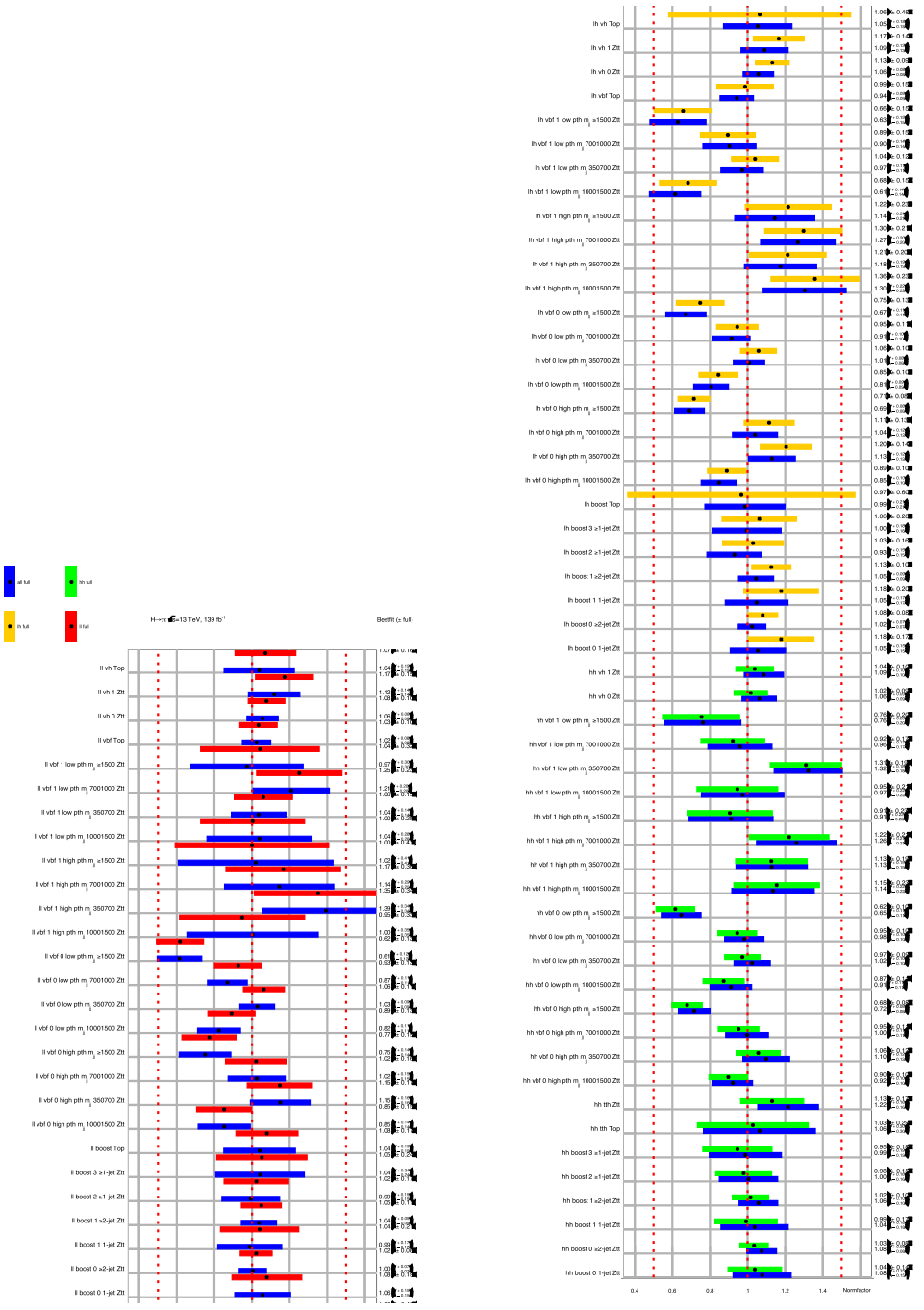


Figure D.2: 18POI sensitivity studies with Asimov data. The common setup is depicted in blue. For the results shown in green, a setup using a de-correlated *hh fake ff composition high-deta* as well as *hh fake ff stat 1p lnm* systematic is used. No discrepancies are observed.

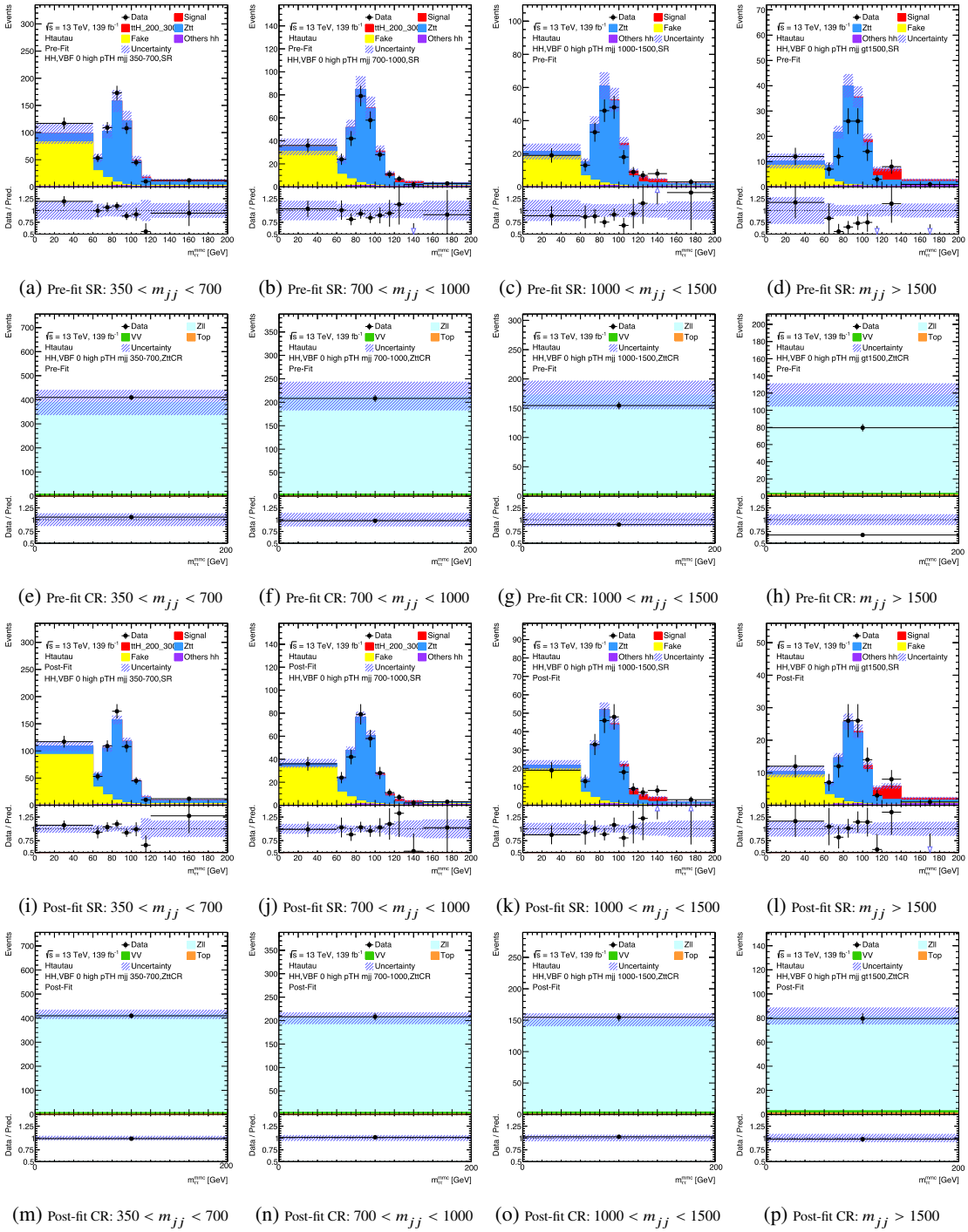
Normalization Factors in Random Scaling Fit



(a) $\tau_{\text{had}}\tau_{\text{had}}$ (b) $\tau_{\text{lep}}\tau_{\text{had}}$, $\tau_{\text{lep}}\tau_{\text{lep}}$

Figure D.3: Normalization factors for Z($\rightarrow \tau\tau$)+jets and top backgrounds in the random μ fit. The fit combining all channels is depicted in blue, the $\tau_{\text{had}}\tau_{\text{had}}$,$\tau_{\text{lep}}\tau_{\text{had}}$,$\tau_{\text{lep}}\tau_{\text{lep}}$ standalone fit in red, yellow, green, respectively.

Unblinded Pre- and Post-fit Distributions



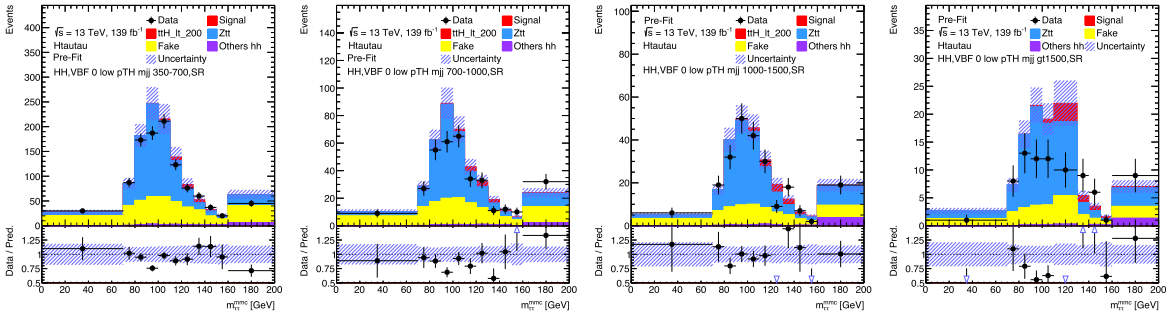
(a) Pre-fit SR: $350 < m_{jj} < 700$ (b) Pre-fit SR: $700 < m_{jj} < 1000$ (c) Pre-fit SR: $1000 < m_{jj} < 1500$ (d) Pre-fit SR: $m_{jj} > 1500$

(e) Pre-fit CR: $350 < m_{jj} < 700$ (f) Pre-fit CR: $700 < m_{jj} < 1000$ (g) Pre-fit CR: $1000 < m_{jj} < 1500$ (h) Pre-fit CR: $m_{jj} > 1500$

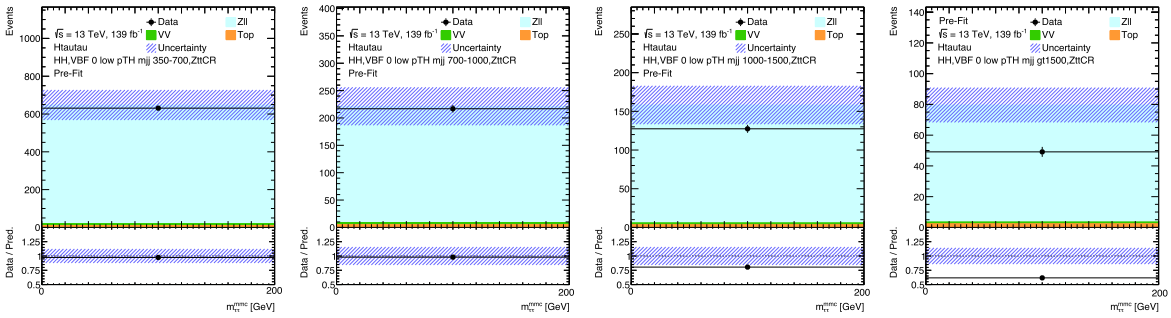
(i) Post-fit SR: $350 < m_{jj} < 700$ (j) Post-fit SR: $700 < m_{jj} < 1000$ (k) Post-fit SR: $1000 < m_{jj} < 1500$ (l) Post-fit SR: $m_{jj} > 1500$

(m) Post-fit CR: $350 < m_{jj} < 700$ (n) Post-fit CR: $700 < m_{jj} < 1000$ (o) Post-fit CR: $1000 < m_{jj} < 1500$ (p) Post-fit CR: $m_{jj} > 1500$

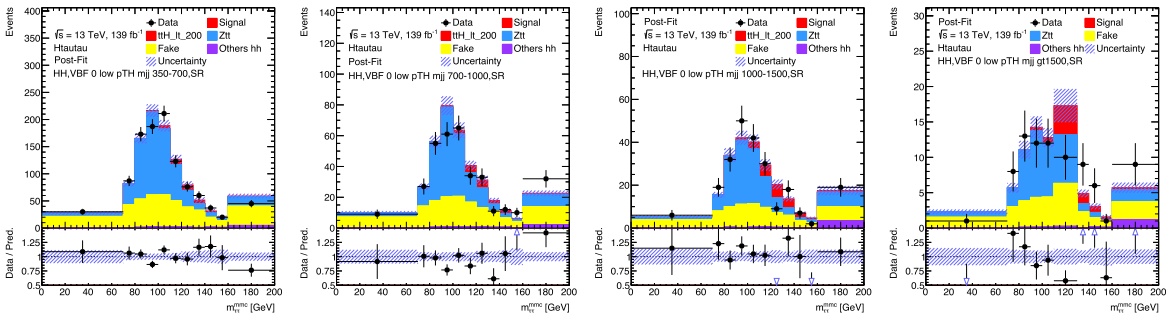
Figure D.4: Pre- and post-fit distributions of the VBF 0 high p_T^H regions in the $\tau_{\text{had}}\tau_{\text{had}}$ channel of the unblinded 18 PoI fit setup.



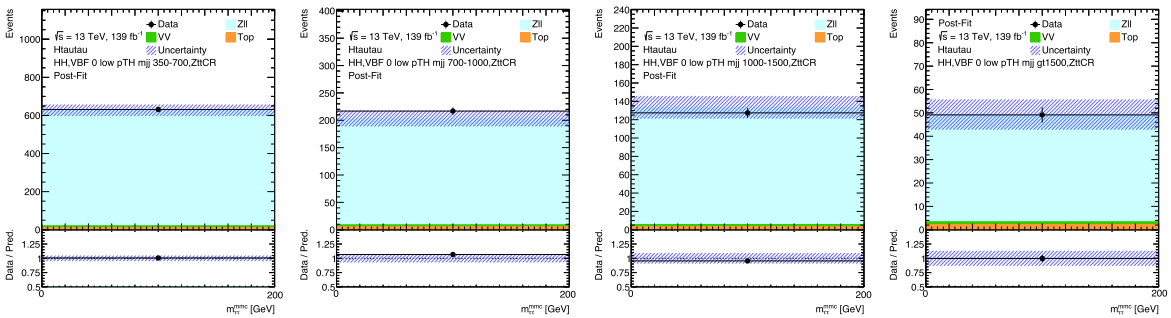
(a) Pre-fit SR: $350 < m_{jj} < 700$ (b) Pre-fit SR: $700 < m_{jj} < 1000$ (c) Pre-fit SR: $1000 < m_{jj} < 1500$ (d) Pre-fit SR: $m_{jj} > 1500$



(e) Pre-fit CR: $350 < m_{jj} < 700$ (f) Pre-fit CR: $700 < m_{jj} < 1000$ (g) Pre-fit CR: $1000 < m_{jj} < 1500$ (h) Pre-fit CR: $m_{jj} > 1500$

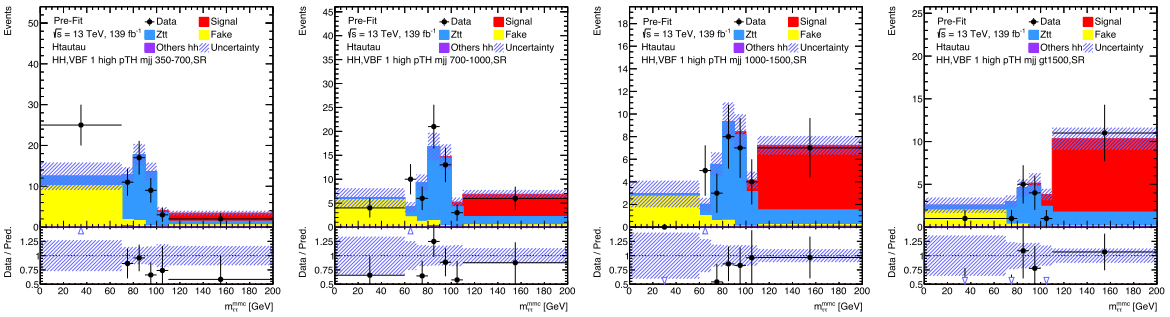


(i) Post-fit SR: $350 < m_{jj} < 700$ (j) Post-fit SR: $700 < m_{jj} < 1000$ (k) Post-fit SR: $1000 < m_{jj} < 1500$ (l) Post-fit SR: $m_{jj} > 1500$

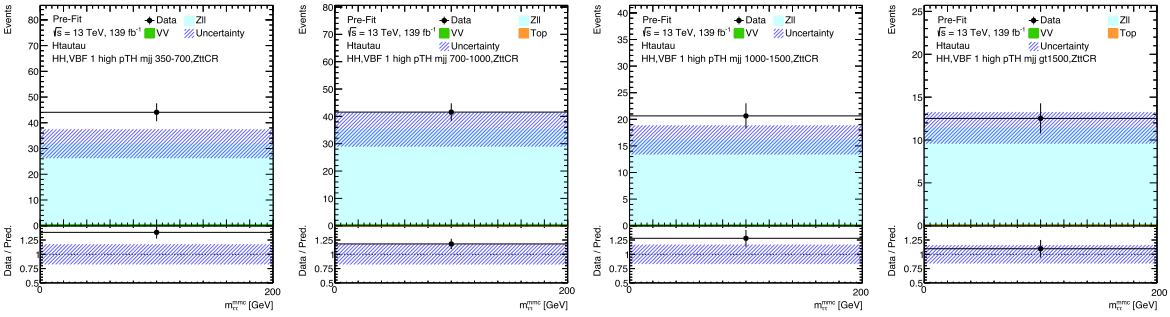


(m) Post-fit CR: $350 < m_{jj} < 700$ (n) Post-fit CR: $700 < m_{jj} < 1000$ (o) Post-fit CR: $1000 < m_{jj} < 1500$ (p) Post-fit CR: $m_{jj} > 1500$

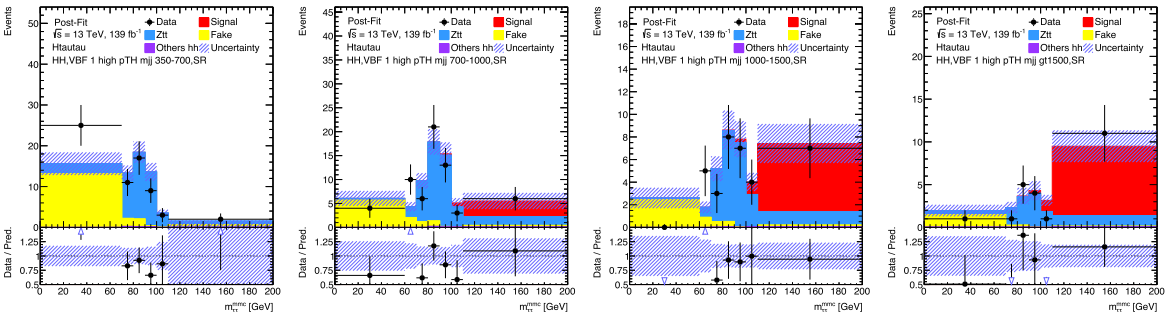
Figure D.5: Pre- and post-fit distributions of the VBF 0 low p_T^H regions in the $\tau_{\text{had}}\tau_{\text{had}}$ channel of the unblinded 18 PoI fit setup.



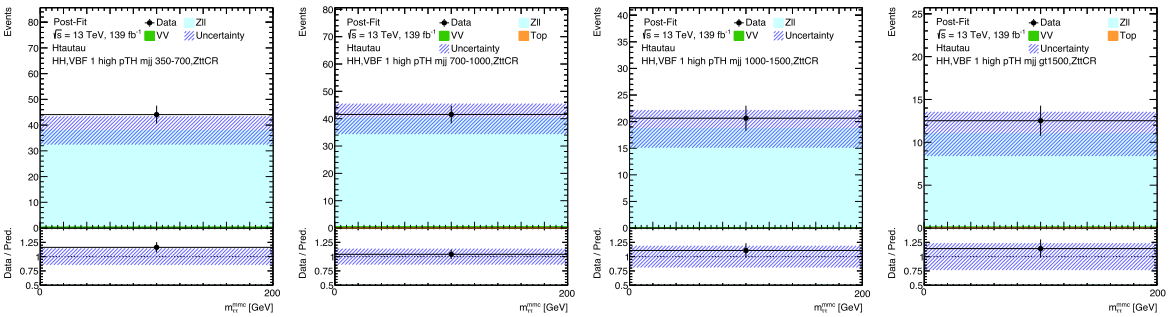
(a) Pre-fit SR: $350 < m_{jj} < 700$ (b) Pre-fit SR: $700 < m_{jj} < 1000$ (c) Pre-fit SR: $1000 < m_{jj} < 1500$ (d) Pre-fit SR: $m_{jj} > 1500$



(e) Pre-fit CR: $350 < m_{jj} < 700$ (f) Pre-fit CR: $700 < m_{jj} < 1000$ (g) Pre-fit CR: $1000 < m_{jj} < 1500$ (h) Pre-fit CR: $m_{jj} > 1500$

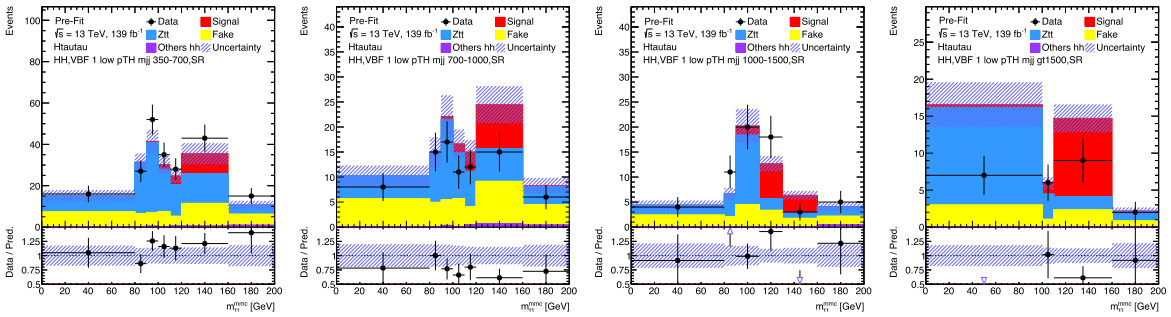


(i) Post-fit SR: $350 < m_{jj} < 700$ (j) Post-fit SR: $700 < m_{jj} < 1000$ (k) Post-fit SR: $1000 < m_{jj} < 1500$ (l) Post-fit SR: $m_{jj} > 1500$

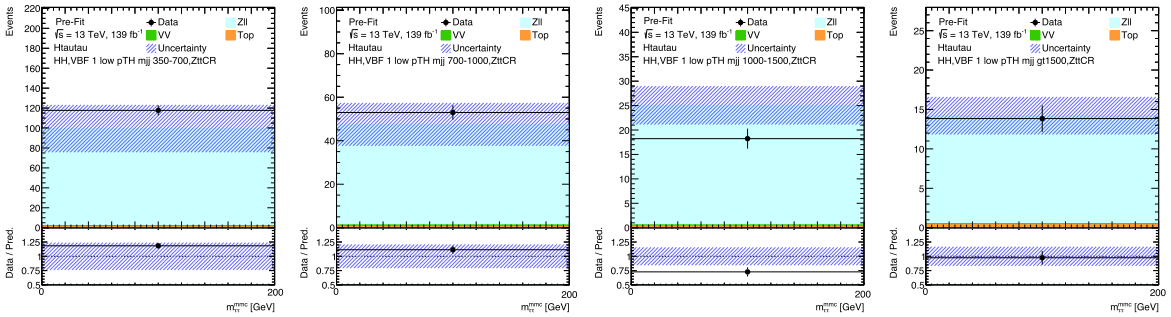


(m) Post-fit CR: $350 < m_{jj} < 700$ (n) Post-fit CR: $700 < m_{jj} < 1000$ (o) Post-fit CR: $1000 < m_{jj} < 1500$ (p) Post-fit CR: $m_{jj} > 1500$

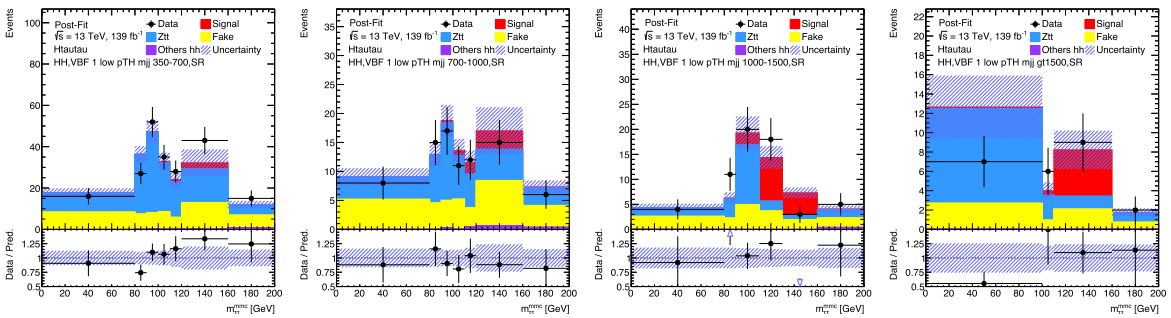
Figure D.6: Pre- and post-fit distributions of the VBF 1 high p_T^H regions in the $\tau_{\text{had}}\tau_{\text{had}}$ channel of the unblinded 18 PoI fit setup.



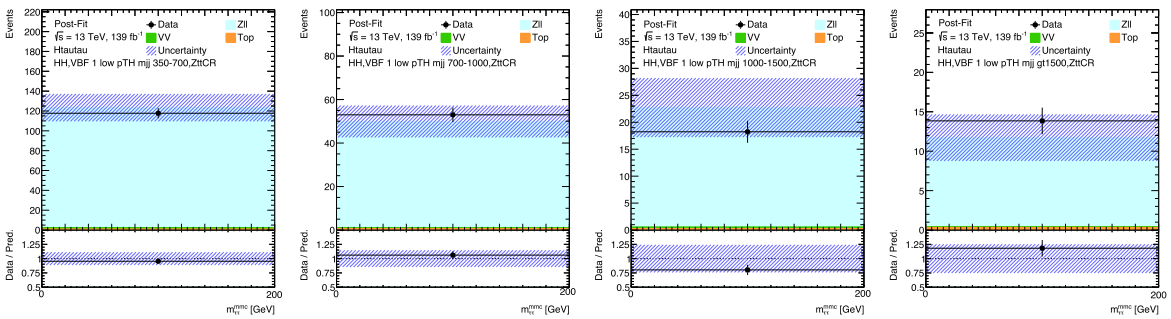
(a) Pre-fit SR: $350 < m_{jj} < 700$ (b) Pre-fit SR: $700 < m_{jj} < 1000$ (c) Pre-fit SR: $1000 < m_{jj} < 1500$ (d) Pre-fit SR: $m_{jj} > 1500$



(e) Pre-fit CR: $350 < m_{jj} < 700$ (f) Pre-fit CR: $700 < m_{jj} < 1000$ (g) Pre-fit CR: $1000 < m_{jj} < 1500$ (h) Pre-fit CR: $m_{jj} > 1500$

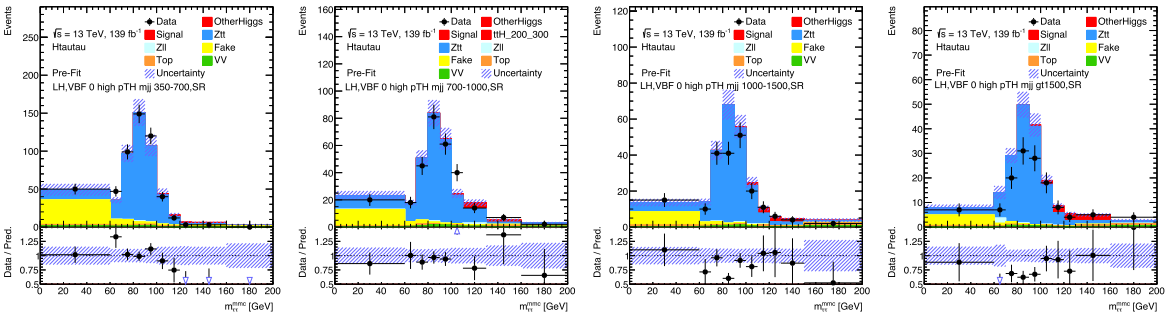


(i) Post-fit SR: $350 < m_{jj} < 700$ (j) Post-fit SR: $700 < m_{jj} < 1000$ (k) Post-fit SR: $1000 < m_{jj} < 1500$ (l) Post-fit SR: $m_{jj} > 1500$

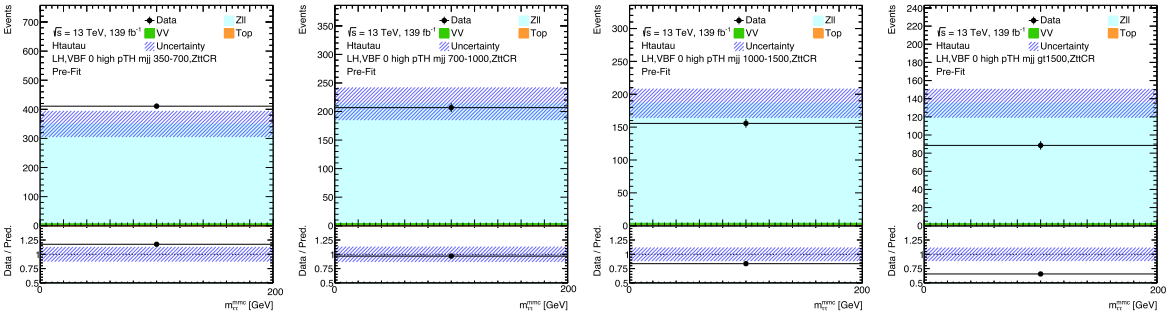


(m) Post-fit CR: $350 < m_{jj} < 700$ (n) Post-fit CR: $700 < m_{jj} < 1000$ (o) Post-fit CR: $1000 < m_{jj} < 1500$ (p) Post-fit CR: $m_{jj} > 1500$

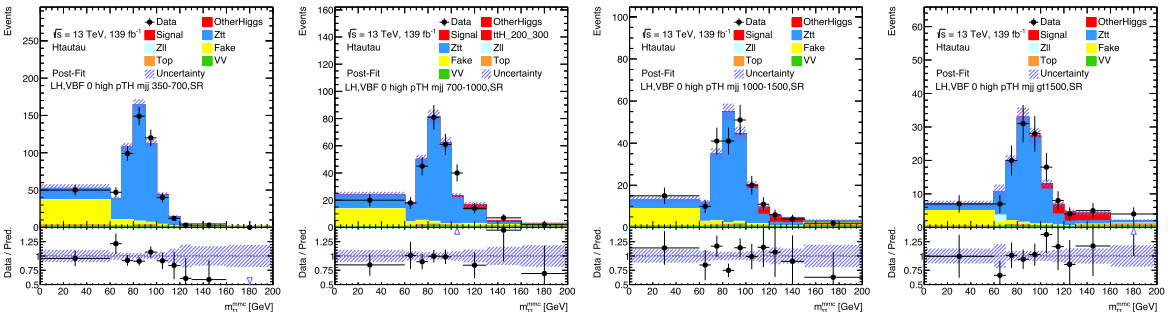
Figure D.7: Pre- and post-fit distributions of the VBF 1 low p_T^H regions in the $\tau_{\text{had}}\tau_{\text{had}}$ channel of the unblinded 18 PoI fit setup.



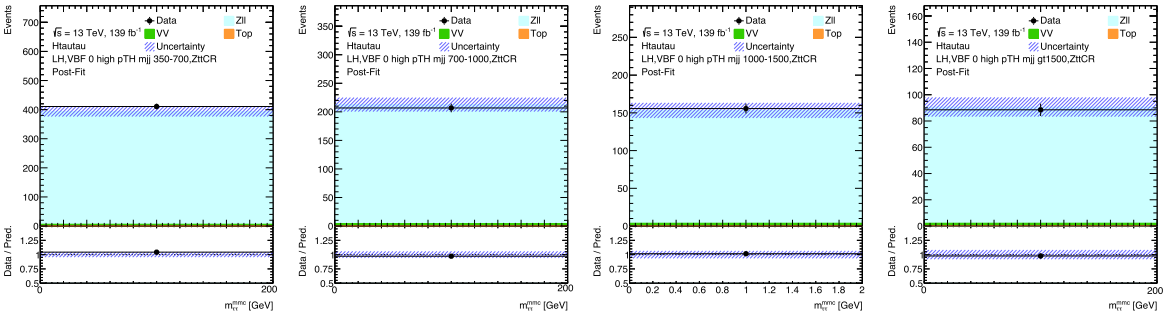
(a) Pre-fit SR: $350 < m_{jj} < 700$ (b) Pre-fit SR: $700 < m_{jj} < 1000$ (c) Pre-fit SR: $1000 < m_{jj} < 1500$ (d) Pre-fit SR: $m_{jj} > 1500$



(e) Pre-fit CR: $350 < m_{jj} < 700$ (f) Pre-fit CR: $700 < m_{jj} < 1000$ (g) Pre-fit CR: $1000 < m_{jj} < 1500$ (h) Pre-fit CR: $m_{jj} > 1500$

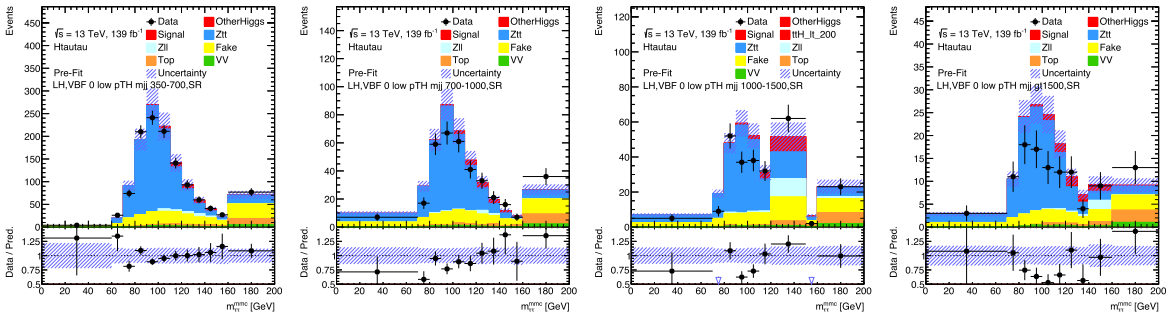


(i) Post-fit SR: $350 < m_{jj} < 700$ (j) Post-fit SR: $700 < m_{jj} < 1000$ (k) Post-fit SR: $1000 < m_{jj} < 1500$ (l) Post-fit SR: $m_{jj} > 1500$



(m) Post-fit CR: $350 < m_{jj} < 700$ (n) Post-fit CR: $700 < m_{jj} < 1000$ (o) Post-fit CR: $1000 < m_{jj} < 1500$ (p) Post-fit CR: $m_{jj} > 1500$

Figure D.8: Pre- and post-fit distributions of the VBF 0 high p_T^H regions in the $\tau_{\text{lep}}\tau_{\text{had}}$ channel of the unblinded 18 PoI fit setup.

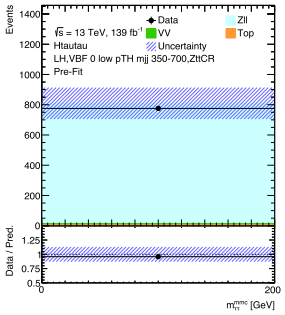


(a) Pre-fit SR: $350 < m_{jj} < 700$

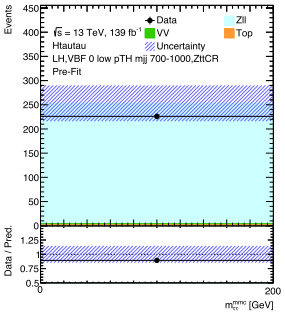
(b) Pre-fit SR: $700 < m_{jj} < 1000$

(c) Pre-fit SR: $1000 < m_{jj} < 1500$

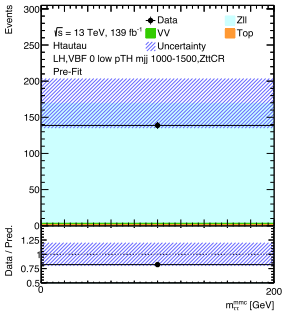
(d) Pre-fit SR: $m_{jj} > 1500$



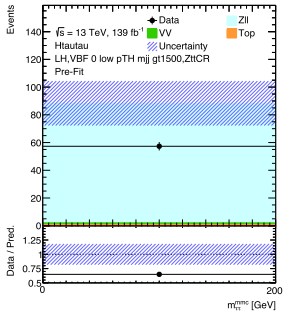
(e) Pre-fit CR: $350 < m_{jj} < 700$



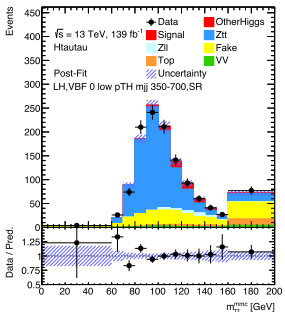
(f) Pre-fit CR: $700 < m_{jj} < 1000$



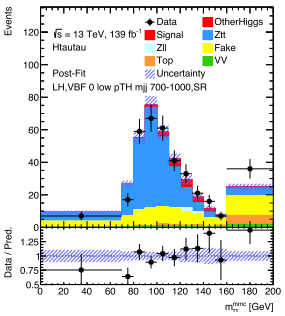
(g) Pre-fit CR: $1000 < m_{jj} < 1500$



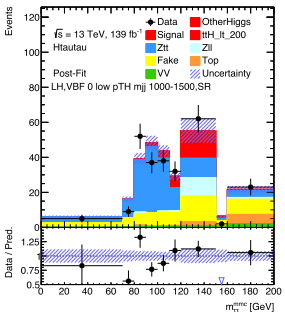
(h) Pre-fit CR: $m_{jj} > 1500$



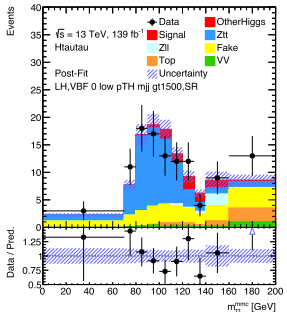
(i) Post-fit SR: $350 < m_{jj} < 700$



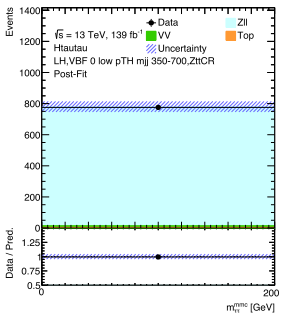
(j) Post-fit SR: $700 < m_{jj} < 1000$



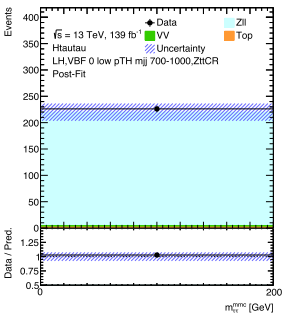
(k) Post-fit SR: $1000 < m_{jj} < 1500$



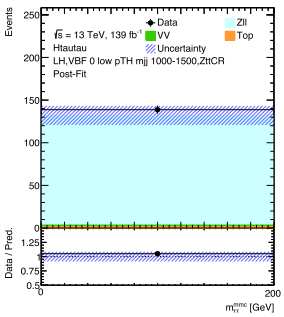
(l) Post-fit SR: $m_{jj} > 1500$



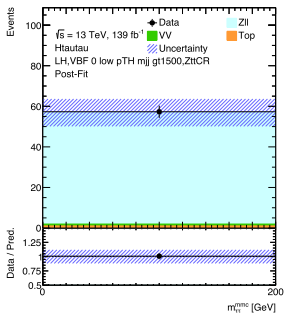
(m) Post-fit CR: $350 < m_{jj} < 700$



(n) Post-fit CR: $700 < m_{jj} < 1000$

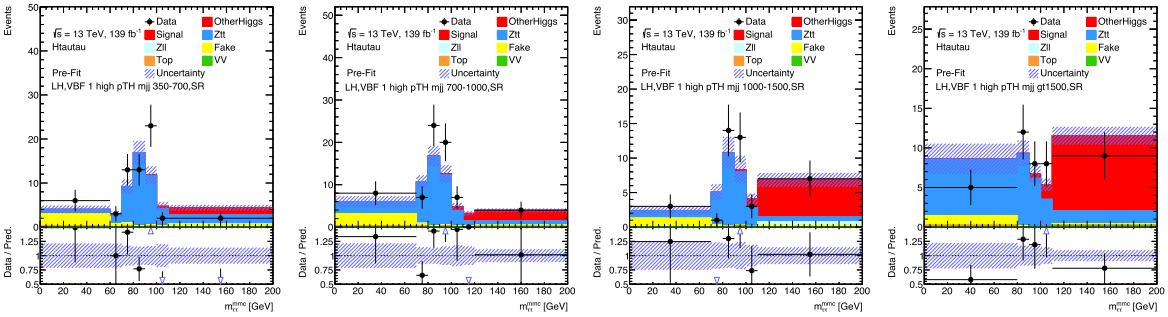


(o) Post-fit CR: $1000 < m_{jj} < 1500$

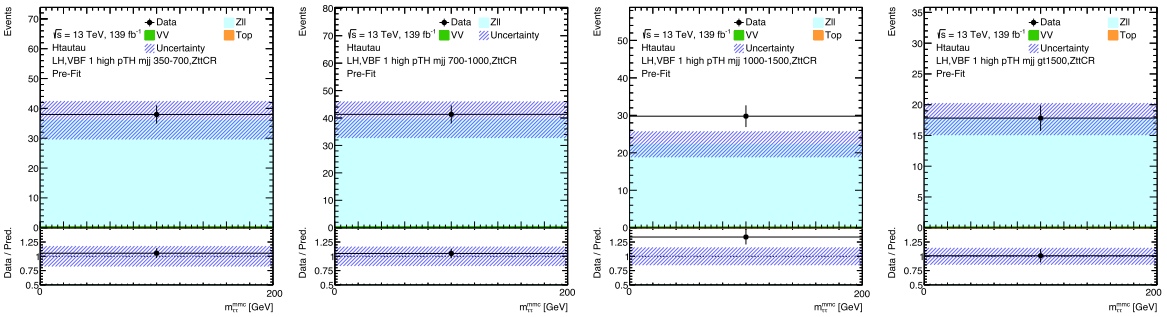


(p) Post-fit CR: $m_{jj} > 1500$

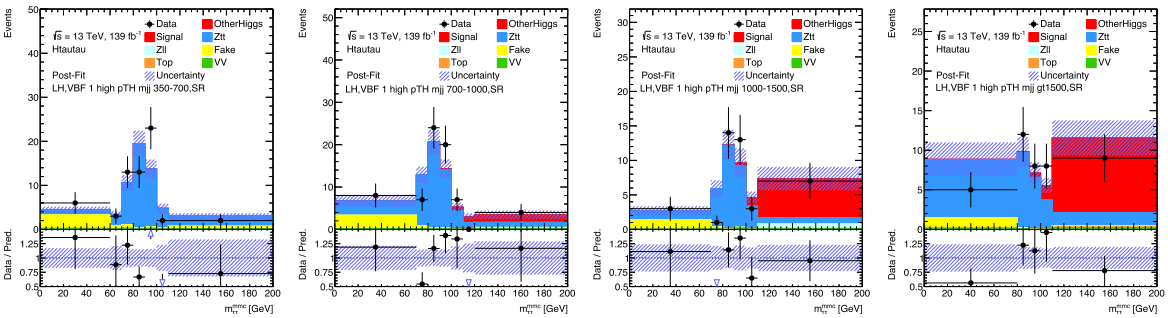
Figure D.9: Pre- and post-fit distributions of the VBF 0 low p_T^H regions in the $\tau_{\text{lep}}\tau_{\text{had}}$ channel of the unblinded 18 PoI fit setup.



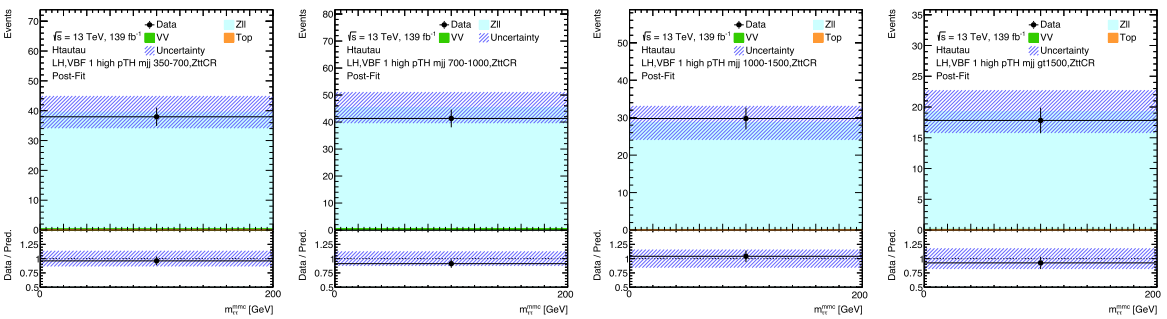
(a) Pre-fit SR: $350 < m_{jj} < 700$ (b) Pre-fit SR: $700 < m_{jj} < 1000$ (c) Pre-fit SR: $1000 < m_{jj} < 1500$ (d) Pre-fit SR: $m_{jj} > 1500$



(e) Pre-fit CR: $350 < m_{jj} < 700$ (f) Pre-fit CR: $700 < m_{jj} < 1000$ (g) Pre-fit CR: $1000 < m_{jj} < 1500$ (h) Pre-fit CR: $m_{jj} > 1500$

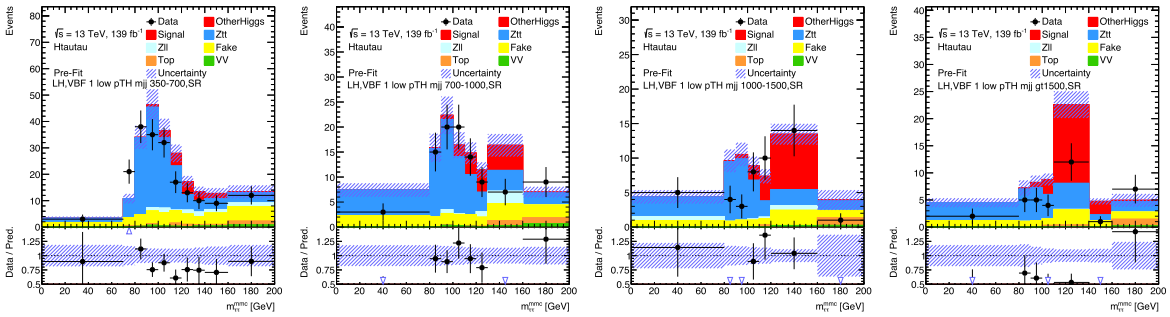


(i) Post-fit SR: $350 < m_{jj} < 700$ (j) Post-fit SR: $700 < m_{jj} < 1000$ (k) Post-fit SR: $1000 < m_{jj} < 1500$ (l) Post-fit SR: $m_{jj} > 1500$

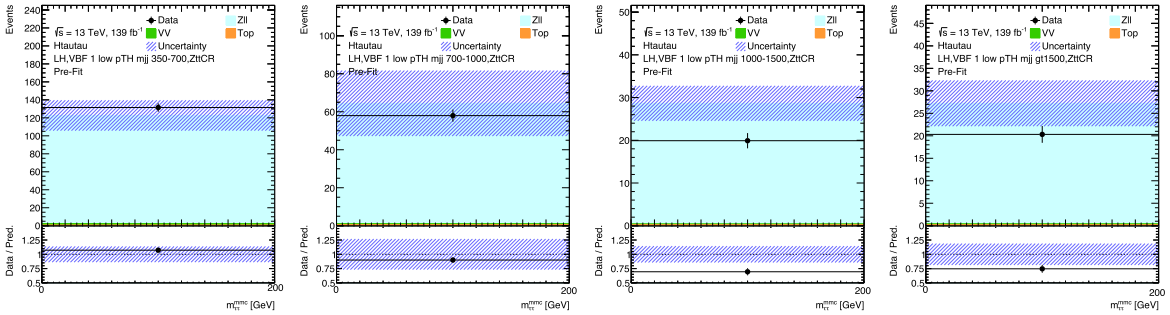


(m) Post-fit CR: $350 < m_{jj} < 700$ (n) Post-fit CR: $700 < m_{jj} < 1000$ (o) Post-fit CR: $1000 < m_{jj} < 1500$ (p) Post-fit CR: $m_{jj} > 1500$

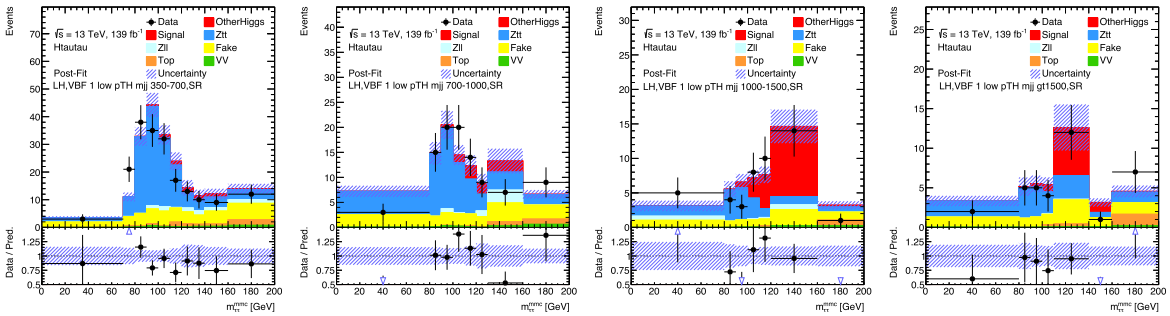
Figure D.10: Pre- and post-fit distributions of the VBF 1 high p_T^H regions in the $\tau_{\text{lep}}\tau_{\text{had}}$ channel of the unblinded 18 PoI fit setup.



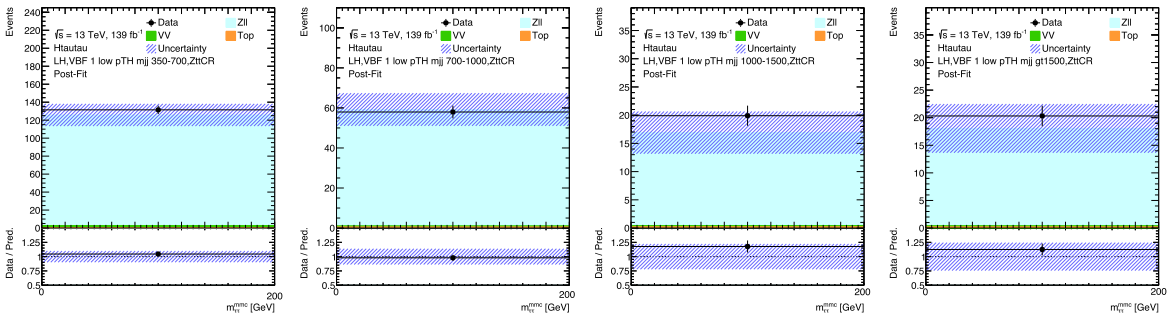
(a) Pre-fit SR: $350 < m_{jj} < 700$ (b) Pre-fit SR: $700 < m_{jj} < 1000$ (c) Pre-fit SR: $1000 < m_{jj} < 1500$ (d) Pre-fit SR: $m_{jj} > 1500$



(e) Pre-fit CR: $350 < m_{jj} < 700$ (f) Pre-fit CR: $700 < m_{jj} < 1000$ (g) Pre-fit CR: $1000 < m_{jj} < 1500$ (h) Pre-fit CR: $m_{jj} > 1500$

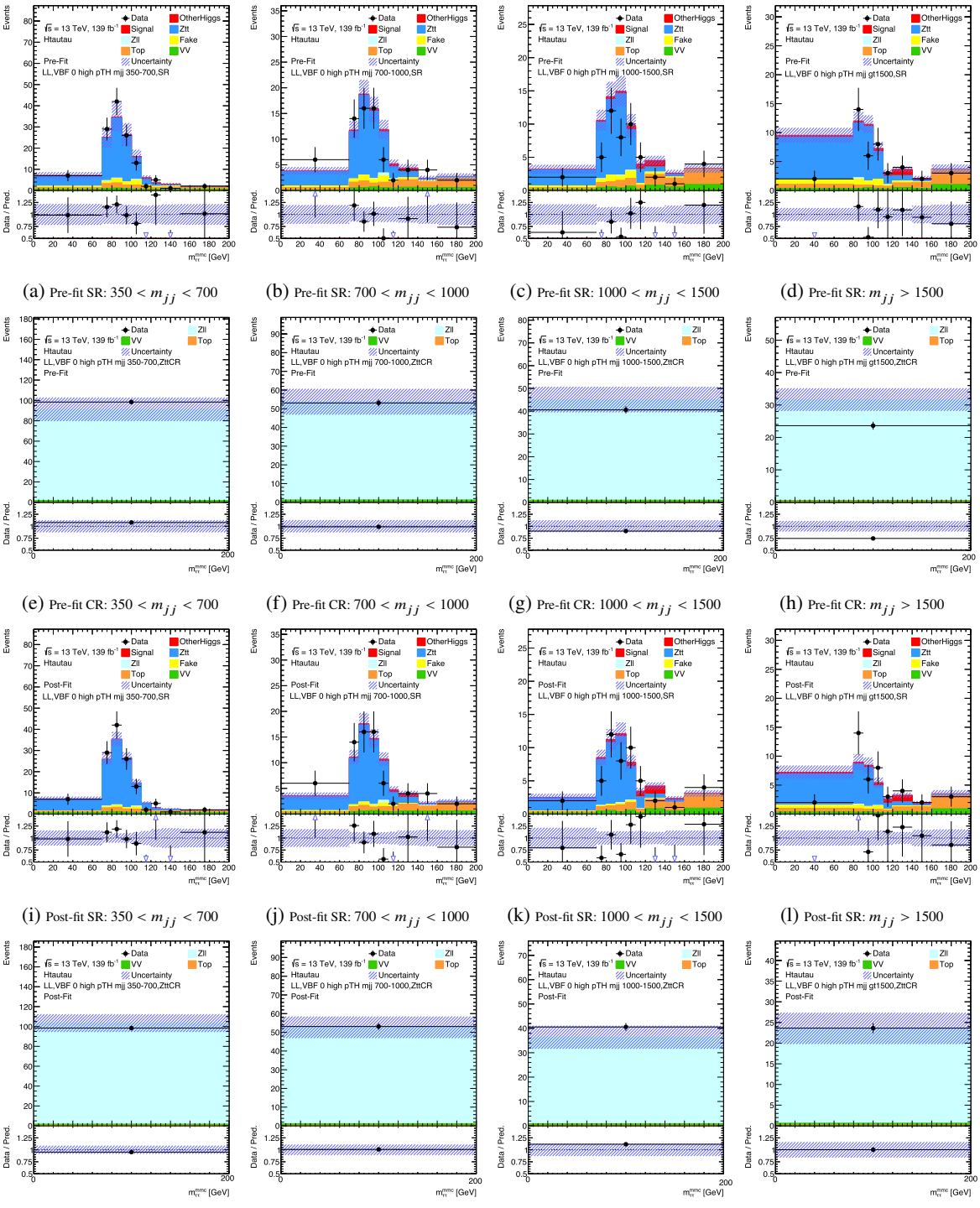


(i) Post-fit SR: $350 < m_{jj} < 700$ (j) Post-fit SR: $700 < m_{jj} < 1000$ (k) Post-fit SR: $1000 < m_{jj} < 1500$ (l) Post-fit SR: $m_{jj} > 1500$



(m) Post-fit CR: $350 < m_{jj} < 700$ (n) Post-fit CR: $700 < m_{jj} < 1000$ (o) Post-fit CR: $1000 < m_{jj} < 1500$ (p) Post-fit CR: $m_{jj} > 1500$

Figure D.11: Pre- and post-fit distributions of the VBF 1 low p_T^H regions in the $\tau_{\text{lep}}\tau_{\text{had}}$ channel of the unblinded 18 PoI fit setup.



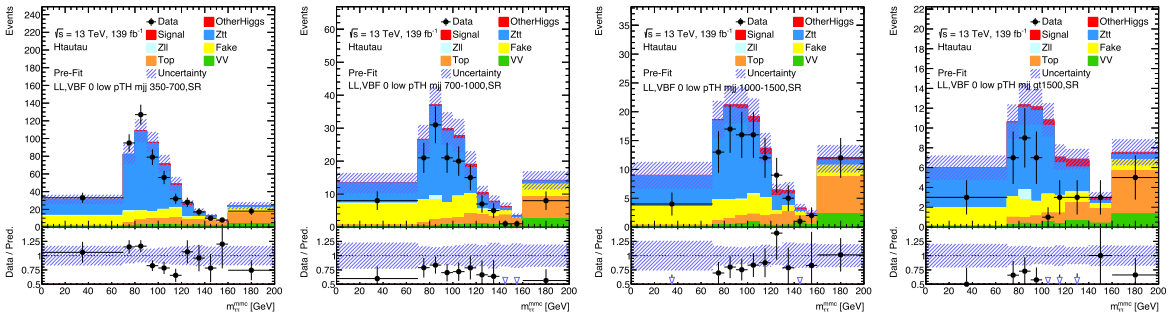
(a) Pre-fit SR: $350 < m_{jj} < 700$ (b) Pre-fit SR: $700 < m_{jj} < 1000$ (c) Pre-fit SR: $1000 < m_{jj} < 1500$ (d) Pre-fit SR: $m_{jj} > 1500$

(e) Pre-fit CR: $350 < m_{jj} < 700$ (f) Pre-fit CR: $700 < m_{jj} < 1000$ (g) Pre-fit CR: $1000 < m_{jj} < 1500$ (h) Pre-fit CR: $m_{jj} > 1500$

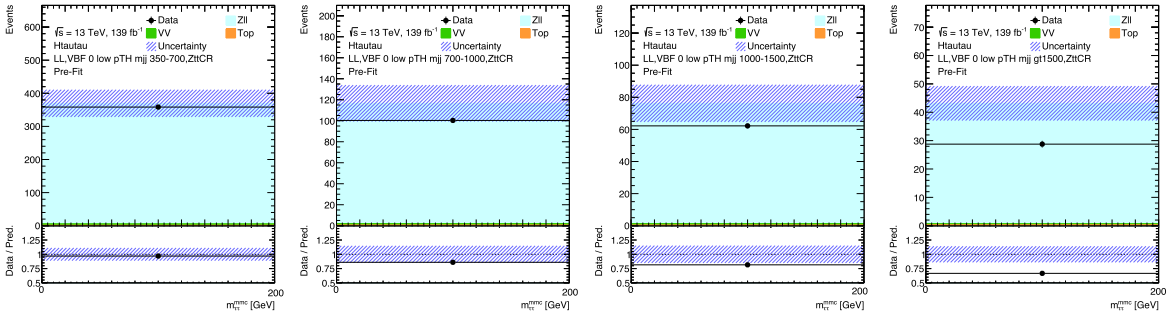
(i) Post-fit SR: $350 < m_{jj} < 700$ (j) Post-fit SR: $700 < m_{jj} < 1000$ (k) Post-fit SR: $1000 < m_{jj} < 1500$ (l) Post-fit SR: $m_{jj} > 1500$

(m) Post-fit CR: $350 < m_{jj} < 700$ (n) Post-fit CR: $700 < m_{jj} < 1000$ (o) Post-fit CR: $1000 < m_{jj} < 1500$ (p) Post-fit CR: $m_{jj} > 1500$

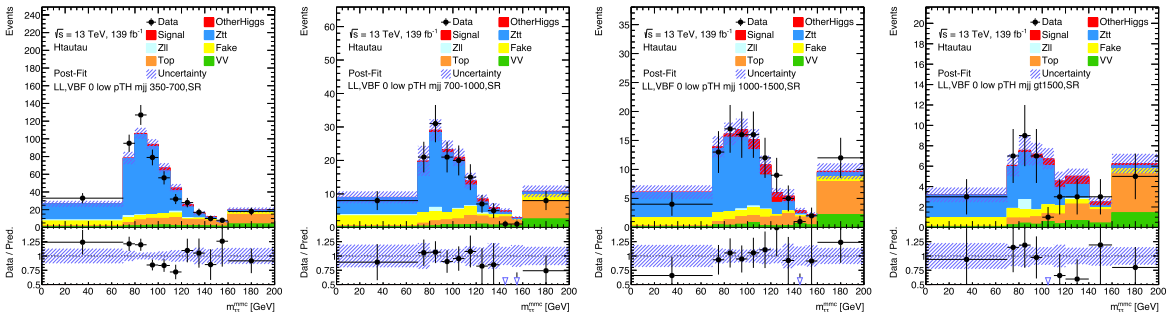
Figure D.12: Pre- and post-fit distributions of the VBF 0 high p_T^H regions in the $\tau_{\text{lep}}\tau_{\text{lep}}$ channel of the unblinded 18 PoI fit setup.



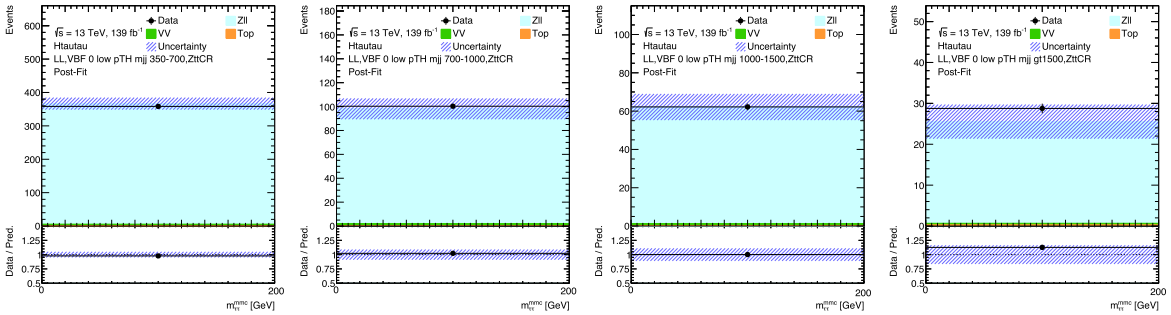
(a) Pre-fit SR: $350 < m_{jj} < 700$ (b) Pre-fit SR: $700 < m_{jj} < 1000$ (c) Pre-fit SR: $1000 < m_{jj} < 1500$ (d) Pre-fit SR: $m_{jj} > 1500$



(e) Pre-fit CR: $350 < m_{jj} < 700$ (f) Pre-fit CR: $700 < m_{jj} < 1000$ (g) Pre-fit CR: $1000 < m_{jj} < 1500$ (h) Pre-fit CR: $m_{jj} > 1500$

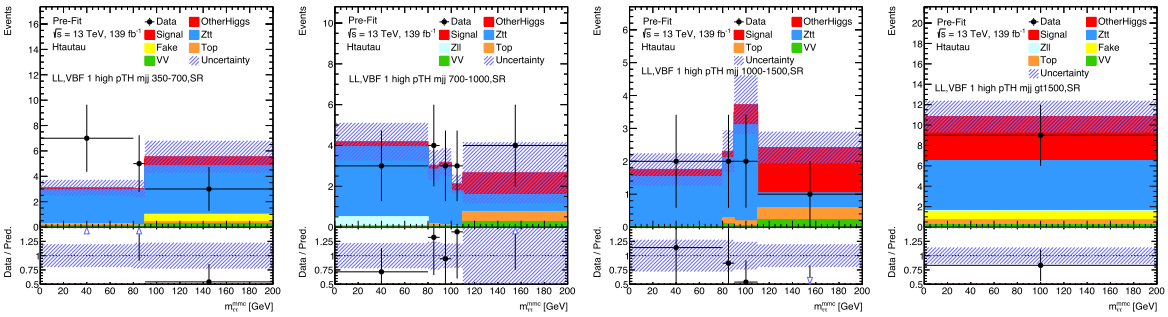


(i) Post-fit SR: $350 < m_{jj} < 700$ (j) Post-fit SR: $700 < m_{jj} < 1000$ (k) Post-fit SR: $1000 < m_{jj} < 1500$ (l) Post-fit SR: $m_{jj} > 1500$

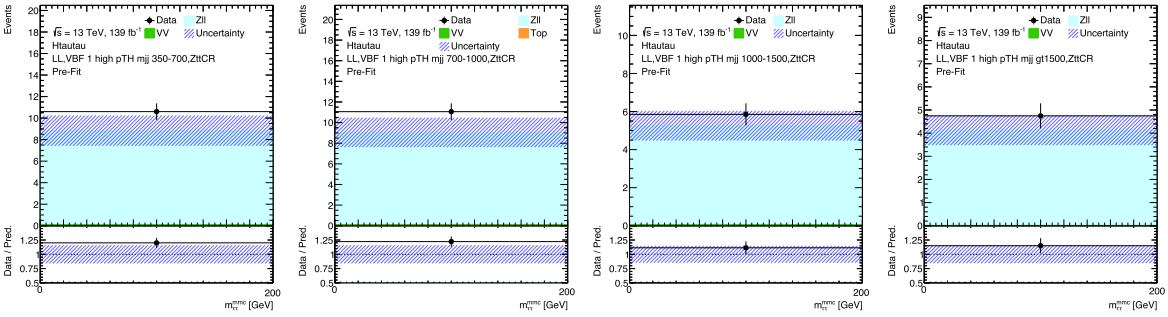


(m) Post-fit CR: $350 < m_{jj} < 700$ (n) Post-fit CR: $700 < m_{jj} < 1000$ (o) Post-fit CR: $1000 < m_{jj} < 1500$ (p) Post-fit CR: $m_{jj} > 1500$

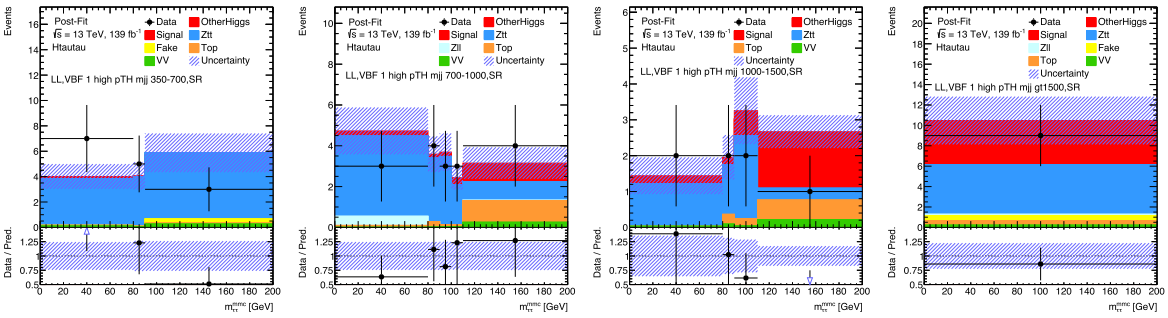
Figure D.13: Pre- and post-fit distributions of the VBF 0 low p_T^H regions in the $\tau_{\text{lep}}\tau_{\text{lep}}$ channel of the unblinded 18 PoI fit setup.



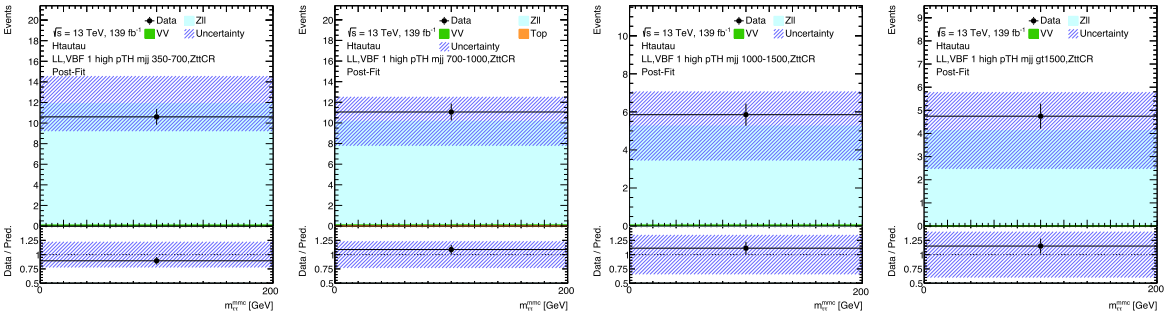
(a) Pre-fit SR: $350 < m_{jj} < 700$ (b) Pre-fit SR: $700 < m_{jj} < 1000$ (c) Pre-fit SR: $1000 < m_{jj} < 1500$ (d) Pre-fit SR: $m_{jj} > 1500$



(e) Pre-fit CR: $350 < m_{jj} < 700$ (f) Pre-fit CR: $700 < m_{jj} < 1000$ (g) Pre-fit CR: $1000 < m_{jj} < 1500$ (h) Pre-fit CR: $m_{jj} > 1500$

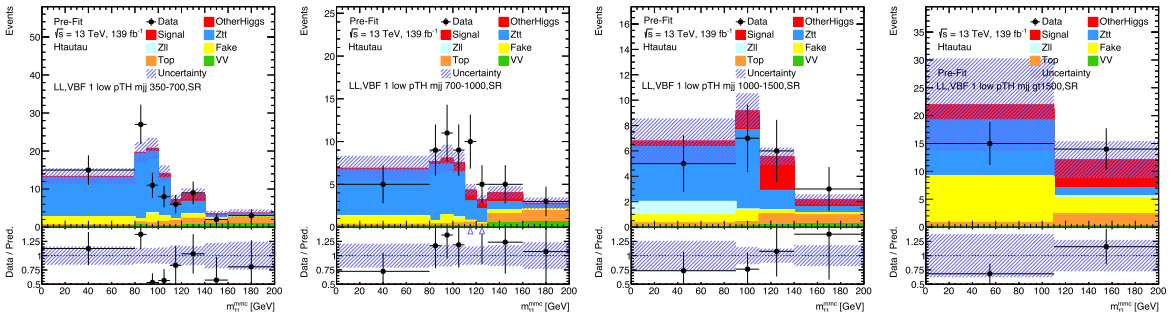


(i) Post-fit SR: $350 < m_{jj} < 700$ (j) Post-fit SR: $700 < m_{jj} < 1000$ (k) Post-fit SR: $1000 < m_{jj} < 1500$ (l) Post-fit SR: $m_{jj} > 1500$

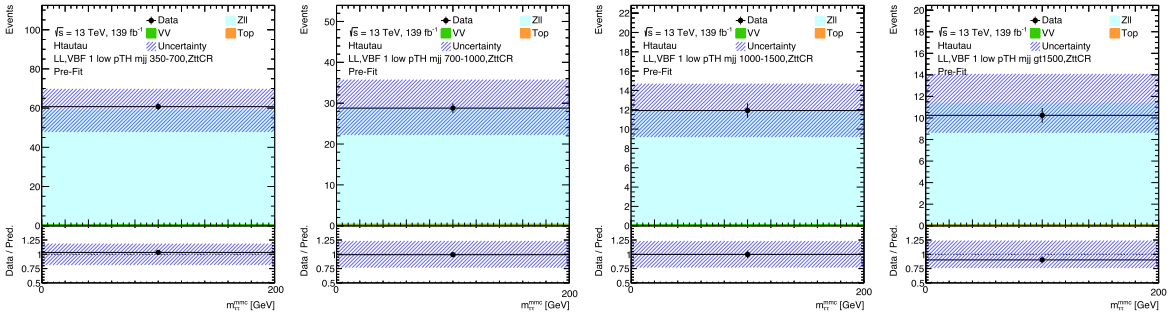


(m) Post-fit CR: $350 < m_{jj} < 700$ (n) Post-fit CR: $700 < m_{jj} < 1000$ (o) Post-fit CR: $1000 < m_{jj} < 1500$ (p) Post-fit CR: $m_{jj} > 1500$

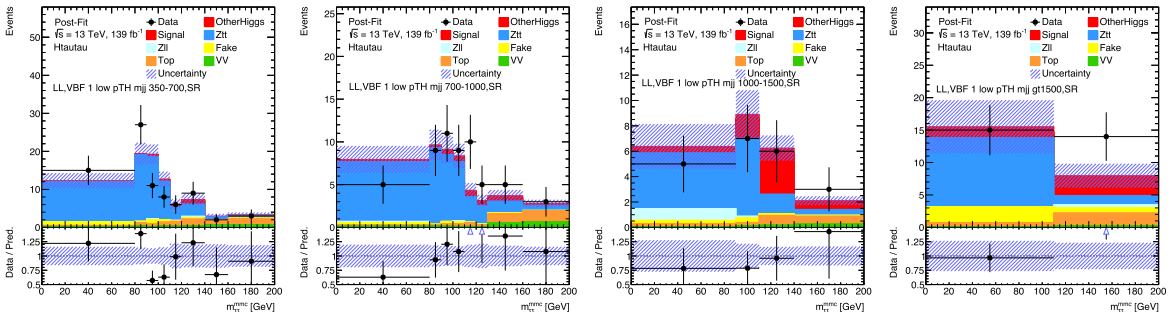
Figure D.14: Pre- and post-fit distributions of the VBF 1 high p_T^H regions in the $\tau_{\text{lep}}\tau_{\text{lep}}$ channel of the unblinded 18 PoI fit setup.



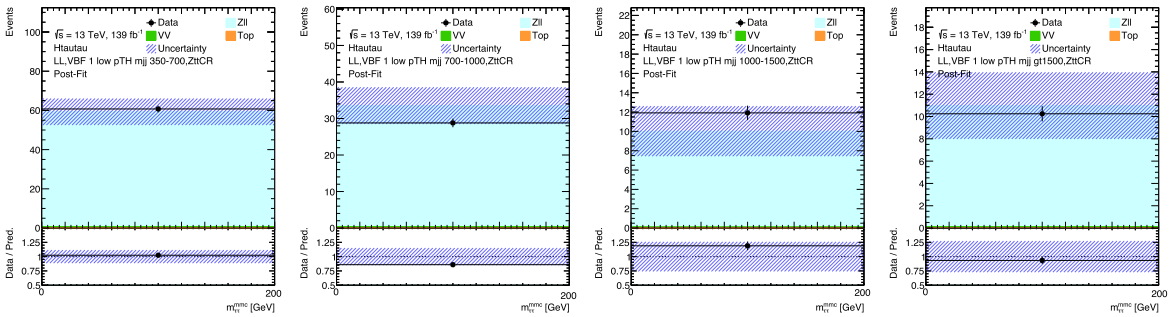
(a) Pre-fit SR: $350 < m_{jj} < 700$ (b) Pre-fit SR: $700 < m_{jj} < 1000$ (c) Pre-fit SR: $1000 < m_{jj} < 1500$ (d) Pre-fit SR: $m_{jj} > 1500$



(e) Pre-fit CR: $350 < m_{jj} < 700$ (f) Pre-fit CR: $700 < m_{jj} < 1000$ (g) Pre-fit CR: $1000 < m_{jj} < 1500$ (h) Pre-fit CR: $m_{jj} > 1500$



(i) Post-fit SR: $350 < m_{jj} < 700$ (j) Post-fit SR: $700 < m_{jj} < 1000$ (k) Post-fit SR: $1000 < m_{jj} < 1500$ (l) Post-fit SR: $m_{jj} > 1500$



(m) Post-fit CR: $350 < m_{jj} < 700$ (n) Post-fit CR: $700 < m_{jj} < 1000$ (o) Post-fit CR: $1000 < m_{jj} < 1500$ (p) Post-fit CR: $m_{jj} > 1500$

Figure D.15: Pre- and post-fit distributions of the VBF 1 low p_T^H regions in the $\tau_{\text{lep}}\tau_{\text{lep}}$ channel of the unblinded 18 PoI fit setup.

Validation Studies for Combined Fake Templates

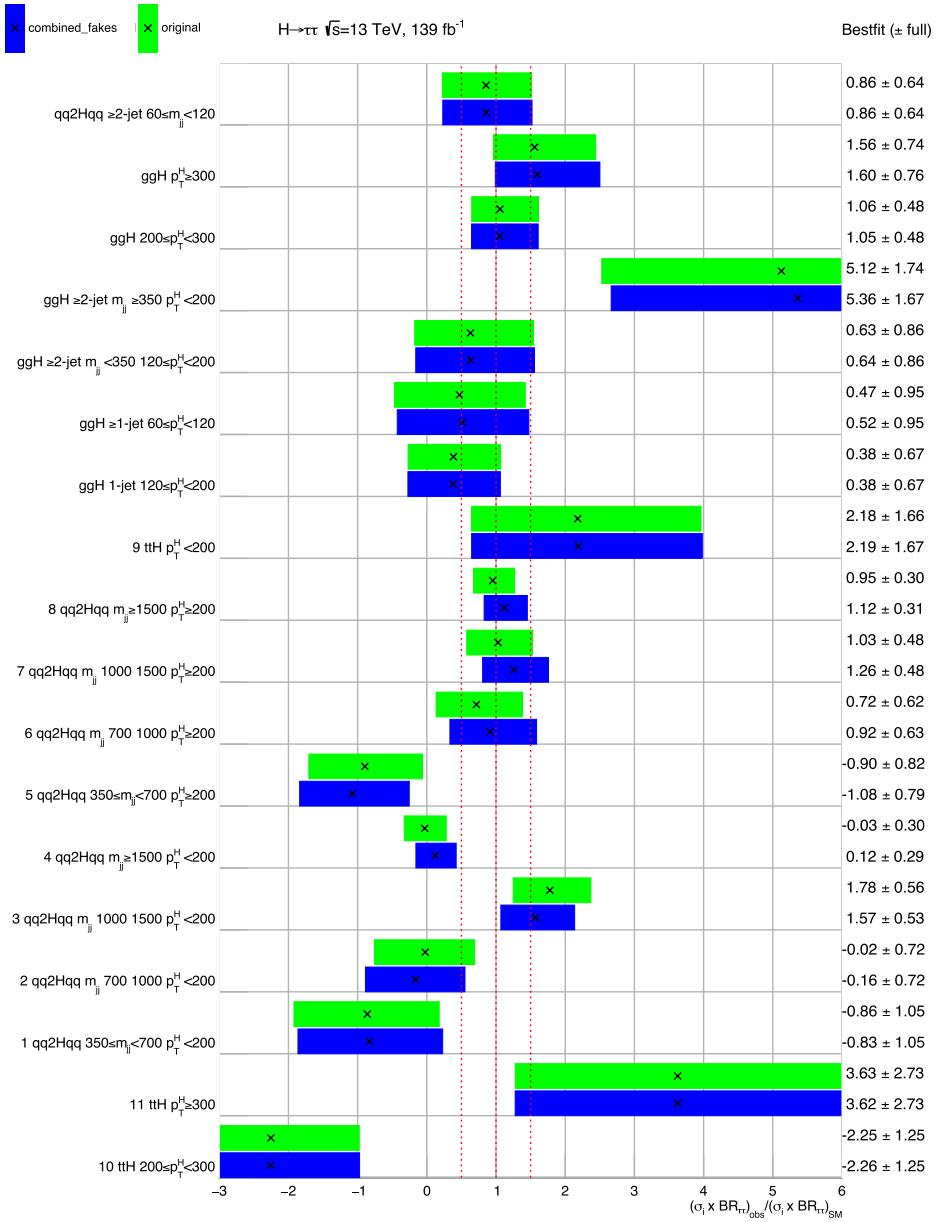
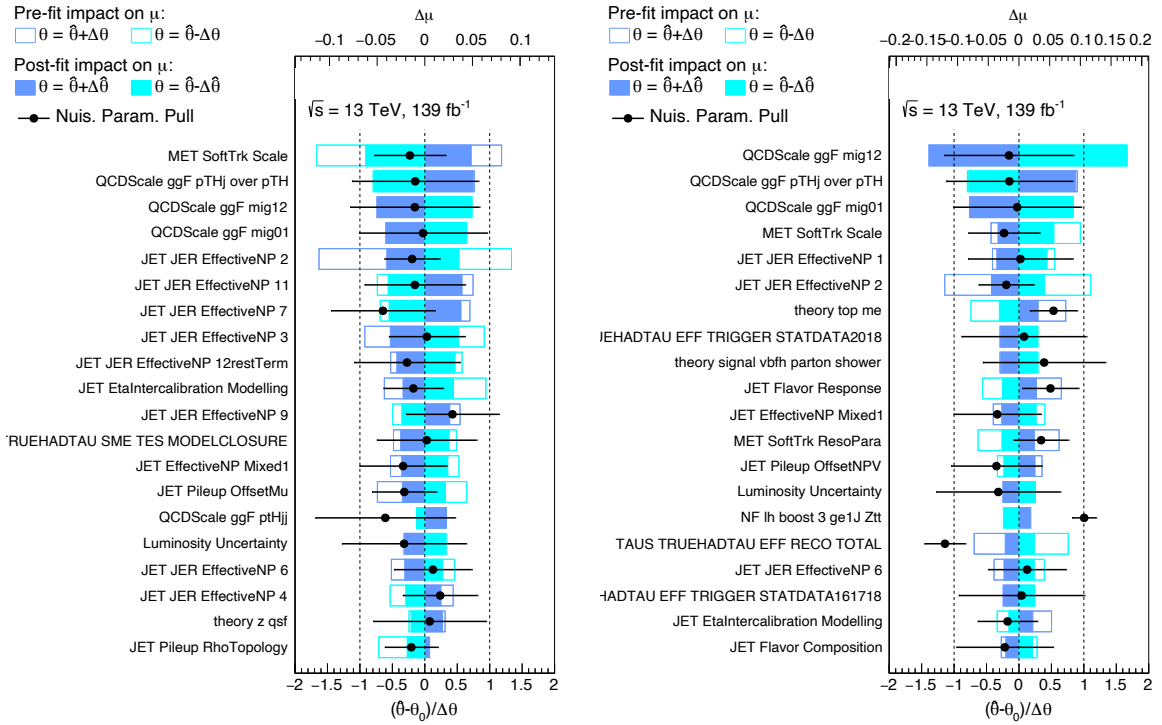


Figure D.16: 18 PoI measurement in the unblinded fit. No discrepancies have been identified between a setup using combined (blue) and the original fake templates (green).

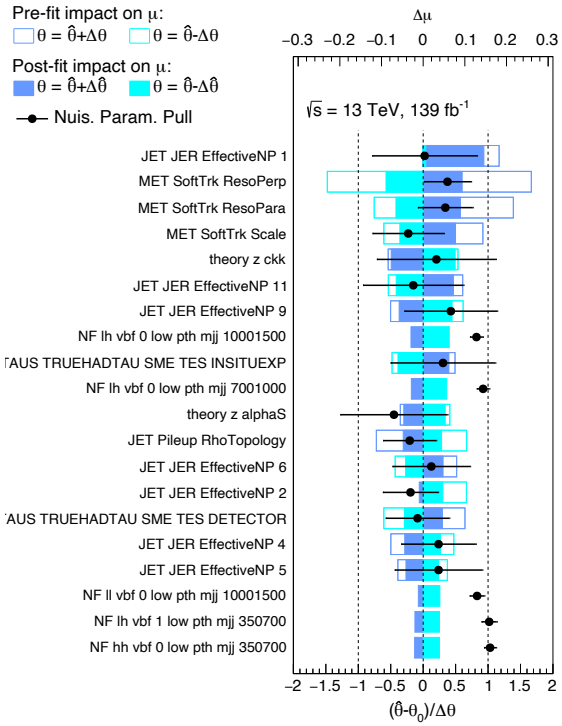
Ranking Plots



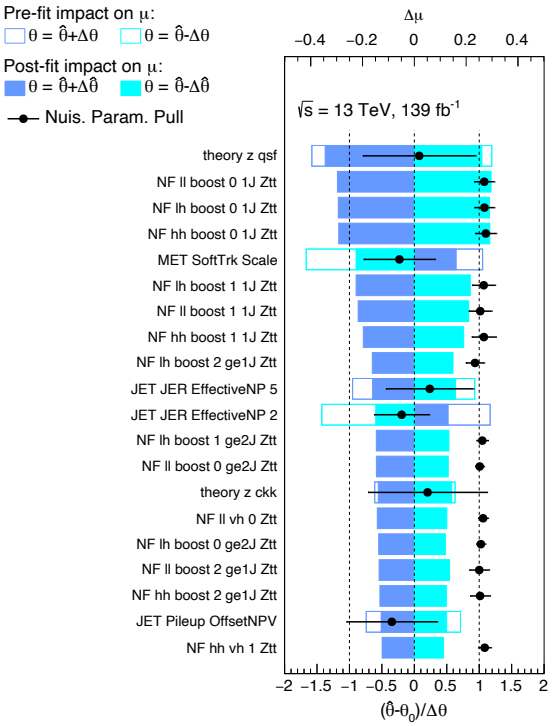
(a) r_ggF_gg2H_ptH_200_300

(b) r_ggF_gg2H_ptH_gt300

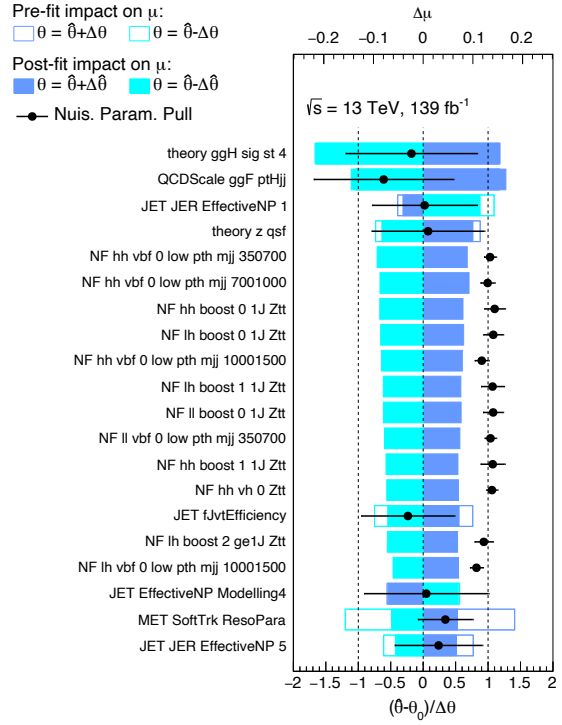
Figure D.17: Systematic uncertainty ranking for the ggF PoIs 200 GeV $< p_T^H <$ 300 GeV and $p_T^H >$ 300 GeV.



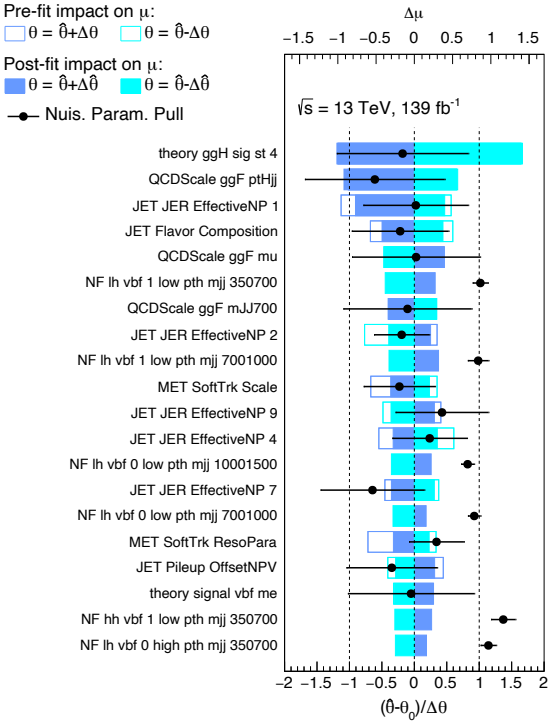
(a) r_ggF_gg2H_1J_ptH_120_200



(b) r_ggF_gg2H_ge1J_ptH_60_120

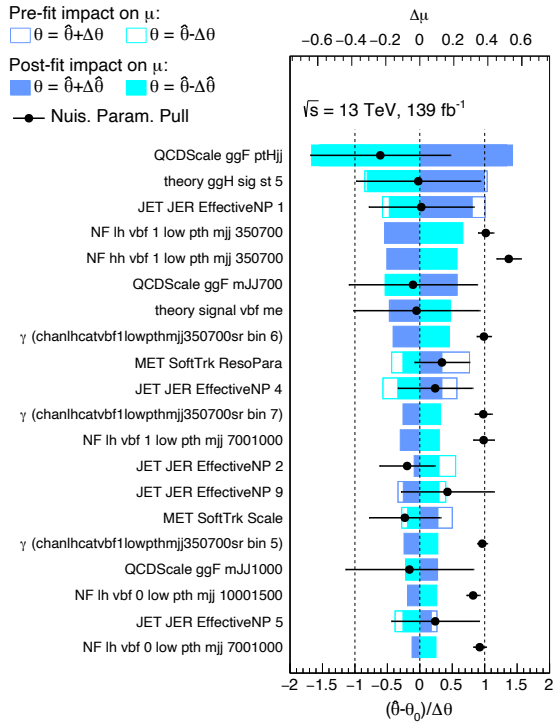


(c) r_ggF_gg2H_ge2J_mJJ_0_350_ptH_120_200

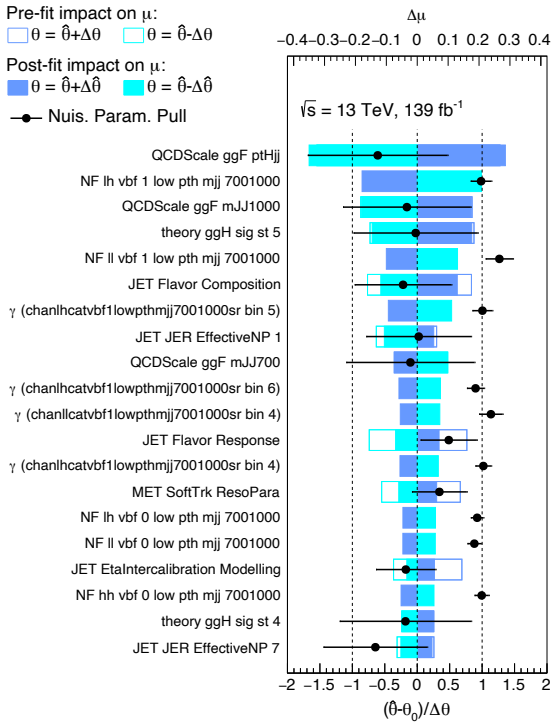


(d) r_ggF_gg2H_ge2J_mJJ_ge350_ptH_0_200

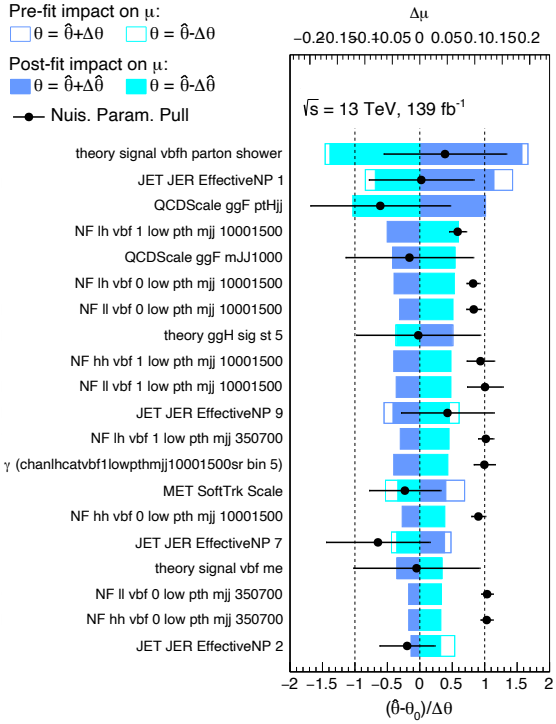
Figure D.18: Systematic uncertainty ranking for the ggF PoIs with requirements on the number of jets.



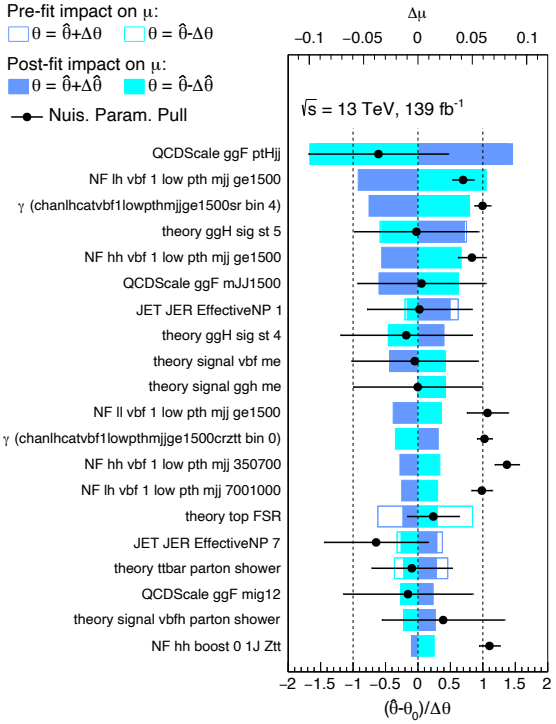
(a) r_1_qq2Hqq_mJJ_350_700_ptH_0_200



(b) r_2_qq2Hqq_mJJ_700_1000_ptH_0_200

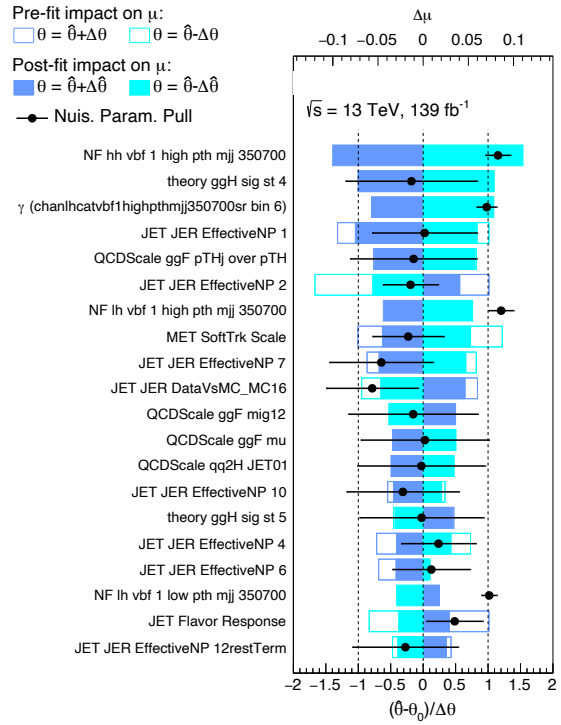


(c) r_3_qq2Hqq_mJJ_1000_1500_ptH_0_200

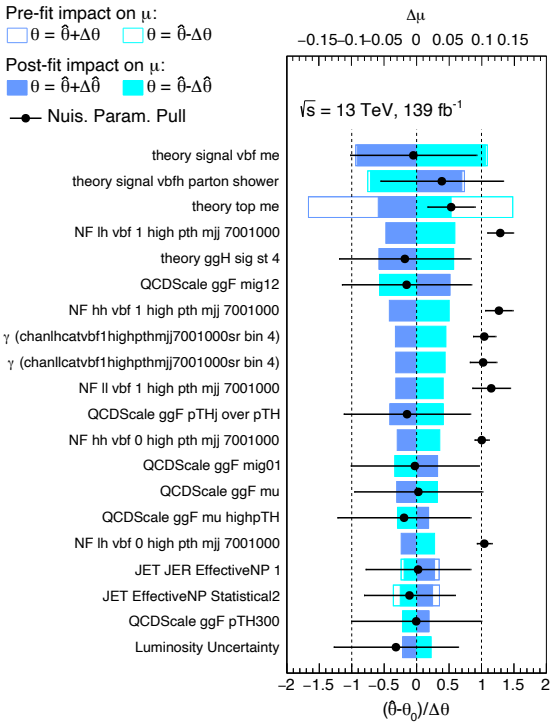


(d) r_4_qq2Hqq_mJJ_gt1500_ptH_0_200

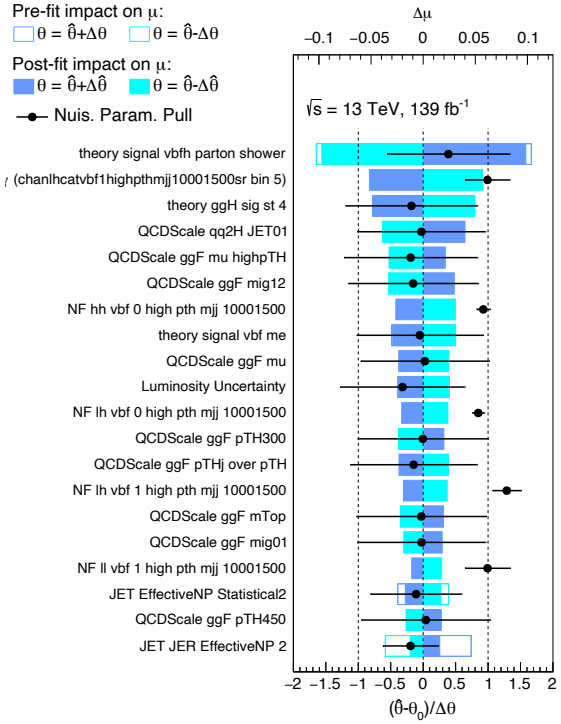
Figure D.19: Systematic uncertainty ranking for the low p_T^H VBF PoIs.



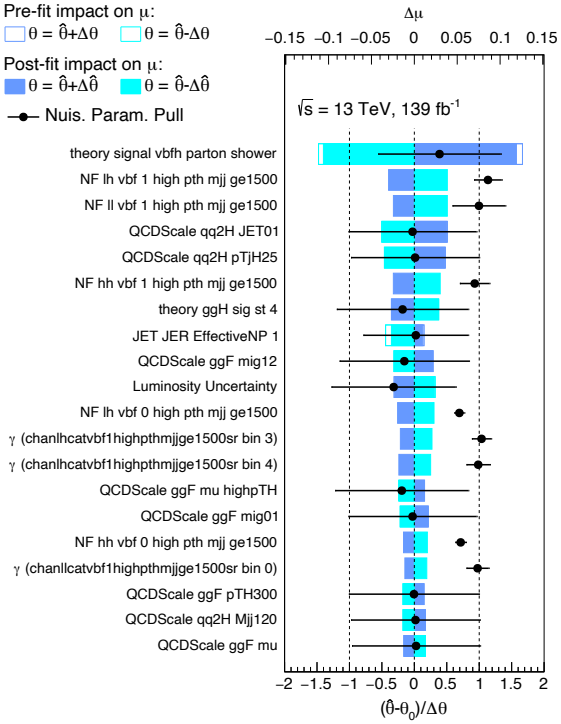
(a) r_5_qq2Hqq_mJJ_350_700_ptH_gt200



(b) r_6_qq2Hqq_mJJ_700_1000_ptH_gt200

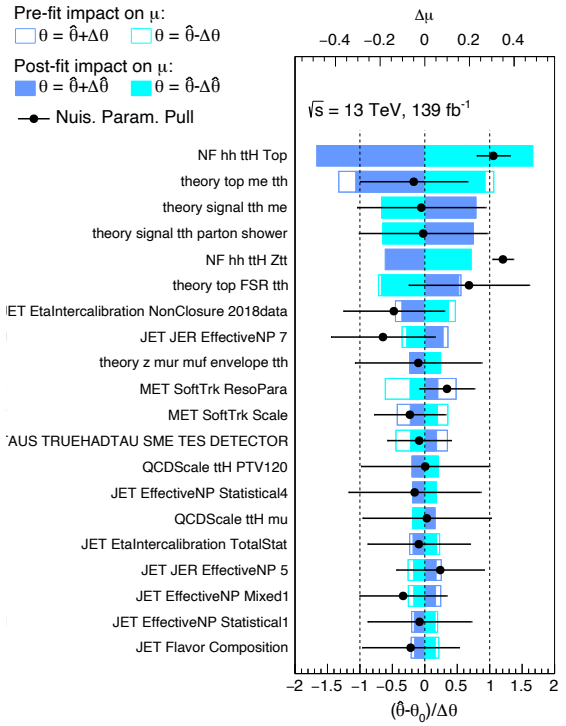


(c) r_7_qq2Hqq_mJJ_1000_1500_ptH_gt200

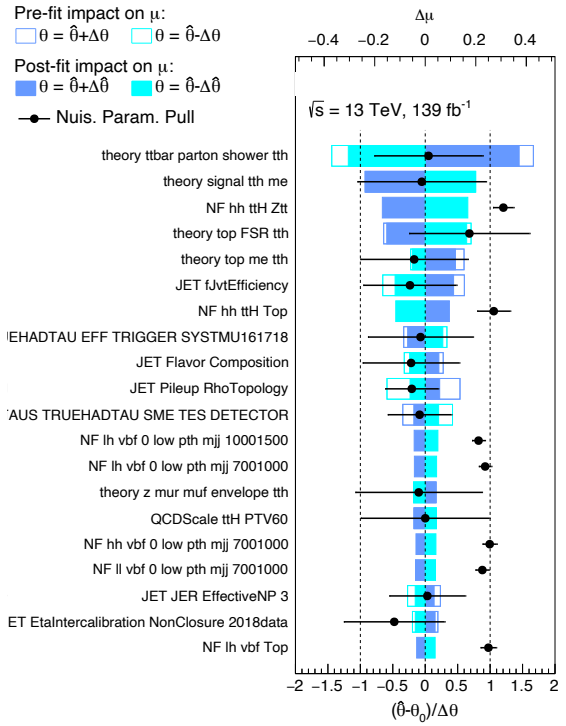


(d) r_8_qq2Hqq_mJJ_gt1500_ptH_gt200

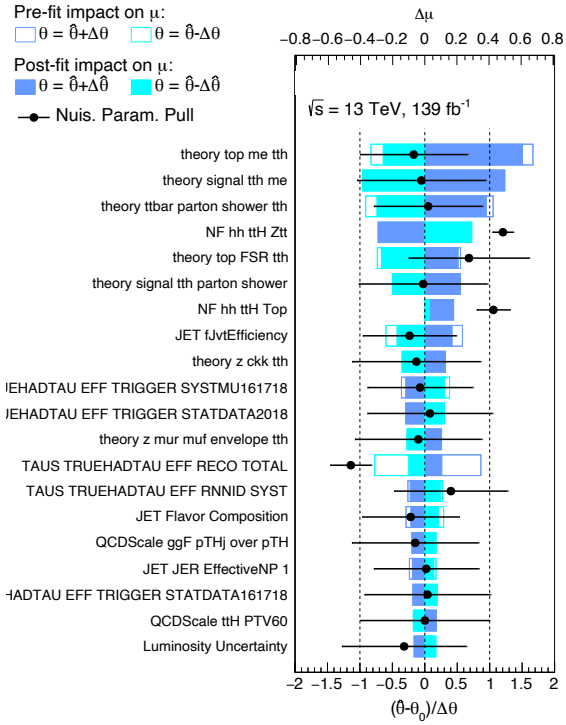
Figure D.20: Systematic uncertainty ranking for the high p_T^H VBF PoIs.



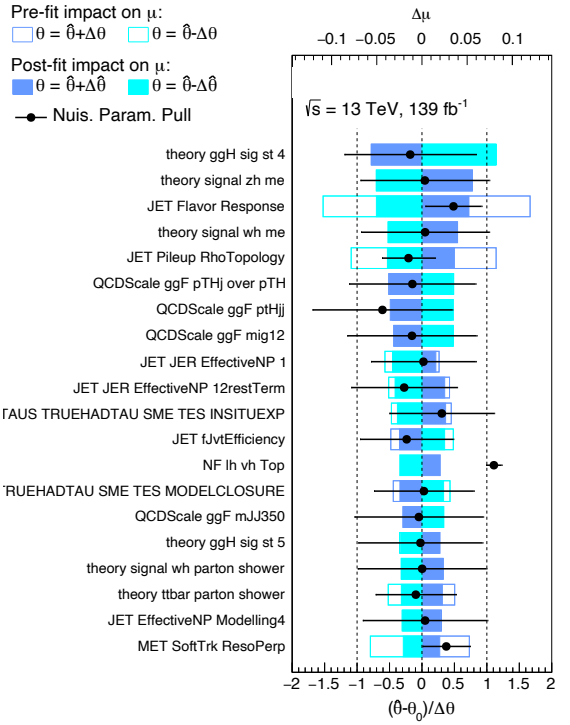
(a) r_9_ttH_ptH_0_200



(b) r_10_ttH_ptH_200_300



(c) r_11_ttH_ptH_gt300



(d) r_qq2Hqq_ge2J_mJJ_60_120.pdf

Figure D.21: Systematic uncertainty ranking for the $t\bar{t}H$ and VH PoIs.

Bibliography

[1] ATLAS Collaboration, *Organisational Structure*, URL: https://atlas.cern/Discover/Collaboration (visited on 17/08/2024) (cit. on p. vii).

[2] L. Herrmann, *Optimization of the Recurrent Neural Network for the Run 3 PID in the TRT*, ATL-COM-INDET-2022-006, University of Bonn, 2022 (cit. on pp. vii, 45).

[3] ATLAS Collaboration, *Differential cross-section measurements of Higgs boson production in the $H \to \tau^+\tau^-$ decay channel in pp collisions at $\sqrt{s}$ = 13 TeV with the ATLAS detector*, 2024, arXiv: 2407.16320 [hep-ex], URL: https://arxiv.org/abs/2407.16320 (cit. on pp. vii, 2, 25, 32, 61, 69–71, 75, 77–79, 124, 131, 133).

[4] O. Brüning and L. Rossi, *The High Luminosity Large Hadron Collider - New Machine for Illuminating the Mysteries of the Universe*, https://doi.org/10.1142/13487, 2024 (cit. on p. 1).

[5] J. de Blas et al., *Global SMEFT Fits at Future Colliders*, 2024, arXiv: 2206.08326 [hep-ph], URL: https://arxiv.org/abs/2206.08326 (cit. on p. 2).

[6] ATLAS Collaboration, *Evidence for the Higgs-boson Yukawa coupling to tau leptons with the ATLAS detector*, JHEP **04** (2015), arXiv: 1501.04943 [hep-ph] (cit. on p. 2).

[7] CMS Collaboration, *Evidence for the 125 GeV Higgs boson decaying to a pair of tau leptons*, JHEP **05** (2014), arXiv: 1401.5041 [hep-ph] (cit. on p. 2).

[8] ATLAS and CMS Collaboration, *Measurements of the Higgs boson production and decay rates and constraints on its couplings from a combined ATLAS and CMS analysis of the LHC pp collision data at $\sqrt{s}$= 7 and 8 TeV*, JHEP **08** (2016), arXiv: 1606.02266 [hep-ex] (cit. on p. 2).

[9] ATLAS Collaboration, *A detailed map of Higgs boson interactions by the ATLAS experiment ten years after the discovery*, (2023), arXiv: 2207.00092v2 [hep-ex] (cit. on pp. 2, 133).

[10] M. Ciccolini, A. Denner and S. Dittmaier, *Strong and Electroweak Corrections to the Production of a Higgs Boson+2 jets via Weak Interactions at the Large Hadron Collider*, Physical Review Letters **99** (2007), ISSN: 1079-7114, URL: http://dx.doi.org/10.1103/PhysRevLett.99.161803 (cit. on p. 2).

[11] ATLAS Collaboration, *Luminosity determination in pp collisions at $\sqrt{s}$ = 13 TeV using the ATLAS detector at the LHC*, The European Physical Journal C **83** (2023), ISSN: 1434-6052, URL: http://dx.doi.org/10.1140/epjc/s10052-023-11747-w (cit. on pp. 2, 23, 61, 133).

[12] R. L. Workman et al., *Review of Particle Physics*, PTEP **2022** (2022) 083C01 (cit. on pp. 2, 14–16, 35, 40, 41, 56, 69, 84, 94).

[13] M. Grazzini, A. Ilnicka, M. Spira and M. Wiesemann, *Modeling BSM effects on the Higgs transverse-momentum spectrum in an EFT approach*, Journal of High Energy Physics **2017** (2017), URL: https://doi.org/10.1007%2Fjhep03%282017%29115 (cit. on pp. 2, 68).

[14] M. A. Thomson, *Modern particle physics*, Cambridge University Press, 2013, ISBN: 978-1-107-03426-6 (cit. on pp. 5, 7–10, 12–15, 19, 20, 22, 23).

[15] F. Hasert et al., *Observation of neutrino-like interactions without muon or electron in the gargamelle neutrino experiment*, Physics Letters B **46** (1973) 138, ISSN: 0370-2693, URL: https://www.sciencedirect.com/science/article/pii/0370269373904991 (cit. on p. 5).

[16] G. Arnison et al., *Experimental observation of isolated large transverse energy electrons with associated missing energy at s=540 GeV*, Physics Letters B **122** (1983) 103, ISSN: 0370-2693, URL: https://www.sciencedirect.com/science/article/pii/0370269383911772 (cit. on p. 5).

[17] M. Banner et al., *Observation of single isolated electrons of high transverse momentum in events with missing transverse energy at the CERN pp collider*, Physics Letters B **122** (1983) 476, ISSN: 0370-2693, URL: https://www.sciencedirect.com/science/article/pii/0370269383916052 (cit. on p. 5).

[18] L. Di Lella and C. Rubbia, *The Discovery of the W and Z Particles*, Adv. Ser. Dir. High Energy Phys. **23** (2015) 137, URL: https://cds.cern.ch/record/2103277 (cit. on p. 5).

[19] J. E. Augustin et al., *Discovery of a Narrow Resonance in e^+e^- Annihilation*, Phys. Rev. Lett. **33** (23 1974) 1406, URL: https://link.aps.org/doi/10.1103/PhysRevLett.33.1406 (cit. on p. 5).

[20] J. J. Aubert et al., *Experimental Observation of a Heavy Particle J*, Phys. Rev. Lett. **33** (23 1974) 1404, URL: https://link.aps.org/doi/10.1103/PhysRevLett.33.1404 (cit. on p. 5).

[21] S. W. Herb et al., *Observation of a Dimuon Resonance at 9.5 GeV in 400-GeV Proton-Nucleus Collisions*, Phys. Rev. Lett. **39** (5 1977) 252, URL: https://link.aps.org/doi/10.1103/PhysRevLett.39.252 (cit. on p. 5).

[22] F. Abe and A. et al, *Observation of Top Quark Production in $p\bar{p}$ Collisions with the Collider Detector at Fermilab*, Physical Review Letters **74** (1995) 2626, ISSN: 1079-7114, URL: http://dx.doi.org/10.1103/PhysRevLett.74.2626 (cit. on p. 5).

[23] CMS Collaboration,
Observation of a new boson at a mass of 125 GeV with the CMS experiment at the LHC,
Physics Letters B **716** (2012) 30, ISSN: 0370-2693,
URL: http://dx.doi.org/10.1016/j.physletb.2012.08.021 (cit. on p. 5).

[24] ATLAS Collaboration, *Observation of a new particle in the search for the Standard Model Higgs boson with the ATLAS detector at the LHC*, Physics Letters B **716** (2012) 1,
ISSN: 0370-2693, URL: http://dx.doi.org/10.1016/j.physletb.2012.08.020
(cit. on p. 5).

[25] Izaak Neutelings, Janosh Riebesell, *Tikz figures*, https://tikz.net/axis3d_cms/,
https://tikz.net/jet_tau/, https://tikz.net/sm_particles/,
https://tikz.net/complex/, https://tikz.net/mexican-hat/,
(visited on 22/01/2024) (cit. on pp. 6, 12, 26, 39).

[26] R. Wolf, *The Higgs Boson Discovery at the Large Hadron Collider*, Springer, 2015,
ISBN: 978-3-319-18511-8 (cit. on pp. 7–11, 13).

[27] E. Noether, *Invariant variation problems*,
Transport Theory and Statistical Physics **1** (1971) 186, ISSN: 1532-2424,
URL: http://dx.doi.org/10.1080/00411457108231446 (cit. on p. 9).

[28] C. S. Wu, E. Ambler, R. W. Hayward, D. D. Hoppes and R. P. Hudson,
Experimental Test of Parity Conservation in Beta Decay, Phys. Rev. **105** (4 1957) 1413,
URL: https://link.aps.org/doi/10.1103/PhysRev.105.1413 (cit. on p. 10).

[29] N. Cabibbo, *Unitary Symmetry and Leptonic Decays*, Phys. Rev. Lett. **10** (12 1963) 531,
URL: https://link.aps.org/doi/10.1103/PhysRevLett.10.531 (cit. on p. 10).

[30] M. T. Kobayashi Makoto, *CP-Violation in the Renormalizable Theory of Weak Interaction*,
Prog Theor Phys **49** (2 1973), URL: https://doi.org/10.1143/PTP.49.652
(cit. on p. 10).

[31] *The Nobel Prize in Physics 1979*,
URL: https://www.nobelprize.org/prizes/physics/1979/summary/ (visited on 14/07/2024) (cit. on p. 10).

[32] M. L. Perl, "Evidence for, and Properties of, the New Charged Heavy Lepton",
12th Rencontres de Moriond, Session 1: High-Energy Leptonic Interactions, 1977 75
(cit. on p. 15).

[33] A. Pich, *Precision tau physics*, Progress in Particle and Nuclear Physics **75** (2014) 41,
ISSN: 0146-6410, URL:
https://www.sciencedirect.com/science/article/pii/S0146641013001087
(cit. on p. 15).

[34] N. A. Tornqvist, *The A1 Mass From $\tau \to A1$ Neutrino Decay*, (1987),
URL: https://inspirehep.net/literature/247060 (cit. on pp. 15, 94).

[35] R. L. Workman et al., *Status of Higgs Boson Physics*, PTEP **2022** (2022) 083C01
(cit. on pp. 17–19).

[36] P. Nath, *Perspectives on Higgs Boson and Supersymmetry*, 2013,
arXiv: 1302.1863 [hep-ph] (cit. on p. 17).

[37] A. D. Sakharov,
Violation of CP invariance, C asymmetry, and baryon asymmetry of the universe,
Soviet Physics Uspekhi **34** (1991) 392,
URL: https://dx.doi.org/10.1070/PU1991v034n05ABEH002497 (cit. on p. 19).

[38] M. Vretenar et al., *Linac4 design report*, vol. 6, CERN Yellow Reports: Monographs,
Geneva: CERN, 2020, URL: https://cds.cern.ch/record/2736208 (cit. on p. 21).

[39] S. Albright et al.,
New Longitudinal Beam Production Methods in the CERN Proton Synchrotron Booster.,
JACoW IPAC **'21** (2021) 4130, URL: https://cds.cern.ch/record/2811646
(cit. on p. 21).

[40] *The Proton Synchrotron*, (2012), URL: https://cds.cern.ch/record/1997189
(cit. on p. 21).

[41] *The Super Proton Synchrotron*, (2012), URL: https://cds.cern.ch/record/1997188
(cit. on p. 21).

[42] O. S. Brüning et al., *LHC Design Report*, CERN Yellow Reports: Monographs,
Geneva: CERN, 2004, URL: https://cds.cern.ch/record/782076 (cit. on pp. 21, 61).

[43] *The CERN accelerator complex*, URL:
https://cds.cern.ch/images/CERN-GRAPHICS-2022-001-1 (visited on 21/11/2022)
(cit. on p. 22).

[44] *Mean number of interactions per crossing*,
URL: https://atlas.web.cern.ch/Atlas/GROUPS/DATAPREPARATION/
PublicPlots/2023/DataSummary/figs/mu_run123.pdf (visited on 15/01/2024)
(cit. on p. 23).

[45] *High-Luminosity Large Hadron Collider (HL-LHC): Technical design report*,
CERN Yellow Reports: Monographs, Geneva: CERN, 2020,
URL: https://cds.cern.ch/record/2749422 (cit. on pp. 23, 24, 134).

[46] *LHC/HL-LHC Plan*,
URL: https://hilumilhc.web.cern.ch/sites/default/files/HL-
LHC_Janvier2022.pdf (visited on 03/07/2024) (cit. on p. 23).

[47] *Snowmass White Paper Contribution: Physics with the Phase-2 ATLAS and CMS Detectors*,
tech. rep., CERN, 2022, URL: https://cds.cern.ch/record/2805993 (cit. on p. 24).

[48] ATLAS Collaboration, *The ATLAS Experiment at the CERN Large Hadron Collider*,
Journal of Instrumentation **3** (2008) S08003,
URL: https://dx.doi.org/10.1088/1748-0221/3/08/S08003 (cit. on p. 24).

[49] ATLAS Collaboration, *Charged-particle multiplicities in pp interactions at* $\sqrt{s} = 900GeV$
measured with the ATLAS detector at the LHC, Physics Letters B **688** (2010) 21,
ISSN: 0370-2693, URL: http://dx.doi.org/10.1016/j.physletb.2010.03.064
(cit. on p. 25).

[50] J. Pequenao, *Computer generated image of the whole ATLAS detector*,
URL: https://cds.cern.ch/images/CERN-GE-0803012-01 (visited on 25/10/2022)
(cit. on p. 25).

[51] *The Inner Detector*, URL: https://atlas.cern/Discover/Detector/Inner-Detector (visited on 03/07/2024) (cit. on p. 26).

[52] M. Capeans et al., *ATLAS Insertable B-Layer Technical Design Report*, tech. rep., 2010, URL: https://cds.cern.ch/record/1291633 (cit. on p. 26).

[53] *Performance of the ATLAS Transition Radiation Tracker in Run 1 of the LHC: tracker properties*, Journal of Instrumentation **12** (2017) P05002, ISSN: 1748-0221, URL: http://dx.doi.org/10.1088/1748-0221/12/05/P05002 (cit. on pp. 27, 46).

[54] *Muon spectrometer*, URL: https://atlas.cern/Discover/Detector/Muon-Spectrometer (visited on 03/07/2024) (cit. on p. 27).

[55] T. Kawamoto et al., *New Small Wheel Technical Design Report*, tech. rep., 2013, URL: https://cds.cern.ch/record/1552862 (cit. on p. 27).

[56] A. M. Rodriguez Vera, L. Kretschmann and U. A. E. Bilow, *Magnet System - ATLAS Fact Sheet [German]*, (2023), URL: https://cds.cern.ch/record/2850747 (cit. on p. 28).

[57] ATLAS Collaboration, *The ATLAS trigger system for LHC Run 3 and trigger performance in 2022*, Journal of Instrumentation **19** (2024) P06029, ISSN: 1748-0221, URL: http://dx.doi.org/10.1088/1748-0221/19/06/P06029 (cit. on p. 28).

[58] ATLAS Outreach, "ATLAS Fact Sheet : To raise awareness of the ATLAS detector and collaboration on the LHC", 2010, URL: https://cds.cern.ch/record/1457044 (cit. on p. 28).

[59] ATLAS Collaboration, *Summary plots from the ATLAS Standard Model physics group*, URL: https://atlas.web.cern.ch/Atlas/GROUPS/PHYSICS/CombinedSummaryPlots/SM/index.html#ATLAS_b_SMSummary_FiducialXsect (visited on 29/03/2024) (cit. on p. 29).

[60] J. Catmore, *A New Petabyte-scale Data Derivation Framework for ATLAS*, (2015), URL: https://cds.cern.ch/record/2004909 (cit. on p. 29).

[61] S. Höche, *Introduction to parton-shower event generators*, 2015, arXiv: 1411.4085 [hep-ph], URL: https://arxiv.org/abs/1411.4085 (cit. on pp. 30, 31).

[62] B. Andersson, G. Gustafson, G. Ingelman and T. Sjöstrand, *Parton fragmentation and string dynamics*, Physics Reports **97** (1983) 31, ISSN: 0370-1573, URL: https://www.sciencedirect.com/science/article/pii/0370157383900807 (cit. on p. 31).

[63] B. Webber, *A QCD model for jet fragmentation including soft gluon interference*, Nuclear Physics B **238** (1984) 492, ISSN: 0550-3213, URL: https://www.sciencedirect.com/science/article/pii/055032138490333X (cit. on p. 31).

[64] *Geant4—a simulation toolkit*, Nuclear Instruments and Methods in Physics Research Section A: Accelerators, Spectrometers, Detectors and Associated Equipment **506** (2003) 250, ISSN: 0168-9002, URL: https://www.sciencedirect.com/science/article/pii/S0168900203013688 (cit. on p. 31).

[65] E. Bothmann et al., *Event generation with Sherpa 2.2*, SciPost Phys. **7** (2019) 034, arXiv: 1905.09127 [hep-ph] (cit. on p. 31).

[66] P. Nason and C. Oleari, *NLO Higgs boson production via vector-boson fusion matched with shower in POWHEG*, JHEP **02** (2010) 037, arXiv: 0911.5299 [hep-ph] (cit. on p. 31).

[67] S. Alioli, P. Nason, C. Oleari and E. Re, *A general framework for implementing NLO calculations in shower Monte Carlo programs: the POWHEG BOX*, JHEP **06** (2010) 043, arXiv: 1002.2581 [hep-ph] (cit. on p. 31).

[68] P. Nason, *A new method for combining NLO QCD with shower Monte Carlo algorithms*, JHEP **11** (2004) 040, arXiv: hep-ph/0409146 (cit. on p. 31).

[69] S. Frixione, P. Nason and C. Oleari, *Matching NLO QCD computations with parton shower simulations: the POWHEG method*, JHEP **11** (2007) 070, arXiv: 0709.2092 [hep-ph] (cit. on p. 31).

[70] T. Sjöstrand et al., *An introduction to PYTHIA 8.2*, Computer Physics Communications **191** (2015) 159, ISSN: 0010-4655, URL: http://dx.doi.org/10.1016/j.cpc.2015.01.024 (cit. on p. 31).

[71] ATLAS Collaboration, *Measurements of Higgs boson production cross-sections in the $H \to \tau^+\tau^-$ decay channel in pp collisions at $\sqrt{s} = 13\ TeV$ with the ATLAS detector*, Journal of High Energy Physics **2022** (2022) 175, URL: https://doi.org/10.1007/JHEP08(2022)175 (cit. on pp. 32, 61, 68, 71, 74, 78, 79, 81, 85, 88, 123, 141).

[72] J. Butterworth et al., *PDF4LHC recommendations for LHC Run II*, Journal of Physics G: Nuclear and Particle Physics **43** (2016) 023001, ISSN: 1361-6471, URL: http://dx.doi.org/10.1088/0954-3899/43/2/023001 (cit. on p. 32).

[73] R. D. Ball et al., *Parton distributions for the LHC run II*, Journal of High Energy Physics **2015** (2015), ISSN: 1029-8479, URL: http://dx.doi.org/10.1007/JHEP04(2015)040 (cit. on p. 32).

[74] ATLAS Collaboration, *Measurement of the Z/γ^* boson transverse momentum distribution in pp collisions at $\sqrt{s} = 7$ TeV with the ATLAS detector*, Journal of High Energy Physics **2014** (2014), ISSN: 1029-8479, URL: http://dx.doi.org/10.1007/JHEP09(2014)145 (cit. on p. 32).

[75] ATLAS Collaboration, *ATLAS Pythia 8 tunes to 7 TeV data*, tech. rep., CERN, 2014, URL: https://cds.cern.ch/record/1966419 (cit. on p. 32).

[76] J. Pequenao and P. Schaffner, *How ATLAS detects particles: diagram of particle paths in the detector*, 2013, URL: https://cds.cern.ch/record/1505342 (cit. on p. 34).

[77] ATLAS Collaboration, *Luminosity determination in pp collisions at $\sqrt{s}$ = 13 TeV using the ATLAS detector at the LHC*, tech. rep., CERN, 2019, URL: https://cds.cern.ch/record/2677054 (cit. on p. 33).

[78] ATLAS Collaboration, *Luminosity determination in pp collisions at $\sqrt{s}$=13 TeV using the ATLAS detector at the LHC*, (2022), arXiv: 2212.09379 (cit. on p. 33).

[79] R. L. Workman et al., *Passage of Particles Through Matter*, PTEP **2022** (2022) 083C01 (cit. on pp. 33, 46).

[80] ATLAS Collaboration, *Electron reconstruction and identification in the ATLAS experiment using the 2015 and 2016 LHC proton–proton collision data at $\sqrt{s}$ = 13 TeV*, The European Physical Journal C **79** (), ISSN: 1434-6052, URL: http://dx.doi.org/10.1140/epjc/s10052-019-7140-6 (cit. on pp. 33–35).

[81] ATLAS Collaboration, *Electron and photon energy calibration with the ATLAS detector using LHC Run 2 data*, Journal of Instrumentation **19** (2024) P02009, ISSN: 1748-0221, URL: http://dx.doi.org/10.1088/1748-0221/19/02/P02009 (cit. on p. 33).

[82] R. Frühwirth, *A Gaussian-mixture approximation of the Bethe–Heitler model of electron energy loss by bremsstrahlung*, Computer Physics Communications **154** (2003) 131, ISSN: 0010-4655, URL: https://www.sciencedirect.com/science/article/pii/S0010465503002923 (cit. on p. 34).

[83] *Electron and photon performance measurements with the ATLAS detector using the 2015–2017 LHC proton-proton collision data*, Journal of Instrumentation **14** (2019) P12006, ISSN: 1748-0221, URL: http://dx.doi.org/10.1088/1748-0221/14/12/P12006 (cit. on p. 35).

[84] ATLAS Collaboration, *Muon reconstruction and identification efficiency in ATLAS using the full Run 2 pp collision data set at $\sqrt{s}$ = 13TeV*, The European Physical Journal C **81** (2021), ISSN: 1434-6052, URL: http://dx.doi.org/10.1140/epjc/s10052-021-09233-2 (cit. on pp. 35, 36, 69).

[85] M. Aaboud and all, *Jet reconstruction and performance using particle flow with the ATLAS Detector*, The European Physical Journal C **77** (2017), ISSN: 1434-6052, URL: http://dx.doi.org/10.1140/epjc/s10052-017-5031-2 (cit. on p. 36).

[86] G. a. Aad, *Topological cell clustering in the ATLAS calorimeters and its performance in LHC Run 1*, The European Physical Journal C **77** (2017), ISSN: 1434-6052, URL: http://dx.doi.org/10.1140/epjc/s10052-017-5004-5 (cit. on p. 36).

[87] *Jet energy scale and resolution measured in proton–proton collisions at $\sqrt{s}$ = 13 TeV with the ATLAS detector*, The European Physical Journal C **81** (2021), ISSN: 1434-6052, URL: http://dx.doi.org/10.1140/epjc/s10052-021-09402-3 (cit. on pp. 37, 63).

[88] *Graph Neural Network Jet Flavour Tagging with the ATLAS Detector*, tech. rep., CERN, 2022, URL: https://cds.cern.ch/record/2811135 (cit. on p. 37).

[89] ATLAS Collaboration, *The performance of missing transverse momentum reconstruction and its significance with the ATLAS detector using 140 fb^{-1} of $\sqrt{s}$ = 13 TeV pp collisions*, 2024, arXiv: 2402.05858 [hep-ex], URL: https://arxiv.org/abs/2402.05858 (cit. on p. 37).

[90] ATLAS Collaboration, *Reconstruction, Identification, and Calibration of hadronically decaying tau leptons with the ATLAS detector for the LHC Run 3 and reprocessed Run 2 data*, ATL-PHYS-PUB-2022-044, CERN, 2022, URL: https://cds.cern.ch/record/2827111 (cit. on pp. 38, 40, 41, 45).

[91] ATLAS Collaboration, *Measurement of the tau lepton reconstruction and identification performance in the ATLAS experiment using pp collisions at $\sqrt{s}$ = 13 TeV*, tech. rep., CERN, 2017, URL: https://cds.cern.ch/record/2261772 (cit. on p. 38).

[92] ATLAS Collaboration, *Identification of hadronic tau lepton decays using neural networks in the ATLAS experiment*, ATL-PHYS-PUB-2019-033, CERN, 2019 (cit. on pp. 38, 40).

[93] ATLAS Collaboration, *Reconstruction, Identification, and Calibration of hadronically decaying tau leptons with the ATLAS detector for the LHC Run 3 and reprocessed Run 2 data*, ATL-PHYS-PUB-2022-044, 2022, URL: https://cds.cern.ch/record/2827111/files/ATL-PHYS-PUB-2022-044.pdf (cit. on p. 39).

[94] ATLAS Collaboration, *Identification of hadronic tau lepton decays using neural networks in the ATLAS experiment*, ATL-PHYS-PUB-2019-033, 2019, URL: https://cds.cern.ch/record/2688062/files/ATL-PHYS-PUB-2019-033.pdf (cit. on p. 39).

[95] *Reconstruction of hadronic decay products of tau leptons with the ATLAS experiment*, The European Physical Journal C **76** (2016), ISSN: 1434-6052, URL: http://dx.doi.org/10.1140/epjc/s10052-016-4110-0 (cit. on p. 40).

[96] R. et al., *Higgs decay to $\tau^+\tau^-$ A possible signature of intermediate mass Higgs bosons at high energy hadron colliders*, Nuclear Physics B (1988), URL: https://doi.org/10.1016/0550-3213(88)90019-3 (cit. on p. 41).

[97] A. Elagin, P. Murat, A. Pranko and A. Safonov, *A new mass reconstruction technique for resonances decaying to*, Nuclear Instruments and Methods in Physics Research Section A: Accelerators, Spectrometers, Detectors and Associated Equipment **654** (2011) 481, ISSN: 0168-9002, URL: http://dx.doi.org/10.1016/j.nima.2011.07.009 (cit. on pp. 41, 42).

[98] Michael Hübner, *Higgs Boson Production Cross-Section Measurements in the Di-Tau Final State at ATLAS*, https://bonndoc.ulb.uni-bonn.de/xmlui/handle/20.500.11811/9734: Rheinische Friedrich-Wilhelms-Universität, 2022 (cit. on pp. 43, 76).

[99] A. Joseph,
Markov Chain Monte Carlo Methods in Quantum Field Theories: A Modern Primer,
Springer International Publishing, 2020, ISBN: 9783030460440,
URL: http://dx.doi.org/10.1007/978-3-030-46044-0 (cit. on p. 43).

[100] Y. Buchholzer, *Rekonstruktion der invarianten Masse des H->tautau Zerfalles mit einem neuronalen Netzwerk*, MA thesis: Physikalisches Institut, 2024 (cit. on p. 43).

[101] R. Hmaid,
Ditau Reconstruction with a Deep Neural Network using Spin-1 and Spin-0 Datasets,
MA thesis: Physikalisches Institut, 2022 (cit. on p. 43).

[102] E. Hines, *Particle Identification with the ATLAS Transition Radiation Tracker*, tech. rep.,
CERN, 2011, URL: https://cds.cern.ch/record/1400442 (cit. on p. 45).

[103] Arif Bayirli,
Particle Identification with Machine Learning in Transition Radiation Tracker at ATLAS,
ATLAS-COM-INDET-2020-001, 2020, URL: https://cds.cern.ch/record/2705706
(cit. on pp. 45, 52, 56, 58).

[104] S. Mehlhase,
Electron Identification with the TRT and the W Boson Mass Measurement at ATLAS,
MA thesis: Niels Bohr Institute, 2007 (cit. on p. 46).

[105] E. Celebi et al., *Test beam studies of the TRD prototype filled with different gas mixtures based on Xe, Kr, and Ar*, Journal of Physics: Conference Series **798** (2017) 012172,
URL: https://dx.doi.org/10.1088/1742-6596/798/1/012172 (cit. on pp. 46, 59).

[106] *TRT available gas scenarios*, TrtSoftware, 2022,
URL: https://twiki.cern.ch/twiki/bin/view/Atlas/TRT_geometries (visited on 26/06/2024) (cit. on p. 47).

[107] S. Hochreiter and J. Schmidhuber, *Long Short-term Memory*,
Neural computation **9** (1997) 1735 (cit. on p. 47).

[108] colah's blog, *Understanding LSTM Networks*,
URL: https://colah.github.io/posts/2015-08-Understanding-LSTMs/ (visited on 31/07/2024) (cit. on p. 48).

[109] Aleksanr Petukhov,
Refinement of the TRT PID algorithm based on Recurrent Neural Networks,
ATLAS-COM-INDET-2021-021, 2021, URL: https://cds.cern.ch/record/2783151
(cit. on pp. 48, 49, 51).

[110] *Tracking CP Recommendations*, InDetTrackingPerformance,
URL: https://twiki.cern.ch/twiki/bin/viewauth/AtlasProtected/TrackingCPRecsEarly2018 (visited on 28/04/2022) (cit. on p. 50).

[111] *Definitions of common TRT offline software quantities*, TrtSoftware, 2022,
URL: https://twiki.cern.ch/twiki/bin/view/Atlas/TrtSoftwareDefinitions
(visited on 17/01/2022) (cit. on p. 50).

[112] Philipp König, *Particle Identification at High Occupancy with the Transition Radiation1 Tracker (TRT) at ATLAS*, ATL-COM-INDET-2018-017, 2018, URL: https://cds.cern.ch/record/2312153/files/ATL-COM-INDET-2018-017.pdf (cit. on p. 51).

[113] *Vol. 3 (2023): CERN Environment Report—Rapport sur l'environnement 2021–2022*, URL: https://doi.org/10.25325/CERN-Environment-2023-003 (visited on 30/06/2024) (cit. on p. 59).

[114] B. Mindur, *ATLAS Transition Radiation Tracker (TRT): Straw tubes for tracking and particle identification at the Large Hadron Collider*, Nuclear Instruments and Methods in Physics Research Section A: Accelerators, Spectrometers, Detectors and Associated Equipment **845** (2017) 257, Proceedings of the Vienna Conference on Instrumentation 2016, ISSN: 0168-9002, URL: https://www.sciencedirect.com/science/article/pii/S0168900216301905 (cit. on p. 59).

[115] L. Meng and A. Collaboration, *ATLAS ITk Pixel Detector Overview*, tech. rep., CERN, 2021, URL: https://cds.cern.ch/record/2767329 (cit. on p. 59).

[116] ATLAS Collaboration, *Fiducial and STXS cross-sections*, URL: https://twiki.cern.ch/twiki/bin/view/LHCPhysics/LHCHWGFiducialAndSTXS (visited on 03/11/2023) (cit. on pp. 61, 66, 67).

[117] K. Cranmer, G. Lewis, L. Moneta, A. Shibata and W. Verkerke, *HistFactory: A tool for creating statistical models for use with RooFit and RooStats*, tech. rep., New York U., 2012, URL: https://cds.cern.ch/record/1456844 (cit. on p. 63).

[118] Z.-T. Wei, *Sudakov form factor in effective field theory*, 2004, arXiv: hep-ph/0403069 [hep-ph], URL: https://arxiv.org/abs/hep-ph/0403069 (cit. on p. 63).

[119] B. Amini et al., *Differential measurements of the production of the Higgs boson through Vector Boson Fusion in the $\tau^+\tau^-$ channel with the ATLAS detector : Internal Documentation*, tech. rep., CERN, 2023, URL: https://cds.cern.ch/record/2858708 (cit. on pp. 63, 65, 68, 76, 82, 128).

[120] *1974 CERN School of Computing, Godoysund, Norway, 11-24 Aug 1974: Proceedings*, CERN Yellow Reports: School Proceedings, 1974 (cit. on p. 64).

[121] *TRExFitter source code*, ATLAS Collaboration, 2024, URL: https://gitlab.cern.ch/ATauLeptonAnalysiS/TRExFitter/-/tree/vbf-stxs-development/config?ref_type=heads (visited on 23/09/2024) (cit. on pp. 64, 65, 107).

[122] James F., *MINUIT: Function Minimization and Error Analysis Reference Manual*, CERNLIB-D506, 1994, URL: https://cds.cern.ch/record/2296388/files/minuit.pdf (cit. on p. 65).

[123] L. L. et al, *Statistical Methods for Data Analysis With Application in Particle Physics*, Springer, 2023, ISBN: 9783031199349, URL: https://link-springer-com.ezproxy.cern.ch/book/10.1007/978-3-031-19934-9 (cit. on pp. 65, 66).

[124] G. Cowan, K. Cranmer, E. Gross and O. Vitells,
Asymptotic formulae for likelihood-based tests of new physics,
The European Physical Journal C **71** (2011), ISSN: 1434-6052,
URL: http://dx.doi.org/10.1140/epjc/s10052-011-1554-0 (cit. on p. 66).

[125] N. Berger et al., *Simplified Template Cross Sections - Stage 1.1*, 2019,
arXiv: 1906.02754 [hep-ph], URL: https://arxiv.org/abs/1906.02754
(cit. on p. 66).

[126] C. M. P. Govoni, *Z production via Vector Boson Fusion at LHC*, (2010), arXiv: 1001.4357v1
(cit. on p. 68).

[127] *Performance of electron and photon triggers in ATLAS during LHC Run 2*,
The European Physical Journal C **80** (2020), ISSN: 1434-6052,
URL: http://dx.doi.org/10.1140/epjc/s10052-019-7500-2 (cit. on p. 68).

[128] *Performance of the ATLAS muon triggers in Run 2*,
Journal of Instrumentation **15** (2020) P09015, ISSN: 1748-0221,
URL: http://dx.doi.org/10.1088/1748-0221/15/09/p09015 (cit. on p. 68).

[129] *The ATLAS inner detector trigger performance in pp collisions at 13 TeV during LHC Run 2*,
The European Physical Journal C **82** (2022), ISSN: 1434-6052,
URL: http://dx.doi.org/10.1140/epjc/s10052-021-09920-0 (cit. on p. 68).

[130] *Performance of the ATLAS Level-1 topological trigger in Run 2*,
The European Physical Journal C **82** (2022), ISSN: 1434-6052,
URL: http://dx.doi.org/10.1140/epjc/s10052-021-09807-0 (cit. on p. 68).

[131] *Performance of the ATLAS Level-1 topological trigger in Run 2*,
The European Physical Journal C **82** (2022), ISSN: 1434-6052,
URL: http://dx.doi.org/10.1140/epjc/s10052-021-09807-0 (cit. on p. 69).

[132] *Electron and photon efficiencies in LHC Run 2 with the ATLAS experiment*,
Journal of High Energy Physics **2024** (2024), ISSN: 1029-8479,
URL: http://dx.doi.org/10.1007/JHEP05(2024)162 (cit. on p. 69).

[133] *Identification and rejection of pile-up jets at high pseudorapidity with the ATLAS detector*,
The European Physical Journal C **77** (2017), ISSN: 1434-6052,
URL: http://dx.doi.org/10.1140/epjc/s10052-017-5081-5 (cit. on p. 69).

[134] *ATLAS flavour-tagging algorithms for the LHC Run 2 pp collision dataset*,
The European Physical Journal C **83** (2023), ISSN: 1434-6052,
URL: http://dx.doi.org/10.1140/epjc/s10052-023-11699-1 (cit. on p. 69).

[135] F. H. Becherer et al., *Measurement of the Higgs boson coupling properties in the $H\rightarrow \tau\tau$ decay channel at $\sqrt{s}$ = 13 TeV with the ATLAS detector*, tech. rep., CERN, 2020,
URL: https://cds.cern.ch/record/2741326 (cit. on pp. 71, 114, 115).

[136] *Measurement of the production cross section of jets in association with a Z boson in pp collisions at $\sqrt{s}$ = 7 TeV with the ATLAS detector*,
Journal of High Energy Physics **2013** (2013), ISSN: 1029-8479,
URL: http://dx.doi.org/10.1007/JHEP07(2013)032 (cit. on p. 73).

[137] The ATLAS collaboration,
Modelling $Z \to \tau\tau$ processes in ATLAS with τ-embedded $Z \to \mu\mu$ data,
Journal of Instrumentation **10** (2015) P09018, ISSN: 1748-0221,
URL: http://dx.doi.org/10.1088/1748-0221/10/09/P09018 (cit. on p. 73).

[138] M. L. Ojeda, Q. Buat, P.-O. Deviveiros and A. De Maria, *Modelling $Z \to \tau\tau$ events through object-level embedding of reconstructed τ decay products in $Z \to ee$ and $Z \to \mu\mu$ events*, tech. rep., CERN, 2020, URL: https://cds.cern.ch/record/2741436 (cit. on p. 73).

[139] ATLAS Collaboration, *Estimation of non-prompt and fake lepton backgrounds in final states with top quarks produced in proton-proton collisions at $\sqrt{s}$=8 TeV with the ATLAS detector*, ATLAS-CONF-2014-058, 2014,
URL: https://cds.cern.ch/record/1951336/files/ATLAS-CONF-2014-058.pdf (cit. on pp. 74, 81).

[140] ATLAS Collaboration,
Measurements of Higgs boson production and couplings in the four-lepton channel in pp collisions at center-of-mass energies of 7 and 8 TeV with the ATLAS detector,
Physical Review D **91** (2015), ISSN: 1550-2368,
URL: http://dx.doi.org/10.1103/PhysRevD.91.012006 (cit. on pp. 74, 81).

[141] ATLAS Collaboration, *Differential cross-section measurements for the electroweak production of dijets in association with a Z boson in proton–proton collisions at ATLAS*, The European Physical Journal C **81** (2021), ISSN: 1434-6052,
URL: http://dx.doi.org/10.1140/epjc/s10052-020-08734-w (cit. on p. 79).

[142] *ROOT Chi2Test function*, URL: https://root.cern/doc/master/classTH1.html#ab7d63c7c177ccbf879b5dc31f2311b27 (visited on 05/04/2024) (cit. on p. 99).

[143] Glen Cowan, Kyle Cranmer, Eilam Gross, Ofer Vitells,
Asymptotic formulae for likelihood-based tests of new physics, (2013), arXiv: 1007.1727v3 (cit. on p. 107).

[144] I. Asimov, *Franchise*,
https://www.astro.sunysb.edu/fwalter/HON301/franchise.pdf, 1955 (cit. on p. 107).

[145] *Collection of public plots for JHEP 08 (2022) 175*,
https://atlas.web.cern.ch/Atlas/GROUPS/PHYSICS/PAPERS/HIGG-2019-09/, (visited on 06/06/2024) (cit. on p. 123).

[146] *Evaluation of QCD uncertainties for Higgs boson production through gluon fusion and in association with two top quarks for simplified template cross-section measurements*, tech. rep., CERN, 2023, URL: https://cds.cern.ch/record/2878797 (cit. on p. 123).

[147] T. Junk, *Confidence level computation for combining searches with small statistics*, Nuclear Instruments and Methods in Physics Research Section A: Accelerators, Spectrometers, Detectors and Associated Equipment **434** (1999) 435, ISSN: 0168-9002,
URL: http://dx.doi.org/10.1016/S0168-9002(99)00498-2 (cit. on p. 124).

[148] CMS Collaboration, *Measurements of Higgs boson production in the decay channel with a pair of τ-leptons in proton–proton collisions at $\sqrt{s} = 13\ TeV$*,
The European Physical Journal C **83** (2023) 562,
URL: https://doi.org/10.1140/epjc/s10052-023-11452-8 (cit. on pp. 130, 131).

[149] CMS Collaboration,
An embedding technique to determine $\tau\tau$ backgrounds in proton-proton collision data,
Journal of Instrumentation **14** (2019) P06032, ISSN: 1748-0221,
URL: http://dx.doi.org/10.1088/1748-0221/14/06/P06032 (cit. on p. 130).

[150] ATLAS Collaboration, *Measurement of the properties of Higgs boson production at $\sqrt{s}$ =13 TeV in the $H \to \gamma\gamma$ channel using 139 fb^{-1} of pp collision data with the ATLAS experiment*,
Journal of High Energy Physics **2023** (2023), ISSN: 1029-8479,
URL: http://dx.doi.org/10.1007/JHEP07(2023)088 (cit. on p. 131).

[151] ATLAS Collaboration,
Measurements of Higgs boson production by gluon-gluon fusion and vector-boson fusion using $H \to WW* \to e\nu\mu\nu$ decays in pp collisions at $\sqrt{s} = 13\ TeV$ with the ATLAS detector,
Physical Review D **108** (2023), ISSN: 2470-0029,
URL: http://dx.doi.org/10.1103/PhysRevD.108.032005 (cit. on p. 131).

List of Figures

2.1 The Standard Model particles. . . . 6
2.2 Illustration of the Mexican hat potential with $\mu < 0$. . . . 12
2.3 Feynman diagram of possible τ lepton decays. . . . 16
2.4 τ decay branching ratios. . . . 16
2.5 Leading order Feynman diagrams of the main Higgs production modes. . . . 18
2.6 Cross-section of SM Higgs boson production modes as a function of the center of mass energy in pp collisions 18
2.7 Branching ratios of the SM Higgs boson. . . . 19

3.1 The CERN accelerator complex. . . . 22
3.2 Average number of interactions per bunch crossing. . . . 23
3.3 Expected uncertainty on Higgs cross-section measurements per-production-mode normalized to the SM predictions for combined ATLAS and CMS performance in the HL-LHC project. . . . 24
3.4 Schematic view of the ATLAS detector in Run 2. . . . 25
3.5 ATLAS coordinate system. . . . 26
3.6 Cross-sections of Standard Model processes for different center-of-mass scenarios. . 29
3.7 Illustration of a simulation in hadron-hadron collision. . . . 30

4.1 Particle signatures in the ATLAS detector. . . . 34
4.2 QCD jet and τ_{had} lepton signatures. . . . 39
4.3 Background rejection of 1- and 3-prong τ_{had} candidates in dependence of the truth $\tau_{\text{had,vis}}$ efficiency for the RNN based identification algorithm. . . . 39
4.4 Fake rejection for medium τ-ID in bins of the transverse momentum and the pseudorapidity. . . . 40
4.5 Reconstruction efficiency matrix for the five τ_{had} decay modes with a BDT-based classifier in $\gamma* \rightarrow \tau\tau$ events. . . . 41

5.1 Signal creation in the TRT. . . . 46
5.2 Changes in the TRT gas geometry over time. . . . 47
5.3 Schematic of a LSTM network. . . . 48
5.4 RNN architecture. . . . 49
5.5 Idealized score distributions of background and signal samples. . . . 52
5.6 Investigation of the relevance of the inputs. . . . 53
5.7 Current activation functions in blue and their potential replacements in red. . . . 55

5.8 RNN performance depending on the number of nodes or activation functions. 55
5.9 Performance comparison between the initial RNN setup and the reduced-complexity model. 56
5.10 Performance comparison of models trained on muon and pion background. 57
5.11 ΔR-dependent ROC curves. 58
5.12 RNN and eProbHT ROC curves based on Run 3 Monte Carlo, barrel region. 58
5.13 Comparison between the RNN and eProbHT background rejection at 90 % signal efficiency per momentum bin. 59

6.1 Shape and normalization variations of systematic uncertainties. 63
6.2 Impact of the Twosided as well as Presmocorrect symmetrisation strategies on the envelop of the Jet Flavor Response systematic. 64
6.3 Profile likelihood scan of the NP norm_ll_vbf_1_high_pth_mjj_ge1500_Ztt. 65
6.4 Definition of stage 1.2 STXS bins. 67
6.5 Di-tau mass distribution and corresponding yield table in the VBF production. 72
6.6 Feynman diagrams of prominent detector signatures. 73
6.7 Sketch of the event categorization as well as the 18 targeted STXS stage 1.2 bins. . . 76
6.8 Expected signal purity per signal region. 77
6.9 Visualization of the Legacy analysis design. 78

7.1 Visualization of the Fake Factor method. 83
7.2 Feynman diagram of the W + jet process. 83
7.3 Schematic diagram of the Fake Factor method. 84
7.4 Not-medium and loose-not-medium fake factors for 1prong events applied in the $\tau_{\text{had}}\tau_{\text{had}}$ channel. 86
7.5 Possible τ-ID combinatorics in the $\tau_{\text{had}}\tau_{\text{had}}$ channel. 87
7.6 Decay-mode dependent background composition in the $\tau_{\text{lep}}\tau_{\text{had}}$ channel at pre-selection level. 90
7.7 WCRs used for 1p0n fake factor calculation in the end-cap region 91
7.8 Decay-mode dependent Fake Factors 92
7.9 Comparison of inclusive and decay-mode dependent fake template in the high $\Delta\eta$-region. 93
7.10 Di-tau mass distributions of the VBF category in the decay-mode grouping. 95
7.11 Leading visible τ mass of the $Z \rightarrow \tau\tau$ process split in decay-modes. 96
7.12 Di-tau mass distribution for common and newly defined VBF pre-selection with focus on the signal yield. 97
7.13 Comparison of 1σ statistical uncertainties on Fake Factors due to limited sample size in W + jets CR. 98
7.14 Fake templates of the $\tau_{\text{had}}\tau_{\text{had}}$ channel. 100
7.15 Fake templates of the $\tau_{\text{lep}}\tau_{\text{had}}$ channel. 101
7.16 Fake templates of the $\tau_{\text{lep}}\tau_{\text{lep}}$ channel. 102
7.17 Fake template and its combined replacement. 103
7.18 Fake template and its inclusive replacement, which considers all templates of the group. 104
7.19 Visualization of a normalization uncertainty. 105

8.1 Expected sensitivity per measured STXS bin in Asimov studies. 109

8.2 Comparison of statistical uncertainties on the MC prediction per histogram bin for the original and the combined fake templates. . . . 112
8.3 Normalization uncertainties in the $\tau_{\text{had}}\tau_{\text{had}}$ VBF 0 regions. . . . 113
8.4 Pulls and constraints of $\tau_{\text{had}}\tau_{\text{had}}$ fake systematic uncertainties in 4PoI random scaling fits. . . . 115
8.5 Correlation of the $\tau_{\text{had}}\tau_{\text{had}}$ fake systematics in a $\tau_{\text{had}}\tau_{\text{had}}$ standalone 4PoI random scaling fit. . . . 116
8.6 $\tau_{\text{had}}\tau_{\text{had}}$ fake systematic uncertainties in production mode dependent standalone 4PoI random μ fits. . . . 117
8.7 De-correlation of the hh fake ff composition high-deta uncertainty across VBF regions. 118
8.8 Random μ 4PoI standalone fit comparison between the common setup and de-correlated $\tau_{\text{had}}\tau_{\text{had}}$ fake systematics across VBF regions. . . . 119
8.9 Collection of pre- and corresponding post-fit plots. . . . 121
8.10 $Z \to \tau\tau$ normalization factors for the VBF SRs determined in the sideband fit. . . . 122
8.11 Fit results of the 18 parameters of interest using the full Run 2 data set. . . . 125
8.12 Correlations of the 18 PoIs measured in the unblinded setup. . . . 126
8.13 Comparison of pre- and post-fit distributions of the low p_T^H, 350 GeV<m_{jj} < 700 GeV SR in the VBF 0 and VBF 1 selection, respectively. . . . 127
8.14 Ranking of systematic uncertainties for the VBF PoI with 350 GeV < m_{jj} < 700 GeV and p_T^H < 200 GeV . . . 129
8.15 Signal strength measurements of the CMS and the ATLAS collaboration. . . . 131

A.1 Track-level variables after re-weighting. . . . 136
A.2 Hit-level variables after re-weighting. . . . 137
A.3 Performance comparison between the Run 3 RNN and the likelihood-based approach in different pile-up regions. . . . 138
A.4 Performance comparison between the Run 3 RNN and the likelihood-based approach in different occupancy regions. . . . 139
A.5 Performance comparison between the Run 3 RNN and the likelihood-based approach in dependence on the number of hits. . . . 140

B.1 Targeted cross-sections and the event categorization in the 2022 analysis. . . . 141

C.1 WCRs used for 1p0n fake factor calculation . . . 143
C.2 WCRs used for 1p1n fake factor calculation . . . 144
C.3 WCRs used for 1p0n fake factor calculation . . . 145
C.4 WCRs used for 3p0n fake factor calculation . . . 146
C.5 WCRs used for 3pXn fake factor calculation . . . 147
C.6 Envelops of the fake shape combination normalization uncertainty in the $\tau_{\text{had}}\tau_{\text{had}}$ VBF 0 channel. . . . 148
C.7 Envelops of the fake shape combination normalization uncertainty in the $\tau_{\text{had}}\tau_{\text{had}}$ VBF 1 channel. . . . 149
C.8 Envelops of the fake shape combination normalization uncertainty in the $\tau_{\text{lep}}\tau_{\text{had}}$ VBF 0 channel. . . . 150

C.9 Envelops of the fake shape combination normalization uncertainty in the $\tau_{\text{lep}}\tau_{\text{had}}$ VBF 1 channel. . . . 151
C.10 Envelops of the fake shape combination normalization uncertainty in the $\tau_{\text{lep}}\tau_{\text{lep}}$ VBF 0 channel. . . . 152
C.11 Envelops of the fake shape combination normalization uncertainty in the $\tau_{\text{lep}}\tau_{\text{lep}}$ VBF 1 channel. . . . 153
C.12 Constraints on the Normalization Uncertainty in all channels (Asimov fit). . . . 154

D.1 Correlation of the $\tau_{\text{had}}\tau_{\text{had}}$ fake systematics in a VBF standalone 4PoI random scaling fit. 155
D.2 18 POI sensitivity comparison between usual and de-correlated setup in hh fake ff composition high-deta and hh fake ff stat 1p lnm . . . 156
D.3 Normalization factors in the random μ fit. . . . 157
D.4 Pre- and post-fit distributions of the VBF 0 high p_T^H regions in the $\tau_{\text{had}}\tau_{\text{had}}$ channel of the unblinded 18 PoI fit setup. . . . 158
D.5 Pre- and post-fit distributions of the VBF 0 low p_T^H regions in the $\tau_{\text{had}}\tau_{\text{had}}$ channel of the unblinded 18 PoI fit setup. . . . 159
D.6 Pre- and post-fit distributions of the VBF 1 high p_T^H regions in the $\tau_{\text{had}}\tau_{\text{had}}$ channel of the unblinded 18 PoI fit setup. . . . 160
D.7 Pre- and post-fit distributions of the VBF 1 low p_T^H regions in the $\tau_{\text{had}}\tau_{\text{had}}$ channel of the unblinded 18 PoI fit setup. . . . 161
D.8 Pre- and post-fit distributions of the VBF 0 high p_T^H regions in the $\tau_{\text{lep}}\tau_{\text{had}}$ channel of the unblinded 18 PoI fit setup. . . . 162
D.9 Pre- and post-fit distributions of the VBF 0 low p_T^H regions in the $\tau_{\text{lep}}\tau_{\text{had}}$ channel of the unblinded 18 PoI fit setup. . . . 163
D.10 Pre- and post-fit distributions of the VBF 1 high p_T^H regions in the $\tau_{\text{lep}}\tau_{\text{had}}$ channel of the unblinded 18 PoI fit setup. . . . 164
D.11 Pre- and post-fit distributions of the VBF 1 low p_T^H regions in the $\tau_{\text{lep}}\tau_{\text{had}}$ channel of the unblinded 18 PoI fit setup. . . . 165
D.12 Pre- and post-fit distributions of the VBF 0 high p_T^H regions in the $\tau_{\text{lep}}\tau_{\text{lep}}$ channel of the unblinded 18 PoI fit setup. . . . 166
D.13 Pre- and post-fit distributions of the VBF 0 low p_T^H regions in the $\tau_{\text{lep}}\tau_{\text{lep}}$ channel of the unblinded 18 PoI fit setup. . . . 167
D.14 Pre- and post-fit distributions of the VBF 1 high p_T^H regions in the $\tau_{\text{lep}}\tau_{\text{lep}}$ channel of the unblinded 18 PoI fit setup. . . . 168
D.15 Pre- and post-fit distributions of the VBF 1 low p_T^H regions in the $\tau_{\text{lep}}\tau_{\text{lep}}$ channel of the unblinded 18 PoI fit setup. . . . 169
D.16 Comparison of unblinded fit results based on original and combined fake templates. . 170
D.17 Systematic uncertainty ranking for the ggF PoIs $200\,\text{GeV} < p_T^H < 300\,\text{GeV}$ and $p_T^H > 300\,\text{GeV}$. . . . 171
D.18 Systematic uncertainty ranking for the ggF PoIs with requirements on the number of jets. 172
D.19 Systematic uncertainty ranking for the low p_T^H VBF PoIs. . . . 173
D.20 Systematic uncertainty ranking for the high p_T^H VBF PoIs. . . . 174
D.21 Systematic uncertainty ranking for the $t\bar{t}H$ and VH PoIs. . . . 175

List of Tables

3.1 Specification of event generation. 32

5.1 Default hyperparameter setting of the Run 2 setup. 49
5.2 Track selection criteria. 50
5.3 Node dependent CPU time for 100 events measured in the TrackCollectionMerger. . 54
5.4 CPU time dependent on selected activation function for 100 events measured in the TrackCollectionMerger. 55

6.1 Trigger signatures and the corresponding p_T threshold used in the event selection. . . 69
6.2 Baseline selection of the three channels $\tau_e\tau_\mu$, $\tau_{\text{lep}}\tau_{\text{had}}$ and $\tau_{\text{had}}\tau_{\text{had}}$. 70
6.3 Event categorization in the four dominant Higgs production modes. 71

7.1 Decay-mode grouping. 93
7.2 Selection cuts for the introduction of a decay-mode dependent efficiency correction factor measurement in the fit. 97
7.3 χ^2-compatibility test per combination group. 101

8.1 Grouped impact for low p_T^H VBF related PoIs in an original setting as well as in a fit based on combined fake templates. 110
8.2 Grouped impact for high p_T^H VBF related PoIs in an original setting as well as in a fit based on combined fake templates. 110
8.3 Measured $\sigma_H \times B(H \rightarrow \tau\tau)$ relative to SM expectation in the four dominant production modes. 123